Microscopic modelling of organic and iron-based superconductors

Dissertation

zur Erlangung des Doktorgrades

der Naturwissenschaften

vorgelegt beim Fachbereich Physik

der Johann Wolfgang Goethe-Universität

in Frankfurt am Main

von

Daniel Guterding

aus Wetzlar

Frankfurt am Main (2016)

vom Fachbereich Physik der

Johann Wolfgang Goethe-Universität als Dissertation angenommen.

Dekan: Prof. Dr. Owe Philipsen
Gutachter: Prof. Dr. Roser Valentí
Dr. Igor I. Mazin (Naval Research Laboratory, Washington, DC, USA)
Prof. Dr. Rafael Fernandes (Univ. of Minnesota, Minneapolis, MN, USA)

Datum der Disputation: 27. April 2017

Zusammenfassung

Der Begriff der *Supraleitung* beschreibt das Phänomen eines verschwindenden elektrischen Widerstandes in einem Material, welches dann als *Supraleiter* bezeichnet wird, unterhalb einer typischerweise sehr niedrigen kritischen Temperatur. Seit der Entdeckung der Supraleitung in Quecksilber im Jahre 1911 wurden viele weitere Supraleiter gefunden. Dazu gehören unter anderem die kupferbasierten Supraleiter, welche bereits in vielen technischen Gebieten Anwendung finden, die vor allem als Modellsysteme interessanten organischen Supraleiter mit relativ niedrigen kritischen Temperaturen, und die relativ jungen eisenbasierten Supraleiter, die in Zukunft möglicherweise für technische Anwendungen in Frage kommen. Die kritische Temperatur, unterhalb der Supraleitung auftritt, konnte in Wasserstoffverbindungen unter extremen Drücken kürzlich sogar in Temperaturbereiche angehoben werden, die während eines kalten antarktischen Winters anzutreffen sind.

Aufgrund ihrer besonderen Eigenschaften sind Supraleiter ein vielversprechender Ersatz für normalleitende Komponenten, die derzeit noch in den meisten elektronischen Geräten Anwendung finden. So können sie als Material für nahezu verlustfreie Kabel zur Energieübertragung, als Spulenmaterial in Magneten für die Erzeugung starker Magnetfelder oder in verschiedenen elektronischen Geräten, wie zum Beispiel in Detektoren für Magnetfelder, eingesetzt werden. Trotz dieser offensichtlichen Vorteile hängen die Kosten bei der Verwendung supraleitender Materialien in erster Linie vom Kühlaufwand ab, der benötigt wird, um den supraleitenden Zustand zu erreichen. Daher ist die Suche nach einem Supraleiter mit kritischer Temperatur oberhalb der Zimmertemperatur, welcher schließlich ein spezialisiertes Kühlsystem überflüssig machen würde, eines der wichtigsten Projekte derzeitiger Forschung im Bereich der Festkörperphysik.

Während eine Theorie der Supraleitung in einfachen Metallen basierend auf der Wechselwirkung von Gitterschwingungen und Elektronen bereits in den 1950er Jahren entwickelt wurde, hat sich inzwischen herausgestellt, dass viele Supraleiter in dem Sinne unkonventionell sind, dass ihr Verhalten nicht durch die zuvor genannte Theorie beschrieben wird. Unkonventionelle Supraleitung zeichnet sich gegenüber der konventionellen Supraleitung in erster Linie darin aus, dass die räumliche Symmetrie des zum supraleitenden Zustand gehörigen Ordnungsparameters eine andere ist. Während konventionelle Supraleiter einen räumlich uniformen Ordnungsparameter besitzen, weist der Ordnungsparameter unkonventioneller Supraleiter eine Struktur auf. Selbstverständlich wurden zur Beschreibung unkonventioneller Supraleiter alternative theoretische Ansätze entwickelt, aber die Debatte über deren Korrektheit dauert weiterhin an. Derzeit werden vorwiegend Theorien basierend auf Spin- oder Ladungsfluktuationen diskutiert. Letztlich führt das Fehlen einer vollständigen Theorie der Supraleitung jedoch dazu, dass eine gezielte Suche nach einem Supraleiter bei Zimmertemperatur praktisch unmöglich ist. Neue theoretische Ansätze werden daher ständig entwickelt, müssen ihren Wert aber zuerst durch die korrekte Vorhersage des supraleitenden Ordnungsparameters und weiterer Materialeigenschaften beweisen. Insbesondere für die Vorhersage der Übergangstemperatur in unkonventionellen Supraleitern existiert

jedoch, überwiegend aufgrund vieler technischer Schwierigkeiten bei der Lösung der zugrundeliegenden Modelle, noch keine quantitative Theorie.

Die vorliegende Arbeit stellt einen Beitrag zur Suche nach einer Theorie der unkonventionellen Supraleitung dar. Konkret wird eine Theorie der Supraleitung diskutiert, welche auf Spinfluktuationen durch Elektron-Elektron-Wechselwirkungen basiert und durch ihren Erfolg bei der Beschreibung der in den 1980er Jahren aufgekommenen kupferbasierten Supraleiter im Laufe der letzten Jahrzehnte eine gewisse Popularität erlangt hat. Dabei handelt es sich um die sogenannte *Näherung zufälliger Phase* für das *Hubbard-Modell*. Das Hubbard-Modell ist ein einfaches Modell, welches Elektronen beschreibt, die sich auf einem Gitter bewegen können. Zwischen den Elektronen gibt es eine starke Coulombabstoßung, wenn sie sich auf demselben Gitterplatz befinden. Erweiterungen des Hubbard-Modells existieren, zum Beispiel als Hubbard-Modell mit mehreren Orbitalen pro Gitterplatz, welches auch Terme wie die Interorbitalcoulombabstoßung, die Hundschen Regeln und Paarhüpfterme berücksichtigt. In Dimensionen größer als eins ist keine exakte Lösung des Hubbardmodells bekannt, weshalb man bei seiner Lösung auf Näherungsverfahren angewiesen ist. Eines dieser Verfahren ist die zuvor genannte Näherung zufälliger Phase. Diese basiert auf einer Störungsentwicklung der Suszeptibilität und summiert bestimmte elektronische Prozesse bis zu unendlicher Ordnung in der Wechselwirkung auf, während andere Prozesse vernachlässigt werden. Dadurch ergibt sich eine letztlich unkontrollierte Approximation, die praktisch jedoch sinnvolle Ergebnisse bei verhältnismäßig niedrigem Rechenaufwand liefert, sodass auch Modelle mit mehreren Orbitalen und komplizierten Wechselwirkungen untersucht werden können. Diese Methode wird in der vorliegenden Arbeit als diagrammatische Vielteilchentheorie detailliert hergeleitet und auf Modellsysteme angewendet, die im Rahmen der Dichtefunktionaltheorie für bestimmte Materialklassen aus *ab initio* Rechnungen konstruiert werden. Die Dichtefunktionaltheorie ist eine etablierte Technik zum Berechnen der elektronischen und magnetischen Eigenschaften von Materialien ausgehend nur von deren Kristallstruktur. Sie basiert auf der Idee, dass die Energie eines Vielteilchensystems ein Funktional der Elektronendichte ist. Ausgehend von dieser Idee lässt sich eine prinzipiell exakte iterative Methode zum Finden der Grundzustandsdichte und der Grundzustandswellenfunktion eines Vielteilchensystems formulieren. Die vorliegende Arbeit stellt die grundlegenden Theoreme und die zugehörigen Beweise detailliert vor. Die praktische Umsetzung dieser Theorie in Computerprogrammen erfordert jedoch gewisse Näherungen, welche ebenfalls erläutert werden, die wiederum eine korrekte Beschreibung komplizierter Vielteilchenphänomene wie der Supraleitung verhindern. Nichtsdestotrotz gibt die Methode Aufschluss über die Eigenschaften des Normalzustandes eines Materials, in welchem bei niedrigen Temperaturen Supraleitung auftritt. Der in dieser Arbeit entwickelte Ansatz benutzt die aus den *ab initio* Rechnungen gewonnenen Informationen und kombiniert sie mit einer diagrammatischen Vielteilchentechnik, um sich dem supraleitenden Zustand vom normalleitenden Zustand aus anzunähern. Solch eine Kombination verschiedener Rechentechniken bedeutet einen hohen Implementierungsaufwand in Form von Computerprogrammen. Den gesamten Programmcode in dieser Arbeit abzudrucken wäre weder der Übersichtlichkeit des Gesamtwerks, noch dem Verständnis der Methode zuträglich. Weil die Herleitung der Methode jedoch bereits einige Näherungen enthält, die auf Anforderungen einer numerischen Implementierung eingehen, wird die Umsetzung als

Computerprogramm umfassend erläutert.

Die erste Klasse von Materialien, auf welche die zuvor beschriebenen Rechenmethoden in der vorliegenden Arbeit angewendet werden, sind quasi-zweidimensionale organische Ladungstransfersalze. Diese quasi-zweidimensionalen organischen Materialien sind seit mehr als zwei Jahrzehnten ein Gebiet aktiver Forschung, welche im Laufe der Zeit viele chemische Verbindungen mit zahlreichen Polymorphen hervorgebracht hat. Organische Ladungstransfersalze sind jedoch nicht nur aufgrund ihrer chemischen Flexibilität, sondern auch aufgrund ihrer unter anderem durch Druck oder Bestrahlung leicht manipulierbaren Eigenschaften für die Festkörperforschung interessant. Ein Beispiel für diese leichte Einstellbarkeit von gewünschten Eigenschaften ist der kürzlich experimentell beobachtete reversible Metall-Isolator-Übergang in Abhängigkeit der Probenabkühlrate. Dieses Phänomen wird in der vorliegenden Arbeit basierend auf Rechnungen im Rahmen der Dichtefunktionaltheorie und mit Hilfe von Literaturergebnissen zum Hubbard-Modell auf dem anisotropen Dreiecksgitter erklärt. Insbesondere wird gezeigt, dass die Konformationen von Molekülen in molekularen Festkörpern erheblichen Einfluss auf die elektronischen Eigenschaften haben können. Dies führt aufgrund metastabiler Konformationen, welche sowohl die Coulombabstoßung auf den Molekülen, als auch die kinetische Energie der Elektronen beeinflussen, unter anderem zu dem beobachteten Metall-Isolator-Übergang. Zudem wurden an organischen Materialien, insbesondere an der Untergruppe der sogenannten *Kappa-Typ* Materialien, eine Vielzahl von Experimenten zur Bestimmung der Eigenschaften des supraleitenden Zustandes durchgeführt. Obwohl sich inzwischen die Meinung etabliert hat, dass organische Ladungstransfersalze unkonventionelle Supraleiter sind, so bleiben die experimentellen Ergebnisse in Bezug auf die genaue Symmetrie des supraleitenden Ordnungsparameters doch widersprüchlich.

Zudem ist die komplizierte experimentelle Situation nur schwer mit dem theoretischen Konsens zu vereinbaren, der lediglich eine bestimmte Symmetrie vorhersagt, die nur in einem Bruchteil der Experimente tatsächlich beobachtet wird. Die meisten der relevanten theoretischen Arbeiten basieren jedoch auf einem stark vereinfachten Modell. In der vorliegenden Arbeit werden diese Vereinfachungen vermieden, indem die Modelle für organische Ladungstransfersalze, im Gegensatz zu den zuvor genannten Studien, aus *ab initio* Rechnungen konstruiert werden. Das neue Modell basiert im Gegensatz zu früheren nicht auf einem anisotropen Dreiecksgitter von dimerisierten Molekülen, sondern auf einem verallgemeinerten Shastry-Sutherland-Gitter der einzelnen Moleküle. Zudem wird die Coulombabstoßung nicht pro Moleküldimer, sondern auf jedem einzelnen Molekül betrachtet. Schließlich wird gezeigt, dass die existierenden theoretischen Ergebnisse von diesem neuen Modell in einem bestimmten Grenzfall reproduziert werden. Darüber hinaus zeigt das vollständige Modell jedoch einen Phasenübergang zwischen zwei supraleitenden Zuständen mit unterschiedlicher Symmetrie. Mit deren Hilfe lassen sich die meisten der experimentellen Ergebnisse erklären. Das auf *ab initio* Rechnungen basierende Modell hat daher das Potential die sich bereits über mehrere Jahrzehnte erstreckende Diskussion über die Symmetrie des supraleitenden Ordnungsparameters in quasi-zweidimensionalen organischen Ladungstransfersalzen vom Kappa-Typ zu entscheiden. Darüber hinaus werden verschiedene Ansätze für weitere Forschung auf Grundlage des neuen Modells vorgeschlagen.

Die zweite Klasse von Materialien, welche im Rahmen dieser Arbeit untersucht wird, sind eisenbasierte Supraleiter. Obwohl es sich dabei um ein recht junges Forschungsgebiet handelt, wurde bereits eine Vielzahl von supraleitenden eisenbasierten Verbindungen hergestellt. Wie in den quasi-zweidimensionalen organischen Materialien lässt sich der physikalische Grundzustand leicht durch äußeren Druck, aber auch durch veränderte chemische Zusammensetzung und die damit einhergende Dotierung mit Ladungsträgern einstellen. Das Verhalten vieler Materialien in dieser Klasse ist jedoch noch nicht gut verstanden.

In der vorliegenden Arbeit wird zuerst der supraleitende Zustand von Eisenselenid untersucht, welches mit Lithium und Ammoniak interkaliert ist. Zu dieser Verbindung existiert eine Vielzahl von Analoga, die durch Verwendung anderer Alkali- oder Erdalkalimetalle und eines anderen Lösungsmittels erzeugt werden. All diese Materialien teilen sich jedoch die Eigenschaft, dass ein größerer Abstand zwischen den Eisenselenidlagen die kritische Temperatur der Supraleitung im Vergleich zu reinem Eisenselenid erhöht. Leider ist dieser Effekt jedoch empirisch auf eine Erhöhung der kritischen Temperatur auf etwa 46 Kelvin beschränkt. Mit Hilfe der Dichtefunktionaltheorie wird in der vorliegenden Arbeit gezeigt, dass der erhöhte Abstand zwischen den Eisenselenidlagen zu einer Reduktion der elektronischen Dimensionalität führt. Anschließend wird der Einfluss der Elektronendotierung auf die Struktur der nichtwechselwirkenden Suszeptibilität im Impulsraum analysiert. Diese Untersuchung gibt Aufschluss darüber, warum in elektronendotiertem Eisenselenid bisher keine magnetische Ordnung gemessen wurde. Darauf folgt eine Analyse des supraleitenden Zustandes basierend auf der Näherung zufälliger Phase als Funktion des Abstandes zwischen den Eisenselenidlagen und der Elektronendotierung. Es zeigt sich, dass die Annäherung an eine perfekt zweidimensionale elektronische Struktur die kritische Temperatur des supraleitenden Überganges erhöht. Des Weiteren ergibt die Untersuchung des Einflusses von Ladungsdotierung, dass sich die supraleitende Übergangstemperatur durch Elektronendotierung mittels der interkalierten Alkaliatome einstellen lässt. Dieses Verhalten wird im Rahmen einer Analyse der elektronischen Zustandsdichte, und damit verbunden der nichtwechselwirkenden Suszeptibilität, plausibel gemacht. Die vorliegende Studie stellt daher insbesondere eine wertvolle Ressource für Kristallzüchter dar, die sich mit der Optimierung interkalierten Eisenselenids befassen.

Das zweite Material aus der Familie der eisenbasierten Supraleiter, welches in der vorliegenden Arbeit untersucht wird, ist KFe_2As_2 unter Hochdruck. Dieses Material erlangte unter anderem dadurch Berühmtheit, dass es als eines von wenigen eisenbasierten Materialien ohne die Notwendigkeit chemischer Dotierung bei niedrigen Temperaturen supraleitend ist. Unter Hochdruck ereignet sich in KFe_2As_2 bei einem bestimmten kritischen Druck ein Volumenkollaps von mehreren Prozent, der mit einer starken Erhöhung der kritischen supraleitenden Temperatur einhergeht. Solche volumenkollabierten Phasen sind bereits aus anderen Eisenpniktidverbindungen wie $CaFe_2As_2$ bekannt, jedoch wurde bisher angenommen, dass solche volumenkollabierten Phasen niemals Supraleitung zeigen. Das besondere Verhalten von KFe_2As_2 wird hier mit Hilfe der Dichtefunktionaltheorie und der Näherung zufälliger Phase erklärt. Es wird gezeigt, dass sich die elektronische Struktur von KFe_2As_2 durch den Volumenkollaps abrupt ändert. Zu Vergleichszwecken wird die nichtwechselwirkende Suszeptibilität im Impulsraum sowohl für volumenkollabiertes KFe_2As_2, als auch für kollabiertes $CaFe_2As_2$ berechnet. Diese zeigt in $CaFe_2As_2$ keine auffälligen Strukturen, wohingegen in KFe_2As_2 die üblichen Siganturen eisenbasierter Supraleitung zu sehen sind.

Durch die intrinsiche Lochdotierung dieses Materials besitzt es im Gegensatz zu anderen Eisenpniktiden auch in der volumenkollabierten Phase sowohl Loch-, als auch Elektronenzustände im Bereich der Fermienergie, ganz ähnlich wie andere Verbindungen ohne Volumenkollaps und ohne starke Dotierung. Daher ist es plausibel, dass sich KFe_2As_2 in der volumenkollabierten Phase ähnlich verhält wie unkollabierte Eisenpniktide und dass der Mechanismus der Supraleitung in diesen Materialien identisch ist.

Zu guter Letzt widmet sich die vorliegende Arbeit der Unterfamilie der Eisengermanide. Diese sind isoelektronisch und isostrukturell zu Eisenpniktiden und Eisenchalcogeniden. Da die elektronischen Zustände dieser Materialien im Bereich der Fermienergie praktisch identisch sind, könnte man erwarten, dass auch Eisengermanide gute Supraleiter sind. Tatsächlich sind diese jedoch entweder bei sehr niedrigen Temperaturen oder überhaupt nicht supraleitend. Um diesem Phänomen auf den Grund zu gehen, widmet sich die vorliegende Arbeit einem bisher vernachlässigten Bestandteil vieler Eisenpniktide und -germanide. So wurden Alkali-, Erdalkali- und Übergangsmetallatome zwischen den zweidmensionalen Eisengermanid- oder Eisenpniktidschichten bisher nur als Ladungsreservoire wahrgenommen, die ansonsten für die Physik der eisenbasierten Supraleiter irrelevant sind. In der vorliegenden Arbeit wird jedoch gezeigt, dass diese entscheidend an der Unterdrückung der Supraleitung in Eisengermaniden beteiligt sind. Eine eingehende Analyse der Eisengermanide zeigt, dass diese im Gegensatz zu Eisenpniktiden oder -chalcogeniden ferromagnetische statt antiferromagnetische Tendenzen aufweisen. Mittels des erweiterten Stoner-Formalismus wird geklärt, dass diese ferromagnetischen Tendenzen, entgegen einiger Spekulationen in der Literatur, nicht auf den Volumenkollaps oder die Lochdotierung einiger Eisengermanidverbindungen zurückgehen, sondern generell in allen Eisengermaniden auftreten. Stattdessen haben die Zustände der zuvor nur für Ladungsreservoire gehaltenen Atome in den Zwischenebenen einen entscheidenden Einfluss auf die elektronische Struktur in der Nähe der Fermienergie. Tatsächlich führt die Anwesenheit di- und trivalenter Ionen in den Zwischenebenen der Eisengermanide zu einem starken Abflachen bestimmter elektronischer Zustände in der Nähe des Ferminiveaus. Zudem konnten durch Modifikation der Kristallstruktur im Bereich der zuvor nur für Ladungsreservoire gehaltenen Alkaliatome zwischen den eisenhaltigen Schichten sogar in einem Eisenpniktid ferromagnetische Tendenzen induziert werden. Obwohl deren mikroskopischer Ursprung noch ungeklärt ist, zeigt dies, dass das Auftreten von Ferromagnetismus in eisenbasierten Verbindungen auch nicht von der Anwesenheit von Germanium abhängt, sondern dass ein *bis dato* unbekannter Effekt am Werk ist, der auch in bereits bekannten supraleitenden Verbindungen versteckt eine Rolle spielen könnte. Die vorliegende Studie widerlegt die weit verbreitete Annahme, die Atome zwischen den eisenhaltigen Schichten stellten lediglich Ladungsreservoire dar und könnten ansonsten vernachlässigt werden. Stattdessen wird vorgeschlagen, die üblichen Modelle für eisenbasierte Supraleiter auf alle Konstituenten der kristallografischen Einheitszelle zu erweitern, um zu einem vollständigen Verständnis der Abwesenheit von Supraleitung in Eisengermaniden zu kommen.

Abstract

The term *superconductivity* describes the phenomenon of vanishing electrical resistivity in a certain material, then called a *superconductor*, below a critical typically very low temperature. Since the discovery of superconductivity in mercury in 1911 many other superconductors have been found and the critical temperature below which superconductivity occurs could recently be raised to the temperatures encountered in a cold antarctic winter.

Superconductors are promising materials for applications. They can serve as nearly loss-free cables for energy transmission, in coils for the generation of high magnetic fields or in various electronic devices, such as detectors for magnetic fields. Despite their obvious advantages, the cost for using superconductors, however, depends a lot on the cooling effort needed to realize the superconducting state. Therefore, the search for a superconductor with critical temperature above room-temperature, which would avoid the need for any specialized cooling system, is one of the main projects of contemporary research in condensed matter physics.

While a theory of superconductivity in simple metals has already been developed in the 1950s, it has meanwhile been recognized that many superconductors are unconventional in the sense that their behavior does not follow the aforementioned theory. Unconventional superconductors differ from conventional superconductors mainly by the momentum- and real-space symmetry of the order parameter, which is associated with the superconducting state. While conventional superconductors have a uniform order parameter, unconventional superconductors can have an order parameter that bears structure. Of course, alternative theoretical descriptions have been suggested, but the discussion on the right theory for unconventional superconductivity has not yet been settled. Ultimately, this lack of a general theory of superconductivity prevents a targeted search for the room-temperature superconductor. Any new theoretical approach must, however, prove its value by correctly predicting the structure of the superconducting order parameter and further material properties.

In this work we participate in the search for a theory of unconventional superconductivity. We discuss the theory of superconductivity mediated by electron-electron interactions, which has been popular in the last few decades due to its success in explaining various properties of the copper-based superconductors that emerged in the 1980s. We give a detailed derivation of the so-called *random phase approximation* for the *Hubbard model* in terms of a diagrammatic many-body theory and apply it in conjunction with low-energy kinetic Hamiltonians, which we construct from first principles calculations in the framework of density functional theory. Density functional theory is an established technique for calculating the electronic and magnetic properties of materials solely based on their crystal structure. Its practical implementations in computer codes, however, do for example not describe complicated many-electron phenomena like the superconducting state that we are interested in here. Nevertheless, it can provide important information about the properties

of the normal state of the material, which superconductivity emerges from. In our theory we use these information and approach the superconducting state from the normal state.

Such an interfacing of different calculational techniques requires a lot of implementation work in the form of computer code. Inclusion of the computer code into this work would consume by far too much space, but since some of the decisions on approximations in the calculational formalism are guided by the feasibility of the associated computer calculations, we discuss the numerical implementation in great detail.

One class of materials that we apply our computer codes to are quasi-two-dimensional organic charge transfer salts. Quasi-two-dimensional organic materials have been a topic of active research for more than two decades. This family of materials contains many compounds with various polymorphs. Those materials are not only chemically very flexible, but their properties can also easily be tuned by application of pressure or irradiation. An example of this tunability is the reversible cooling-rate dependent metal-to-insulator transition, which has recently been demonstrated experimentally. A multitude of experiments has also been performed to elucidate the nature of the superconducting state in organic charge transfer salts, and in particular on the kappa-type materials, which denote a certain subclass of quasi-two-dimensional organics. Although the consensus seems to be that the mechanism in these materials must be unconventional, experimental results on the precise symmetry of the order parameter remain contradictory.

The complex experimental situation in turn can not be reconciled with a theoretical consensus that predicts a certain symmetry of the order parameter, which is only found by a fraction of the experiments. Most of those theoretical predictions are, however, based on a certain simplified model. We construct a model from first principles calculations, discarding simplifications made in previous studies, and arrive at a description, which reproduces previously obtained theoretical results in a certain limit. Moreover, we find a phase-transition between two different symmetries for the order parameter in our model, which is, therefore, able to explain most of the experimental results in the literature. Our model has the potential of settling the decades-long discussion about the symmetry of the superconducting state in kappa-type organic charge transfer salts.

The other class of materials we are interested in are iron-based superconductors. Despite being a relatively young field of research, iron-based superconductors have been synthesized in a great variety of compositions. Like the quasi-two-dimensional organic materials they are easily tunable by pressure, but also by charge doping through varied chemical composition. The behavior of many compounds in this class of materials is still not well understood. We start by investigating the superconducting state of iron selenide intercalated with lithium and ammonia. There are many analogous compounds produced from other alkaline or alkaline earth atoms and a different solvent. However, they all share the characteristic that larger separation of the iron selenide layers enhances superconductivity compared to bulk FeSe and that the superconducting transition temperature seems to be limited to about 46 Kelvin. We show that superconductivity is enhanced as the larger separation of the iron selenide layers makes the electronic properties of the material almost two-dimensional. Furthermore, the exact value of the superconducting transition temperature is tuned by the level of electron doping from the alkaline atoms into the iron selenide layers. Our study provides important guidance to experimentalists trying to design new intercalates of iron selenide.

The second iron-based material we are interested in is KFe_2As_2 under high pressure. This material undergoes a large abrupt change in volume, the so-called collapse, at very high pressures. Such collapsed phases have been observed in other iron pnictides, but they always turned out to be non-superconducting. However, KFe_2As_2 features superconductivity in the collapsed phase at even higher temperatures than in the non-collapsed low-pressure crystal structure. We explain this behavior by a reconstruction of the electronic structure upon the volume collapse and the hole doping of KFe_2As_2 compared to other iron pnictides.

Finally, we investigate the family of iron germanide materials. These are isoelectronic and isostructural to iron pnictides and chalcogenides. Based on the fact that their low-energy electronic structure is virtually identical to that of most iron-based superconductors, one would also expect iron germanides to be good superconductors. They, however, either superconduct at much lower temperatures or not at all. Challenging the previous notion that alkaline or alkaline earth atoms between the iron germanide or iron pnictide layers only play the role of charge reservoirs, we show that they are decisive in inducing ferromagnetic tendencies in iron germanides, which in turn suppress superconductivity in this class of materials. We present an analysis of these ferromagnetic tendencies within the extended Stoner formalism and demonstrate that ferromagnetism in iron germanides is a general trait. Using structural modifications only in the interlayer region previously deemed a charge reservoir, we are able to also induce ferromagnetism in a hypothetical iron pnictide compound, proving that not even the presence of germanium is a necessary condition for ferromagnetic tendencies to appear. Our study suggests that the common notion of interlayer atoms being irrelevant for the physics of iron-based superconductors beyond their role as charge reservoirs is incorrect. We propose instead that superconductivity in iron-based materials can only be fully understood based on models that include all constituents of the crystallographic unit cell.

Contents

1 Introduction **1**
- 1.1 From the ab initio Hamiltonian to the lattice description of solids 1
- 1.2 Superconductivity 3
- 1.3 Kappa-type organic charge transfer salts 4
- 1.4 Iron-based superconductors 7

2 Density functional theory **11**
- 2.1 Born-Oppenheimer approximation 11
- 2.2 Foundations of density functional theory 14
  - 2.2.1 Hohenberg-Kohn theorem 14
  - 2.2.2 Kohn-Sham auxiliary system 16
- 2.3 Practical approximations 18
  - 2.3.1 Local density approximation 18
  - 2.3.2 Generalized gradient approximation 19
- 2.4 Basis sets 19
  - 2.4.1 Full-potential local-orbital formulation 19
  - 2.4.2 Projector augmented wave formulation 22
- 2.5 Structural optimization 24
- 2.6 Wannier functions 25

3 The Green's function formalism **29**
- 3.1 Green's functions at zero temperature 29
  - 3.1.1 Interaction representation 29
  - 3.1.2 S matrix 30
  - 3.1.3 Real-time Green's functions at zero temperature 31
  - 3.1.4 Wick's theorem 32
  - 3.1.5 Feynman diagrams 34
  - 3.1.6 Linked cluster theorem 36
  - 3.1.7 Real-frequency Green's functions at zero temperature 37
- 3.2 Green's functions at finite temperature 38
  - 3.2.1 Imaginary-time Green's functions 38
  - 3.2.2 Imaginary-frequency Green's functions 39

4 Random phase approximation for the multi-orbital Hubbard model **43**
- 4.1 Preparations for the analytical derivation 44
  - 4.1.1 Kubo formula on the Matsubara axis 44
  - 4.1.2 Unperturbed charge susceptibility 44

4.1.3 Unperturbed spin susceptibility 45
4.1.4 Explicit expression for the unperturbed paramagnetic susceptibility 46
4.1.5 Connection between static susceptibility and real-space ordering . . 48
4.2 Analytical derivation in terms of Feynman diagrams 49
4.2.1 Fourier transformation of the interaction Hamiltonian 49
4.2.2 Diagrammatic expansion for the intra-orbital Coulomb repulsion . . 52
4.2.3 Diagrammatic expansion for the inter-orbital Coulomb repulsion . . 55
4.2.4 Diagrammatic expansion for the Hund's rule coupling 57
4.2.5 Diagrammatic expansion for the pair-hopping term 60
4.2.6 Tensor formulation of the multi-orbital susceptibility 62
4.2.7 Approximation for the two-electron pairing vertex in terms of susceptibilities 63
4.2.8 Eigenvalue equation for the two-electron pairing vertex 67
4.2.9 Diagrammatic structure of the two-particle vertex in the multi-orbital case 68
4.3 Numerical implementation 69
4.3.1 Prerequesites 69
4.3.2 Efficient calculation of the unperturbed susceptibility 70
4.3.3 Finding the Fermi surface 71
4.3.4 Efficient calculation of the two-particle pairing vertex 74

5 Influence of molecular conformations on the electronic structure of kappa-type organic charge transfer salts 77
5.1 Methodology and calculation setup 78
5.2 Results and discussion 81
5.3 Summary and outlook 83

6 Symmetry of the superconducting pairing in kappa-type organic charge transfer salts 85
6.1 Methods and models 86
6.1.1 Ab initio calculations and model Hamiltonian 86
6.1.2 RPA spin-fluctuation calculations 89
6.1.3 Simulation of tunneling spectra in the superconducting state 90
6.2 Results and discussion 93
6.2.1 Ab initio calculations 93
6.2.2 Pairing symmetry in the dimer model 94
6.2.3 Pairing symmetry in the molecule model 95
6.2.4 Pairing symmetry phase diagram of the molecule model 99
6.2.5 Simulation of scanning tunneling spectroscopy 101
6.3 Summary and outlook 104

7 Importance of charge doping and interlayer distance in intercalated FeSe107
7.1 Methods and materials 109
7.2 Results and discussion 110

7.3 Summary 116

8 Symmetry of the superconducting pairing in KFe_2As_2 under pressure 117
8.1 Methods 118
8.2 Results and discussion 121
8.3 Summary 124

9 Non-trivial role of interlayer cations in iron-based superconductors 125
9.1 Methods and materials 126
9.2 Results and discussion 128
9.3 Summary and outlook 133

10 Summary and Outlook 135

Bibliography 137

Chapter 1

Introduction

In this first chapter Hamiltonians governing the physics of solids, methods to solve these Hamiltonians, and the phenomenon of superconductivity are discussed. Subsequently, the classes of materials investigated in this thesis are introduced.

1.1 From the ab initio Hamiltonian to the lattice description of solids

Solid state systems consist of a collection of atoms, containing positively charged nuclei and negatively charged electrons. Therefore, the only fundamental interaction of interest for a solid state physicist is the electromagnetic interaction between the nuclei and the electrons. The so-called *ab initio* Hamiltonian describing these interactions is given by

$$\begin{aligned} H &= T_{nuc} + T_{el} + V_{nuc-nuc} + V_{el-el} + V_{nuc-el} \qquad (1.1)\\ &= -\sum_{\alpha} \frac{\hbar^2 \nabla_\alpha^2}{2M_\alpha} - \sum_{j} \frac{\hbar^2 \nabla_j^2}{2m_e} \\ &\quad + \frac{1}{4\pi\epsilon_0} \left(\sum_{\alpha<\beta} \frac{Z_\alpha Z_\beta e^2}{|\mathbf{R}_\alpha - \mathbf{R}_\beta|} + \sum_{j<k} \frac{e^2}{|\mathbf{r}_j - \mathbf{r}_k|} - \sum_{j,\alpha} \frac{Z_\alpha e^2}{|\mathbf{r}_j - \mathbf{R}_\alpha|} \right), \qquad (1.2) \end{aligned}$$

where the first two terms T_{nuc} and T_{el} denote the kinetic energy of the nuclei and the electrons, the terms $V_{nuc-nuc}$, V_{el-el} and V_{nuc-el} describe the nucleus-nucleus, electron-electron and nucleus-electron interactions respectively. The term *ab initio* is used in this context, because Eq. 1.2 contains the full Coulomb interaction without any approximations.

The main reason why the *ab initio* Hamiltonian is hard to solve lies in the nature of the interaction term, through which each particle in the system of interest interacts with all other particles in that system. Therefore, the Hamiltonian cannot be separated into one-particle contributions and the problem has to be solved within a full many-body description. An exact solution of this problem is only feasible for few numbers of interacting particles, such as in small molecules, because the state space within a full quantum mechanical description grows exponentially with the number of involved particles.

For this reason, constructing an optimal approximate solution to the full *ab initio* problem is one of the key objectives of solid state physics. The most basic, although optional, simplification of Eq. 1.2 is the decoupling of ion and electron dynamics, which goes by the name of *Born-Oppenheimer approximation.* Further approximations can be introduced either in the form of approximate algorithms for solving the full *ab initio* problem or by treating an effective problem in a reduced state space.

Today, the first approach is widely used under the label of *density functional theory* (DFT), which exactly reformulates the *ab initio* problem in a form that is amenable for numerical approximations to the interaction terms. Density functional theory programs are commercially available and employed to solve problems ranging from dye chemistry to the magnetic properties of crystals.

The alternative route, i.e. solving effective problems, is often taken by solid state physicists. In crystalline systems the discrete nature of the atomic positions can be exploited to formulate an effective lattice problem, replacing the continuum *ab initio* Hamiltonian (Eq. 1.2). In second quantization the effective lattice Hamiltonian including one- and two-electron terms is given by

$$H = -\sum_{ij\sigma} t_{ij} c^{\dagger}_{i\sigma} c_{j\sigma} + \sum_{ijkl\sigma\sigma'} V^{jk}_{il} c^{\dagger}_{i\sigma} c^{\dagger}_{j\sigma'} c_{k\bar{\sigma}'} c_{l\sigma}, \tag{1.3}$$

where σ denotes the spin of the electrons and $\{i, j, k, l\}$ are generalized lattice site and atomic orbital indices. The operators $c^{\dagger}_{i\sigma}$ and $c_{i\sigma}$ create and annihilate an electron with spin σ on the lattice site and orbital indexed by i. The nature of the atoms on the crystal lattice is now encoded in the effective parameters t_{ij} and V^{jk}_{il}. Usually, the treatment is restricted to a small number of *active* orbitals, which considerably simplifies the problem. Such simplifications are often justified based on a separation of energy scales. For example, electrons strongly bound in low-energy states cannot be expected to play a role in processes that involve energies orders of magnitude smaller than the binding energy.

The challenge is now to choose the set of active orbitals and interaction terms so that the physics of interest is correctly described. This difficult problem is at the heart of what is called *modelling* a physical system. In this thesis a hybrid approach is taken, where the one-electron terms t_{ij} are calculated within a restricted subset of states using density functional theory, and the two-electron interaction terms are treated as parameters.

By restricting the two-electron interaction terms to intra-atomic processes, which means discarding off-site interactions, the problem is reduced to the *multi-orbital Hubbard Hamiltonian*

$$\begin{aligned} H =& H_0 + H_{\text{int}} \\ =& -\sum_{i,j,l_1,l_2\sigma} t^{l_1 l_2}_{ij} c^{\dagger}_{il_1\sigma} c_{jl_2\sigma} + U \sum_{i,l} n_{il\uparrow} n_{il\downarrow} + \frac{V}{2} \sum_{i,l_1,l_2\neq l_1} n_{il_1} n_{il_2} \\ & - \frac{J}{2} \sum_{i,l_1,l_2\neq l_1} \mathbf{S}_{il_1} \cdot \mathbf{S}_{il_2} + \frac{J'}{2} \sum_{i,l_1,l_2\neq l_1,\sigma} c^{\dagger}_{il_1\sigma} c^{\dagger}_{il_1\bar{\sigma}} c_{il_2\bar{\sigma}} c_{il_2\sigma}, \end{aligned} \tag{1.4}$$

where i, j now denote only lattice sites, the l_i denote atomic orbitals and σ is the spin of the electrons. The number operator is given by $n_{il\sigma} = c^{\dagger}_{il\sigma} c_{il\sigma}$. The interaction parameters are the intra-orbital Coulomb repulsion (U), the inter-orbital Coulomb repulsion (V), the

Hund's rule coupling (J) and the pair-hopping term (J'). Effective Hamiltonians of this form are routinely considered in the modelling of transition metal compounds.

In cases where only one orbital per lattice site is relevant, the problem can be simplified to take the form of the *single-orbital Hubbard Hamiltonian*

$$H = H_0 + H_{\text{int}} = -\sum_{ij\sigma} t_{ij} c^{\dagger}_{i\sigma} c_{j\sigma} + U \sum_{i} n_{i\uparrow} n_{i\downarrow}, \tag{1.5}$$

where only the hopping and intra-orbital Coulomb repulsion terms remain. This type of Hamiltonian is the minimal model for the physics of strongly correlated electrons and often used in the context of cuprate or organic superconductors.

1.2 Superconductivity

Superconductivity is a quantum mechanical phenomenon that manifests itself macroscopically in the total vanishing of electrical resistivity and the perfect expulsion of any magnetic fields from a sample. After the initial 1911 discovery of superconductivity in mercury below a temperature of 4.2 K [1] many other elements and more complex materials have been found to superconduct below a material-specific critical temperature T_c [2].

The phenomenon gained widespread attention with the advent of copper-based *high-temperature superconductors* [3], which were quickly improved to superconduct above the boiling point of nitrogen (77 K) [4], allowing the switch from liquid helium to this much cheaper cooling medium. Meanwhile, the record critical temperature has been raised to 203 K in sulfur hydride under extremely high pressures [5]. Devices built from superconductors comprise sensitive magnetometers, power cables and superconducting electromagnets, such as those used in magnetic resonance imaging.

The first microscopic theory of superconductivity was developed by Bardeen, Cooper and Schrieffer (BCS) in 1957 [6]. It is built around the idea that the interaction between electrons and lattice vibrations, called *phonons*, can lead to an effective attraction between electrons. The ground state of the superconductor is formed by bound pairs of electrons with opposite momentum $\mathbf{k}$ and spin σ, whose average excitation energy above the Fermi sea is about $\Delta = k_B T_c$. Therefore, unlike conduction electrons in a metal, these so-called *Cooper pairs* do not scatter, which explains the lack of resistivity at temperatures below T_c. For historical reasons, superconductors that follow the predictions of the BCS theory or its extensions are called *conventional*. This class comprises, for example, elements, simple alloys and hydrogen-rich materials.

Obviously, there are also several classes of *unconventional* superconductors, where the electron pairing is not believed to be of phononic origin. This class of materials comprises, for example, cuprates, organic charge transfer salts and iron-based compounds. For all of these materials the electron pairing mechanism has been speculated to have a magnetic origin [7]. Physics of this kind is contained in the Hubbard Hamiltonian (Eq. 1.5), which describes repulsive interactions in real-space. When Fourier transformed into momentum space, these interactions can however be attractive for certain regions in $\mathbf{k}$-space and lead to electron pairing. In multi-orbital models (Eq. 1.3 and 1.4) several interaction terms

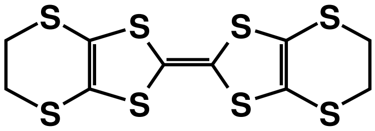

Figure 1.1: Structural formula of the bis-ethylenedithio-tetrathiafulvalene (BEDT-TTF or ET) molecule. The outermost carbon atoms are implied to bond to two hydrogen atoms each.

compete with each other, but again the electron-electron interaction can become attractive in momentum space.

A complete microscopic theory of superconductivity mediated by magnetic fluctuations has not been developed yet, because of difficulties in solving realistic multi-orbital Hamiltonians. Even the single-orbital Hubbard model poses a considerable challenge and no exact solution exists in dimensions larger than one. Therefore, a variety of approximations has been introduced, based on which some properties of unconventional superoconductors can be calculated.

While conventional superconductors feature a near uniform excitation gap Δ, a momentum dependence of this excitation gap is a hallmark of unconventional superconductivity. In cuprate superconductors it has been established experimentally that the gap $\Delta_{\mathbf{k}}$ goes to zero in so-called *nodal regions* and changes sign under rotation by 90 degrees [8]. Usually, the symmetry of the superconducting gap is classified using spherical harmonics. For example, the superconducting order parameter in cuprates has a $d_{x^2-y^2}$ symmetry.

The symmetry of the superconducting gap, and in particular the nodal structure, crucially influences thermodynamic and transport properties in unconventional superconductors. Therefore, most theoretical studies concentrate on predicting the symmetry of the superconducting state, which is a qualitative property, instead of trying to quantitatively predict the critical temperature, which strongly depends on the approximations employed.

1.3 Kappa-type organic charge transfer salts

A charge transfer complex is comprised of molecules which exchange charges and get stabilized by the resulting electrostatic forces. The electron donor molecules are called *cations*, while the electron acceptors are called *anions*. Some charge transfer complexes can condense in crystallized form.

Many different donor molecules are available and form crystals with certain electron acceptor complexes. The electron donor complex of central interest for this thesis is bis-ethylenedithio-tetrathiafulvalene ($C_{10}H_8S_8$), often abbreviated as BEDT-TTF or ET, which is shown in Fig. 1.1. The molecule contains three double bonds, so that it can easily donate electrons to an acceptor molecule. A wide variety of acceptor complexes exists, many of them forming polymeric chains.

The combination of ET donors and various acceptor molecules yields a large family of materials, the ET-based *organic charge transfer salts*. Interestingly, the ET molecules can be packed in various different ways that result in distinct physical behavior [9]. The

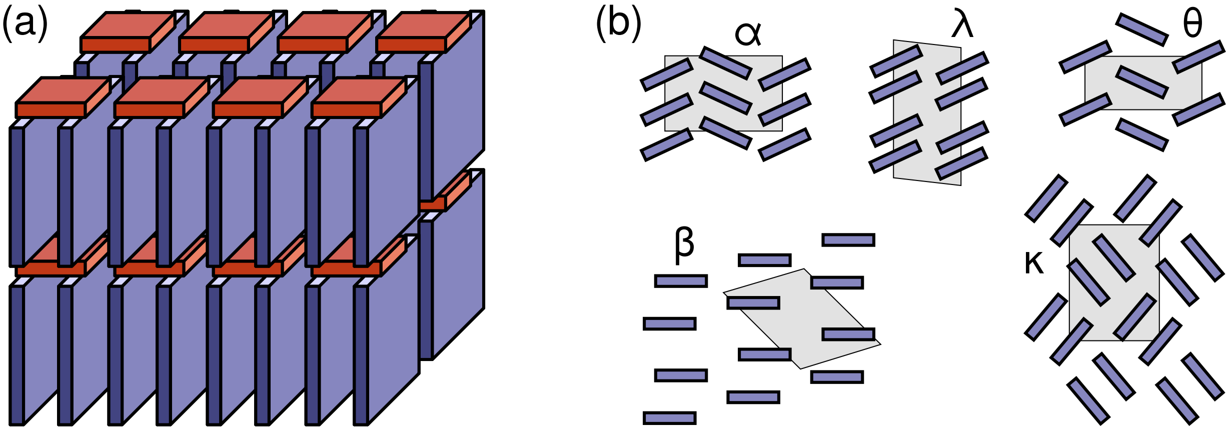

Figure 1.2: (a) Schematic three-dimensional arrangement of ET molecules (depicted as blue plates) and anions (red plates) within an organic charge transfer salt. Figure adapted from Ref. [10]. (b) Various possible packing motifs (top view) within the two-dimensional ET layer. The unit cells are shown as grey shaded areas. Figure adapted from Ref. [9].

compound name usually carries a prepended greek letter indicating the packing motif, for example κ-(ET)$_2$I$_3$, because many organic charge transfer salts exist as polymorphs.

Materials based on ET are often called *quasi-two-dimensional* for the reason that they feature a layered structure of donors and insulating acceptors. The schematic crystal structure and some packing motifs of the donor layer are shown in Fig. 1.2. The focus of the present thesis lies on the κ-motif, in which dimers of ET molecules donate one electron to the anion layer, which in turn becomes insulating. The ET molecules are connected in a quasi-two-dimensional network consisting of dimers rotated with respect to each other. On average half a hole resides on each ET molecule.

Based on the fractional band filling one would expect metallic conductance for κ-type materials. Experimentally they are however found to show a wide variety of behaviors including bad metallicity, Mott insulator, unconventional superconductor and quantum spin-liquid [9, 11–15], which can be tuned by the application of pressure. The competition of many exotic states of matter is the hallmark of organic charge transfer salts and other quasi-two-dimensional materials. Similarities between the superconducting states of cuprates and organics have been noted in the literature [16].

The current theoretical understanding of κ-type organics is based on the anisotropic triangular lattice model with on-site Coulomb repulsion (see Eq. 1.5), also called the anisotropic triangular lattice Hubbard model. Obviously, this model does not correspond to the complex geometry of the κ-layer shown in Fig. 1.2. However, the anisotropic triangular lattice Hubbbard model can be obtained as a simplification of a realistic Hamiltonian in a certain limit [17, 18].

The anisotropic triangular lattice Hubbard model has been quite successful at explaining the overall phase-diagram of κ-type organics, reproducing the bad metal, Mott insulator and quantum spin-liquid ground states observed in experiment. Many theoretical meth-

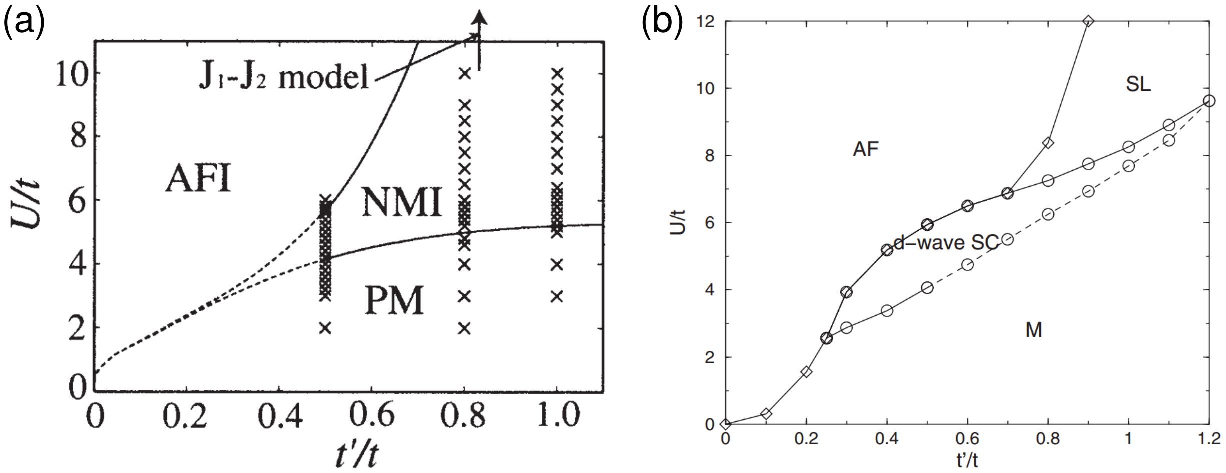

Figure 1.3: Phase diagram of the anisotropic triangular lattice Hubbard model calculated using (a) the path-integral renormalization group [23] and (b) cluster dynamical mean field theory [25]. The parameter t'/t is the ratio of the hopping amplitudes on a triangle, where t' is associated with one side of the triangle and t with the other two sides. A perfect triangular lattice is reached in the limit $t'/t = 1$. The parameter U/t controls the strength of the Coulomb repulsion. The phases encountered are antiferromagnetic insulator (AFI, AF), non-magnetic insulator (NMI, SL), paramagnetic metal (PM, M) and d-wave superconductor.

ods, such as the fluctuation-exchange approximation (FLEX) [19–22], the path-integral renormalization group [23], cluster dynamical mean field theory [24–26], variational Monte Carlo [27–30] and exact diagonalization [31, 32] have been used to calculate the phase diagram of the anisotropic triangular lattice Hubbard model and they all roughly agree with each other (see Fig. 1.3).

Currently, the existence of a superconducting phase in the anisotropic triangular lattice Hubbard model is controversial. Those studies that do find evidence for superconductivity (see for example Refs. [19, 25]) predict it to have the same type of d-wave order parameter as in high-temperature cuprate superconductors [7].

Interestingly, the experimental situation is even more confusing. Even though superconducting κ-type charge transfer salts have been investigated in studies of specific heat [12, 33–37], surface impedance [38], thermal conductivity [39], millimeter-wave transmission [40], scanning tunneling spectroscopy (STS) [41–44] and elastic constants [45], the nature of superconductivity or even the symmetry of the order parameter could not be determined definitely yet. Some of the experiments are in favor of s-wave symmetry [12, 33, 34], while other studies have proposed d-wave states with contradictory positions of the nodes in the superconducting order parameter [35–43]. Evidence for a mixed-symmetry order parameter was recently provided in Refs. [44, 45] and evidence for phase separation of different d-wave states has recently been reported in Ref. [43].

Furthermore, a reversible cooling-rate dependent metal-to-insulator transition has re-

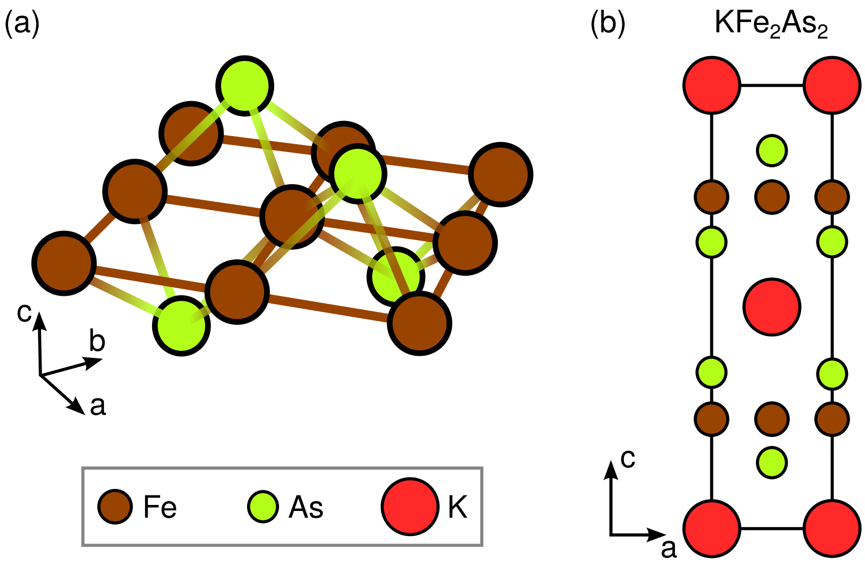

Figure 1.4: (a) Characteristic iron-arsenide layer of iron-based superconductors. For the central iron atom the imperfect tetrahedral coordination of the surrounding arsenic atoms is visible. (b) Crystal structure of KFe_2As_2, which is a representative of the 122 family of iron pnictides.

cently been observed in κ-$(ET)_2Cu[N(CN)_2]Br$ [46–48]. It has been associated with a freezing of intramolecular degrees of freedom, namely the orientation of ethylene endgroups within an ET molecule. With the exception of Ref. [49], this effect has surprisingly been interpreted as a sole consequence of lattice disorder, although a metal-to-insulator transition controlled by geometric frustration and correlation strength is present in the anisotropic triangular lattice Hubbard model (see Fig. 1.3). The effect of different molecular conformations on the electronic structure of κ-type charge transfer salts has been investigated in a single material using the extended Hückel method [50]. For ET molecules in vacuum more calculations are available [48, 51, 52].

Within this thesis the origin of the reversible cooling-rate dependent metal-to-insulator transition and the symmetry of the superconducting pairing are clarified within a theoretical approach.

1.4 Iron-based superconductors

Superconductivity in iron-based materials was initially discovered in 2008 in the layered $LaO_{1-x}F_xFeAs$ compound [53]. Subsequently, a large variety of materials containing either layers of iron and pnictogen atoms or iron and chalcogen atoms have been synthesized [54]. The prototypical crystal structure is shown in Fig. 1.4. The near-tetrahedral pnictogen or chalcogen environment of the iron atoms leads to a splitting of the iron atomic energy levels, so that only d_{xz} and d_{yz} remain degenerate. A large energy gap exists between the t_{2g} (d_{xy}, d_{xz}, d_{yz}) and e_g ($d_{x^2-y^2}$, d_{z^2}) states. Minor energy gaps are induced within these manifolds by the distortion of the tetrahedra. Therefore, the physics of iron-based

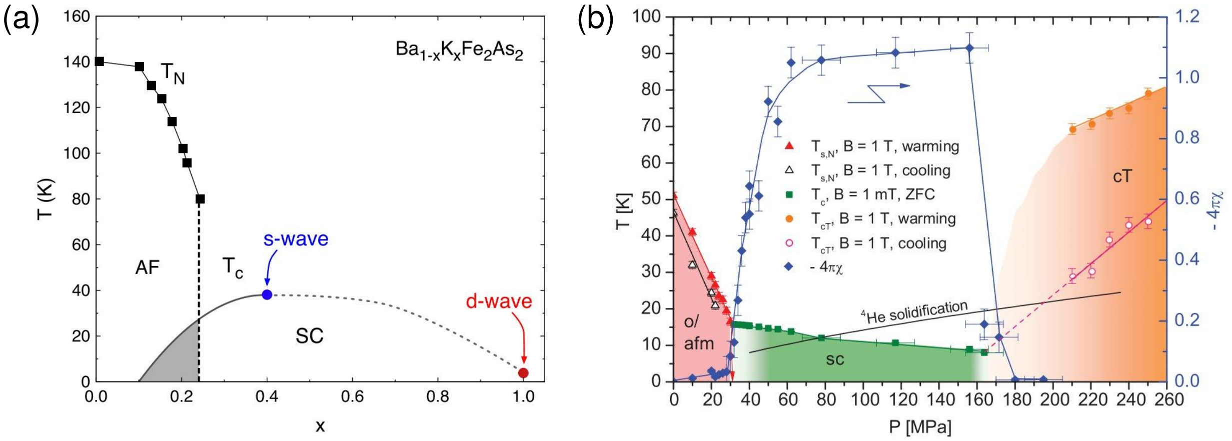

Figure 1.5: (a) Schematic phase diagram of $Ba_{1-x}K_xFe_2As_2$ [56]. Upon replacement of barium by potassium, which increases the nominal oxidation state of iron from Fe^{2+} to $Fe^{2.5+}$, the ground state evolves from an antiferromagnetic metal to a high-temperature s-wave superconductor at intermediate doping and finally to a low-temperature d-wave superconductor in the KFe_2As_2 limit. (b) Pressure phase diagram of $Ca(Fe_{0.972}Co_{0.028})_2As_2$ [57], in which a metallic antiferromagnet evolves into a superconductor and finally into a metallic volume-collapsed phase with increasing pressure.

superconductors is a multi-orbital problem.

Most iron pnictides and chalcogenides can be classified in so-called *families*, which share a common structural motif and nominal chemical composition. For example, materials like $BaFe_2As_2$, $CaFe_2As_2$ and KFe_2As_2 are called the *122-family* of iron pnictides. LiFeAs and NaFeAs are typical representatives of the *111-family* and LaOFeAs is the prototypical compound of the *1111-family*. Because the nominal charge distribution in iron arsenide layers is $Fe^{2+}As^{3-}$ or $Fe^{2.5+}As^{3-}$, additional atoms or layers, which are often insulating, must reside between the iron arsenide layers for charge neutrality. Iron selenide is the most important member of the *11-family*. It does not need any spacer layer, because the nominal charge distribution is $Fe^{2+}Se^{2-}$. However, spacer layers can also be inserted into iron selenide, which leads to so-called *intercalates* [55].

Often the spacer layers can be modified chemically, so that they inject or remove electrons from the iron pnictide or iron chalcogenide layer without introducing defects in the conductive layer. Such modifications are crucial in establishing high-temperature superconductivity, as most stoichiometric iron arsenide compounds (so-called *parent compounds*) are antiferromagnetic metals (see Fig. 1.5). The highest value of the superconducting transition temperature T_c achieved by electron doping of bulk materials is roughly 55 K in iron pnictides [58] and slightly lower in iron chalcogenides. Strongly electron-doped monolayers of iron selenide have also received a lot of attention, because they were recently reported to show superconductivity above 100 K [59]. Iron-based superconductors are however not only sensitive to charge doping, but also to pressure, which can be used to tune between different ground states (see Fig. 1.5).

The situation in iron pnictides and chalcogenides is decidedly different from that in iron germanide materials, which are isoelectronic and isostructural to the parent compounds of iron-based superconductors. Iron germanides are either non-supercon-ducting [60–63] or have been reported to superconduct at very low temperatures [64, 65].

Superconductivity in iron-based materials has become a vast field of research, where questions are often centered on the behavior of materials as a function of temperature, pressure or charge doping. Since a complete theory of superconductivity in these materials is currently missing, many slightly different theoretical approaches have been developed to explain the properties of individual materials or entire sub-families. Fortunately, density functional theory, a standard theoretical method, has been applied to iron-based superconductors with great success.

However, to obtain information on the superconducting state, further calculations are necessary. The model usually considered in this context is the multi-orbital Hubbard model (Eq. 1.4), which is very hard to solve because of the rapid growth of the Hilbert space with system size. Therefore, adequate approximations have been developed, which usually rely to some degree on input from density functional theory to take into account the material-specific details.

Within this thesis one of these approximations will be used to elucidate the importance of electron doping for high-temperature superconductivity in intercalated iron selenide and to investigate the pairing symmetry of KFe_2As_2 under pressure. Furthermore, a hidden ferromagnetic instability in iron-based superconductors is uncovered, which suppresses superconducting transition temperatures in iron germanides and is expected to be an important ingredient in a quantitative theory of superconductivity in iron-based materials.

Alternatives to the microscopic modelling attempted in this work exist in the form of effective Ginzburg-Landau type models for the phase transitions in iron-based materials [66–68]. These do not attempt to model materials based on atomic electronic states, but rather rely on the important symmetries of the problem to explain the qualitative phenomena instead of trying to generate quantitative results.

Chapter 2

Density functional theory

Density functional theory (DFT) is a standard method for solving the many-electron problem. It is a formally exact reformulation of the *ab initio* Hamiltonian based on the idea that any property of a system of many interacting particles can be viewed as a functional of its ground state density [69].

Although the reformulation is formally exact, any practical implementation of density functional theory has to rely on approximations to the electron-electron interaction and has to expand the electronic wavefunctions in a certain basis set. The precise nature of these approximations is a matter of choice, which is usually associated with a tradeoff between accuracy and computation time.

Within this chapter the theoretical foundations of density functional theory and aspects of practical implementation are explained. Furthermore, the prediction of crystal structures and the construction of lattice Hamiltonians from density functional theory are discussed. The presentation within this chapter is based on Ref. [69].

2.1 Born-Oppenheimer approximation

The first step in making the treatment of the *ab initio* Hamiltonian (Eq. 1.2) feasible is the decoupling of the nuclei and the electronic degrees of freedom, which goes by the name of Born-Oppenheimer approximation [70]. It is based on the idea that the dynamics of the nuclei is much slower than the electron dynamics, because the ratio of the electron mass over the nuclear mass is about $m/M \sim 10^{-4}$ to 10^{-5}.

Neglecting the kinetic energy of the nuclei, the *ab initio* Hamiltonian can be written as

$$\begin{aligned} H_{\text{el}} &= T_{el}(\underline{r}) + V_{nuc-nuc}(\underline{R}) + V_{el-el}(\underline{r}) + V_{nuc-el}(\underline{r},\underline{R}) && (2.1) \\ &= -\sum_j \frac{\hbar^2 \nabla_j^2}{2m_e} + \frac{1}{4\pi\epsilon_0}\left(\sum_{\alpha<\beta} \frac{Z_\alpha Z_\beta e^2}{|\mathbf{R}_\alpha - \mathbf{R}_\beta|} + \sum_{j<k} \frac{e^2}{|\mathbf{r}_j - \mathbf{r}_k|} - \sum_{j,\alpha} \frac{Z_\alpha e^2}{|\mathbf{r}_j - \mathbf{R}_\alpha|}\right), && (2.2) \end{aligned}$$

where $\underline{r} = \{\mathbf{r}_1, \mathbf{r}_2, \ldots, \mathbf{r}_{N_{\text{el}}}\}$ denotes the set of all electron positions and $\underline{R} = \{\mathbf{R}_1, \mathbf{R}_2, \ldots, \mathbf{R}_{N_{\text{nuc}}}\}$ denotes the set of all nuclear positions.

Assuming that the Schrödinger equation associated with Eq. 2.2 can be solved for a fixed set of nuclear parameters $\underline{R}$, the solution is given by

$$H_{\text{el}}\, \phi_\alpha(\underline{r},\underline{R}) = \varepsilon_\alpha(\underline{R})\phi_\alpha(\underline{r},\underline{R}), \qquad (2.3)$$

where α denotes a set of electronic quantum numbers and $\phi_\alpha(\underline{r}, \underline{R})$ is the electronic wavefunction, which depends on the nuclear configuration $\underline{R}$ in a parametric way. Note how fixing the nuclear environment has effectively reduced the full problem of nuclei and electrons to finding the electronic configuration within a fixed external potential provided by the nuclei.

Of course, the solution $\psi(\underline{r}, \underline{R})$ of the full *ab initio* Hamiltonian (Eq. 1.2) can be recovered from the solution of Eq. 2.3 as

$$H\,\psi(\underline{r}, \underline{R}) = E\,\psi(\underline{r}, \underline{R}), \tag{2.4}$$

because the full wavefunction $\psi(\underline{r}, \underline{R})$ can be expanded in terms of the solutions $\phi_\alpha(\underline{r}, \underline{R})$ of the electronic problem for each fixed set of nuclear parameters $\underline{R}$.

$$\psi(\underline{r}, \underline{R}) = \sum_\alpha \chi_\alpha(\underline{R})\phi_\alpha(\underline{r}, \underline{R}) \tag{2.5}$$

Here, $\chi_\alpha(\underline{R})$ are the $\underline{R}$-dependent expansion coefficients for each set of electronic quantum numbers α. The summation over α is necessary for taking into account all possible configurations of the electronic system.

Within this framework the secular equation (Eq. 2.4) can be rewritten as

$$\begin{aligned} 0 = (H - E)\,\psi(\underline{r}, \underline{R}) &= (H_{\mathrm{el}} + T_{nuc} - E)\,\psi(\underline{r}, \underline{R}) && (2.6)\\ &= \sum_\alpha \left(\varepsilon_\alpha(\underline{R}) + T_{nuc} - E\right)\chi_\alpha(\underline{R})\phi_\alpha(\underline{r}, \underline{R}), && (2.7)\end{aligned}$$

where we inserted the expansion of the full wavefunction (Eq. 2.5) and used the electronic Schrödinger equation (Eq. 2.3). This reformulation is formally exact and the complexity of the problem is still present, but hidden in the expansion coefficients $\chi_\alpha(\underline{R})$.

The objective is now to find a good approximation to these expansion coefficients that allows for an effective separation of electronic and nuclear dynamics. We start by integrating out the electronic degrees of freedom after multiplying Eq. 2.7 with $\phi^*_\beta(\underline{r}, \underline{R})$ from the left.

$$\begin{aligned} 0 &= \sum_\alpha \int d\underline{r}\,\phi^*_\beta(\underline{r}, \underline{R})\,(H_{\mathrm{el}} + T_{nuc} - E)\,\chi_\alpha(\underline{R})\phi_\alpha(\underline{r}, \underline{R}) && (2.8)\\ &= [\varepsilon_\beta(\underline{R}) - E]\,\chi_\beta(\underline{R}) + \underbrace{\sum_\alpha \int d\underline{r}\,\phi^*_\beta(\underline{r}, \underline{R})\,T_{nuc}\,\chi_\alpha(\underline{R})\phi_\alpha(\underline{r}, \underline{R})}_{=T_{nuc}\,\chi_\beta(\underline{R}) + \sum_\alpha A_{\beta\alpha}(\underline{R})\chi_\alpha(\underline{R})} && (2.9)\end{aligned}$$

Neglecting the matrix elements $A_{\beta\alpha}(\underline{R})$, a step which will be justified at the end of this section, we obtain an effective Schrödinger equation for the expansion coefficients $\chi_\alpha(\underline{R})$ given by

$$[T_{\mathrm{nuc}} + \varepsilon_\beta(\underline{R})]\,\chi_\beta(\underline{R}) = E\,\chi_\beta(\underline{R}), \tag{2.10}$$

where the eigenenergies $\varepsilon_\beta(\underline{R})$ of the reduced Hamiltonian (Eq. 2.2) take the role of an effective potential for the nuclei.

Using these results, a recipe for solving the full *ab initio* Hamiltonian can now be formulated, provided that the nuclear positions $\underline{R}$ are known:

1. Solve the electronic Schrödinger equation (Eq. 2.3) within the fixed external potential provided by the nuclei.
2. Solve the effective Schrödinger equation (Eq. 2.10) for the expansion coefficients of the full wavefunction.
3. Reconstruct the full wavefunction from Eq. 2.5.

In case the configuration of the nuclei is not known, a self-consistent cycle of these steps might be necessary, where, based on a trial set of $\underline{R}$, successively improving approximations for $\underline{R}$ are calculated from step 3 and re-inserted in step 1 until the full wavefunction converges. This formalism can be used to predict the spatial distribution of atoms within molecules and crystals, which is discussed in one of the following sections.

Now we are left with the task of providing a justification for neglecting the matrix elements $A_{\beta\alpha}(\underline{R})$, which are given by

$$\begin{aligned} A_{\beta\alpha}(\underline{R}) &= -\frac{\hbar^2}{2M_{\underline{R}}} \sum_{\alpha} \int d\underline{r} \left[2\phi^*_\beta(\underline{r},\underline{R}) \frac{\partial \phi_\alpha(\underline{r},\underline{R})}{\partial \underline{R}} \frac{\partial}{\partial \underline{R}} + \phi^*_\beta(\underline{r},\underline{R}) \frac{\partial^2 \phi_\alpha(\underline{r},\underline{R})}{\partial \underline{R}^2} \right] && (2.11) \\ &= \frac{1}{2M_{\underline{R}}} \sum_{\alpha} \int d\underline{r} \, \left[2\phi^*_\beta(\underline{r},\underline{R}) \left(p_{\underline{R}}\, \phi_\alpha(\underline{r},\underline{R})\right) p_{\underline{R}} + \phi^*_\beta(\underline{r},\underline{R}) \left(p^2_{\underline{R}} \phi_\alpha(\underline{r},\underline{R})\right) \right]. && (2.12) \end{aligned}$$

The $p_{\underline{R}}$ are the momentum operators acting within the Hilbert space of the nuclei. The $\underline{R}$-dependence of the electronic wavefunctions $\phi_\alpha(\underline{r},\underline{R})$ stems mostly from the electron-nucleus interaction, which depends only on the relative distance between electron and nucleus (see Eq. 2.2). Therefore, we can transform the momentum operators $p_{\underline{R}}$ that act on $\phi_\alpha(\underline{r},\underline{R})$ into $p_{\underline{r}}$, which acts within the Hilbert space of the electrons. Within this approximation we calculate the expectation value for $A_{\beta\alpha}(\underline{R})$, which is given by

$$\sum_{\alpha\beta} \chi_\beta(\underline{R}) A_{\beta\alpha}(\underline{R}) \chi_\alpha(\underline{R}) \propto \frac{1}{M} \langle p_{\mathrm{el}} \rangle \langle p_{\mathrm{nuc}} \rangle + \frac{1}{2M} \langle p^2_{\mathrm{el}} \rangle. \qquad (2.13)$$

Now we need approximations for the kinetic energy of the electrons and the nuclei. Assuming an effective harmonic potential for the nuclei and one Hartree ($1\mathrm{Ha} = me^4/\hbar^2$) as the energy scale of the kinetic energy of the electrons, we can roughly estimate the kinetic energy of the nuclei. We assume one Bohr, denoted by $a_0 = \hbar^2/(me^2)$ as the typical displacement of nuclei from their equilibrium position. The kinetic energy of the nuclei is then given by

$$T_{\mathrm{nuc}} \approx \hbar \sqrt{\frac{T_{\mathrm{el}}/a_0^2}{M}} = \sqrt{\frac{m}{M}} T_{\mathrm{el}}. \qquad (2.14)$$

The second term on the right-hand side of Eq. 2.13 is a factor m/M smaller than the kinetic energy of the electrons and therefore also a factor $\sqrt{m/M}$ smaller than the kinetic energy of the nuclei. Using $\sqrt{T_{\text{nuc}} T_{\text{el}}} \approx \sqrt{m/M} \langle p_{\text{nuc}} \rangle / \langle p_{\text{el}} \rangle$ and Eq. 2.14, the first term on the right-hand side of Eq. 2.13 can be approximated by

$$\frac{1}{M} \langle p_{\text{el}} \rangle \langle p_{\text{nuc}} \rangle \approx \frac{1}{M} \sqrt[4]{\frac{m}{M}} \langle p_{\text{nuc}} \rangle^2 \approx \sqrt[4]{\frac{m}{M}} T_{\text{nuc}}. \tag{2.15}$$

Therefore, the expectation value of $A_{\beta\alpha}(\underline{R})$ is at least one order of magnitude smaller than the kinetic energy of the nuclei, which should again be about two orders of magnitude smaller than the kinetic energy of the electrons. This justifies neglecting the contribution from $A_{\beta\alpha}(\underline{R})$ in Eq. 2.9 and, therewith, the decoupling of electron and nucleus dynamics within the Born-Oppenheimer approximation.

In this section we assumed that Eq. 2.3 can in principle be solved, but we did not specify how this is done in practice. Formulating the electronic problem in a way that it can be solved is the objective of the next section.

2.2 Foundations of density functional theory

2.2.1 Hohenberg-Kohn theorem

The basic theorems of density functional theory, which establish the unique connection between ground state density and external potential, were introduced by Hohenberg and Kohn in 1964 [71]. They are valid for any kind of particles, possibly with complicated interactions, moving in a fixed external potential. Therefore, they naturally apply to the problem of interacting electrons moving in the potential provided by fixed nuclei. The presentation of the theorems and proofs closely follows Ref. [69].

Theorem 1. *The external potential $V_{ext}(\mathbf{r})$ of any system of interacting particles is determined uniquely, except for a constant, by the ground state particle density $n_0(\mathbf{r})$.*

Proof. The proof proceeds by *reductio ad absurdum.* We assume that there are two external potentials $V^{(1)}_{\text{ext}}(\mathbf{r})$ and $V^{(2)}_{\text{ext}}(\mathbf{r})$, which differ by more than a constant, but lead to the same ground state density $n_0(\mathbf{r})$. If the external potentials are different, so are the corresponding Hamiltonians $H^{(1)}$ and $H^{(2)}$ and the corresponding ground state wavefunctions $\psi^{(1)}$ and $\psi^{(2)}$. Assuming that the ground state is non-degenerate, we obtain the inequality

$$E^{(1)} = \langle \psi^{(1)} | H^{(1)} | \psi^{(1)} \rangle < \langle \psi^{(2)} | H^{(1)} | \psi^{(2)} \rangle, \tag{2.16}$$

which holds because $\psi^{(2)}$ is not the ground state wavefunction of $H^{(1)}$. The last term in Eq. 2.16 can be rewritten as

$$\begin{aligned} \langle \psi^{(2)} | H^{(1)} | \psi^{(2)} \rangle &= \langle \psi^{(2)} | H^{(2)} | \psi^{(2)} \rangle + \langle \psi^{(2)} | H^{(1)} - H^{(2)} | \psi^{(2)} \rangle & (2.17) \\ &= E^{(2)} + \int d\mathbf{r} \, \left[V^{(1)}_{\text{ext}}(\mathbf{r}) - V^{(2)}_{\text{ext}}(\mathbf{r}) \right] n_0(\mathbf{r}). & (2.18) \end{aligned}$$

As Eq. 2.16 is also true under exchange of indices (1) and (2), we obtain two inequalities by inserting Eq. 2.18.

$$E^{(1)} < E^{(2)} + \int d\mathbf{r} \left[V_{\text{ext}}^{(1)}(\mathbf{r}) - V_{\text{ext}}^{(2)}(\mathbf{r})\right] n_0(\mathbf{r}) \tag{2.19}$$

$$E^{(2)} < E^{(1)} + \int d\mathbf{r} \left[V_{\text{ext}}^{(2)}(\mathbf{r}) - V_{\text{ext}}^{(1)}(\mathbf{r})\right] n_0(\mathbf{r}) \tag{2.20}$$

Adding Eqs. 2.19 and 2.20 a contradiction is obtained.

$$E^{(1)} + E^{(2)} < E^{(2)} + E^{(1)} \tag{2.21}$$

Therefore, the external potential $V_{\text{ext}}(\mathbf{r})$ is uniquely determined by the ground state density $n_0(\mathbf{r})$. □

Corollary 1. *It follows that the many-body wavefunction for ground and excited states of that system is determined by the ground state particle density* $n_0(\mathbf{r})$. *Therefore, all properties of the system are completely determined by the ground state particle density* $n_0(\mathbf{r})$.

Proof. Theorem 1 states that the Hamiltonian is uniquely determined by the ground state density $n_0(\mathbf{r})$. Therefore, the corresponding set of ground state and excited state wavefunctions can be obtained as eigenfunctions of the associated Schrödinger equation (Eq. 2.3). Based on these many-body wavefunctions any property of the system can be calculated. □

Theorem 2. *A universal energy functional* $E[n]$ *in terms of the density* $n(\mathbf{r})$ *can be defined and is valid for any external potential* $V_{ext}(\mathbf{r})$. *For any particular external potential* $V_{ext}(\mathbf{r})$ *the exact ground state energy of the system is the global minimum value of this functional and the density* $n(\mathbf{r})$ *that minimizes the value of the energy functional is the exact ground state density* $n_0(\mathbf{r})$ *of the system.*

Proof. Corollary 1 states that all properties of the system are determined by the ground state density $n_0(\mathbf{r})$. Therefore, the kinetic energy and the energy contribution from electron-electron interaction can be viewed as a functional of the particle density n. In analogy to the Hamiltonian given by Eq. 2.1 we define an energy functional.

$$E_{\text{HK}}[n] = T_{\text{el}}[n] + E_{\text{nuc-nuc}} + E_{\text{el-el}}[n] + \int d\mathbf{r}\, V_{\text{ext}}(\mathbf{r}) n(\mathbf{r}) \tag{2.22}$$

$$= F_{\text{HK}}[n] + \int d\mathbf{r}\, V_{\text{ext}}(\mathbf{r}) n(\mathbf{r}) + E_{\text{nuc-nuc}} \tag{2.23}$$

The Hohenberg-Kohn functional $F_{\text{HK}}[n]$ contains the kinetic energy of the electrons and the electron-electron interaction term. By construction this functional is universal for all electronic systems, since the constituent terms are functionals only of the electron density.

Now we take a ground state density $n^{(1)}(\mathbf{r})$ corresponding to an external potential $V_{\text{ext}}^{(1)}(\mathbf{r})$. This fixes the unique ground state energy $E^{(1)}$, which is equal to the value of the energy functional for that density.

$$E^{(1)} = E_{\text{HK}}[n^{(1)}] = \langle \psi^{(1)} | H^{(1)} | \psi^{(1)} \rangle \tag{2.24}$$

Considering some other density $n^{(2)}$ with associated wavefunction $\psi^{(2)}$ leads to an inequality, if we substitute $\psi^{(2)}$ into Eq. 2.24, since $\psi^{(2)}$ is not the ground state wavefunction of $H^{(1)}$.

$$E^{(1)} = \langle\psi^{(1)}|H^{(1)}|\psi^{(1)}\rangle < \langle\psi^{(2)}|H^{(1)}|\psi^{(2)}\rangle = E^{(2)} \tag{2.25}$$

Therefore, it is clear that the value of the energy functional $E_{\mathrm{HK}}[n]$ for any density that is not the ground state must be larger than the ground state energy. Therefore, the functional $E_{\mathrm{HK}}[n]$ has a unique global minimum for $n = n_0(\mathbf{r})$. □

Corollary 2. *The functional* $E[n]$ *alone is sufficient to determine the exact ground state energy and density.*

Proof. The value of the energy functional for a particular density configuration $n(\mathbf{r})$ can be obtained from Eq. 2.23. It follows from theorem 2 that a minimization of the energy functional $E_{\mathrm{HK}}[n]$ with respect to the density $n(\mathbf{r})$ yields the ground state density $n_0(\mathbf{r})$. □

The Hohenberg-Kohn theorem however provides no practical way to find the ground state density and in particular still requires the evaluation of the full electron-electron interaction (see Eq. 2.23), as well as the many-body Schrödinger equation (see Eq. 2.3) in order to obtain the many-body wavefunction and calculate any properties of the system beyond the ground state density. These shortcomings are addressed in the next subsection.

2.2.2 Kohn-Sham auxiliary system

In order to devise a feasible calculational method from the formally exact Hohenberg-Kohn theorem further developments are necessary. The most serious problem of the Hohenberg-Kohn method is that a full solution of the many-body Schrödinger equation is still required to calculate properties of the system of interest.

The Kohn-Sham approach, formulated in 1965 [72], is to replace the interacting problem (Eq. 2.2) by an effective non-interacting problem, which has the same ground state density, but is much easier to solve, as it only involves single-particle wavefunctions in a much smaller Hilbert space. However, as density is the basic variable, the properties of the original interacting system and the Kohn-Sham auxiliary system are identical. The existence of the auxiliary non-interacting system is not obvious and has to be put as an assumption for which no rigorous proof exists. Therefore, the Kohn-Sham approach can be summarized as a set of two assumptions.

Assumption 1. *The exact ground state density can be represented by the ground state density of an auxiliary system of non-interacting particles.*

Assumption 2. *The auxiliary Hamiltonian consists of the kinetic energy operator and an effective local potential* $V_{\mathit{eff}}(\mathbf{r})$.

Following this prescription, we define the Kohn-Sham energy functional $E_{\mathrm{KS}}[n]$ in analogy to the Hohenberg-Kohn energy functional (Eq. 2.23).

$$E_{\mathrm{KS}}[n] = F_{\mathrm{KS}}[n] + \int d\mathbf{r}\, V_{\mathrm{ext}}(\mathbf{r})n(\mathbf{r}) + E_{\text{nuc-nuc}} \tag{2.26}$$

The functional $F_{\text{KS}}[n]$ contains the kinetic energy of the electrons and their interaction with the effective potential, which replaces the complicated electron-electron interaction term. In particular, the functional $F_{\text{KS}}[n]$ can be written as the sum of the kinetic energy functional $T_{\text{el}}[n]$, the Hartree energy functional $E_{\text{Hartree}}[n]$, which describes the classical Coulomb interaction of a density with itself, and all other electron-electron interactions, which are put into the exchange-correlation functional $E_{\text{xc}}[n]$.

$$F_{\text{KS}}[n] = T_{\text{el}}[n] + E_{\text{Hartree}}[n] + E_{\text{xc}}[n] \tag{2.27}$$

The Hartree contribution can be calculated explicitly from the charge density distribution $n(\mathbf{r})$.

$$E_{\text{Hartree}}[n] = \frac{1}{8\pi\varepsilon_0} \int d\mathbf{r}\, d\mathbf{r}'\, \frac{n(\mathbf{r})n(\mathbf{r}')}{|\mathbf{r} - \mathbf{r}'|} \tag{2.28}$$

In practical calculations it is more convenient to deal with the problem of solving an equation instead of finding the ground state density distribution $n(\mathbf{r})$ by optimizing the value of the energy functional. Therefore, we construct the Kohn-Sham Hamiltonian $H_{\text{KS}}(\mathbf{r})$ and the corresponding Schrödinger-like equation by taking the variation of the Kohn-Sham energy functional $E_{\text{KS}}[n]$ (Eq. 2.26 and 2.27) with respect to the wave function and introducing energy eigenvalues ε_i as Lagrange multipliers. The Kohn-Sham Hamiltonian is given by

$$H_{\text{KS}}(\mathbf{r}) = -\frac{\hbar^2}{2m_e} \sum_j \nabla_j^2 + \frac{\delta E_{\text{Hartree}}[n]}{\delta n(\mathbf{r})} + \frac{\delta E_{\text{xc}}[n]}{\delta n(\mathbf{r})} + V_{\text{ext}}(\mathbf{r}) \tag{2.29}$$

$$= -\frac{\hbar^2}{2m_e} \sum_j \nabla_j^2 + \underbrace{V_{\text{Hartree}}(\mathbf{r}) + V_{\text{xc}}(\mathbf{r}) + V_{\text{ext}}(\mathbf{r})}_{=V_{\text{KS}}(\mathbf{r})}, \tag{2.30}$$

while the corresponding Schrödinger-like equation reads

$$\left(H_{\text{KS}}(\mathbf{r}) - \varepsilon_i\right) \psi_i(\mathbf{r}) = 0. \tag{2.31}$$

Although the Kohn-Sham Schrödinger-like equation (Eq. 2.31) is formally similar to the full many-body Schrödinger equation (Eq. 2.3), the Kohn-Sham equation is much easier to solve, because it only involves single-particle wavefunctions coupled effectively through the exchange-correlation potential $V_{\text{xc}}(\mathbf{r})$, whereas the many-body Schrödinger equation includes these exchange and correlation processes explicitly in the many-body wavefunction.

Nevertheless, the exchange-correlation functional contains in principle the full complexity of the original many-body problem. However, it turns out that the explicit separation into kinetic energy, long-range Hartree interaction and exchange-correlation term makes it possible to approximate $E_{\text{xc}}[n]$ by a nearly local functional.

Eventually, it is evident that the Kohn-Sham equation has to be solved self-consistently, because the Hartree and exchange-correlation potentials depend on the electron density, which is the result we are looking for. The recipe for obtaining the ground state density distribution $n(\mathbf{r})$ can be summarized as follows:

1. Propose an initial electron density $n(\mathbf{r})$.
2. Solve the Kohn-Sham equation (Eq. 2.31) to obtain the eigenfunctions $\psi_i(\mathbf{r})$.
3. Calculate the new density from the wavefunctions via $n(\mathbf{r}) = \sum\limits_i |\psi_i(\mathbf{r})|^2$.
4. If initial and calculated density do not agree based on a certain measure, restart from step 1 using the calculated density as the new initial density.

The wavefunctions $\psi_i(\mathbf{r})$ and energy eigenvalues ε_i obtained with the converged ground state density $n_0(\mathbf{r})$ are usually interpreted as eigenstates and eigenenergies of the original many-body Hamiltonian. However, this interpretation can not be justified rigorously, just like the entire Kohn-Sham ansatz.

The two most important practical aspects of solving the Kohn-Sham equation are the choice of approximation for the exchange-correlation functional and the choice of wavefunction basis set. These are elucidated in the next sections.

2.3 Practical approximations

2.3.1 Local density approximation

The *local density approximation* (LDA) mimics the exact exchange-correlation functional $E_{\mathrm{xc}}[n]$, which can in principle depend on the electron density in a non-local way, by a local functional $E_{\mathrm{xc}}^{\mathrm{LDA}}[n]$.

$$E_{\mathrm{xc}}[n] \approx E_{\mathrm{xc}}^{\mathrm{LDA}}[n] = \int d\mathbf{r}\, n(\mathbf{r})\, \epsilon_{\mathrm{xc}}^{\mathrm{LDA}}\big(n(\mathbf{r})\big) \tag{2.32}$$

The value of $\epsilon_{\mathrm{xc}}^{\mathrm{LDA}}\big(n(\mathbf{r})\big)$ as a function of the density $n(\mathbf{r})$ can be calculated from the homogeneous electron gas, which has the property of full locality by construction. The homogeneous electron gas has been solved with stochastic methods [73] and analytic representations of the resulting dependence of the exchange-correlation energy on the density are available [74].

Although the density distribution in real systems might be inhomogeneous, density functional theory in the local density approximation still gives reasonable results. That is the case, because the homogeneous electron gas is just an intermediate trick to obtain a local expression for the exchange-correlation energy, which can be evaluated like a function of the density $n(\mathbf{r})$ at any point in space. The actual density distribution in DFT-LDA can still be inhomogeneous and the validity of this approximation is only limited by the extent to which the true exchange-correlation functional $E_{\mathrm{xc}}[n]$ is non-local in the density.

Of course, such a treatment is not without problems. First, there is in general no way to know the error of an approximation to the exchange-correlation functional, except for a few cases where an exact solution is available. Second, the tendency towards electron localization is systematically underestimated, which leads to too large bandwidths and the absence of Mott insulating behavior in LDA. Therefore, many strongly correlated electron systems are predicted to be metallic in LDA, while they are in reality insulating.

For example, LDA overestimates the bandwidth of iron states in iron-pnictides by about a factor of three and predicts all κ-type organics as metallic, while some of them are insulating. Superconducting pairing is also not included in LDA. Calculations for systems with spin-polarization are however possible by introducing spin explicitly into the Kohn-Sham equation.

2.3.2 Generalized gradient approximation

The *generalized gradient approximation* (GGA) improves upon LDA by taking into account also powers of the gradient of the density $|\nabla^m n|$. Within the generalized gradient approximation the exchange-correlation functional can be written as

$$E_{\mathrm{xc}}[n] \approx E_{\mathrm{xc}}^{\mathrm{GGA}}[n] = \int d\mathbf{r}\, n(\mathbf{r})\, \epsilon_{\mathrm{xc}}^{\mathrm{GGA}}\big(n(\mathbf{r}), |\nabla n(\mathbf{r})|, |\nabla^2 n(\mathbf{r})|, \dots\big). \tag{2.33}$$

Of course there are many ways in which such an approximation can be constructed. Therefore, many variants of GGA exist. The most popular version used in solid state physics is the GGA by Perdew, Burke and Ernzerhof (PBE) [75], which, for example, improves over the ionization energies predicted for several small molecules by LDA.

The possiblities in constructing exchange-correlation potentials are sheer endless. Approaches beyond LDA and GGA, for example, calculate the exchange term exactly or mix exact exchange with a density functional (so-called hybrid functionals). In this thesis we employ only the LDA and GGA-PBE functionals, because we are interested mostly in the conducting state and the superconducting state, for which further many-body calculations are indispensable. DFT calculations are usually reliable, if the quantity of interest depends little on the choice of the exchange-correlation functional, given that there is not systematic problem with the exchange-correlation functionals employed.

2.4 Basis sets

2.4.1 Full-potential local-orbital formulation

For a numerical solution of the Kohn-Sham equation both the potential terms in the Hamiltonian and the electronic wavefunctions must be represented numerically with high accuracy. The *full-potentuial local-orbital* (FPLO) method introduced by Koepernik and Eschrig [76] expands both the potential terms and the electronic wavefunctions in terms of real spherical harmonics $Y_L(\mathbf{r})$ localized at the atomic positions, where $L = \{n, l, m\}$ contains the principal quantum number n, the angular momentum quantum number l and the magnetic quantum number m. For example, the crystal potential is given by

$$v(\mathbf{r}) = \sum_{\mathbf{R}+\mathbf{s},L} v_{\mathbf{s},L}(|\mathbf{r}-\mathbf{R}-\mathbf{s}|) Y_L(\mathbf{r}-\mathbf{R}-\mathbf{s}), \tag{2.34}$$

which converges rapidly in L. Therefore, a cutoff L_{max} can be introduced in practice to make the number of coefficients finite in a physically meaningful way. $\mathbf{R}$ is a vector of the Bravais lattice and $\mathbf{s}$ is the coordinate of an atom within the unit cell.

The electronic state labelled by crystal momentum $\mathbf{k}$ and band index n is constructed from a linear combination of Bloch sums.

$$|\mathbf{k}n\rangle = \sum_{\mathbf{Rs}L} |\mathbf{Rs}L\rangle c^{\mathbf{k}n}_{L\mathbf{s}}\, e^{i\mathbf{k}(\mathbf{R}+\mathbf{s})} \tag{2.35}$$

Inserting Eq. 2.35 into the Kohn-Sham equation (Eq. 2.31) transformed into momentum space and multiplied with a localized state from the left yields

$$\sum_{\mathbf{Rs}L} [\underbrace{\langle \mathbf{0s}'L'|H|\mathbf{Rs}L\rangle}_{=H^{L'L}_{\mathbf{0s}'\mathbf{Rs}}} - \underbrace{\langle \mathbf{0s}'L'|\mathbf{Rs}L\rangle}_{=S^{L'L}_{\mathbf{0s}'\mathbf{Rs}}}\,\varepsilon^{\mathbf{k}n}] c^{\mathbf{k}n}_{L\mathbf{s}} e^{i\mathbf{k}(\mathbf{R}+\mathbf{s}-\mathbf{s}')} = 0, \tag{2.36}$$

where $H^{L'L}_{\mathbf{0s}'\mathbf{Rs}}$ and $S^{L'L}_{\mathbf{0s}'\mathbf{Rs}}$ are the Hamiltonian and overlap matrix elements respectively.

In this form the problem includes all electrons within the unit cell explicitly. The main advantage of a local basis is that locality of the electronic states can be used to significantly reduce the dimension of the electronic problem. States strongly localized close to the atomic nucleus do not significantly deviate from the states of an isolated atom, because close to an atomic nucleus the actual crystal potential (Eq. 2.34) does not deviate significantly from the potential of that atom alone. Therefore, a distinction between *core* and *valence* orbitals can be introduced as a physically motivated approximation.

The core orbitals are orthonormal and have well-defined energy levels. Here, the index c denotes a core state, while v denotes a valence state.

$$\langle \mathbf{R}'\mathbf{s}'c'|\mathbf{Rs}c\rangle = \delta_{c'c}\delta_{\mathbf{R}'+\mathbf{s}',\mathbf{R}+\mathbf{s}} \tag{2.37}$$

$$H|\mathbf{Rs}c\rangle = |\mathbf{Rs}c\rangle\varepsilon_{\mathbf{s}c} \tag{2.38}$$

Using these relations we can write down a simplified overlap matrix S, which consists of four blocks.

$$S = \begin{pmatrix} S_{cc} & S_{cv} \\ S_{vc} & S_{vv} \end{pmatrix} = \begin{pmatrix} \delta_{c'c}\delta_{\mathbf{R}'+\mathbf{s}',\mathbf{R}+\mathbf{s}} & \langle \mathbf{R}'\mathbf{s}'c'|\mathbf{Rs}v\rangle \\ \langle \mathbf{R}'\mathbf{s}'v'|\mathbf{Rs}c\rangle & \langle \mathbf{R}'\mathbf{s}'v'|\mathbf{Rs}v\rangle \end{pmatrix} \tag{2.39}$$

The block-partitioned overlap matrix (Eq. 2.39) and Eq. 2.38 can in turn be used to express the Hamiltonian in block-form

$$H = \begin{pmatrix} H_{cc} & H_{cc}S_{cv} \\ S^{\dagger}_{cv}H_{cc} & H_{vv} \end{pmatrix}, \tag{2.40}$$

where the matrix elements are given by

$$H_{cc} = \langle \mathbf{R}'\mathbf{s}'c'|H|\mathbf{Rs}c\rangle = \varepsilon_{\mathbf{s}c}\,\delta_{c'c}\delta_{\mathbf{R}'+\mathbf{s}',\mathbf{R}+\mathbf{s}} \tag{2.41}$$

$$H_{vv} = \langle \mathbf{R}'\mathbf{s}'v'|H|\mathbf{Rs}v\rangle. \tag{2.42}$$

In this representation it is evident that the numerical effort of calculating all matrix elements has been reduced to calculating the elements of the overlap matrices S_{cv} and S_{vv} and the matrix elements of the valence-valence Hamiltonian H_{vv}.

The special form of overlap matrix and Hamiltonian can be used to further simplify the Kohn-Sham equation (Eq. 2.36), so that it reduces to calculating the energies and eigenfunctions only for the valence states, involving, however, the overlap matrix between core and valence states S_{cv}. This is achieved by introducing a decomposition for the overlap matrix.

$$S = AB = \begin{pmatrix} 1 & 0 \\ A_{vc} & A_{vv} \end{pmatrix} \begin{pmatrix} 1 & B_{cv} \\ 0 & B_{vv} \end{pmatrix} = \begin{pmatrix} 1 & B_{cv} \\ A_{vc} & A_{vc}B_{cv} + A_{vv}B_{vv} \end{pmatrix} \tag{2.43}$$

Comparison of the expanded expression (Eq. 2.43) to the original block-form (Eq. 2.39) reveals the relation between matrices A, B and S.

$$S_{cv} = B_{cv} = A_{vc}^{\dagger} \tag{2.44}$$

$$S_{vv} - S_{cv}^{\dagger} S_{cv} = A_{vv} B_{vv} \tag{2.45}$$

The inverse matrices, which will also be needed, are given by

$$A^{-1} = \begin{pmatrix} 1 & 0 \\ -A_{vv}^{-1} S_{cv}^{\dagger} & A_{vv}^{-1} \end{pmatrix} \tag{2.46}$$

$$B^{-1} = \begin{pmatrix} 1 & -S_{cv} B_{vv}^{-1} \\ 0 & B_{vv}^{-1} \end{pmatrix}. \tag{2.47}$$

By writing $C = c_{\mathbf{Ls}}^{\mathbf{k}n}$ and $E = \mathrm{diag}(\varepsilon^{\mathbf{k}n})$ the Kohn-Sham equation (Eq. 2.36) can be rewritten as

$$HC = SCE. \tag{2.48}$$

Here, we make use of the matrix expansion $S = AB$ (Eq. 2.43) and multiply by the inverse of A (Eq. 2.46) from the left. Furthermore, we insert unity as $1 = B^{-1}B$ to the right of the Hamiltonian.

$$\underbrace{A^{-1}HB^{-1}}_{=H'} \underbrace{BC}_{=D} = A^{-1}SCE = \underbrace{BC}_{=D} E \tag{2.49}$$

This generates an effective eigenvalue problem $H'D = DE$, where the matrix H' is given by

$$H' = A^{-1}HB^{-1} = \begin{pmatrix} 1 & 0 \\ -A_{vv}^{-1} S_{cv}^{\dagger} & A_{vv}^{-1} \end{pmatrix} \begin{pmatrix} H_{cc} & H_{cc}S_{cv} \\ S_{cv}^{\dagger} H_{cc} & H_{vv} \end{pmatrix} \begin{pmatrix} 1 & -S_{cv} B_{vv}^{-1} \\ 0 & B_{vv}^{-1} \end{pmatrix} \tag{2.50}$$

$$= \begin{pmatrix} H_{cc} & 0 \\ 0 & A_{vv}^{-1} \left[S_{cv}^{\dagger} H_{cc} S_{cv} + H_{vv} \right] B_{vv}^{-1} \end{pmatrix} \tag{2.51}$$

We choose $D_{cc} = 1$ and $D_{vc} = D_{cv} = 0$, so that the only non-trivial part of the resulting Kohn-Sham equation is the valence-valence part given by

$$A_{vv}^{-1} \left[S_{cv}^{\dagger} H_{cc} S_{cv} + H_{vv} \right] B_{vv}^{-1} D_{vv} = D_{vv} E_v. \tag{2.52}$$

After solving this equation for D_{vv}, the coefficients of the wavefunctions can be obtained from $C = B^{-1}D$.

As a consequence of the core-valence distinction, the presence of a large fraction of core states accelerates practical calculations, since the relevant matrices have smaller dimensions, which significantly reduces the numerical effort for multiplication and diagonalization. Of course, the actual FPLO implementation relies on many more numerical technicalities, which are documented in Ref. [76]. The presentation of the method given here is solely meant to convey the general idea of the FPLO method.

In summary, the FPLO scheme provides an efficient way to solve the Kohn-Sham equations relying only on the physically motivated approximations of (i) a cutoff in the angular momentum in the real spherical harmonics expansion for potentials and wavefunctions and (ii) a distinction of core and valence electrons.

2.4.2 Projector augmented wave formulation

The *projector augmented wave* (PAW) method was introduced by Blöchl in 1994 [77]. It is based on a representation of wavefunctions in terms of both plane waves and localized functions. The main idea behind the PAW formalism is that electronic wavefunctions in a solid are smooth functions of the spatial coordinates, except for the regions close to the nucleus. The expansion of smooth functions in terms of plane waves requires few expansion coefficients for convergence and leads to an efficient numerical representation. However, the regions of space close to the nuclei require special care, because there might be localized states, which are very hard to expand in terms of plane waves. In the PAW method this problem is solved by introducing non-overlapping so-called *augmentation spheres* around the nuclei, in which the wavefunctions are subject to special treatment by means of a linear transformation T.

We define a smooth wavefunction $|\tilde{\psi}\rangle$, which is expanded in terms of some basis, for example plane waves, labelled by m.

$$|\tilde{\psi}\rangle = \sum_m c_m |\tilde{\psi}_m\rangle \tag{2.53}$$

The full wavefunction, possibly including rapid variations as a function of space, is related to the smooth wavefunction by a linear transformation.

$$|\psi\rangle = T|\tilde{\psi}\rangle = \sum_m c_m |\psi_m\rangle \tag{2.54}$$

Therefore, the full wavefunction $|\psi\rangle$ can be expressed in terms of the smooth wavefunction $|\tilde{\psi}\rangle$ and the difference between full and smooth wavefunction within the augmentation sphere.

$$|\psi\rangle = |\tilde{\psi}\rangle + \sum_{\mathbf{R}+\mathbf{s},m} c_{\mathbf{R}+\mathbf{s},m}(|\psi_{\mathbf{R}+\mathbf{s},m}\rangle - |\tilde{\psi}_{\mathbf{R}+\mathbf{s},m}\rangle) \tag{2.55}$$

Since the full and the smooth wavefunctions are assumed to be identical outside of the augmentation sphere, the linear operator T must be unity plus a sum of atom-centered contributions.

$$T = 1 + \sum_{\mathbf{R}+\mathbf{s},m} T_{\mathbf{R}+\mathbf{s},m} \tag{2.56}$$

The expansion coefficients can be written as the projection of the smooth wavefunction $|\psi\rangle$ onto some functions $|\tilde{p}\rangle$, which live inside the augmentation spheres.

$$c_{\mathbf{R}+\mathbf{s},m} = \langle \tilde{p}_{\mathbf{R}+\mathbf{s},m}|\tilde{\psi}\rangle \tag{2.57}$$

Inserting this expression into Eq. 2.56, we can infer the explicit form of the linear transformation T.

$$
\begin{aligned}
|\psi\rangle &= |\tilde{\psi}\rangle + \sum_{\mathbf{R}+\mathbf{s},m} \langle \tilde{p}_{\mathbf{R}+\mathbf{s},m}|\tilde{\psi}\rangle (|\psi_{\mathbf{R}+\mathbf{s},m}\rangle - |\tilde{\psi}_{\mathbf{R}+\mathbf{s},m}\rangle) && (2.58)\\
&= |\tilde{\psi}\rangle + \sum_{\mathbf{R}+\mathbf{s},m} \langle \tilde{p}_{\mathbf{R}+\mathbf{s},m}|(|\psi_{\mathbf{R}+\mathbf{s},m}\rangle - |\tilde{\psi}_{\mathbf{R}+\mathbf{s},m}\rangle)|\tilde{\psi}\rangle && (2.59)\\
&= \underbrace{\left[1 + \sum_{\mathbf{R}+\mathbf{s},m} \langle \tilde{p}_{\mathbf{R}+\mathbf{s},m}|(|\psi_{\mathbf{R}+\mathbf{s},m}\rangle - |\tilde{\psi}_{\mathbf{R}+\mathbf{s},m}\rangle)\right]}_{=T} |\tilde{\psi}\rangle && (2.60)
\end{aligned}
$$

The expression for the projection operator T obviously involves the full wavefunction $|\psi\rangle$. At first glance it seems that the partitioning of wavefunctions into smooth and rapidly varying contributions is useless, since knowledge of the full wavefunction is still required. The point of Eq. 2.60 is, however, that knowledge of both smooth and full wavefunction are only required within the augmentation sphere, which does not overlap with the augmentation sphere of other atoms. Therefore, the transformation T can be precalculated for each element in the periodic table from an atomic DFT program.

Using Eq. 2.60, the Kohn-Sham equation (see Eq. 2.31) within the PAW formalism can, therefore, be rewritten completely in terms of the smooth wavefunctions $|\tilde{\psi}\rangle$.

$$
T^\dagger H T|\tilde{\psi}_n(\mathbf{k})\rangle = \varepsilon_n(\mathbf{k}) T^\dagger T|\tilde{\psi}_n(\mathbf{k})\rangle \tag{2.61}
$$

After solving Eq. 2.61 for the smooth wavefunction, the full wavefunction $|\psi\rangle$ can be reconstructed using the linear transformation T (Eq. 2.60). The introduction of the linear transformation only reduces the numerical effort for storing accurate wavefunctions, but not the number of states for which the Kohn-Sham equation must be solved.

In principle the PAW Kohn-Sham equation yields the wavefunction for all states in the solid. Since the PAW formalism contains the distinction of different areas of space by construction, it is natural to classify also the electronic states into core states, which only live within the augmentation spheres, and valence states that contribute also beyond the augmentation spheres. The fact that core states localized within the augmentation sphere do not deviate significantly from their atomic configuration when put in a solid leads to the so-called *frozen core approximation*, in which a selection of core states is considered fully occupied and orthogonal to all other states [78].

In practice this means that, within the frozen core approximation, only valence states are considered in the expansion of full and smooth wavefunctions. The size of the Hamiltonian matrix is, therefore, reduced compared to a full calculation. Note, however, that the frozen core approximation, in contrast to the prescription used in the FPLO method (see Eq. 2.52), also discards the valence-core interaction. A computationally efficient implementation of the PAW formalism of course requires many further technicalities, which are discussed, for example, in Ref. [79].

2.5 Structural optimization

Density functional theory within the Born-Oppenheimer approximation in principle provides a way to calculate the total energy of a collection of atoms. The equilibrium arrangement of the atoms is realized when the total energy reaches its global minimum, that is where the forces on the nuclei vanish. Density functional theory can be used to calculate forces on the nuclei and predict stable crystal structures.

The basis of calculating quantum mechanical forces is the so-called *force theorem* [80], also called Hellmann-Feynman theorem.

Theorem 3. *The derivative of the total energy with respect to a parameter is given by the expectation value of the derivative of the Hamiltonian with respect to that parameter.*

$$\frac{\partial E}{\partial \lambda} = \langle \psi(\lambda) | \frac{\partial H(\lambda)}{\partial \lambda} | \psi(\lambda) \rangle \tag{2.62}$$

Proof. We only need elementary quantum mechanics, such as $\langle \psi | \psi \rangle = 1$, $\langle \psi | H = \langle \psi | E$ and $H | \psi \rangle = E | \psi \rangle$. The proof proceeds as follows:

$$\begin{aligned}
\frac{\partial E}{\partial \lambda} &= \partial_\lambda \langle \psi(\lambda) | H(\lambda) | \psi(\lambda) \rangle && (2.63)\\
&= \langle \frac{\partial \psi(\lambda)}{\partial \lambda} | H(\lambda) | \psi(\lambda) \rangle + \langle \psi(\lambda) | \frac{\partial H(\lambda)}{\partial \lambda} | \psi(\lambda) \rangle + \langle \psi(\lambda) | H(\lambda) | \frac{\partial \psi(\lambda)}{\partial \lambda} \rangle && (2.64)\\
&= \langle \psi(\lambda) | \frac{\partial H(\lambda)}{\partial \lambda} | \psi(\lambda) \rangle + E(\lambda)\, \partial_\lambda \underbrace{\langle \psi(\lambda) | \psi(\lambda) \rangle}_{=1} && (2.65)\\
&= \langle \psi(\lambda) | \frac{\partial H(\lambda)}{\partial \lambda} | \psi(\lambda) \rangle && (2.66)
\end{aligned}$$

□

Theorem 3 can be used directly to calculate the forces on the nuclei $\mathbf{F}_l$ from the Kohn-Sham energy functional (Eq. 2.26) or, equivalently, the Kohn-Sham Hamiltonian (Eq. 2.30). The nuclear coordinates are given by $\mathbf{R}_l$.

$$\mathbf{F}_l = -\frac{\partial E_{\mathrm{KS}}}{\partial \mathbf{R}_l} = -\int d\mathbf{r}\, \frac{\partial V_{\mathrm{ext}}(\mathbf{r})}{\partial \mathbf{R}_l} n(\mathbf{r}) - \frac{\partial E_{\text{nuc-nuc}}}{\partial \mathbf{R}_l} \tag{2.67}$$

The last term in Eq. 2.67 is the trivial Coulomb-interaction between the nuclei, which does not appear in the Kohn-Sham Hamiltonian, but is of course relevant for the forces on the nuclei. Additional terms may appear if the basis of wavefunctions is not complete or the wavefunctions are not exact eigenstates of the Hamiltonian. Therefore, the expression for the force can depend on the actual implementation in the respective DFT code.

The forces calculated in this way can be used to solve the full ab initio problem in Born-Oppenheimer approximation or to minimize the force on the nuclei, neglecting their kinetic energy. In the latter approach any numerical optimization algorithm can be used to find the minimum in total energy as a function of the nuclear positions $\mathbf{R}_l$.

Optimally, the algorithm exploits the gradient information, that is the forces provided by the DFT program, to approach the minimum in energy. In this thesis we use the limited-memory Broyden-Fletcher-Goldfarb-Shanno (L-BFGS) algorithm [81].

2.6 Wannier functions

The solutions of the Schrödinger equation in a periodic potential, such as encountered in crystalline systems, are the Bloch functions $\psi_{n\mathbf{k}}(\mathbf{r})$ with periodic functions $u_{n\mathbf{k}}(\mathbf{r})$ for each band index n.

$$\psi_{n\mathbf{k}}(\mathbf{r}) = u_{n\mathbf{k}}(\mathbf{r})\, e^{i\mathbf{k}\mathbf{r}} \tag{2.68}$$

An alternative representation of the electronic wavefunction is given by so-called *Wannier functions* [82], which are localized in space. They are not eigenstates of the Hamiltonian, but they can be used to analyse chemical bonding and provide an efficient basis for real materials calculations. The Wannier functions $w_{n\mathbf{R}}(\mathbf{r})$ are given by

$$w_{n\mathbf{R}}(\mathbf{r}) = \frac{V}{(2\pi)^3} \int_{\mathrm{BZ}} d\mathbf{k}\, e^{-i\mathbf{k}\mathbf{r}} \psi_{n\mathbf{k}}(\mathbf{r}), \tag{2.69}$$

where V is the volume of the real-space primitive cell and $\mathbf{R}$ is a lattice vector. Wannier functions are orthonormal. The inverse transformation is given by

$$\psi_{n\mathbf{k}}(\mathbf{r}) = \sum_{\mathbf{R}} e^{i\mathbf{k}\mathbf{R}} w_{n\mathbf{R}}(\mathbf{r}). \tag{2.70}$$

Bloch functions $\psi_{n\mathbf{k}}(\mathbf{r})$ and Wannier functions $w_{n\mathbf{R}}(\mathbf{r})$ are obviously connected by a unitary transformation.

The main advantage of using a Wannier representation, including a limited number of bands, as opposed to the full DFT wavefunction is that many physical properties depend only on states in a certain energy window in the vicinity of the Fermi energy. The easiest way to construct Wannier functions is by projection. We select a manifold of DFT bands labelled by m and an equal number of corresponding localized trial orbitals $g_n(\mathbf{r})$. The projection of Bloch states $|\psi_{m\mathbf{k}}\rangle$ onto the localized states can be expressed in terms of matrix elements $P_{mn}(\mathbf{k}) = \langle \psi_{m\mathbf{k}} | g_n \rangle$.

$$|\phi_{n\mathbf{k}}\rangle = \sum_{m=m_{\min}}^{m_{\max}} |\psi_{m\mathbf{k}}\rangle \langle \psi_{m\mathbf{k}} | g_n \rangle = \sum_{m=m_{\min}}^{m_{\max}} |\psi_{m\mathbf{k}}\rangle P_{mn}(\mathbf{k}) \tag{2.71}$$

Since the sum over m is not complete, the resulting states $|\phi_{n\mathbf{k}}\rangle$ are not orthonormal. Orthonormality can, however, be achieved by means of Löwdin-orthonormalization using the overlap matrix $S_{mn}(\mathbf{k}) = \langle \phi_{m\mathbf{k}} | \phi_{n\mathbf{k}} \rangle$. The orthonormalized states are given by

$$|\tilde{\psi}_{n\mathbf{k}}\rangle = \sum_{m=m_{\min}}^{m_{\max}} |\phi_{m\mathbf{k}}\rangle [S_{mn}(\mathbf{k})]^{-1/2}. \tag{2.72}$$

The new Bloch-like states span only the bands that were chosen for the projection (Eq. 2.71). Therefore, Wannier functions are particularly helpful in constructing effective models of reduced dimension by retaining only a set of orbitals/bands that is expected to be relevant.

For practical calculations it is more convenient to store the Hamiltonian in real-space than eigenvalues and wavefunctions for selected momenta $\mathbf{k}$, since both of the latter can in

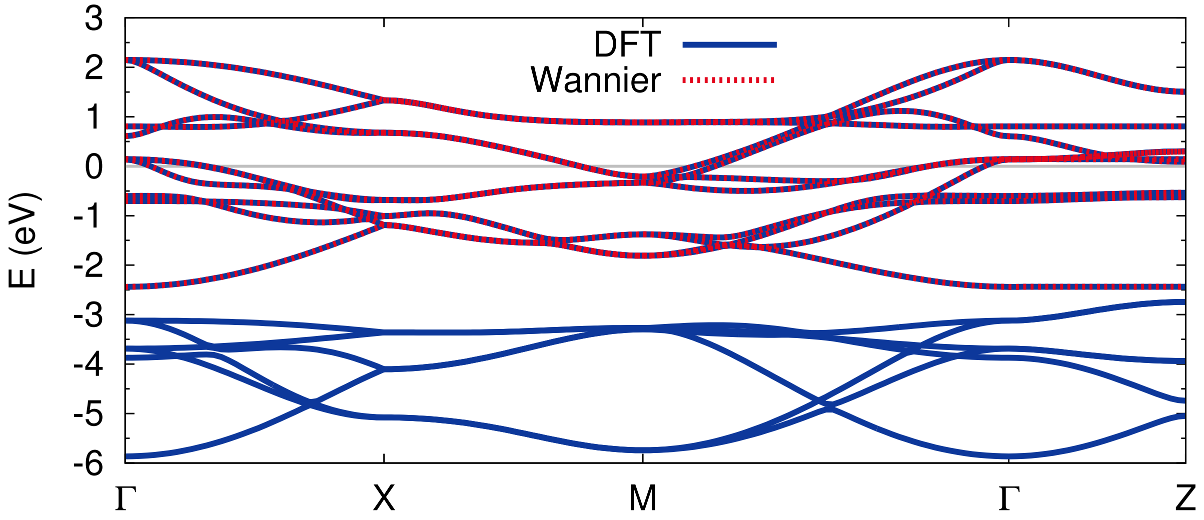

Figure 2.1: Comparison of DFT and Wannier bands for FeSe calculated from FPLO. The Wannier states included are the Fe 3d states of the two iron atoms in the crystallographic unit cell.

principle be reconstructed for arbitrary $\mathbf{k}$ from the real-space Hamiltonian. This procedure goes by the name of *Wannier interpolation* [82]. Using the Fourier transformation of the Wannier states, the Hamiltonian in the Wannier subspace can be written as

$$H^W_{nm}(\mathbf{k}) = \langle\tilde{\psi}_{n\mathbf{k}}|H|\tilde{\psi}_{m\mathbf{k}}\rangle = \sum_{\mathbf{R}} e^{i\mathbf{k}\mathbf{R}} \underbrace{\langle n\mathbf{0}|H|m\mathbf{R}\rangle}_{=t^{nm}_{\mathbf{0R}}}, \tag{2.73}$$

where $|m\mathbf{R}\rangle$ denotes the real-space Wannier functions given by Eq. 2.69.

Such a representation is particularly compact, since the matrix elements $t^{nm}_{\mathbf{0R}}$ should decay rapidly with increasing distance $\mathbf{R}$ between the Wannier function centers due to the localization of the Wannier states $|m\mathbf{R}\rangle$. The matrix elements $t^{nm}_{\mathbf{0R}}$ can be calculated from a converged DFT calculation and provide a way to construct the kinetic part of lattice Hamiltonians (see Eq. 1.4). Calculating Wannier representations of the full Hamiltonian is especially simple within the FPLO method, since it expresses all quanitities in terms of local functions, which can naturally be used as the localized trial wavefunctions $g_n(\mathbf{r})$ required in the Wannierization procedure (see Eq. 2.71).

The Wannier Hamiltonian $H^W_{nm}(\mathbf{k})$ is in general not a diagonal matrix. The eigenenergies and eigenstates can, however, be obtained numerically from a diagonalization of $H^W_{nm}(\mathbf{k})$ using standard numerical libraries. In cases where multiple Wannier function centers are located within the same unit cell one also has to store the intra-cell distance vectors previously denoted as $\mathbf{s}$ and transform $\mathbf{R} \to \mathbf{R} + \mathbf{s}$ in Eq. 2.73.

As an example, a comparison of the DFT and Wannier bandstructures of FeSe are shown in Fig. 2.1. Both bandstructures are calculated using the FPLO method. The Wannier calculation is based on the Fe 3d states of the two iron atoms in the crystallographic unit cell. The DFT calculation actually contains many more bands both above and below the energy window shown in Fig. 2.1.

The band manifold shown is comprised mainly of Fe 3d and Se 4p states. The iron states are predominant between -3 and +3 eV, while the selenium states are predominant between -6 and -3 eV. In the Wannier calculation the block of bands, which is dominated by iron states in the DFT calculation, becomes composed exclusively of iron states. Therefore, the Wannier construction of the low-energy model neglects the selenium states. It is of course also possible to include the Se 4p states and neglect all other states lying outside of the shown window. The inclusion of more orbitals increases the dimensions of the Hamiltonian matrix, which results in increased cost of diagonalization. The set of orbitals used for the Wannier construction is a matter of choice, usually based on the energy scale of the problem under investigation. Any quantity that involves energy scales below 2 eV can probably be calculated with high accuracy using the Fe 3d Wannier representation of FeSe.

Here it should be noted that Wannierization of the electronic bandstructure of FeSe in terms of iron states works very well in the sense that DFT and Wannier bandstructures are hardly discernible on the energy scale shown in Fig. 2.1. As hybridizations between the constitutents of the unit cell become more involved, few-band Wannier models can deviate strongly from the DFT bandstructure they are based on, if too few atomic orbitals are included in the low-energy model.

Chapter 3

The Green's function formalism

This chapter deals with the method of Green's functions, which can be used to find approximate solutions to Hamiltonians which cannot be solved exactly, such as the Hubbard Hamiltonian (see Eq. 1.4 and 1.5) in dimensions larger than one.

In the method of Green's functions the Hamiltonian is partitioned in a part that can be solved exactly and a part that cannot be solved exactly. The idea behind an approximate solution is to treat the part without exact solution as a perturbation to the part for which an exact solution is feasible. The exact solution of the full Hamiltonian is then expressed as a series in terms of the part for which no exact solution exists. To arrive at a practical approximation, the series is truncated or restricted to a certain subclass of terms, which can be rewritten in a closed form.

The method of Green's functions can be formulated both at zero and at finite temperature. The latter is particularly useful, since it is amenable to implementation in computer programs. Both formulations are introduced in this chapter, where we follow the presentation in Ref. [83].

3.1 Green's functions at zero temperature

3.1.1 Interaction representation

Quantum mechanics can be formulated in three formally different, but equivalent ways in the sense that they yield identical expectation values: the *Schrödinger representation*, in which wavefunctions are time-dependent and operators are independent of time, the *Heisenberg representation*, in which wavefunctions are independent of time and operators are time-dependent, and the *Dirac* or *Interaction representation*, in which both wavefunctions and operators are time-dependent.

At first glance the interaction representation seems like a complication, but it becomes useful when the Hamiltonian H can be split in an exactly solvable part H_0 and an interaction term V, for which no exact solution exists.

$$H = H_0 + V \tag{3.1}$$

The time-dependence of the operators within the interaction representation is given by:

$$O(t) = e^{iH_0 t} O e^{-iH_0 t} \tag{3.2}$$

The time-dependence of the wavefunctions within the interaction representation is given by

$$\psi(t) = \underbrace{e^{iH_0t}e^{-iHt}}_{=U(t)}\psi(0), \tag{3.3}$$

where $U(t) = e^{iH_0t}e^{-iHt}$ is the *time-evolution operator*. In general the operators H_0 and V do not commute, so that the exponentials cannot be combined.

The wavefunction in interaction representation fulfills a differential equation that involves the interaction term V.

$$\begin{aligned} \partial_t\psi(t) &= ie^{iH_0t}(H_0 - H)e^{-iHt}\psi(0) \\ &= -ie^{iH_0t}Ve^{-iHt}\psi(0) \\ &= -ie^{iH_0t}Ve^{-iH_0t}e^{iH_0t}e^{-iHt}\psi(0) \\ &= -iV(t)\psi(t) \end{aligned} \tag{3.4}$$

While a given operator at any time can be obtained trivially from H_0 (Eq. 3.2), the wavefunction at general time t however requires a solution for the full Hamiltonian H (Eq. 3.3). Within the interaction representation the problem of finding the wavefunction at general time t therefore reduces to finding the time-evolution $U(t)$ operator for the given full Hamiltonian.

The differential equation for the time-evolution operator is given by

$$\partial_t U(t) = -iV(t)U(t), \tag{3.5}$$

which is equivalent to Eq. 3.4. The solution of this differential equation is given by a time-ordered series:

$$U(t) = 1 + \sum_{n=1}^{\infty} \frac{(-1)^n}{n!} \int_0^t dt_1 \int_0^t dt_2 \cdots \int_0^t dt_n \, T\left[V(t_1)V(t_2)\cdots V(t_n)\right] \tag{3.6}$$

$$= T \exp\left[-i\int_0^t dt_1 V(t_1)\right] \tag{3.7}$$

T here denotes the *time-ordering operator*, which acts on a group of time-dependent operators and arranges them so that the timepoints are ordered with the earliest times to the right.

The representation of the time-evolution operator in terms of a series itself does not achieve anything with respect to solving the full Hamiltonian. However, it can be used to define further quantities, which allow for a transparent approximation scheme to the full problem.

3.1.2 S matrix

The S matrix is a generalization of the time-evolution operator $U(t)$ (Eq. 3.7). In contrast to $U(t)$ it connects two arbitrary timepoints and therefore acquires matrix-structure.

$$\psi(t) = S(t, t')\psi(t') \tag{3.8}$$

The S matrix has various properties, which will be used in further derivations.

$$S(t,t') = U(t)U^\dagger(t') \tag{3.9}$$
$$S(t,t) = 1 \tag{3.10}$$
$$S^\dagger(t,t') = S(t',t) \tag{3.11}$$
$$S(t,t')S(t',t'') = S(t,t'') \tag{3.12}$$

Completely analogous to the time-evolution operator $U(t)$, the S matrix can be expressed in terms of a time-ordered exponential of the interaction part V of the Hamiltonian.

$$S(t,t') = T\exp\left[-i\int_{t'}^{t} dt_1 V(t_1)\right] \tag{3.13}$$

The important property of the S matrix is that it can be used to connect the ground state wavefunction ϕ_0, corresponding to the exactly solvable part of H_0 of the full Hamiltonian, and the ground state wavefunction $\psi(0)$ of the full Hamiltonian via the theorem of Gell-Mann and Low [84].

$$\psi(0) = \psi_0 = S(0,-\infty)\phi_0 \tag{3.14}$$

3.1.3 Real-time Green's functions at zero temperature

A basic quantity of interest is the one-particle retarded Green's function, which contains all information about single-particle properties of the system.

$$G^r(\lambda, t-t') = -i\Theta(t-t')\langle c_\lambda(t)c^\dagger_\lambda(t')\rangle \tag{3.15}$$

Here, $\Theta(t)$ denotes the Heaviside function, while c and $c^\dagger$ are the electron annihilation and creation operators respectively. The relevant quantum numbers are denoted by λ. In the present form the Green's function cannot be evaluated, because the expectation value has to be taken with respect to the ground state wavefunction of the full Hamiltonian, which we do not know.

Now we assume we want to obtain a time-ordered expectation value with respect to the ground state wavefunction ψ_0 of the full Hamiltonian. The states and operators are given in the Heisenberg representation.

$$\begin{aligned}
G(\lambda, t-t') =& -i\langle\psi_0|Tc_\lambda(t)c^\dagger_\lambda(t')|\psi_0\rangle \\
=& -i\Theta(t-t')\langle\psi_0|c_\lambda(t)c^\dagger_\lambda(t')|\psi_0\rangle + i\Theta(t'-t)\langle\psi_0|c^\dagger_\lambda(t')c_\lambda(t)|\psi_0\rangle \\
=& -i\Theta(t-t')\langle\psi_0|e^{iHt}c_\lambda e^{-iHt}e^{iHt'}c^\dagger_\lambda e^{-iHt'}|\psi_0\rangle \\
&+ i\Theta(t'-t)\langle\psi_0|e^{iHt'}c^\dagger_\lambda e^{-iHt'}e^{iHt}c_\lambda e^{-iHt}|\psi_0\rangle
\end{aligned} \tag{3.16}$$

Inserting the interaction representation for the operators (Eq. 3.2) and using the theorem of Gell-Mann and Low (Eq. 3.14) we can rewrite the expectation value, so that the S

matrix appears.

$$\begin{aligned}
G(\lambda, t-t') =& - i\Theta(t-t')\langle\psi_0|\underbrace{e^{iHt}e^{-iH_0t}}_{=U^\dagger(t)=S(0,t)}c_\lambda(t)\underbrace{e^{iH_0t}e^{-iHt}}_{=U(t)=S(t,0)}\underbrace{e^{iHt'}e^{-iH_0t'}}_{=U^\dagger(t')}c^\dagger_\lambda(t')\underbrace{e^{iH_0t'}e^{-iHt'}}_{=U(t')}|\psi_0\rangle \\
&+ i\Theta(t'-t)\langle\psi_0|e^{iHt'}e^{-iH_0t'}c^\dagger_\lambda(t')e^{iH_0t'}e^{-iHt'}e^{iHt}e^{-iH_0t}c_\lambda(t)e^{iH_0t}e^{-iHt}|\psi_0\rangle \\
=& - i\Theta(t-t')\langle\phi_0|S(-\infty,0)S(0,t)c_\lambda(t)S(t,0)S(0,t')c^\dagger_\lambda(t')S(t',0)S(0,-\infty)|\phi_0\rangle \\
&+ i\Theta(t'-t)\langle\phi_0|S(-\infty,0)S(0,t')c^\dagger_\lambda(t')S(t',0)S(0,t)c_\lambda(t)S(t,0)S(0,-\infty)|\phi_0\rangle \\
=& - i\Theta(t-t')\langle\phi_0|S(-\infty,t)c_\lambda(t)S(t,t')c^\dagger_\lambda(t')S(t',-\infty)|\phi_0\rangle \\
&+ i\Theta(t'-t)\langle\phi_0|S(-\infty,t')c^\dagger_\lambda(t')S(t',t)c_\lambda(t)S(t,-\infty)|\phi_0\rangle
\end{aligned} \tag{3.17}$$

At this point we need another identity from the paper of Gell-Mann and Low [84].

$$\langle\phi_0|S(-\infty,0) = \frac{\langle\phi_0|S(\infty,0)}{\langle\phi_0|S(\infty,-\infty)|\phi_0\rangle} \tag{3.18}$$

Using Eq. 3.18 we can rewrite Eq. 3.17 in a more compact form.

$$G(\lambda, t-t') = -i\frac{\langle\phi_0|Tc_\lambda(t)c^\dagger_\lambda(t')S(\infty,-\infty)|\phi_0\rangle}{\langle\phi_0|S(\infty,-\infty)|\phi_0\rangle} \tag{3.19}$$

This result is extremely important, since it allows for the evaluation of expectation values based on the known ground state wavefunction ϕ_0 corresponding to H_0 and the S matrix.

The unperturbed Green's function G_0 will also be needed later on. It is defined by a vanishing perturbation $V = 0$, so that the S matrix becomes the identity ($S = 1$).

$$G_0(\lambda, t-t') = -i\langle\phi_0|Tc_\lambda(t)c^\dagger_\lambda(t')|\phi_0\rangle \tag{3.20}$$

3.1.4 Wick's theorem

The evaluation of the S matrix in Eq. 3.19 proceeds by inserting the exponential representation given by Eq. 3.13 expanded in a series. Here, we only concentrate on the enumerator, but in principle the same has to be done for the denominator.

$$\begin{aligned}
G(\lambda, t-t') =& - i\sum_{n=0}^{\infty}\frac{(-i)^n}{n!}\int_{-\infty}^{\infty}dt_1\int_{-\infty}^{\infty}dt_2\cdots\int_{-\infty}^{\infty}dt_n \\
&\times\frac{\langle\phi_0|Tc_\lambda(t)c^\dagger_\lambda(t')V(t_1)V(t_2)\cdots V(t_n)|\phi_0\rangle}{\langle\phi_0|S(\infty,-\infty)|\phi_0\rangle}
\end{aligned} \tag{3.21}$$

Although one can hardly make any statement about convergence of the series in Eq. 3.21, there is now hope that some of the terms in this series can be evaluated, at least for low expansion order n.

For this purpose, we need to calculate expectation values of time-ordered products of operators. The number of creation and annihilation operators in the product must always be equal, because the system has to return to the ground state ϕ_0 after all operators have been applied. Otherwise the expectation value vanishes.

What complicates the evaluation of such time-ordered products most is the large number of possible combinations. The task of going through all possible combinations is considerably simplified by *Wick's theorem* [85]. In the presentation of this theorem we rely on Ref. [86].

First, we define the product of a set of operators $A, B, C, \ldots$ as *normal*, if all creation operators appear to the left of the annihilation operators and if the sign corresponds to the parity of the permutation of Fermi operators needed to achieve the correct ordering. The normal product of operators $A, B, C, \ldots$ is denoted as $N(A, B, C, \ldots)$, while the time-ordered product is denoted by $T(A, B, C, \ldots)$. The *pairing* of two operators is then given by

$$\overbracket{AB} = T(AB) - N(AB). \tag{3.22}$$

Theorem 4. *Any time-ordered product of operators can be expressed as a sum of all possible normal-ordered products with all possible pairings.*

$$\begin{aligned} T(ABCD\cdots XYZ) =& N(ABCD\cdots XYZ) + N(\overbracket{AB}CD\cdots XYZ) \\ &+ N(\overbracket{ABC}D\cdots XYZ) + \cdots + N(\overbracket{A\overbracket{BC}\cdots X}\overbracket{YZ}) \end{aligned} \tag{3.23}$$

Proof. The simultaneous permutation of operators on both sides of Eq. 3.23 obviously does not influence its validity. Therefore, we assume without loss of generality that operators $ABCD\cdots XYZ$ are time-ordered. Starting from the time-ordered product, the normal-ordered product is obtained by performing all operator permutations needed for bringing the creation operators to the left of the annihilation operators. The result is a sum of normal-ordered products with pairings only of those operators, which appear in different order in the time-ordered and normal-ordered products. However, the permutation procedure actually generates all possible pairings, since the pairing of operators for which time-order and normal-order are identical vanishes according to Eq. 3.22. This proves Wick's theorem (Eq. 3.23). □

The expectation value of the normal-ordered product with the ground state, however, vanishes by definition. Therefore, the expectation value of a time-ordered product of two operators is equal to their pairing.

$$\langle\phi_0|\overbracket{AB}|\phi_0\rangle = \langle\phi_0|T(AB)|\phi_0\rangle \tag{3.24}$$

Taking the ground state expectation value of Eq. 3.23, consequently, leads to a much simpler expression.

$$\begin{aligned} \langle T(ABCD\cdots XYZ)\rangle =& \langle T(AB)\rangle\langle T(CD)\rangle\cdots\langle T(YZ)\rangle \\ &\pm \langle T(AC)\rangle\langle T(BD)\rangle\cdots\langle T(YZ)\rangle \pm \cdots \end{aligned} \tag{3.25}$$

Such products of averages over pairs of time-ordered operators can in fact be evaluated easily. The calculation of the Green's function defined in Eq. 3.21 is only limited by the fact that evaluation of an infinite number of terms is in practice not feasible.

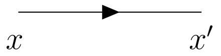

Figure 3.1: Feynman diagram representation of the unperturbed Green's function $G_0(x, x')$.

Fortunately, a diagrammatic representation of the pairings between operators exists, which allows for a more intuitive approach. In particular it allows for selecting specific contributions out of the infinite number of possible pairings, sometimes also called *contractions*, possibly based on physical intuition. Based on such a selection process many different approximate schemes for calculating expectation values have been developed. The diagrammatic language is introduced in the following subsection.

3.1.5 Feynman diagrams

A diagrammatic representation of the terms in Eq. 3.21 is given by so-called *Feynman diagrams* [87]. In those diagrams sets of space-time coordinates, denoted by $x = (t, \mathbf{r})$, are represented as points in the plane. Points that appear as arguments x and x' of a single unperturbed Green's function $G_0(x, x')$ are connected by a solid line. The unperturbed Green's function is, therefore, represented by the diagram in Fig. 3.1. Points x_1 and x_2 that belong to a two-point interaction $V(x_1 - x_2)$ are connected by a wavy line.

In order to demonstrate the use of Feynman diagrams to represent higher-order contributions to the full Green's function defined by Eq. 3.21, we follow Ref. [86] and assume an interaction in real-space of the form

$$V = \frac{1}{2} \int d\mathbf{r_1} d\mathbf{r_2}\, c^\dagger_\alpha(\mathbf{r_1}) c^\dagger_\beta(\mathbf{r_2}) U(\mathbf{r_1} - \mathbf{r_2}) c_\beta(\mathbf{r_2}) c_\alpha(\mathbf{r_1}). \tag{3.26}$$

Inserting this interaction into Eq. 3.21, the order $n = 1$ term is given by

$$\begin{aligned} \delta G_1(x, x') = & \frac{1}{2\langle\phi_0|S(\infty, -\infty)|\phi_0\rangle} \int dx_1 dx_2 \\ & \times \langle T c_\alpha(x) c^\dagger_\beta(x') c^\dagger_\gamma(x_1) c^\dagger_\delta(x_2) c_\delta(x_2) c_\gamma(x_1)\rangle U(\mathbf{r_1} - \mathbf{r_2}) \delta(t_1 - t_2). \end{aligned} \tag{3.27}$$

The matrix element in the enumerator of Eq. 3.27 can be rewritten using Eq. 3.25 and the

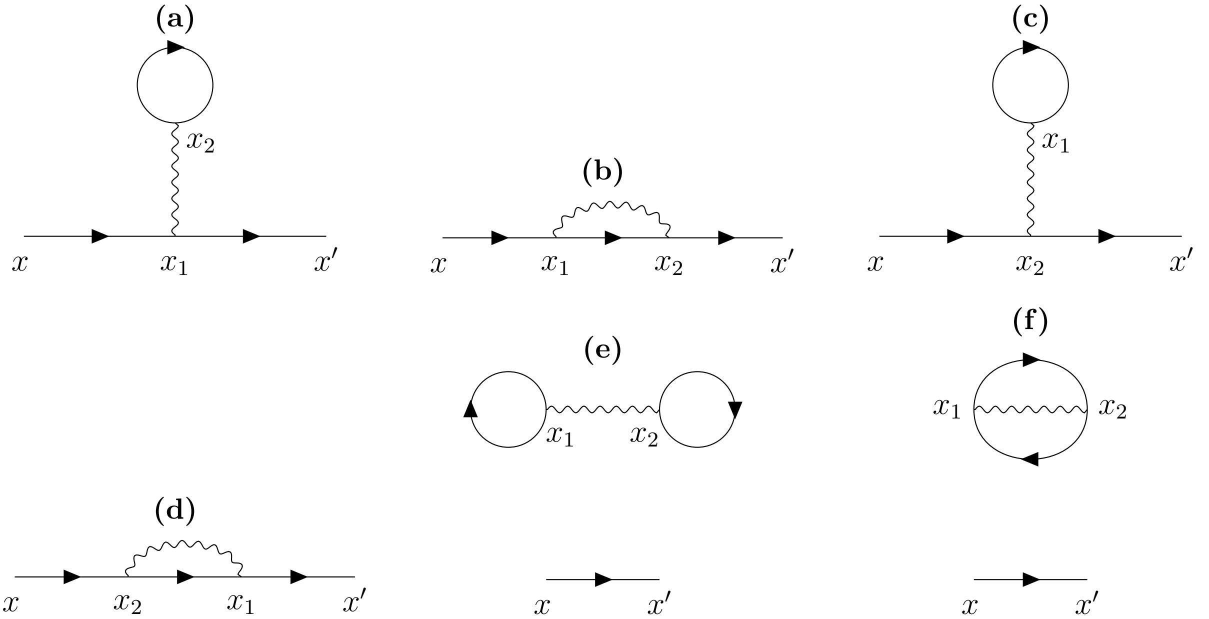

Figure 3.2: Feynman diagrams representing the six products of Green's functions in Eq. 3.28. Diagram (a) corresponds to the first term in Eq. 3.28, diagram (b) corresponds to the second term and so on.

definition of the unperturbed Green's function given by Eq. 3.20.

$$\begin{aligned}
&\langle Tc_\alpha(x)c^\dagger_\beta(x')c^\dagger_\gamma(x_1)c^\dagger_\delta(x_2)c_\delta(x_2)c_\gamma(x_1)\rangle \\
=&-\langle Tc_\alpha(x)c^\dagger_\gamma(x_1)\rangle\langle Tc_\delta(x_2)c^\dagger_\delta(x_2)\rangle\langle Tc_\gamma(x_1)c^\dagger_\beta(x')\rangle \\
&+\langle T(c_\alpha(x)c^\dagger_\gamma(x_1)\rangle\langle Tc_\gamma(x_1)c^\dagger_\delta(x_2)\rangle\langle Tc_\delta(x_2)c^\dagger_\beta(x')\rangle \\
&-\langle Tc_\alpha(x)c^\dagger_\delta(x_2)\rangle\langle Tc_\gamma(x_1)c^\dagger_\gamma(x_1)\rangle\langle Tc_\delta(x_2)c^\dagger_\beta(x')\rangle \\
&+\langle Tc_\alpha(x)c^\dagger_\delta(x_2)\rangle\langle Tc_\delta(x_2)c^\dagger_\gamma(x_1)\rangle\langle Tc_\gamma(x_1)c^\dagger_\beta(x')\rangle \\
&-\langle Tc_\alpha(x)c^\dagger_\beta(x')\rangle\langle Tc_\gamma(x_1)c^\dagger_\gamma(x_1)\rangle\langle Tc_\delta(x_2)c^\dagger_\delta(x_2)\rangle \\
&+\langle Tc_\alpha(x)c^\dagger_\beta(x')\rangle\langle Tc_\delta(x_2)c^\dagger_\gamma(x_1)\rangle\langle Tc_\gamma(x_1)c^\dagger_\delta(x_2)\rangle \\
=&\quad iG_0^{\alpha\gamma}(x,x_1)G_0^{\delta\delta}(x_2,x_2)G_0^{\gamma\beta}(x_1,x')-iG_0^{\alpha\gamma}(x,x_1)G_0^{\gamma\delta}(x_1,x_2)G_0^{\delta\beta}(x_2,x') \\
&+iG_0^{\alpha\delta}(x,x_2)G_0^{\gamma\gamma}(x_1,x_1)G_0^{\delta\beta}(x_2,x')-iG_0^{\alpha\delta}(x,x_2)G_0^{\delta\gamma}(x_2,x_1)G_0^{\gamma\beta}(x_1,x') \\
&+iG_0^{\alpha\beta}(x,x')G_0^{\gamma\gamma}(x_1,x_1)G_0^{\delta\delta}(x_2,x_2)-iG_0^{\alpha\beta}(x,x')G_0^{\delta\gamma}(x_2,x_1)G_0^{\gamma\delta}(x_1,x_2)
\end{aligned} \tag{3.28}$$

The diagrammatic representation of the terms in Eq. 3.28 is shown in Fig. 3.2. Diagrams (a),(c) and (b),(d) are so-called *connected* diagrams that pairwise have the same topology. Diagrams (e) and (f) are so-called *disconnected* diagrams, meaning that not all lines in the diagram are connected to the *external* coordinates x and x'.

The distinction between connected and disconnected diagrams can be used to further simplify Eq. 3.21, especially with respect to the matrix element $\langle\phi_0|S(\infty,-\infty)|\phi_0\rangle$ in the denominator, which we have ignored so far. The theorem related to this simplification is explained in the next subsection.

3.1.6 Linked cluster theorem

The linked cluster theorem can be used to simplify the calculation of Green's functions using diagrammatic techniques [86]. In particular it states that unconnected diagrams can be neglected when calculating expectation values.

Theorem 5. *The Green's function can be written purely in terms of connected diagrams.*

$$G(\lambda, t-t') = -i\langle\phi_0|Tc_\lambda(t)c^\dagger_\lambda(t')S(\infty,-\infty)|\phi_0\rangle_{con} \tag{3.29}$$

Proof. We first consider a term of fixed order in n from Eq. 3.21. Now we pick some particular contraction from the right-hand side of Eq. 3.25, which contains a disconnected part. For a diagram to be disconnected means that at least one of the interaction terms $V(t)$ is not connected in any way to the external operators $c_\lambda(t)$ and $c^\dagger_\lambda(t')$. Obviously, the expectation value corresponding to such a diagram can be factorized into a connected part and an unconnected part.

$$\begin{aligned}\delta G_n(\lambda, t-t') =& -i\frac{(-i)^n}{n!}\int dt_1\cdots t_n\,\langle\phi_0|Tc_\lambda(t)c^\dagger_\lambda(t')V(t_1)V(t_2)\cdots V(t_n)|\phi_0\rangle\\ =& -i\frac{(-i)^n}{n!}\int dt_1\cdots dt_m\,\langle\phi_0|Tc_\lambda(t)c^\dagger_\lambda(t')V(t_1)\cdots V(t_m)|\phi_0\rangle_{\mathrm{con}}\\ &\times\int dt_{m+1}\cdots dt_n\,\langle\phi_0|TV(t_{m+1})\cdots V(t_n)|\phi_0\rangle\end{aligned} \tag{3.30}$$

Furthermore, all diagrams that are generated by just permuting the operators $V_i(t)$ give the same contribution. The number of possible combinations in which m out of n total operators are connected is given by $M = n!/(m!(n-m)!)$. Therefore, among all possible contractions, there are M diagrams that give exactly the same contribution as the term written out in Eq. 3.30.

$$\begin{aligned}M\delta G_n(\lambda, t-t') =& -i\frac{(-i)^m}{m!}\int dt_1\cdots t_n\,\langle\phi_0|Tc_\lambda(t)c^\dagger_\lambda(t')V(t_1)\cdots V(t_m)|\phi_0\rangle_{\mathrm{con}}\\ &\times\frac{(-i)^{n-m}}{(n-m)!}\int dt_{m+1}\cdots dt_n\,\langle\phi_0|TV(t_{m+1})\cdots V(t_n)|\phi_0\rangle\end{aligned} \tag{3.31}$$

Now we lift the constraint of all terms belonging to a particular expansion order n and instead focus on all contractions that involve the same connected part and contain some arbitrary disconnected part.

$$\begin{aligned}
&\sum_{n=m}^{\infty}[M\delta G_n(\lambda,t-t')]\\
&=-i\frac{(-i)^m}{m!}\int dt_1\cdots t_n\,\langle\phi_0|Tc_\lambda(t)c_\lambda^\dagger(t')V(t_1)\cdots V(t_m)|\phi_0\rangle_{\text{con}}\\
&\quad\times\Bigg[1-i\int dt_{m+1}\langle\phi_0|V(t_{m+1})|\phi_0\rangle \qquad (3.32)\\
&\qquad-\frac{1}{2}\int dt_{m+1}dt_{m+2}\langle\phi_0|TV(t_{m+1})V(t_{m+2})|\phi_0\rangle+\cdots\\
&\qquad+\frac{(-i)^k}{k!}\int dt_{m+1}\cdots dt_{m+k}\langle\phi_0|TV(t_{m+1})\cdots V(t_{m+k})|\phi_0\rangle+\cdots\Bigg]
\end{aligned}$$

The term within the rectangular brackets on the right-hand side of Eq. 3.32 is, however, precisely the series expansion of $S(\infty,-\infty)$ defined by Eq. 3.13. Therefore, the matrix element in the enumerator of Eq. 3.19 for the Green's function can be expressed as

$$\begin{aligned}
&\langle\phi_0|Tc_\lambda(t)c_\lambda^\dagger(t')S(\infty,-\infty)|\phi_0\rangle\\
=&\langle\phi_0|Tc_\lambda(t)c_\lambda^\dagger(t')S(\infty,-\infty)|\phi_0\rangle_{\text{con}}\langle\phi_0|S(\infty,-\infty)|\phi_0\rangle.
\end{aligned} \tag{3.33}$$

Therefore, the expectation value of the S matrix in the denominator (see Eq. 3.19) drops out and we arrive at the final expression of the Green's function in terms of connected diagrams.

$$G(\lambda,t-t')=-i\langle\phi_0|Tc_\lambda(t)c_\lambda^\dagger(t')S(\infty,-\infty)|\phi_0\rangle_{\text{con}} \tag{3.34}$$

$$=-i\sum_{n=0}^{\infty}\frac{(-i)^n}{n!}\int_{-\infty}^{\infty}dt_1\cdots dt_n\,\langle\phi_0|Tc_\lambda(t)c_\lambda^\dagger(t')V(t_1)\cdots V(t_n)|\phi_0\rangle_{\text{con}} \tag{3.35}$$

□

The proof of the linked cluster theorem for the Green's function can be carried out analogously also for correlation functions of higher order [86]. Therefore, any ground state expectation value can in principle be calculated by summing up all connected Feynman diagrams or, in practice, by summing up a carefully chosen finite subset of those diagrams.

3.1.7 Real-frequency Green's functions at zero temperature

So far, we only considered Green's functions in real-time. The previous chapter on density functional theory however discussed at length how to obtain the electronic bandstructure of solids. Therefore, it is logical to consider Green's functions with frequency ω as a variable. Frequency ω and energy E are directly related by $E=\hbar\omega$. Time and frequency are conjugate variables. Therefore, we can obtain the Green's function in real-frequencies by Fourier-transforming the real-time Green's function.

At this point we go back to the definition of the one-particle retarded Green's function (Eq. 3.15). We assume that the system we are interested in can be solved exactly. That means, the interaction term V in the Hamiltonian vanishes. We represent the time-dependent operators according to Eq. 3.2 and insert two complete basis sets. The energy relative to the ground state of the state with quantum numbers λ is denoted as E_λ.

$$\begin{aligned} G_0^r(\lambda, t-t') &= -i\Theta(t-t')\langle c_\lambda(t) c_\lambda^\dagger(t')\rangle \\ &= -i\Theta(t-t')\sum_{n,m}\langle\phi_0|e^{iH_0t}|n\rangle\langle n|c_\lambda e^{-iH_0(t-t')}c_\lambda^\dagger|m\rangle\langle m|e^{-iH_0t'}|\phi_0\rangle \qquad (3.36) \\ &= -i\Theta(t-t')e^{-iE_\lambda(t-t')} \qquad (3.37) \end{aligned}$$

Now we rewrite Eq. 3.37 with $u = t - t'$ and execute the Fourier transformation.

$$G_0^r(\lambda,\omega) = \int_{-\infty}^{\infty} du\, e^{iu\omega} G_0^r(\lambda, u) = -i\int_{-\infty}^{\infty} du\, \Theta(u) e^{iu\omega} e^{-iE_\lambda u} \qquad (3.38)$$

$$= -i\int_0^{\infty} du\, e^{iu(\omega - E_\lambda)} \qquad (3.39)$$

$$= \frac{-1}{\omega - E_\lambda}\left[e^{iu(\omega-E_\lambda)}\right]_0^\infty \qquad (3.40)$$

This expression has two obvious problems: First, it does not converge at the upper limit. Second, it is singular for $\omega = E_\lambda$. Both problems can be somewhat redeemed by artificially introducing a small imaginary part $i\eta$ in the frequency ($\omega \to \omega + i\eta$), which provides convergence for the integral and suppresses the sharp singularity in the denominator.

$$G_0^r(\lambda,\omega) = \lim_{\eta\to 0}\frac{1}{\omega - E_\lambda + i\eta}\left[e^{-u\eta}e^{iu(\omega-E_\lambda)}\right]_\infty^0 = \lim_{\eta\to 0}\frac{1}{\omega - E_\lambda + i\eta} \qquad (3.41)$$

Nevertheless, the limit of $\eta \to 0$ is hard to control and not well-suited for numerical treatment. In the next section we develop the formalism of Green's functions at finite temperatures, which provides additional insight and is more amenable to numerical calculations.

3.2 Green's functions at finite temperature

3.2.1 Imaginary-time Green's functions

Within a temperature-dependent formalism expectation values must be calculated as average over thermodynamic ensembles. If we would introduce the thermodynamic weighting factor $e^{-\beta H}$ with $\beta = (k_B T)^{-1}$ and temperature T into the real-time formalism, the interaction V would occur both in the thermodynamic weighting factor and in the e^{-iVt} term of the S matrix (see Eq. 3.13), which makes the formalism unpleasant to work with.

An alternative is provided by the notion of *complex time* and *complex temperature*. The expressions $e^{-\beta H}$ and e^{-iHt} are similar in that they contain the Hamiltonian H as the non-trivial part, which suggests that treating them simultaneously may be possible. Within the Matsubara method time is indeed treated as a complex temperature given by $\tau = it$. The related formalism will be explained in the following.

We define the electron Green's function as a function of quantum numbers λ and complex timepoints τ and τ'.

$$G(\lambda, \tau - \tau') = -\langle T_\tau c_\lambda(\tau) c^\dagger_\lambda(\tau') \rangle \tag{3.42}$$

$$= -\mathrm{Tr}\left[e^{-\beta(H-\mu N-\Omega)} T_\tau e^{\tau(H-\mu N)} c_\lambda e^{-(\tau-\tau')(H-\mu N)} c^\dagger_\lambda e^{-\tau'(H-\mu N)}\right] \tag{3.43}$$

The angular brackets $\langle \cdots \rangle$ also imply taking the thermodynamic average within a grand-canonical ensemble. The chemical potential is denoted by μ and N is the particle number. The quantity $e^{-\beta\Omega}$ is defined by taking the trace over $e^{-\beta(H-\mu N)}$. Note that T_τ denotes the time-ordering operator, not the temperature. Since the trace is invariant under cyclic permutations and the operator $H - \mu N$ commutes with itself and the scalar Ω, Eq. 3.43 can be rewritten as a function of the difference in imaginary-time only. The second imaginary-time variable τ' can in principle be neglected.

$$\begin{aligned} G(\lambda, \tau - \tau') = &- \Theta(\tau - \tau')\mathrm{Tr}\left[e^{-\beta(H-\mu N-\Omega)} e^{(\tau-\tau')(H-\mu N)} c_\lambda e^{-(\tau-\tau')(H-\mu N)} c^\dagger_\lambda\right. \\ &+ \Theta(\tau' - \tau)\mathrm{Tr}\left.\left[e^{-\beta(H-\mu N-\Omega)} e^{-(\tau-\tau')(H-\mu N)} c^\dagger_\lambda e^{(\tau-\tau')(H-\mu N)} c_\lambda\right]\right. \end{aligned} \tag{3.44}$$

From Eq. 3.44 it is apparent that the imaginary-time Green's function has a specific property due to the cyclic invariance of the trace.

$$G(\lambda, \tau - \beta) = -G(\lambda, \tau) \qquad (-\beta < \tau < 0) \tag{3.45}$$

For bosons the same equality holds, but without the minus sign. Eq. 3.45 means that all information about the imaginary-time Green's function is contained in the window $-\beta < \tau < 0$, proving indeed the equivalence of temperature and imaginary time.

3.2.2 Imaginary-frequency Green's functions

Building on Eq. 3.45 one can define the Green's function in imaginary-frequencies, also called the *Matsubara Green's function*, on a *discrete* set of frequencies ω_n.

$$G(\lambda, i\omega_n) = \int_0^\beta d\tau\, e^{i\omega_n \tau} G(\lambda, \tau) \tag{3.46}$$

The inverse transformation is given by

$$G(\lambda, \tau) = \frac{1}{\beta}\sum_n e^{-i\omega_n \tau} G(\lambda, i\omega_n). \tag{3.47}$$

Using Eq. 3.45 and the previously defined inverse transformation one can infer the values of the discrete so-called *Matsubara frequencies* ω_n.

$$\begin{aligned} 0 =& G(\lambda,\tau) + G(\lambda,\tau-\beta) \\ =& \frac{1}{\beta}\sum_n e^{-i\omega_n\tau}\underbrace{\left(1+e^{i\omega_n\beta}\right)}_{=0} G(\lambda, i\omega_n) \end{aligned} \tag{3.48}$$

The condition $-1 = e^{i\omega_n\beta}$ is fulfilled for $\omega_n = (2n+1)\pi/\beta$ with n being an integer. For bosons one obtains $1 = e^{i\omega_n\beta}$ and $\omega_n = 2n\pi/\beta$. Furthermore, the difference between two fermionic Matsubara frequencies is a bosonic Matsubara frequency.

Numerical calculations involving real-frequency Green's functions $G(\lambda,\omega)$ would require us to artificially discretize the frequency-axis and sample the Green's function on that discretized axis. The accuracy of such a sampling is highly questionable due to the divergent nature of the real-frequency Green's function (see Eq. 3.40). Within the Matsubara method the frequency axis is naturally discrete, which makes it perfectly suitable for numerical calculations.

Now we derive an explicit expression for the unperturbed Matsubara Green's function. First, we need the Baker-Campbell-Hausdorff theorem. For operators A and B it reads

$$e^A B e^{-A} = \sum_{n=0}^{\infty} \frac{1}{n!}[A,B]_n, \quad [A,B]_0 = B, \quad [A,B]_n = [A,[A,B]_{n-1}]. \tag{3.49}$$

Using the commutators $[c_\alpha^\dagger c_\alpha, c_\beta] = -\delta_{\alpha\beta}c_\beta$ and $[c_\alpha^\dagger c_\alpha, c_\beta^\dagger] = \delta_{\alpha\beta}c_\beta^\dagger$ one can write out the series in Eq. 3.49. At every stage of the recursion the same operators are reproduced, but in the case of the annihilator an additional minus sign is acquired. Therefore, the operators can actually be pulled out of the series, which gives an exponential that contains only scalars and considerably simplifies the imaginary-time evolution of creation and annihilation operators for the free system.

$$c_\lambda(\tau) = e^{\tau(H_0-\mu N)} c_\lambda e^{-\tau(H_0-\mu N)} = \sum_{n=0}^{\infty}\frac{[-\tau(E_\lambda-\mu)]^n}{n!}c_\lambda = e^{-\tau(E_\lambda-\mu)}c_\lambda \tag{3.50}$$

$$c_\lambda^\dagger(\tau) = e^{\tau(H_0-\mu N)} c_\lambda^\dagger e^{(-\tau(H_0-\mu N))^n} = \sum_{n=0}^{\infty}\frac{[\tau(E_\lambda-\mu)]^n}{n!}c_\lambda^\dagger = e^{\tau(E_\lambda-\mu)}c_\lambda^\dagger \tag{3.51}$$

To derive the explicit expression for the unperturbed Matsubara Green's function we start from the unperturbed imaginary-time Green's function (Eq. 3.42) and insert Eqs. 3.50 and 3.51. The thermodynamic expectation value of the fermionic number operator $c^\dagger c$ is of course the Fermi function n_F.

$$G_0(\lambda,\tau) = -\,\Theta(\tau)e^{-\tau(E_\lambda-\mu)}\langle c_\lambda c_\lambda^\dagger\rangle + \Theta(-\tau)e^{-\tau(E_\lambda-\mu)}\langle c_\lambda^\dagger c_\lambda\rangle \tag{3.52}$$

$$= -\,e^{-\tau(E_\lambda-\mu)}\left\{\Theta(\tau)[1-n_F(E_\lambda-\mu)] - \Theta(-\tau)n_F(E_\lambda-\mu)\right\} \tag{3.53}$$

$$= -\,e^{-\tau(E_\lambda-\mu)}\left\{\Theta(\tau) - n_F(E_\lambda-\mu)\right\} \tag{3.54}$$

Now we calculate the Fourier transform of Eq. 3.54 according to Eq. 3.46. We use that $e^{i\beta\omega_n} = -1$ for fermions and the explicit form of the Fermi function given by $n_F(E) = 1/(1+e^{\beta E})$.

$$G_0(\lambda, i\omega_n) = -\int_0^\beta d\tau\, e^{i\omega_n\tau} e^{-\tau(E_\lambda-\mu)} \left\{\Theta(\tau) - n_F(E_\lambda-\mu)\right\} \tag{3.55}$$

$$= -\left(1-n_F(E_\lambda-\mu)\right)\int_0^\beta d\tau\, e^{\tau(i\omega_n-(E_\lambda-\mu))} \tag{3.56}$$

$$= -\frac{1-\frac{1}{1+e^{\beta(E_\lambda-\mu)}}}{i\omega_n - E_\lambda+\mu}\left[e^{\tau(i\omega_n-(E_\lambda-\mu))}\right]_0^\beta \tag{3.57}$$

$$= \frac{1-\frac{e^{-\beta(E_\lambda-\mu)}}{1+e^{-\beta(E_\lambda-\mu)}}}{i\omega_n - E_\lambda+\mu}\left(1+e^{-\beta(E_\lambda-\mu)}\right) \tag{3.58}$$

$$= \frac{1}{i\omega_n - E_\lambda+\mu} \tag{3.59}$$

Eq. 3.59 is the final expression for the unperturbed Matsubara Green's function. Within the Matsubara formalism the temperature dependence appears only implicitly within the Matsubara frequencies ω_n, which makes it very elegant and computationally efficient. In particular, the Matsubara method automatically cures all problems of the real-frequency formalism (see Eq. 3.41) at the price of yielding results on the imaginary-frequency axis. The diagrammatic method introduced for Green's functions in real-valued variables can also be applied to Matsubara Green's functions using analogous expressions.

To compare with experiments, which are obviously done in real-frequencies, one in general has to perform a so-called *analytic continuation* to the real-frequency axis. This is sometimes a non-trivial procedure, but of little concern to the calculations presented in this thesis, as we will see in the following chapter.

Chapter 4

Random phase approximation for the multi-orbital Hubbard model

In this chapter we introduce the so-called *random phase approximation*, often abbreviated as *RPA*, which is a method for calculating properties of electronic systems with a high density [88–90]. When represented in terms of Feynman diagrams it corresponds to the summation of a series of diagrams with particular topology up to infinite order [91]. Therefore, the method does not rely on a small expansion parameter and can be expected to give relevant results also in the non-perturbative regime. Furthermore, the expansion up to infinite order can be expressed in a closed form, which makes the RPA method a computationally efficient tool.

We apply the RPA to the single- and multi-orbital Hubbard model, where we calculate the two-particle pairing vertex, which contains information about the symmetry of the superconducting order parameter. For the single-orbital Hubbard model the complete derivation of the RPA method is contained in the literature [92, 93], while the documentation for the multi-orbital case is somewhat terse [94]. Nevertheless, the method is well-established and extensive literature with applications, also to multi-orbital systems, exists [95–103].

In this chapter we present the derivation for the multi-orbital formalism in all relevant detail. The results we obtained agree with the existing literature [94]. Furthermore, we develop a numerical implementation of the method, which is general and efficient. In particular, we do not make any assumption about the dimensionality of the electronic structure (2D or 3D), the number of active sites in the unit cell (single-site or multi-site) or the number of orbitals associated with each active site (single-orbital or multi-orbital). The only assumption we make is that a Fermi surface exists when only the kinetic part of the model Hamiltonian is diagonalized. Such a general implementation allows us to apply the RPA method to both organic superconductors, which can be represented by two-dimensional multi-site and single-orbital models, and iron-based superconductors, which are represented by three-dimensional single-site multi-orbital models, within a unified computational framework.

4.1 Preparations for the analytical derivation

4.1.1 Kubo formula on the Matsubara axis

The time-ordered expectation value of an operator A_i after a small perturbation of a physical system by operator A_j, where i and j denote a set of quantum numbers, is given by the so-called *Kubo formula* [83].

$$\chi_{ij}(\mathbf{q}, \nu_n) = \int_0^\beta d\tau \, e^{-i\nu_n \tau} \langle T_\tau A_i(\mathbf{q}, \tau) A_j(-\mathbf{q}, 0) \rangle \tag{4.1}$$

It defines the so-called *susceptibility* χ_{ij} associated with operators A_i and A_j. The susceptibility is a two-particle Green's function, which we write on the Matsubara frequency axis as the Fourier transformation of a time-ordered two-particle expectation value. The momentum is denoted by $\mathbf{q}$. We assume momentum conservation, which leads to the different signs of the momentum $\mathbf{q}$ in operators $A_i(\mathbf{q}, \tau)$ and $A_j(-\mathbf{q}, 0)$ in Eq. 4.1. Note that the susceptibility is a function of bosonic Matsubara frequencies ν_n.

In the following subsections we will show that susceptibilities are two-particle Green's functions that are rather easy to calculate. Therefore, we will later on expand the two-particle pairing vertex in terms of those susceptibilities, considering fluctuations both in the charge and in the spin channel. First, we, however, need to elaborate on the form of those susceptibility terms.

4.1.2 Unperturbed charge susceptibility

Using the generalized density operator

$$n_s(\mathbf{q}) = \sum_{\mathbf{k}\alpha} c^\dagger_{s\alpha}(\mathbf{k} + \mathbf{q}) c_{s\alpha}(\mathbf{k}), \tag{4.2}$$

in which s denotes the orbital and α the spin of the electrons, we define the unperturbed charge susceptibility χ_0.

$$(\chi_0)^s_t (\mathbf{q}, i\nu_n) = \frac{1}{2} \int_0^\beta d\tau \, e^{-i\nu_n \tau} \langle T_\tau n_s(\mathbf{q}, \tau) n_t(-\mathbf{q}, 0) \rangle. \tag{4.3}$$

Now we insert the explicit representation of the density operators in terms of fermion operators (Eq. 4.2) and apply Wick's theorem (Eq. 3.25) to the time-ordered expectation value in Eq. 4.3. Note that the Green's function depends on the difference of the imaginary timepoints appearing in the associated operators (see Eq. 3.42).

$$\begin{aligned}(\chi_0)^s_t(\mathbf{q}, i\nu_n) =& \frac{1}{2}\int_0^\beta d\tau\, e^{-i\nu_n\tau}\sum_{\mathbf{k}\mathbf{k}'}\sum_{\alpha\beta}\langle T_\tau c^\dagger_{s\alpha}(\mathbf{k}+\mathbf{q},\tau)c_{s\alpha}(\mathbf{k},\tau)c^\dagger_{t\beta}(\mathbf{k}'-\mathbf{q},0)c_{t\beta}(\mathbf{k}',0)\rangle \quad (4.4)\\ =& \frac{1}{2}\int_0^\beta d\tau\, e^{-i\nu_n\tau}\sum_{\mathbf{k}\mathbf{k}'}\sum_{\alpha\beta}\\ &\times\left[G_{s\alpha}(\mathbf{k},0)G_{t\beta}(\mathbf{k}',0)\delta_{\mathbf{q},0} - G_{s\alpha}(\mathbf{k}',-\tau)G_{t\beta}(\mathbf{k},\tau)\delta_{\mathbf{k}+\mathbf{q},\mathbf{k}'}\right]\delta_{\alpha\beta}\delta_{st} \quad (4.5)\end{aligned}$$

For now, we assumed that the Hamiltonian does not allow for a change in the orbital quantum numbers s, t and the spin quantum numbers α, β. The first term in Eq. 4.5 contributes only for $\mathbf{q} = 0$. Since we are mainly interested in the momentum-dependence of the susceptibility, we drop this term. The second term carries a negative sign due to time-ordering. This leaves us with a simple expression for the charge susceptibility.

$$(\chi_0)^s_t(\mathbf{q}, i\nu_n) = -\frac{1}{2}\int_0^\beta d\tau\, e^{-i\nu_n\tau}\sum_{\mathbf{k},\alpha\beta} G_{t\beta}(\mathbf{k},\tau)G_{s\alpha}(\mathbf{k}+\mathbf{q},-\tau)\delta_{\alpha\beta}\delta_{st} \quad (4.6)$$

4.1.3 Unperturbed spin susceptibility

Using generalized Abrikosov pseudo-fermion operators

$$\mathbf{S}_s(\mathbf{q}) = \frac{1}{2}\sum_{\alpha\beta} c^\dagger_{s\alpha}(\mathbf{k}+\mathbf{q})\boldsymbol{\sigma}_{\alpha\beta}c_{s\beta}(\mathbf{k}), \quad (4.7)$$

in which s denotes the orbital and α, β the spins of the electrons, we define the unperturbed spin susceptibility χ_1.

$$(\chi_1)^s_t(\mathbf{q}, i\nu_n) = \frac{2}{3}\int_0^\beta d\tau\, e^{-i\nu_n\tau}\langle T_\tau \mathbf{S}_s(\mathbf{q},\tau)\cdot\mathbf{S}_t(-\mathbf{q},0)\rangle \quad (4.8)$$

Here, the vector of Pauli matrices is denoted as $\boldsymbol{\sigma}$, which is given by

$$\boldsymbol{\sigma} = (\sigma_x, \sigma_y, \sigma_z), \quad \sigma_x = \begin{pmatrix}0 & 1\\ 1 & 0\end{pmatrix}, \quad \sigma_y = \begin{pmatrix}0 & -i\\ i & 0\end{pmatrix}, \quad \sigma_z = \begin{pmatrix}1 & 0\\ 0 & -1\end{pmatrix}. \quad (4.9)$$

Now we insert the explicit representation of the spin-operators (Eq. 4.7) and the Pauli matrices into Eq. 4.8 and execute the scalar product of spin-operators.

$$\begin{aligned}(\chi_1)^s_t(\mathbf{q}, i\nu_n) =& \frac{1}{6}\int_0^\beta d\tau\, e^{-i\nu_n\tau}\sum_{\mathbf{k}\mathbf{k}'\alpha}\langle T_\tau \\ &\times\Big[2c^\dagger_{s\alpha}(\mathbf{k}+\mathbf{q},\tau)c_{s\bar{\alpha}}(\mathbf{k},\tau)c^\dagger_{t\bar{\alpha}}(\mathbf{k}'-\mathbf{q},0)c_{t\alpha}(\mathbf{k}',0) \\ &+ c^\dagger_{s\alpha}(\mathbf{k}+\mathbf{q},\tau)c_{s\alpha}(\mathbf{k},\tau)c^\dagger_{t\alpha}(\mathbf{k}'-\mathbf{q},0)c_{t\alpha}(\mathbf{k}',0) \\ &- c^\dagger_{s\alpha}(\mathbf{k}+\mathbf{q},\tau)c_{s\alpha}(\mathbf{k},\tau)c^\dagger_{t\bar{\alpha}}(\mathbf{k}'-\mathbf{q},0)c_{t\bar{\alpha}}(\mathbf{k}',0)\Big]\rangle \end{aligned} \tag{4.10}$$

Now we apply Wick's theorem (Eq. 3.25) to Eq. 4.10 and again neglect the term with $\mathbf{q} = 0$. As for the charge susceptibility, we get a negative sign due to time-ordering.

$$(\chi_1)^s_t(\mathbf{q}, i\nu_n) = -\frac{1}{6}\int_0^\beta d\tau\, e^{-i\nu_n\tau}\sum_{\mathbf{k}\alpha\beta}\left[G_{t\beta}(\mathbf{k},\tau)G_{s\alpha}(\mathbf{k}+\mathbf{q},-\tau)(\delta_{\alpha\beta}+2\delta_{\alpha\bar{\beta}})\right]\delta_{st} \tag{4.11}$$

Comparing the expressions for the unperturbed charge susceptibility (Eq. 4.6) and the unperturbed spin susceptibility (Eq. 4.11), we see that they are actually equal in the paramagnetic case, where $G_{s\alpha} = G_{s\bar{\alpha}}$.

Since we will assume that superconductivity emerges from a paramagnetic metal, we can calculate the unperturbed paramagnetic susceptibility and concentrate on it as the central object of our theory. Nevertheless, the spin quantum number can not be neglected in further calculations, since this would lead to diagram counting errors. This point will become more clear in a later section.

4.1.4 Explicit expression for the unperturbed paramagnetic susceptibility

We now derive an explicit expression for the unperturbed paramagnetic susceptibility. In contrast to the previous subsections we assume a multi-orbital kinetic Hamiltonian, which allows for transitions between different orbitals. The unperturbed imaginary-frequency Matsubara Green's function connecting orbitals s and p is defined as a generalization of Eq. 3.59.

$$G_{sq}(\mathbf{k}, i\omega_n) = \sum_\lambda \frac{a^{s*}_\lambda(\mathbf{k})a^q_\lambda(\mathbf{k})}{i\omega_n - E_\lambda} \tag{4.12}$$

Here, we assume that the chemical potential μ is already absorbed into the energy eigenvalues E_λ of the kinetic Hamiltonian. The momentum is denoted as $\mathbf{k}$. The summation over electronic bands is indicated by the sum over λ. Orbital and band space are connected by matrix elements $a^s_\lambda(\mathbf{k})$, which result from the diagonalization of the kinetic part of the Hamiltonian. The star in Eq. 4.12 denotes the complex conjugate.

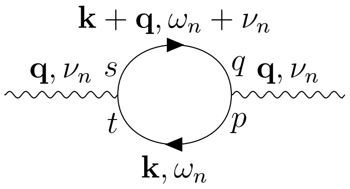

Figure 4.1: Feynman diagram representing the unperturbed susceptibility $\chi^{pq}_{st}(\mathbf{q}, i\nu_n)$.

Now we insert the Fourier transform of the imaginary-time Green's function (Eq. 3.47) into Eq. 4.6, in which we also perform the summation over spins. Furthermore, we use the imaginary-frequency Matsubara Green's function as defined in Eq. 4.12.

$$\chi^{pq}_{st}(\mathbf{q}, i\nu_n) = -\frac{1}{\beta^2}\int_0^\beta d\tau\, e^{-i\nu_n\tau} \sum_{\mathbf{k},\omega_n,\omega'_n} \left[e^{-i\omega_n\tau} G_{pt}(\mathbf{k}, i\omega_n) e^{i\omega'_n\tau} G_{sq}(\mathbf{k}+\mathbf{q}, i\omega'_n)\right] \tag{4.13}$$

$$= -\frac{1}{\beta^2}\sum_{\mathbf{k},\omega_n,\omega'_n} G_{pt}(\mathbf{k}, i\omega_n) G_{sq}(\mathbf{k}+\mathbf{q}, i\omega'_n) \frac{e^{i\beta(\nu_n-\omega_n+\omega'_n)}-1}{i(-\nu_n-\omega_n+\omega'_n)} \tag{4.14}$$

Since we sum over all positive and negative Matsubara frequencies, the fraction in Eq. 4.14 does not contribute, except when $-\nu_n = \omega_n - \omega'_n$. In that case we have to use l'Hopsital's rule to evaluate the fraction.

$$\lim_{-\nu\to\omega_n-\omega'_n} \frac{e^{i\beta(-\nu_n-\omega_n+\omega'_n)}-1}{i(-\nu_n-\omega_n+\omega'_n)} \tag{4.15}$$

$$= \lim_{-\nu\to\omega_n-\omega'_n} \frac{i\beta\left(e^{i\beta(-\nu_n-\omega_n+\omega'_n)}-1\right)}{i} = \beta \tag{4.16}$$

The unperturbed susceptibility, therefore, becomes a Matsubara sum over a product of Green's functions.

$$\chi^{pq}_{st}(\mathbf{q}, i\nu_n) = -\frac{1}{\beta}\sum_{\mathbf{k},\omega_n} G_{pt}(\mathbf{k}, i\omega_n) G_{sq}(\mathbf{k}+\mathbf{q}, i\omega_n + i\nu_n) \tag{4.17}$$

The Feynman diagram associated with this product is shown in Fig. 4.1. The external interaction lines colored in black only indicate that momentum transfer takes place, but are not specified further yet.

Now we insert the explicit form of the Matsubara Green's function in orbital space (Eq. 4.12).

$$\chi^{pq}_{st}(\mathbf{q}, i\nu_n) = -\frac{1}{\beta}\sum_{\mathbf{k},\omega_n}\sum_{l,m} a^{p*}_l(\mathbf{k}) a^t_l(\mathbf{k}) a^{s*}_m(\mathbf{k}+\mathbf{q}) a^q_m(\mathbf{k}+\mathbf{q})$$

$$\times \frac{1}{i\omega_n - E_l(\mathbf{k})} \frac{1}{i\omega_n + i\nu_n - E_m(\mathbf{k}+\mathbf{q})} \tag{4.18}$$

The summation over Matsubara frequencies can be evaluated via the residue theorem. In the last step we used the definition of the Fermi function.

$$\frac{1}{\beta}\sum_{\omega_n}\frac{1}{i\omega_n - E_l(\mathbf{k})}\frac{1}{i\omega_n + i\nu_n - E_m(\mathbf{k}+\mathbf{q})} \tag{4.19}$$

$$\begin{aligned}=&-\frac{1}{\beta}\left[\lim_{z\to E_l(\mathbf{k})}\frac{1}{z+i\nu_n-E_m(\mathbf{k}+\mathbf{q})}\frac{-\beta}{1+e^{\beta z}}\right.\\ &\left.+\lim_{z\to -i\nu_n+E_m(\mathbf{k}+\mathbf{q})}\frac{1}{z-E_l(\mathbf{k})}\frac{-\beta}{1+e^{\beta z}}\right]\end{aligned} \tag{4.20}$$

$$=\frac{n_F(E_l(\mathbf{k}))-n_F(E_m(\mathbf{k}+\mathbf{q}))}{E_l(\mathbf{k})-E_m(\mathbf{k}+\mathbf{q})+i\nu_n} \tag{4.21}$$

Using Eq. 4.21 we can rewrite the unperturbed paramagnetic susceptibility.

$$\begin{aligned}\chi^{pq}_{st}(\mathbf{q},i\nu_n)=&-\sum_{\mathbf{k},l,m}a^{p*}_l(\mathbf{k})a^t_l(\mathbf{k})a^{s*}_m(\mathbf{k}+\mathbf{q})a^q_m(\mathbf{k}+\mathbf{q})\\ &\times\frac{n_F(E_l(\mathbf{k}))-n_F(E_m(\mathbf{k}+\mathbf{q}))}{E_l(\mathbf{k})-E_m(\mathbf{k}+\mathbf{q})+i\nu_n}\end{aligned} \tag{4.22}$$

In this form the paramagnetic susceptibility is a tensor of four orbital indices, the momentum transfer $\mathbf{q}$ and the bosonic Matsubara frequency ν_n. Clearly, it describes bosonic excitations, which are associated with energy- and momentum-state transitions in the electronic bandstructure. Indeed, the diagonalization of the kinetic part of the Hamiltonian is all we need to calculate the unperturbed paramagnetic susceptibility. The continuation to the real-frequency axis can be performed by replacing $i\nu_n \to \nu + i\eta$ and taking the limit of $\eta \to 0$.

4.1.5 Connection between static susceptibility and real-space ordering

In this section we illustrate the physical meaning of the static susceptibility $\chi(\mathbf{q},0)$. We start by writing down the momentum-space spin susceptibility (Eq. 4.8) in terms of the real-space spin operators.

$$\chi_1(\mathbf{q},0)=\frac{2}{3}\sum_{i,j}e^{i\mathbf{q}\cdot(\mathbf{R_i}-\mathbf{R_j})}\langle\mathbf{S}(\mathbf{R_i},0)\cdot\mathbf{S}(\mathbf{R_j},0)\rangle \tag{4.23}$$

For simplicity we now assume that the spins are classical, so that we can obtain the expectation values easily. As an example, we choose two-dimensional antiferromagnetic stripe order, in which up and down spins alternate along the x-direction (lattice constant a), while spins do not alternate along the y-direction (lattice constant b). This situation is shown in Fig. 4.2. Using $-1 = e^{i\pi}$ and neglecting the irrelevant prefactors we obtain the

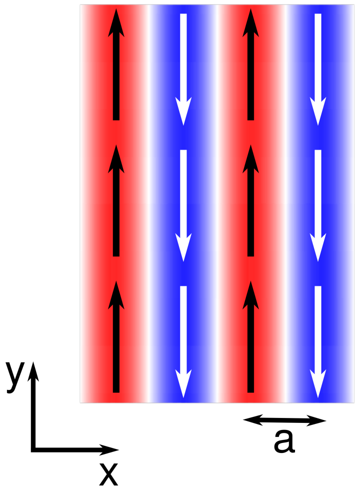

Figure 4.2: Two-dimensional spin pattern, in which up and down spins alternate along the x-direction. This spatial configuration is usually referred to as antiferromagnetic stripe order.

following susceptibility:

$$\chi_1(\mathbf{q},0) = \sum_{m,n} (-1)^m e^{iq_x ma} e^{iq_y nb} \tag{4.24}$$

$$= \sum_m e^{i(q_x \pm \pi/a)ma} \sum_n e^{iq_y nb} \tag{4.25}$$

$$= \delta(q_x \pm \pi/a)\, \delta(q_y) \tag{4.26}$$

The result in Eq. 4.26 relates to the so-called *ordering vector* $\mathbf{q} = (q_x, q_y) = (\pm\pi/a, 0)$ associated with the antiferromagnetic stripe pattern proposed earlier.

These considerations reveal that static ordering tendencies are encoded into the static susceptibility of a system. Although we only treated real-space spin ordering in the example, ordering vectors can also be associated with other order parameters (see, for example, Eq. 4.3).

4.2 Analytical derivation in terms of Feynman diagrams

4.2.1 Fourier transformation of the interaction Hamiltonian

The aim of this section is to go beyond the unperturbed susceptibility and calculate higher order terms. The full susceptibility up to infinite order can be written in analogy to the series expansion of the Green's function (Eq. 3.35). The spin quantum numbers are now denoted as $\alpha, \beta, \delta, \epsilon$.

$$\begin{aligned}\chi_{st}^{pq}(\mathbf{q}, i\nu_n) =&A \int_0^\beta d\tau\, e^{-i\nu_n\tau} \sum_{\mathbf{k}\mathbf{k}'} \sum_{\alpha\beta\delta\epsilon} \sum_{n=0}^{\infty} \frac{(-1)^n}{n!} \\ &\times \left\langle T_\tau c_{p\alpha}^\dagger(\mathbf{k}, \tau) c_{s\beta}^\dagger(\mathbf{k}', 0) c_{t\delta}(\mathbf{k}' - \mathbf{q}, 0) c_{q\epsilon}(\mathbf{k} + \mathbf{q}, \tau) S^n \right\rangle_{\text{con}} \end{aligned} \tag{4.27}$$

With respect to the previous definition of the susceptibility we relabelled the momenta $\mathbf{q} \to -\mathbf{q}$, $\mathbf{k} \to \mathbf{k} + \mathbf{q}$ and $\mathbf{k}' \to \mathbf{k}' - \mathbf{q}$. The prefactor A and the restrictions to spin indices $\alpha, \beta, \delta, \epsilon$ have to be adapted to the charge and spin channel respectively.

To the charge channel terms with $\alpha = \epsilon, \beta = \delta$ contribute with prefactor $A = 1/2$ (see Eq. 4.4). To the spin channel terms $\alpha = \delta, \beta = \epsilon, \alpha \neq \beta$ contribute with prefactor $A = 1/3$, terms $\alpha = \beta = \delta = \epsilon$ contribute with prefactor $A = 1/6$ and terms $\alpha = \epsilon, \beta = \delta, \alpha \neq \beta$ contribute with prefactor $A = -1/6$ (see Eq. 4.10).

Using greek letters to denote tuples of all relevant quantum numbers, the general form of the interaction term, which occurs in higher expansion orders, is given by

$$S = \frac{1}{2} \int_0^\beta d\tau \sum_{\gamma\delta\lambda\mu} (\gamma\delta|V|\lambda\mu) c_\gamma^\dagger c_\delta^\dagger c_\mu c_\lambda. \tag{4.28}$$

The fermionic operators all carry the same index τ in imaginary-time, which means that the interaction is instantaneous.

Since our aim is to calculate the susceptibility in momentum-space (see Eq. 4.27), we need to express also the interaction terms (Eq. 4.28) in momentum-space. Our Hamiltonian of interest is the multi-orbital Hubbard model (Eq. 1.4), which consists of four interaction terms in real-space. Their momentum-space representation is obtained via Fourier transformation.

We start with the intra-orbital Coulomb repulsion and insert the Fourier transformation of the fermionic operators with respect to lattice site coordinates $\mathbf{x}$. The orbital is denoted by index l and σ represents the spin.

$$U \sum_{\mathbf{x}u} n_{\mathbf{x}u\uparrow} n_{\mathbf{x}u\downarrow} = \frac{U}{2} \sum_{\mathbf{x}u\sigma} n_{\mathbf{x}u\sigma} n_{\mathbf{x}u\bar{\sigma}} \tag{4.29}$$

$$= \frac{U}{2} \sum_{\mathbf{x}u\sigma} c_{u\sigma}^\dagger(\mathbf{x}) c_{u\sigma}(\mathbf{x}) c_{u\bar{\sigma}}^\dagger(\mathbf{x}) c_{u\bar{\sigma}}(\mathbf{x}) \tag{4.30}$$

$$= \frac{U}{2} \sum_{\mathbf{x}\mathbf{x}'u\sigma} \underbrace{\delta_{\mathbf{x}\mathbf{x}'}}_{=\sum_{\mathbf{q}} e^{iq(\mathbf{x}-\mathbf{x}')}} c_{u\sigma}^\dagger(\mathbf{x}) c_{u\bar{\sigma}}^\dagger(\mathbf{x}') c_{u\bar{\sigma}}(\mathbf{x}') c_{u\sigma}(\mathbf{x}) \tag{4.31}$$

$$=\frac{U}{2N^2}\sum_{u\sigma}\sum_{\mathbf{x}\mathbf{x}'}\sum_{\substack{\mathbf{q}\mathbf{k}\mathbf{k}'\\ \mathbf{k}''\mathbf{k}'''}} c^\dagger_{u\bar{\sigma}}(\mathbf{k})c^\dagger_{u\sigma}(\mathbf{k}')c_{u\bar{\sigma}}(\mathbf{k}'')c_{u\sigma}(\mathbf{k}''')\underbrace{e^{i\mathbf{x}(\mathbf{q}+\mathbf{k}-\mathbf{k}''')}}_{=\delta_{\mathbf{k},\mathbf{k}'''-\mathbf{q}}}\underbrace{e^{i\mathbf{x}'(\mathbf{k}'-\mathbf{k}''-\mathbf{q})}}_{\delta_{\mathbf{k}',\mathbf{k}''+\mathbf{q}}} \tag{4.32}$$

$$=\frac{U}{2}\sum_{u\sigma}\sum_{\mathbf{q}\mathbf{k}\mathbf{k}'} c^\dagger_{u\sigma}(\mathbf{k}+\mathbf{q})c^\dagger_{u\bar{\sigma}}(\mathbf{k}'-\mathbf{q})c_{u\bar{\sigma}}(\mathbf{k}')c_{u\sigma}(\mathbf{k}) \tag{4.33}$$

The factor N^{-2}, where N is the number of lattice sites, is introduced by the Fourier transformation of the fermionic operators and then cancelled by the summations over lattice sites $\mathbf{x}$ and $\mathbf{x}'$.

In the same way we obtain the Fourier transformation of the inter-orbital Coulomb repulsion.

$$\frac{V}{2}\sum_{\mathbf{x},u,v\neq u} n_{\mathbf{x}u}n_{\mathbf{x}v} =\frac{V}{2}\sum_{\substack{\mathbf{x},\sigma\\ u,v\neq u}}\left(n_{\mathbf{x}u\sigma}n_{\mathbf{x}v\sigma}+n_{\mathbf{x}u\sigma}n_{\mathbf{x}v\bar{\sigma}}\right) \tag{4.34}$$

$$=\frac{V}{2}\sum_{\substack{u,u\neq v\\ \sigma}}\sum_{\mathbf{q}\mathbf{k}\mathbf{k}'}\Big[c^\dagger_{u\sigma}(\mathbf{k}+\mathbf{q})c^\dagger_{v\sigma}(\mathbf{k}'-\mathbf{q})c_{v\sigma}(\mathbf{k}')c_{u\sigma}(\mathbf{k})$$

$$+\,c^\dagger_{u\sigma}(\mathbf{k}+\mathbf{q})c^\dagger_{v\bar{\sigma}}(\mathbf{k}'-\mathbf{q})c_{v\bar{\sigma}}(\mathbf{k}')c_{u\sigma}(\mathbf{k})\Big] \tag{4.35}$$

The Hund's rule coupling (inter-orbital exchange) term contains contributions of the same structure as inter-orbital Coulomb repulsion (see Eq. 4.35).

$$-\frac{J}{2}\sum_{\mathbf{x},u,v\neq u}\mathbf{S}_{\mathbf{x}u}\cdot\mathbf{S}_{\mathbf{x}v} =-\frac{J}{8}\sum_{\substack{u,u\neq v\\ \sigma}}\sum_{\mathbf{q}\mathbf{k}\mathbf{k}'}\Big(2c^\dagger_{u\sigma}(\mathbf{k}+\mathbf{q})c^\dagger_{v\bar{\sigma}}(\mathbf{k}'-\mathbf{q})c_{v\sigma}(\mathbf{k}')c_{u\bar{\sigma}}(\mathbf{k})$$

$$+\,c^\dagger_{u\sigma}(\mathbf{k}+\mathbf{q})c^\dagger_{v\sigma}(\mathbf{k}'-\mathbf{q})c_{v\sigma}(\mathbf{k}')c_{u\sigma}(\mathbf{k})$$

$$-\,c^\dagger_{u\sigma}(\mathbf{k}+\mathbf{q})c^\dagger_{v\bar{\sigma}}(\mathbf{k}'-\mathbf{q})c_{v\bar{\sigma}}(\mathbf{k}')c_{u\sigma}(\mathbf{k})\Big) \tag{4.36}$$

Finally, the pair hopping term has a slightly different structure in orbital-space compared to the inter-orbital exchange (see Eq. 4.36).

$$\frac{J'}{2}\sum_{\substack{\mathbf{x},\sigma\\ u,v\neq u}} c^\dagger_{\mathbf{x}u\sigma}c^\dagger_{\mathbf{x}u\bar{\sigma}}c_{\mathbf{x}v\bar{\sigma}}c_{\mathbf{x}v\sigma} =\frac{J'}{2}\sum_{\substack{u,u\neq v\\ \sigma}}\sum_{\mathbf{q}\mathbf{k}\mathbf{k}'} c^\dagger_{u\sigma}(\mathbf{k}+\mathbf{q})c^\dagger_{u\bar{\sigma}}(\mathbf{k}'-\mathbf{q})c_{v\bar{\sigma}}(\mathbf{k}')c_{v\sigma}(\mathbf{k}) \tag{4.37}$$

Since we have now written down the interaction part of the Hamiltonian in momentum-space and imaginary-time, we can proceed to evaluate higher order terms of the perturbation expansion for the susceptibility (Eq. 4.27). We calculate all first order ($n = 1$) terms, which can be written in terms of the unperturbed susceptibility (Eq. 4.17). This calculation is carried out separately for each of the interaction terms and we determine the corresponding contributions to the perturbation expansion. Afterwards, we collect all terms and construct and expansion up to infinite order in the spirit of the random phase approximation. We show that, for the multi-orbital Hubbard model, a matrix equation can be used to generate all diagrams that can be expressed as products of unperturbed susceptibilities. Finally, we use the perturbation expansion for the susceptibility to construct an approximation for the two-particle pairing vertex and explain how to obtain the momentum-space symmetry of the electron pairing from this object.

4.2.2 Diagrammatic expansion for the intra-orbital Coulomb repulsion

We calculate all possible connected pairings of the first-order term in the perturbation expansion of the susceptibility (Eq. 4.27) using the Fourier transformation of the intra-orbital Coulomb repulsion (Eq. 4.33). The interaction vertex is implicitly assumed to be inserted at imaginary-time τ''.

$$c^\dagger_{p\alpha}(\mathbf{k},\tau)c^\dagger_{s\beta}(\mathbf{k}',0)c_{t\delta}(\mathbf{k}'-\mathbf{q},0)c_{q\epsilon}(\mathbf{k}+\mathbf{q},\tau)c^\dagger_{u\sigma}(\mathbf{k}''+\mathbf{q}')c^\dagger_{u\bar{\sigma}}(\mathbf{k}'''-\mathbf{q}')c_{u\bar{\sigma}}(\mathbf{k}''')c_{u\sigma}(\mathbf{k}'') \tag{4.38}$$

We neglect all terms, which cannot be written in terms of the unperturbed susceptibility and those which contribute only for vanishing external momentum $\mathbf{q} = 0$. Out of all $4! = 24$ possible pairings only four fulfill our criteria.

$$\wick{\c1{c}^\dagger_{p\alpha}(\mathbf{k},\tau)\c2{c}^\dagger_{s\beta}(\mathbf{k}',0)\c3{c}_{t\delta}(\mathbf{k}'-\mathbf{q},0)\c4{c}_{q\epsilon}(\mathbf{k}+\mathbf{q},\tau)\c3{c}^\dagger_{u\sigma}(\mathbf{k}''+\mathbf{q}')\c4{c}^\dagger_{u\bar{\sigma}}(\mathbf{k}'''-\mathbf{q}')\c1{c}_{u\bar{\sigma}}(\mathbf{k}''')\c2{c}_{u\sigma}(\mathbf{k}'')} \tag{4.39}$$

$$\wick{\c1{c}^\dagger_{p\alpha}(\mathbf{k},\tau)\c2{c}^\dagger_{s\beta}(\mathbf{k}',0)\c3{c}_{t\delta}(\mathbf{k}'-\mathbf{q},0)\c4{c}_{q\epsilon}(\mathbf{k}+\mathbf{q},\tau)\c4{c}^\dagger_{u\sigma}(\mathbf{k}''+\mathbf{q}')\c3{c}^\dagger_{u\bar{\sigma}}(\mathbf{k}'''-\mathbf{q}')\c2{c}_{u\bar{\sigma}}(\mathbf{k}''')\c1{c}_{u\sigma}(\mathbf{k}'')} \tag{4.40}$$

$$\wick{\c1{c}^\dagger_{p\alpha}(\mathbf{k},\tau)\c2{c}^\dagger_{s\beta}(\mathbf{k}',0)\c3{c}_{t\delta}(\mathbf{k}'-\mathbf{q},0)\c4{c}_{q\epsilon}(\mathbf{k}+\mathbf{q},\tau)\c4{c}^\dagger_{u\sigma}(\mathbf{k}''+\mathbf{q}')\c3{c}^\dagger_{u\bar{\sigma}}(\mathbf{k}'''-\mathbf{q}')\c1{c}_{u\bar{\sigma}}(\mathbf{k}''')\c2{c}_{u\sigma}(\mathbf{k}'')} \tag{4.41}$$

$$\wick{\c1{c}^\dagger_{p\alpha}(\mathbf{k},\tau)\c2{c}^\dagger_{s\beta}(\mathbf{k}',0)\c3{c}_{t\delta}(\mathbf{k}'-\mathbf{q},0)\c4{c}_{q\epsilon}(\mathbf{k}+\mathbf{q},\tau)\c3{c}^\dagger_{u\sigma}(\mathbf{k}''+\mathbf{q}')\c4{c}^\dagger_{u\bar{\sigma}}(\mathbf{k}'''-\mathbf{q}')\c2{c}_{u\bar{\sigma}}(\mathbf{k}''')\c1{c}_{u\sigma}(\mathbf{k}'')} \tag{4.42}$$

The corresponding Feynman diagrams are shown in Fig. 4.3. The interaction line colored in blue represents the intra-orbital Coulomb repulsion. The external interaction lines colored in black only indicate that momentum transfer takes place, but are not specified further yet.

The spin indices α, β, δ and ϵ are determined from the condition that no Green's function contains different spin operators. This condition is imposed by the kinetic Hamiltonian, which does not allow for transitions between states with different spin (see Eq. 1.4). Furthermore, some of the internal momenta can be determined by imposing momentum conservation. For example, in Eqs. 4.39 and 4.40 the internal momentum $\mathbf{q}'$ at the intra-orbital Coulomb vertex must be equal to $\mathbf{q}$ (see Fig. 4.3).

Note that Fig. 4.3 contains only two types of topologically equivalent diagrams. Diagrams (a) and (b) (often called *bubble diagrams*), as well as diagrams (c) and (d) (often called *ladder diagrams*) become identical after relabelling the spin variable $\sigma \to \bar{\sigma}$. Therefore, they give the same contribution to the susceptibility. For diagrams (a) and (b) it

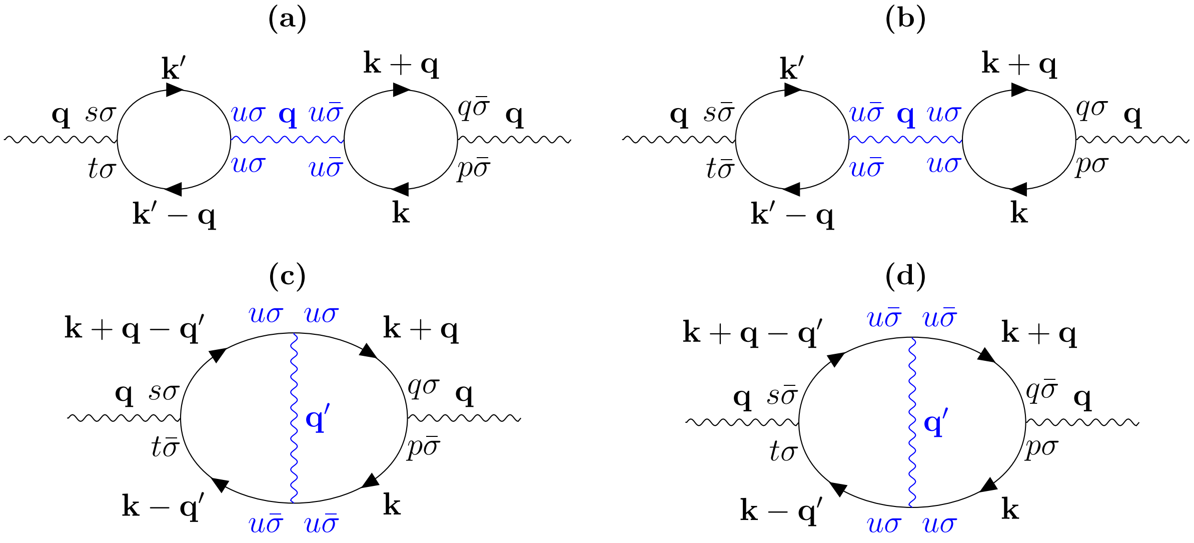
(a)
$\mathbf{k}'$
$\mathbf{k}+\mathbf{q}$
$\mathbf{q}$ $s\sigma$
$u\sigma$ $\mathbf{q}$ $u\bar{\sigma}$
$q\bar{\sigma}$ $\mathbf{q}$
$t\sigma$
$u\sigma$
$u\bar{\sigma}$
$p\bar{\sigma}$
$\mathbf{k}'-\mathbf{q}$
$\mathbf{k}$
(b)
$\mathbf{k}'$
$\mathbf{k}+\mathbf{q}$
$\mathbf{q}$ $s\bar{\sigma}$
$u\bar{\sigma}$ $\mathbf{q}$ $u\sigma$
$q\sigma$ $\mathbf{q}$
$t\bar{\sigma}$
$u\bar{\sigma}$
$u\sigma$
$p\sigma$
$\mathbf{k}'-\mathbf{q}$
$\mathbf{k}$
(c)
$\mathbf{k}+\mathbf{q}-\mathbf{q}'$
$u\sigma$ $u\sigma$
$\mathbf{k}+\mathbf{q}$
$\mathbf{q}$ $s\sigma$
$q\bar{\sigma}$ $\mathbf{q}$
$\mathbf{q}'$
$t\bar{\sigma}$
$p\bar{\sigma}$
$\mathbf{k}-\mathbf{q}'$
$\mathbf{k}$
$u\bar{\sigma}$ $u\bar{\sigma}$
(d)
$\mathbf{k}+\mathbf{q}-\mathbf{q}'$
$u\bar{\sigma}$ $u\bar{\sigma}$
$\mathbf{k}+\mathbf{q}$
$\mathbf{q}$ $s\bar{\sigma}$
$q\bar{\sigma}$ $\mathbf{q}$
$\mathbf{q}'$
$t\sigma$
$p\sigma$
$\mathbf{k}-\mathbf{q}'$
$\mathbf{k}$
$u\sigma$ $u\sigma$

Figure 4.3: Feynman diagrams of the first order contribution in the intra-orbital Coulomb repulsion to the susceptibility corresponding to the operator pairings in (a) Eq. 4.39, (b) Eq. 4.40, (c) Eq. 4.41 and (d) Eq. 4.42.

is already obvious from the Feynman diagram that they can be written as a product of two unperturbed susceptibilities. Diagrams (c) and (d) can also be written as products over unperturbed susceptibilities after grouping the Green's functions on both sides of the intra-orbital Coulomb vertex, since the momentum summations decouple after relabelling $\mathbf{k}-\mathbf{q}' \to \mathbf{k}'$.

The diagrams also carry a minus sign depending on whether the number of fermion operator permutations needed for grouping the connected creators and annihilators is even (positive sign) or odd (negative sign). Therefore the diagrams corresponding to Eqs. 4.39 and 4.40 carry positive sign, while the diagrams corresponding to Eqs. 4.41 and 4.42 carry negative sign.

As explained in the previous subsection, the spin indices α, β, δ and ϵ give a prefactor for the contribution of each diagram to charge and spin susceptibility. Eqs. 4.39 and 4.40 imply that $\alpha = \epsilon$, $\beta = \delta$ and $\alpha \neq \beta$. Therefore, both diagrams contribute to the charge susceptibility with a prefactor of $A = 1/2$. Taking into account the additional minus sign from the expansion order (see Eq. 4.27) the first order contribution in the intra-orbital Coulomb repulsion to the charge susceptibility, therefore, reads

$$-\sum_{u} \chi^{uu}_{st}(\mathbf{q}) U \chi^{pq}_{uu}(\mathbf{q}). \tag{4.43}$$

For the spin susceptibility we get contributions from Eqs. 4.41 and 4.42, which imply $\alpha = \delta$, $\beta = \epsilon$ and $\alpha \neq \beta$, with prefactor $A = 1/3$ and from Eqs. 4.39 and 4.40 with prefactor $A = -1/6$. The signs of the prefactors and the additional negative sign from the expansion order cancel all negative signs of the individual diagrams, so that the first order contribution in the intra-orbital Coulomb repulsion to the spin susceptibility reads

$$+\sum_u \chi_{st}^{uu}(\mathbf{q}) U \chi_{uu}^{pq}(\mathbf{q}). \tag{4.44}$$

At this point we already have enough information to write down the random phase approximation for the single-orbital Hubbard model. In the single-orbital case the tensor χ_{st}^{pq} becomes a scalar. Generating higher order diagrams only means we insert additional interaction vertices into the bubble and ladder topology diagrams. A mixture of both is not allowed, because the kinetic Hamiltonian forbids Green's functions that mix spin. Therefore, the charge and spin susceptibilities of the single-orbital Hubbard model differ only by a minus sign.

$$\chi^c = \chi^0 - \chi^0 U \chi^0 + \chi^0 U \chi^0 U \chi^0 - \ldots = \chi^0 - \chi^0 U \chi^c \tag{4.45}$$

$$\chi^s = \chi^0 + \chi^0 U \chi^0 + \chi^0 U \chi^0 U \chi^0 + \ldots = \chi^0 + \chi^0 U \chi^s \tag{4.46}$$

Here, χ^c denotes the charge susceptibility, χ^s denotes the spin susceptibility and χ^0 denotes the unperturbed susceptibility. Note that we implicitly used the sum formula for a geometric series and assumed that the series converges, which implies $|U\chi^0| < 1$.

In fact, Eqs. 4.45 and 4.46 can be solved for the susceptibilities at infinite expansion order.

$$\chi^c = \frac{\chi^0}{1 + U\chi^0} \tag{4.47}$$

$$\chi^s = \frac{\chi^0}{1 - U\chi^0} \tag{4.48}$$

The most important advantage of restricting the diagrammatic expansion to terms that can be written as products of susceptibilities is apparent from Eqs. 4.47 and 4.48. The restriction in diagram topology yields a closed form for the expansion up to infinite order in terms of only the unperturbed susceptibility and the interaction strength. Of course, such expressions are much easier to evaluate than calculating higher order terms explicitly, since they come with a strongly increasing numerical cost due to additional indices that we have to sum over.

For the multi-orbital Hubbard model we will now follow a similar strategy. From the first order contributions to the susceptibilities we will calculate the elements of interaction tensors U^c and U^s corresponding to each term in the multi-orbital Hubbard model. We will then construct the susceptibilities up to infinite order in analogy to Eqs. 4.47 and 4.48.

In Eqs. 4.43 and 4.44 we have already determined some of the elements in the interaction tensor.

$$(U^c)_{aa}^{aa} = U \tag{4.49}$$

$$(U^s)_{aa}^{aa} = U \tag{4.50}$$

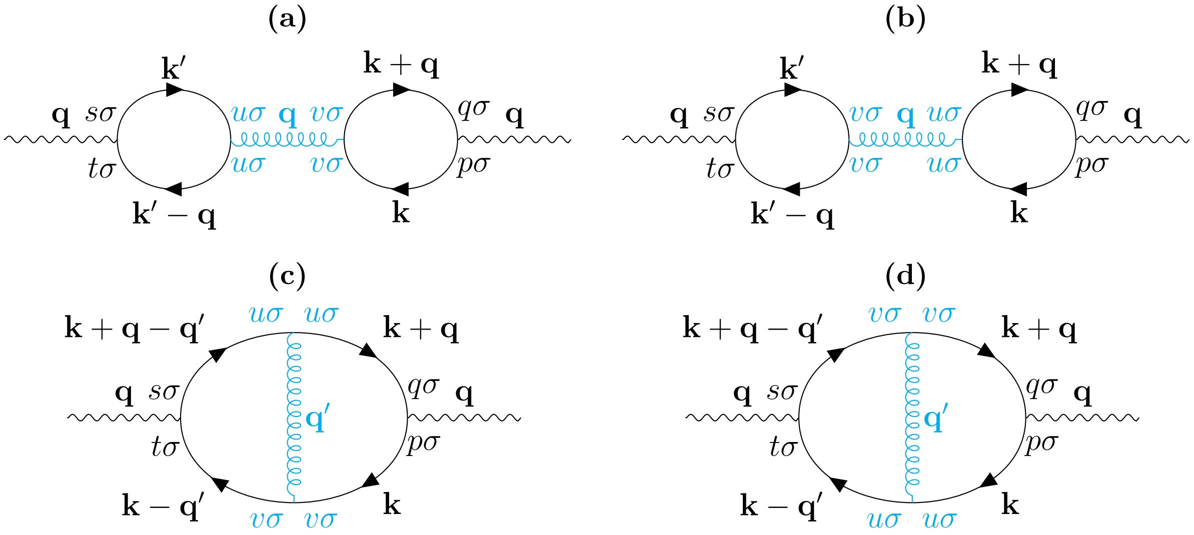

Figure 4.4: Feynman diagrams of the first order contribution in the inter-orbital Coulomb repulsion to the susceptibility corresponding to the operator pairings in (a) Eq. 4.53, (b) Eq. 4.54, (c) Eq. 4.55 and (d) Eq. 4.56.

4.2.3 Diagrammatic expansion for the inter-orbital Coulomb repulsion

Now we calculate the contributions to the susceptibility, which are first order in the inter-orbital Coulomb repulsion, in the same way we treated the inter-orbital Coulomb repulsion. Again we use the perturbation expansion of the susceptibility (Eq. 4.27), but now we insert the Fourier transformation of the inter-orbital Coulomb repulsion (Eq. 4.35). This results in two terms for which we have to calculate the connected pairings.

$$c^\dagger_{p\alpha}(\mathbf{k},\tau)c^\dagger_{s\beta}(\mathbf{k}',0)c_{t\delta}(\mathbf{k}'-\mathbf{q},0)c_{q\epsilon}(\mathbf{k}+\mathbf{q},\tau)c^\dagger_{u\sigma}(\mathbf{k}''+\mathbf{q}')c^\dagger_{v\sigma}(\mathbf{k}'''-\mathbf{q}')c_{v\sigma}(\mathbf{k}''')c_{u\sigma}(\mathbf{k}'') \quad (4.51)$$

$$c^\dagger_{p\alpha}(\mathbf{k},\tau)c^\dagger_{s\beta}(\mathbf{k}',0)c_{t\delta}(\mathbf{k}'-\mathbf{q},0)c_{q\epsilon}(\mathbf{k}+\mathbf{q},\tau)c^\dagger_{u\sigma}(\mathbf{k}''+\mathbf{q}')c^\dagger_{v\bar\sigma}(\mathbf{k}'''-\mathbf{q}')c_{v\bar\sigma}(\mathbf{k}''')c_{u\sigma}(\mathbf{k}'') \quad (4.52)$$

Again only four out of the 24 possible pairings for each of Eqs. 4.51 and 4.52 satisfy the criteria we formulated before. Those are:

$$c^\dagger_{p\alpha}(\mathbf{k},\tau)c^\dagger_{s\beta}(\mathbf{k}',0)c_{t\delta}(\mathbf{k}'-\mathbf{q},0)c_{q\epsilon}(\mathbf{k}+\mathbf{q},\tau)c^\dagger_{u\sigma}(\mathbf{k}''+\mathbf{q}')c^\dagger_{v\sigma}(\mathbf{k}'''-\mathbf{q}')c_{v\sigma}(\mathbf{k}''')c_{u\sigma}(\mathbf{k}'') \quad (4.53)$$

$$c^\dagger_{p\alpha}(\mathbf{k},\tau)c^\dagger_{s\beta}(\mathbf{k}',0)c_{t\delta}(\mathbf{k}'-\mathbf{q},0)c_{q\epsilon}(\mathbf{k}+\mathbf{q},\tau)c^\dagger_{u\sigma}(\mathbf{k}''+\mathbf{q}')c^\dagger_{v\sigma}(\mathbf{k}'''-\mathbf{q}')c_{v\sigma}(\mathbf{k}''')c_{u\sigma}(\mathbf{k}'') \quad (4.54)$$

$$c^\dagger_{p\alpha}(\mathbf{k},\tau)c^\dagger_{s\beta}(\mathbf{k}',0)c_{t\delta}(\mathbf{k}'-\mathbf{q},0)c_{q\epsilon}(\mathbf{k}+\mathbf{q},\tau)c^\dagger_{u\sigma}(\mathbf{k}''+\mathbf{q}')c^\dagger_{v\sigma}(\mathbf{k}'''-\mathbf{q}')c_{v\sigma}(\mathbf{k}''')c_{u\sigma}(\mathbf{k}'') \quad (4.55)$$

$$c^\dagger_{p\alpha}(\mathbf{k},\tau)c^\dagger_{s\beta}(\mathbf{k}',0)c_{t\delta}(\mathbf{k}'-\mathbf{q},0)c_{q\epsilon}(\mathbf{k}+\mathbf{q},\tau)c^\dagger_{u\sigma}(\mathbf{k}''+\mathbf{q}')c^\dagger_{v\sigma}(\mathbf{k}'''-\mathbf{q}')c_{v\sigma}(\mathbf{k}''')c_{u\sigma}(\mathbf{k}'') \quad (4.56)$$

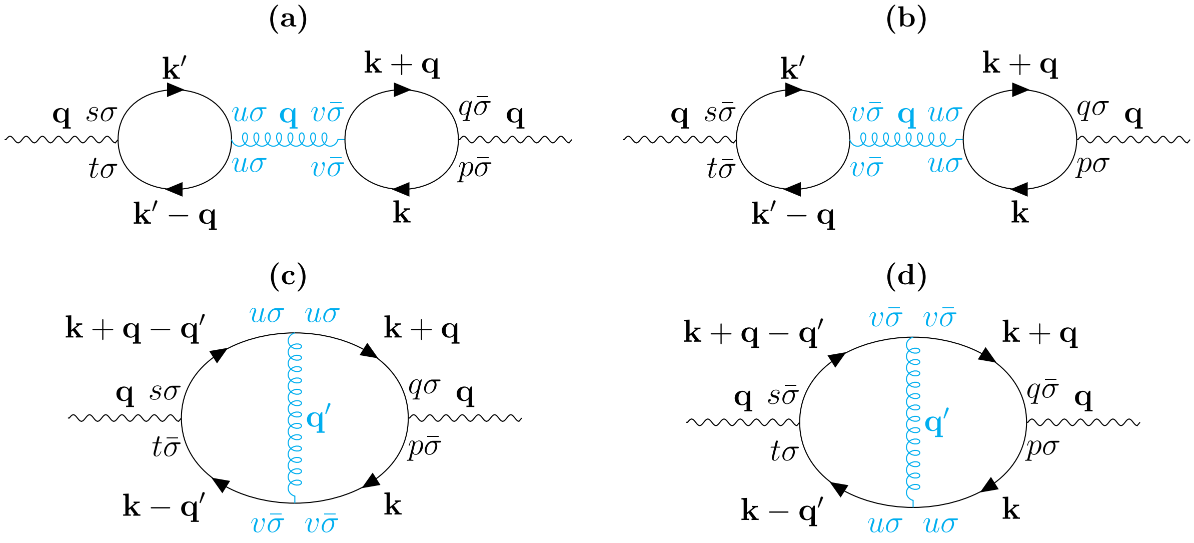

Figure 4.5: Feynman diagrams of the first order contribution in the inter-orbital Coulomb repulsion to the susceptibility corresponding to the operator pairings in (a) Eq. 4.57, (b) Eq. 4.58, (c) Eq. 4.59 and (d) Eq. 4.60.

$$c^\dagger_{p\alpha}(\mathbf{k},\tau)c^\dagger_{s\beta}(\mathbf{k}',0)c_{t\delta}(\mathbf{k}'-\mathbf{q},0)c_{q\epsilon}(\mathbf{k}+\mathbf{q},\tau)c^\dagger_{u\sigma}(\mathbf{k}''+\mathbf{q}')c^\dagger_{v\bar{\sigma}}(\mathbf{k}'''-\mathbf{q}')c_{v\bar{\sigma}}(\mathbf{k}''')c_{u\sigma}(\mathbf{k}'') \tag{4.57}$$

$$c^\dagger_{p\alpha}(\mathbf{k},\tau)c^\dagger_{s\beta}(\mathbf{k}',0)c_{t\delta}(\mathbf{k}'-\mathbf{q},0)c_{q\epsilon}(\mathbf{k}+\mathbf{q},\tau)c^\dagger_{u\sigma}(\mathbf{k}''+\mathbf{q}')c^\dagger_{v\bar{\sigma}}(\mathbf{k}'''-\mathbf{q}')c_{v\bar{\sigma}}(\mathbf{k}''')c_{u\sigma}(\mathbf{k}'') \tag{4.58}$$

$$c^\dagger_{p\alpha}(\mathbf{k},\tau)c^\dagger_{s\beta}(\mathbf{k}',0)c_{t\delta}(\mathbf{k}'-\mathbf{q},0)c_{q\epsilon}(\mathbf{k}+\mathbf{q},\tau)c^\dagger_{u\sigma}(\mathbf{k}''+\mathbf{q}')c^\dagger_{v\bar{\sigma}}(\mathbf{k}'''-\mathbf{q}')c_{v\bar{\sigma}}(\mathbf{k}''')c_{u\sigma}(\mathbf{k}'') \tag{4.59}$$

$$c^\dagger_{p\alpha}(\mathbf{k},\tau)c^\dagger_{s\beta}(\mathbf{k}',0)c_{t\delta}(\mathbf{k}'-\mathbf{q},0)c_{q\epsilon}(\mathbf{k}+\mathbf{q},\tau)c^\dagger_{u\sigma}(\mathbf{k}''+\mathbf{q}')c^\dagger_{v\bar{\sigma}}(\mathbf{k}'''-\mathbf{q}')c_{v\bar{\sigma}}(\mathbf{k}''')c_{u\sigma}(\mathbf{k}'') \tag{4.60}$$

We now use a light blue colored wiggly line to represent the inter-orbital Coulomb repulsion. The Feynman diagrams associated with the possible pairings of Eq. 4.51 are shown in Fig. 4.4, while the diagrams for possible pairings of Eq. 4.52 are shown in Fig. 4.5.

Due to the two different orbital indices at the interaction vertex the contributions to the charge susceptibility have a more complicated orbital structure than in the intra-orbital Coulomb case. Eqs. 4.53, 4.54, 4.57 and 4.58 each give a contribution of

$$-\sum_{u,v\neq u}\chi^{uu}_{st}(\mathbf{q})\frac{V}{2}\chi^{pq}_{vv}(\mathbf{q}), \tag{4.61}$$

while Eqs. 4.55 and 4.56 each give a contribution

$$+\sum_{u,v\neq u}\chi^{uv}_{st}(\mathbf{q})\frac{V}{2}\chi^{pq}_{uv}(\mathbf{q}). \tag{4.62}$$

Therefore, we can write down two further elements of the interaction tensor. Note however that a minus sign is already absorbed in the definition of the charge susceptibility (see Eq. 4.45).

$$(U^c)_{aa}^{bb} = 2V \tag{4.63}$$

$$(U^c)_{ab}^{ab} = -V \tag{4.64}$$

To the spin susceptibility Eqs. 4.59 and 4.60 ($\alpha = \delta$, $\beta = \epsilon$, $\alpha \neq \beta$) each contribute

$$+\sum_{u,v\neq u} \chi_{st}^{uv}(\mathbf{q}) \frac{V}{3} \chi_{uv}^{pq}(\mathbf{q}). \tag{4.65}$$

Eqs. 4.53 and 4.54 ($\alpha = \beta = \delta = \epsilon$) each contribute

$$-\sum_{u,v\neq u} \chi_{st}^{uu}(\mathbf{q}) \frac{V}{6} \chi_{vv}^{pq}(\mathbf{q}), \tag{4.66}$$

while Eqs. 4.55 and 4.56 ($\alpha = \beta = \delta = \epsilon$) each contribute

$$+\sum_{u,v\neq u} \chi_{st}^{uv}(\mathbf{q}) \frac{V}{6} \chi_{uv}^{pq}(\mathbf{q}). \tag{4.67}$$

Furthermore, Eqs. 4.57 and 4.58 ($\alpha = \epsilon$, $\beta = \delta$, $\alpha \neq \beta$) contribute

$$+\sum_{u,v\neq u} \chi_{st}^{uu}(\mathbf{q}) \frac{V}{6} \chi_{vv}^{pq}(\mathbf{q}). \tag{4.68}$$

With these information we can write down the elements of the interaction tensor in the spin channel for the inter-orbital Coulomb repulsion.

$$(U^s)_{aa}^{bb} = 0 \tag{4.69}$$

$$(U^s)_{ab}^{ab} = V \tag{4.70}$$

4.2.4 Diagrammatic expansion for the Hund's rule coupling

Now we calculate the first order contributions to the susceptibility using the Fourier transform of the Hund's rule coupling terms (Eq. 4.36). We obtain three terms for which we have to calculate all possible connected pairings.

$$c_{p\alpha}^\dagger(\mathbf{k},\tau) c_{s\beta}^\dagger(\mathbf{k}',0) c_{t\delta}(\mathbf{k}'-\mathbf{q},0) c_{q\epsilon}(\mathbf{k}+\mathbf{q},\tau) c_{u\sigma}^\dagger(\mathbf{k}''+\mathbf{q}') c_{v\bar{\sigma}}^\dagger(\mathbf{k}'''-\mathbf{q}') c_{v\sigma}(\mathbf{k}''') c_{u\bar{\sigma}}(\mathbf{k}'') \tag{4.71}$$

$$c_{p\alpha}^\dagger(\mathbf{k},\tau) c_{s\beta}^\dagger(\mathbf{k}',0) c_{t\delta}(\mathbf{k}'-\mathbf{q},0) c_{q\epsilon}(\mathbf{k}+\mathbf{q},\tau) c_{u\sigma}^\dagger(\mathbf{k}''+\mathbf{q}') c_{v\sigma}^\dagger(\mathbf{k}'''-\mathbf{q}') c_{v\sigma}(\mathbf{k}''') c_{u\sigma}(\mathbf{k}'') \tag{4.72}$$

$$c_{p\alpha}^\dagger(\mathbf{k},\tau) c_{s\beta}^\dagger(\mathbf{k}',0) c_{t\delta}(\mathbf{k}'-\mathbf{q},0) c_{q\epsilon}(\mathbf{k}+\mathbf{q},\tau) c_{u\sigma}^\dagger(\mathbf{k}''+\mathbf{q}') c_{v\bar{\sigma}}^\dagger(\mathbf{k}'''-\mathbf{q}') c_{v\bar{\sigma}}(\mathbf{k}''') c_{u\sigma}(\mathbf{k}'') \tag{4.73}$$

As before, only four pairings for each of Eqs. 4.71, 4.72 and 4.73 fulfill our criteria for inclusion into the diagrammatic expansion. The terms in Eqs. 4.72 and 4.73 are actually identical to Eqs. 4.51 and 4.52, which we analyzed in the section on the inter-orbital Coulomb repulsion. For further reference we again list all relevant pairings.

$$\wick{\c1{c}^\dagger_{p\alpha}(\mathbf{k},\tau)\c2{c}^\dagger_{s\beta}(\mathbf{k}',0)\c3{c}_{t\delta}(\mathbf{k}'-\mathbf{q},0)\c4{c}_{q\epsilon}(\mathbf{k}+\mathbf{q},\tau)\c3{c}^\dagger_{u\sigma}(\mathbf{k}''+\mathbf{q}')\c4{c}^\dagger_{v\bar{\sigma}}(\mathbf{k}'''-\mathbf{q}')\c1{c}_{v\sigma}(\mathbf{k}''')\c2{c}_{u\bar{\sigma}}(\mathbf{k}'')} \tag{4.74}$$

$$\wick{\c1{c}^\dagger_{p\alpha}(\mathbf{k},\tau)\c2{c}^\dagger_{s\beta}(\mathbf{k}',0)\c3{c}_{t\delta}(\mathbf{k}'-\mathbf{q},0)\c4{c}_{q\epsilon}(\mathbf{k}+\mathbf{q},\tau)\c4{c}^\dagger_{u\sigma}(\mathbf{k}''+\mathbf{q}')\c3{c}^\dagger_{v\bar{\sigma}}(\mathbf{k}'''-\mathbf{q}')\c2{c}_{v\sigma}(\mathbf{k}''')\c1{c}_{u\bar{\sigma}}(\mathbf{k}'')} \tag{4.75}$$

$$\wick{\c1{c}^\dagger_{p\alpha}(\mathbf{k},\tau)\c2{c}^\dagger_{s\beta}(\mathbf{k}',0)\c3{c}_{t\delta}(\mathbf{k}'-\mathbf{q},0)\c4{c}_{q\epsilon}(\mathbf{k}+\mathbf{q},\tau)\c4{c}^\dagger_{u\sigma}(\mathbf{k}''+\mathbf{q}')\c3{c}^\dagger_{v\bar{\sigma}}(\mathbf{k}'''-\mathbf{q}')\c1{c}_{v\sigma}(\mathbf{k}''')\c2{c}_{u\bar{\sigma}}(\mathbf{k}'')} \tag{4.76}$$

$$\wick{\c1{c}^\dagger_{p\alpha}(\mathbf{k},\tau)\c2{c}^\dagger_{s\beta}(\mathbf{k}',0)\c3{c}_{t\delta}(\mathbf{k}'-\mathbf{q},0)\c4{c}_{q\epsilon}(\mathbf{k}+\mathbf{q},\tau)\c3{c}^\dagger_{u\sigma}(\mathbf{k}''+\mathbf{q}')\c4{c}^\dagger_{v\bar{\sigma}}(\mathbf{k}'''-\mathbf{q}')\c2{c}_{v\sigma}(\mathbf{k}''')\c1{c}_{u\bar{\sigma}}(\mathbf{k}'')} \tag{4.77}$$

$$\wick{\c1{c}^\dagger_{p\alpha}(\mathbf{k},\tau)\c2{c}^\dagger_{s\beta}(\mathbf{k}',0)\c3{c}_{t\delta}(\mathbf{k}'-\mathbf{q},0)\c4{c}_{q\epsilon}(\mathbf{k}+\mathbf{q},\tau)\c3{c}^\dagger_{u\sigma}(\mathbf{k}''+\mathbf{q}')\c4{c}^\dagger_{v\sigma}(\mathbf{k}'''-\mathbf{q}')\c1{c}_{v\sigma}(\mathbf{k}''')\c2{c}_{u\sigma}(\mathbf{k}'')} \tag{4.78}$$

$$\wick{\c1{c}^\dagger_{p\alpha}(\mathbf{k},\tau)\c2{c}^\dagger_{s\beta}(\mathbf{k}',0)\c3{c}_{t\delta}(\mathbf{k}'-\mathbf{q},0)\c4{c}_{q\epsilon}(\mathbf{k}+\mathbf{q},\tau)\c4{c}^\dagger_{u\sigma}(\mathbf{k}''+\mathbf{q}')\c3{c}^\dagger_{v\sigma}(\mathbf{k}'''-\mathbf{q}')\c2{c}_{v\sigma}(\mathbf{k}''')\c1{c}_{u\sigma}(\mathbf{k}'')} \tag{4.79}$$

$$\wick{\c1{c}^\dagger_{p\alpha}(\mathbf{k},\tau)\c2{c}^\dagger_{s\beta}(\mathbf{k}',0)\c3{c}_{t\delta}(\mathbf{k}'-\mathbf{q},0)\c4{c}_{q\epsilon}(\mathbf{k}+\mathbf{q},\tau)\c4{c}^\dagger_{u\sigma}(\mathbf{k}''+\mathbf{q}')\c3{c}^\dagger_{v\sigma}(\mathbf{k}'''-\mathbf{q}')\c1{c}_{v\sigma}(\mathbf{k}''')\c2{c}_{u\sigma}(\mathbf{k}'')} \tag{4.80}$$

$$\wick{\c1{c}^\dagger_{p\alpha}(\mathbf{k},\tau)\c2{c}^\dagger_{s\beta}(\mathbf{k}',0)\c3{c}_{t\delta}(\mathbf{k}'-\mathbf{q},0)\c4{c}_{q\epsilon}(\mathbf{k}+\mathbf{q},\tau)\c3{c}^\dagger_{u\sigma}(\mathbf{k}''+\mathbf{q}')\c4{c}^\dagger_{v\sigma}(\mathbf{k}'''-\mathbf{q}')\c2{c}_{v\sigma}(\mathbf{k}''')\c1{c}_{u\sigma}(\mathbf{k}'')} \tag{4.81}$$

$$\wick{\c1{c}^\dagger_{p\alpha}(\mathbf{k},\tau)\c2{c}^\dagger_{s\beta}(\mathbf{k}',0)\c3{c}_{t\delta}(\mathbf{k}'-\mathbf{q},0)\c4{c}_{q\epsilon}(\mathbf{k}+\mathbf{q},\tau)\c3{c}^\dagger_{u\sigma}(\mathbf{k}''+\mathbf{q}')\c4{c}^\dagger_{v\bar{\sigma}}(\mathbf{k}'''-\mathbf{q}')\c1{c}_{v\bar{\sigma}}(\mathbf{k}''')\c2{c}_{u\sigma}(\mathbf{k}'')} \tag{4.82}$$

$$\wick{\c1{c}^\dagger_{p\alpha}(\mathbf{k},\tau)\c2{c}^\dagger_{s\beta}(\mathbf{k}',0)\c3{c}_{t\delta}(\mathbf{k}'-\mathbf{q},0)\c4{c}_{q\epsilon}(\mathbf{k}+\mathbf{q},\tau)\c4{c}^\dagger_{u\sigma}(\mathbf{k}''+\mathbf{q}')\c3{c}^\dagger_{v\bar{\sigma}}(\mathbf{k}'''-\mathbf{q}')\c2{c}_{v\bar{\sigma}}(\mathbf{k}''')\c1{c}_{u\sigma}(\mathbf{k}'')} \tag{4.83}$$

$$\wick{\c1{c}^\dagger_{p\alpha}(\mathbf{k},\tau)\c2{c}^\dagger_{s\beta}(\mathbf{k}',0)\c3{c}_{t\delta}(\mathbf{k}'-\mathbf{q},0)\c4{c}_{q\epsilon}(\mathbf{k}+\mathbf{q},\tau)\c4{c}^\dagger_{u\sigma}(\mathbf{k}''+\mathbf{q}')\c3{c}^\dagger_{v\bar{\sigma}}(\mathbf{k}'''-\mathbf{q}')\c1{c}_{v\bar{\sigma}}(\mathbf{k}''')\c2{c}_{u\sigma}(\mathbf{k}'')} \tag{4.84}$$

$$\wick{\c1{c}^\dagger_{p\alpha}(\mathbf{k},\tau)\c2{c}^\dagger_{s\beta}(\mathbf{k}',0)\c3{c}_{t\delta}(\mathbf{k}'-\mathbf{q},0)\c4{c}_{q\epsilon}(\mathbf{k}+\mathbf{q},\tau)\c3{c}^\dagger_{u\sigma}(\mathbf{k}''+\mathbf{q}')\c4{c}^\dagger_{v\bar{\sigma}}(\mathbf{k}'''-\mathbf{q}')\c2{c}_{v\bar{\sigma}}(\mathbf{k}''')\c1{c}_{u\sigma}(\mathbf{k}'')} \tag{4.85}$$

We now use an orange colored dashed line to represent the Hund's rule coupling. The Feynman diagrams associated with Eq. 4.71 are shown in Fig. 4.6. The diagrams representing pairings of Eqs. 4.72 and 4.73 are the same as in Figs. 4.4 and 4.5, but with the inter-orbital Coulomb interaction lines replaced by Hund's rule interaction lines.

Now we collect the contributions to the charge susceptibility. Eqs. 4.76 and 4.77 each contribute

$$-\sum_{u,v\neq u}\chi^{uv}_{st}(\mathbf{q})\frac{J}{4}\chi^{pq}_{uv}(\mathbf{q}). \tag{4.86}$$

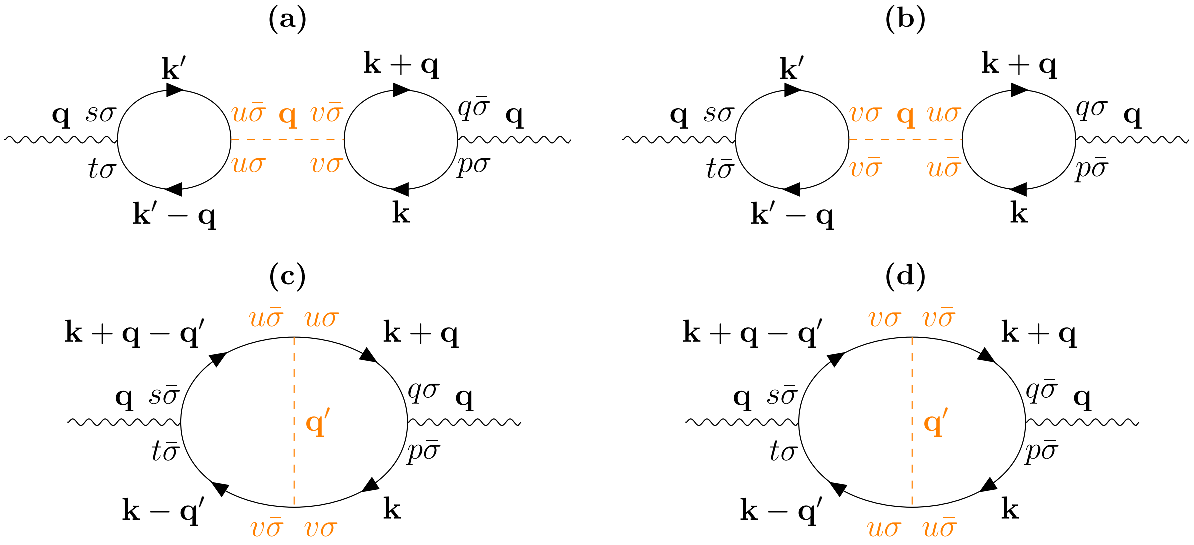
(a)
$\mathbf{k}'$
$\mathbf{q}$ $s\sigma$
$t\sigma$
$\mathbf{k}'-\mathbf{q}$
$u\bar{\sigma}$ $\mathbf{q}$ $v\bar{\sigma}$
$u\sigma$ $v\sigma$
$\mathbf{k}+\mathbf{q}$
$q\bar{\sigma}$ $\mathbf{q}$
$p\sigma$
$\mathbf{k}$
(b)
$\mathbf{k}'$
$\mathbf{q}$ $s\sigma$
$t\bar{\sigma}$
$\mathbf{k}'-\mathbf{q}$
$v\sigma$ $\mathbf{q}$ $u\sigma$
$v\bar{\sigma}$ $u\bar{\sigma}$
$\mathbf{k}+\mathbf{q}$
$q\sigma$ $\mathbf{q}$
$p\bar{\sigma}$
$\mathbf{k}$
(c)
$\mathbf{k}+\mathbf{q}-\mathbf{q}'$
$u\bar{\sigma}$ $u\sigma$
$\mathbf{k}+\mathbf{q}$
$\mathbf{q}$ $s\bar{\sigma}$
$t\bar{\sigma}$
$\mathbf{q}'$
$q\sigma$ $\mathbf{q}$
$p\bar{\sigma}$
$\mathbf{k}-\mathbf{q}'$
$v\bar{\sigma}$ $v\sigma$
$\mathbf{k}$
(d)
$\mathbf{k}+\mathbf{q}-\mathbf{q}'$
$v\sigma$ $v\bar{\sigma}$
$\mathbf{k}+\mathbf{q}$
$\mathbf{q}$ $s\bar{\sigma}$
$t\sigma$
$\mathbf{q}'$
$q\bar{\sigma}$ $\mathbf{q}$
$p\bar{\sigma}$
$\mathbf{k}-\mathbf{q}'$
$u\sigma$ $u\bar{\sigma}$
$\mathbf{k}$

Figure 4.6: Feynman diagrams of the first order contribution in the Hund's rule coupling to the susceptibility corresponding to the operator pairings in (a) Eq. 4.74, (b) Eq. 4.75, (c) Eq. 4.76 and (d) Eq. 4.77.

Eqs. 4.78 and 4.79 each contribute

$$+\sum_{u,v\neq u}\chi^{uu}_{st}(\mathbf{q})\frac{J}{8}\chi^{pq}_{vv}(\mathbf{q}), \tag{4.87}$$

while Eqs. 4.80 and 4.81 each contribute

$$-\sum_{u,v\neq u}\chi^{uv}_{st}(\mathbf{q})\frac{J}{8}\chi^{pq}_{uv}(\mathbf{q}). \tag{4.88}$$

Furthermore, Eqs. 4.82 and 4.83 each contribute

$$-\sum_{u,v\neq u}\chi^{uu}_{st}(\mathbf{q})\frac{J}{8}\chi^{pq}_{vv}(\mathbf{q}). \tag{4.89}$$

From these terms we obtain the total contribution of the Hund's rule coupling to the interaction tensor in the charge channel.

$$(U^c)^{bb}_{aa} = 0 \tag{4.90}$$

$$(U^c)^{ab}_{ab} = \frac{3}{4}J \tag{4.91}$$

To the spin channel Eqs. 4.74 and 4.75 each contribute

$$+\sum_{u,v\neq u}\chi^{uu}_{st}(\mathbf{q})\frac{J}{6}\chi^{pq}_{vv}(\mathbf{q}), \tag{4.92}$$

while Eqs. 4.84 and 4.85 each contribute

$$+\sum_{u,v\neq u}\chi^{uv}_{st}(\mathbf{q})\frac{J}{12}\chi^{pq}_{uv}(\mathbf{q}). \tag{4.93}$$

Eqs. 4.78 and 4.79 each contribute

$$+\sum_{u,v\neq u}\chi^{uu}_{st}(\mathbf{q})\frac{J}{24}\chi^{pq}_{vv}(\mathbf{q}), \tag{4.94}$$

while Eqs. 4.80 and 4.81 each contribute

$$-\sum_{u,v\neq u}\chi^{uv}_{st}(\mathbf{q})\frac{J}{24}\chi^{pq}_{uv}(\mathbf{q}). \tag{4.95}$$

Furthermore, Eqs. 4.76 and 4.77 each contribute

$$+\sum_{u,v\neq u}\chi^{uv}_{st}(\mathbf{q})\frac{J}{12}\chi^{pq}_{uv}(\mathbf{q}), \tag{4.96}$$

while Eqs. 4.82 and 4.83 each contribute

$$+\sum_{u,v\neq u}\chi^{uu}_{st}(\mathbf{q})\frac{J}{24}\chi^{pq}_{vv}(\mathbf{q}). \tag{4.97}$$

Finally, we obtain the total contribution of the Hund's rule coupling to the interaction tensor in the spin channel.

$$(U^s)^{bb}_{aa}=\frac{1}{2}J \tag{4.98}$$

$$(U^s)^{ab}_{ab}=\frac{1}{4}J \tag{4.99}$$

4.2.5 Diagrammatic expansion for the pair-hopping term

In this subsection we calculate the first order contribution to the susceptibility using the Fourier transformation of the pair-hopping term (Eq. 4.37). We have to investigate all possible pairings for the following product of operators:

$$c^\dagger_{p\alpha}(\mathbf{k},\tau)c^\dagger_{s\beta}(\mathbf{k}',0)c_{t\delta}(\mathbf{k}'-\mathbf{q},0)c_{q\epsilon}(\mathbf{k}+\mathbf{q},\tau)c^\dagger_{u\sigma}(\mathbf{k}''+\mathbf{q}')c^\dagger_{u\bar{\sigma}}(\mathbf{k}'''-\mathbf{q}')c_{v\bar{\sigma}}(\mathbf{k}''')c_{v\sigma}(\mathbf{k}'') \tag{4.100}$$

As for all previous interaction terms, only four pairings of Eq. 4.100 fulfill our criteria. Those are:

$$\wick{\c1{c}^\dagger_{p\alpha}(\mathbf{k},\tau)\c2{c}^\dagger_{s\beta}(\mathbf{k}',0)\c3{c}_{t\delta}(\mathbf{k}'-\mathbf{q},0)\c4{c}_{q\epsilon}(\mathbf{k}+\mathbf{q},\tau)\c3{c}^\dagger_{u\sigma}(\mathbf{k}''+\mathbf{q}')\c4{c}^\dagger_{u\bar{\sigma}}(\mathbf{k}'''-\mathbf{q}')\c1{c}_{v\bar{\sigma}}(\mathbf{k}''')\c2{c}_{v\sigma}(\mathbf{k}'')} \tag{4.101}$$

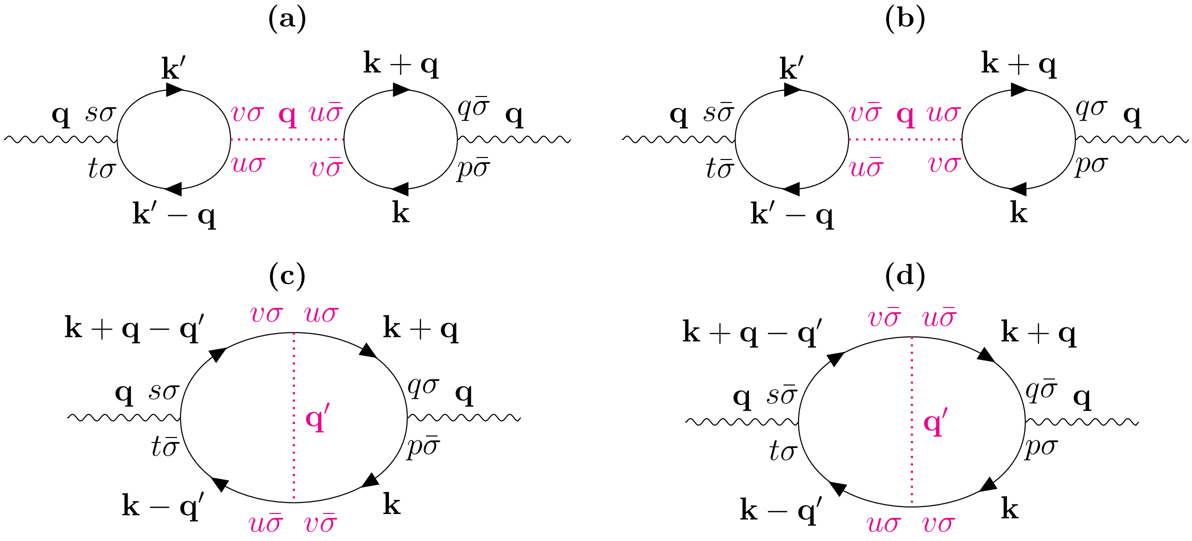
(a)
(b)
(c)
(d)
$\mathbf{k}'$
$\mathbf{k}+\mathbf{q}$
$\mathbf{q}$ $s\sigma$
$t\sigma$
$v\sigma$ $\mathbf{q}$ $u\bar{\sigma}$
$u\sigma$ $v\bar{\sigma}$
$q\bar{\sigma}$ $\mathbf{q}$
$p\bar{\sigma}$
$\mathbf{k}'-\mathbf{q}$
$\mathbf{k}$
$\mathbf{q}$ $s\bar{\sigma}$
$t\bar{\sigma}$
$v\bar{\sigma}$ $\mathbf{q}$ $u\sigma$
$u\bar{\sigma}$ $v\sigma$
$q\sigma$ $\mathbf{q}$
$p\sigma$
$\mathbf{k}+\mathbf{q}-\mathbf{q}'$
$v\sigma$ $u\sigma$
$\mathbf{q}'$
$u\bar{\sigma}$ $v\bar{\sigma}$
$\mathbf{k}-\mathbf{q}'$
$v\bar{\sigma}$ $u\bar{\sigma}$
$u\sigma$ $v\sigma$

Figure 4.7: Feynman diagrams of the first order contribution in the Hund's rule coupling to the susceptibility corresponding to the operator pairings in (a) Eq. 4.101, (b) Eq. 4.102, (c) Eq. 4.103 and (d) Eq. 4.104.

$$\wick{\c1{c^{\dagger}_{p\alpha}}(\mathbf{k},\tau)\c2{c^{\dagger}_{s\beta}}(\mathbf{k}',0)\c3{c_{t\delta}}(\mathbf{k}'-\mathbf{q},0)\c4{c_{q\epsilon}}(\mathbf{k}+\mathbf{q},\tau)\c4{c^{\dagger}_{u\sigma}}(\mathbf{k}''+\mathbf{q}')\c3{c^{\dagger}_{u\bar{\sigma}}}(\mathbf{k}'''-\mathbf{q}')\c2{c_{v\bar{\sigma}}}(\mathbf{k}''')\c1{c_{v\sigma}}(\mathbf{k}'')} \tag{4.102}$$

$$\wick{\c1{c^{\dagger}_{p\alpha}}(\mathbf{k},\tau)\c2{c^{\dagger}_{s\beta}}(\mathbf{k}',0)\c3{c_{t\delta}}(\mathbf{k}'-\mathbf{q},0)\c4{c_{q\epsilon}}(\mathbf{k}+\mathbf{q},\tau)\c4{c^{\dagger}_{u\sigma}}(\mathbf{k}''+\mathbf{q}')\c3{c^{\dagger}_{u\bar{\sigma}}}(\mathbf{k}'''-\mathbf{q}')\c1{c_{v\bar{\sigma}}}(\mathbf{k}''')\c2{c_{v\sigma}}(\mathbf{k}'')} \tag{4.103}$$

$$\wick{\c1{c^{\dagger}_{p\alpha}}(\mathbf{k},\tau)\c2{c^{\dagger}_{s\beta}}(\mathbf{k}',0)\c3{c_{t\delta}}(\mathbf{k}'-\mathbf{q},0)\c4{c_{q\epsilon}}(\mathbf{k}+\mathbf{q},\tau)\c3{c^{\dagger}_{u\sigma}}(\mathbf{k}''+\mathbf{q}')\c4{c^{\dagger}_{u\bar{\sigma}}}(\mathbf{k}'''-\mathbf{q}')\c2{c_{v\bar{\sigma}}}(\mathbf{k}''')\c1{c_{v\sigma}}(\mathbf{k}'')} \tag{4.104}$$

We now use a magneta colored dotted line to represent the pair-hopping interaction. The Feynman diagrams associated with Eq. 4.100 are shown in Fig. 4.7.

To the charge susceptibility Eqs. 4.101 and 4.102 each contribute

$$-\sum_{u,v\neq u}\chi^{uv}_{st}(\mathbf{q})\frac{J'}{2}\chi^{pq}_{vu}(\mathbf{q}). \tag{4.105}$$

The total contribution of the pair-hopping term to the interaction tensor in the charge channel is given by

$$(U^c)^{ba}_{ab}=J'. \tag{4.106}$$

To the spin susceptibility Eqs. 4.103 and 4.104 each contribute

$$+\sum_{u,v\neq u}\chi^{uv}_{st}(\mathbf{q})\frac{J'}{3}\chi^{pq}_{vu}(\mathbf{q}), \tag{4.107}$$

while Eqs. 4.101 and 4.102 each contribute

$$+\sum_{u,v\neq u}\chi^{uv}_{st}(\mathbf{q})\frac{J'}{6}\chi^{pq}_{vu}(\mathbf{q}). \tag{4.108}$$

Therefore, the total contribution of the pair-hopping term to the interaction tensor in the spin channel is given by

$$(U^s)^{ba}_{ab} = J'. \tag{4.109}$$

4.2.6 Tensor formulation of the multi-orbital susceptibility

In the previous subsections we calculated the elements of the interaction tensor, which appears in the random phase approximation for the charge and spin susceptibility in the multi-orbital Hubbard model.

$$(U^c)^{aa}_{aa} = U \qquad (U^c)^{bb}_{aa} = 2V \qquad (U^c)^{ab}_{ab} = \frac{3}{4}J - V \qquad (U^c)^{ba}_{ab} = J' \tag{4.110}$$

$$(U^s)^{aa}_{aa} = U \qquad (U^s)^{bb}_{aa} = \frac{1}{2}J \qquad (U^s)^{ab}_{ab} = \frac{1}{4}J + V \qquad (U^s)^{ba}_{ab} = J' \tag{4.111}$$

In analogy to the scalar equations of the single-orbital case (Eqs. 4.45 and 4.46) we can write down tensor equations for the susceptibilities in the multi-orbital case. Here, we suppressed the momentum argument $\mathbf{q}$ in each of the susceptibilities.

$$(\chi^c)^{pq}_{st} = (\chi^0)^{pq}_{st} - \sum_{\substack{ab\\cd}} (\chi^0)^{ab}_{st} (U^c)^{cd}_{ab} (\chi^0)^{pq}_{cd} + \ldots = (\chi^0)^{pq}_{st} - \sum_{\substack{ab\\cd}} (\chi^0)^{ab}_{st} (U^c)^{cd}_{ab} (\chi^c)^{pq}_{cd} \tag{4.112}$$

$$(\chi^s)^{pq}_{st} = (\chi^0)^{pq}_{st} + \sum_{\substack{ab\\cd}} (\chi^0)^{ab}_{st} (U^s)^{cd}_{ab} (\chi^0)^{pq}_{cd} + \ldots = (\chi^0)^{pq}_{st} + \sum_{\substack{ab\\cd}} (\chi^0)^{ab}_{st} (U^s)^{cd}_{ab} (\chi^s)^{pq}_{cd} \tag{4.113}$$

This set of equations is very elegant, since it automatically generates, in expansion orders $n \geq 2$, also all allowed terms with mixed types of interaction vertices. That is possible, because we have restricted ourselves to contributions that can be represented as products of susceptibilities and interaction vertices. Therefore, incrementing the expansion order simply means multiplication by another interaction vertex and another susceptibility. The rules for such a multiplication are completely determined by the susceptibility terms that are first order in the interaction vertices and which we have used to determine the interaction tensors (Eqs. 4.110 and 4.111).

As in the single-orbital case, the charge and spin susceptibilities up to infinite expansion order can be obtained by inverting Eqs. 4.112 and 4.113 in orbital space.

$$(\chi^c)^{pq}_{st} = \left[\left((\chi^0)^{pq}_{st} \right)^{-1} + \left((U^c)^{pq}_{st} \right)^{-1} \right]^{-1} \tag{4.114}$$

$$(\chi^s)^{pq}_{st} = \left[\left((\chi^0)^{pq}_{st} \right)^{-1} - \left((U^s)^{pq}_{st} \right)^{-1} \right]^{-1} \tag{4.115}$$

Since the interaction tensor is simply a collection of constant numbers, the random phase approximation for the charge and spin susceptibilities up to infinite expansion order can be obtained at the cost of calculating the unperturbed multi-orbital susceptibility and inverting it in orbital space. In fact, computational efficiency is the most important advantage of the RPA method.

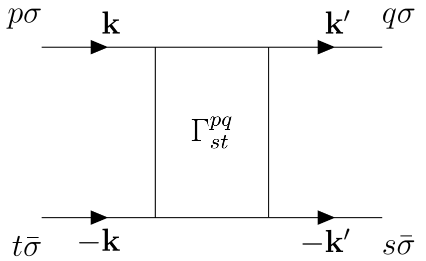

Figure 4.8: Feynman diagram representing the two-particle interaction $V^{pq}_{st}(\mathbf{k},\mathbf{k}',i\nu_n)$.

4.2.7 Approximation for the two-electron pairing vertex in terms of susceptibilities

In this subsection we approach the main goal of this chapter, namely the calculation of the two-electron pairing vertex, which characterizes the symmetry of the superconducting pairing in momentum and orbital space. The perturbation expansion of the particle-particle interaction can be written down similar to the perturbation expansion for the susceptibility (see Eq. 4.27). Again we use greek letters to denote the spins.

$$V^{pq}_{st}(\mathbf{k},\mathbf{k}',i\nu_n) = \int\limits_0^\beta d\tau\, e^{-i\nu_n\tau} \sum_{\mathbf{k}\mathbf{k}'} \sum_{\sigma} \sum_{n=0}^{\infty} \frac{(-1)^n}{n!} \times \left\langle T_\tau c^\dagger_{t\bar{\sigma}}(-\mathbf{k},0) c^\dagger_{p\sigma}(\mathbf{k},0) c_{q\sigma}(\mathbf{k}',\tau) c_{s\bar{\sigma}}(-\mathbf{k}',\tau) S^n \right\rangle_{\mathrm{con}} \tag{4.116}$$

The corresponding Feynman diagram is shown in Fig. 4.8. Because we are interested in spin-singlet superconductivity, we have fixed the spins at the external legs to have opposite directions. We also introduce the two-particle vertex Γ^{pq}_{st}, which is generated from V^{pq}_{st} by cutting off all external legs.

Since diagrams that are zeroth order in the interaction do not contribute to Γ^{pq}_{st}, we now calculate all possible diagrams that are first order in the interaction. The relevant pairings are:

$$\frac{U}{2} c^\dagger_{t\bar{\sigma}}(-\mathbf{k},0) c^\dagger_{p\sigma}(\mathbf{k},0) c_{q\sigma}(\mathbf{k}',\tau) c_{s\bar{\sigma}}(-\mathbf{k}',\tau) c^\dagger_{u\sigma}(\mathbf{k}''+\mathbf{q}') c^\dagger_{u\bar{\sigma}}(\mathbf{k}'''-\mathbf{q}') c_{u\bar{\sigma}}(\mathbf{k}''') c_{u\sigma}(\mathbf{k}'') \tag{4.117}$$

$$\frac{V}{2} c^\dagger_{t\bar{\sigma}}(-\mathbf{k},0) c^\dagger_{p\sigma}(\mathbf{k},0) c_{q\sigma}(\mathbf{k}',\tau) c_{s\bar{\sigma}}(-\mathbf{k}',\tau) c^\dagger_{u\sigma}(\mathbf{k}''+\mathbf{q}') c^\dagger_{v\bar{\sigma}}(\mathbf{k}'''-\mathbf{q}') c_{v\bar{\sigma}}(\mathbf{k}''') c_{u\sigma}(\mathbf{k}'') \tag{4.118}$$

$$-\frac{J}{4} c^\dagger_{t\bar{\sigma}}(-\mathbf{k},0) c^\dagger_{p\sigma}(\mathbf{k},0) c_{q\sigma}(\mathbf{k}',\tau) c_{s\bar{\sigma}}(-\mathbf{k}',\tau) c^\dagger_{u\sigma}(\mathbf{k}''+\mathbf{q}') c^\dagger_{v\bar{\sigma}}(\mathbf{k}'''-\mathbf{q}') c_{v\sigma}(\mathbf{k}''') c_{u\bar{\sigma}}(\mathbf{k}'') \tag{4.119}$$

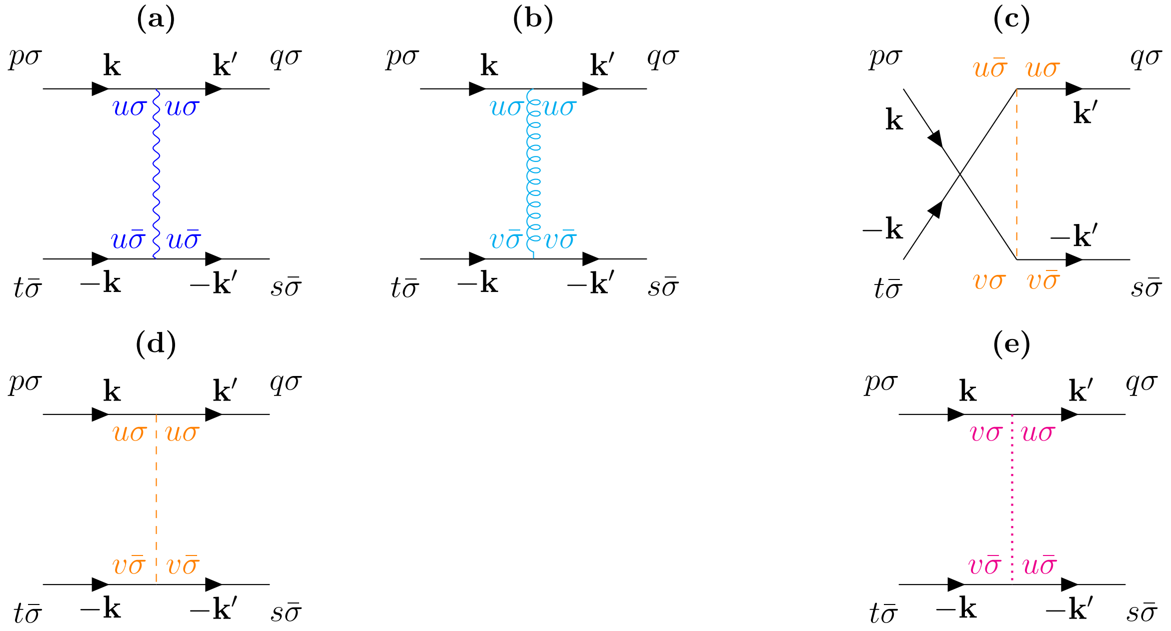
(a)
$p\sigma$ $\mathbf{k}$ $\mathbf{k}'$ $q\sigma$
$u\sigma$ $u\sigma$
$u\bar\sigma$ $u\bar\sigma$
$t\bar\sigma$ $-\mathbf{k}$ $-\mathbf{k}'$ $s\bar\sigma$
(b)
$p\sigma$ $\mathbf{k}$ $\mathbf{k}'$ $q\sigma$
$u\sigma$ $u\sigma$
$v\bar\sigma$ $v\bar\sigma$
$t\bar\sigma$ $-\mathbf{k}$ $-\mathbf{k}'$ $s\bar\sigma$
(c)
$p\sigma$ $u\bar\sigma$ $u\sigma$ $q\sigma$
$\mathbf{k}$ $\mathbf{k}'$
$-\mathbf{k}$ $-\mathbf{k}'$
$t\bar\sigma$ $v\sigma$ $v\bar\sigma$ $s\bar\sigma$
(d)
$p\sigma$ $\mathbf{k}$ $\mathbf{k}'$ $q\sigma$
$u\sigma$ $u\sigma$
$v\bar\sigma$ $v\bar\sigma$
$t\bar\sigma$ $-\mathbf{k}$ $-\mathbf{k}'$ $s\bar\sigma$
(e)
$p\sigma$ $\mathbf{k}$ $\mathbf{k}'$ $q\sigma$
$v\sigma$ $u\sigma$
$v\bar\sigma$ $u\bar\sigma$
$t\bar\sigma$ $-\mathbf{k}$ $-\mathbf{k}'$ $s\bar\sigma$

Figure 4.9: Feynman diagrams of the first order contribution in the interactions to the two-particle interaction vertex corresponding to the operator pairings in (a) Eq. 4.117, (b) Eq. 4.118, (c) Eq. 4.119, (d) Eq. 4.120 and (e) Eq. 4.121. Note the twist in orbital and spin indices on the left side of diagram (c).

$$\frac{J}{8} c^\dagger_{t\bar\sigma}(-\mathbf{k},0)c^\dagger_{p\sigma}(\mathbf{k},0)c_{q\sigma}(\mathbf{k}',\tau)c_{s\bar\sigma}(-\mathbf{k}',\tau)c^\dagger_{u\sigma}(\mathbf{k}''+\mathbf{q}')c^\dagger_{v\bar\sigma}(\mathbf{k}'''-\mathbf{q}')c_{v\bar\sigma}(\mathbf{k}''')c_{u\sigma}(\mathbf{k}'') \tag{4.120}$$

$$\frac{J'}{2} c^\dagger_{t\bar\sigma}(-\mathbf{k},0)c^\dagger_{p\sigma}(\mathbf{k},0)c_{q\sigma}(\mathbf{k}',\tau)c_{s\bar\sigma}(-\mathbf{k}',\tau)c^\dagger_{u\sigma}(\mathbf{k}''+\mathbf{q}')c^\dagger_{u\bar\sigma}(\mathbf{k}'''-\mathbf{q}')c_{v\bar\sigma}(\mathbf{k}''')c_{v\sigma}(\mathbf{k}'') \tag{4.121}$$

Note how Eq. 4.119 includes a twist in the operator pairings with respect to the other pairings. This twist gives an additional minus sign, which cancels the sign in the prefactor. The associated Feynman diagrams are shown in Fig. 4.9, in which we omit to show the internal momenta for clarity. After performing the sum over spins σ, we get the following contributions from those diagrams:

$$\left(\Gamma^1\right)^{aa}_{aa} = U \qquad \left(\Gamma^1\right)^{bb}_{aa} = V + \frac{1}{4}J \qquad \left(\Gamma^1\right)^{ab}_{ab} = \frac{1}{2}J \qquad \left(\Gamma^1\right)^{ba}_{ab} = J' \tag{4.122}$$

These contributions can in fact be represented in terms of the interaction tensors in the charge and spin channel we determined before (see Eqs. 4.110 and 4.111).

$$\left(\Gamma^1\right)^{pq}_{st} = \frac{1}{2}\left[\left(U^c\right)^{pq}_{st} + \left(U^s\right)^{pq}_{st}\right] \tag{4.123}$$

Now we turn to the diagrams, which include a charge or spin susceptibility in random phase approximation to infinite order. Since the possibilities of connecting a charge or spin

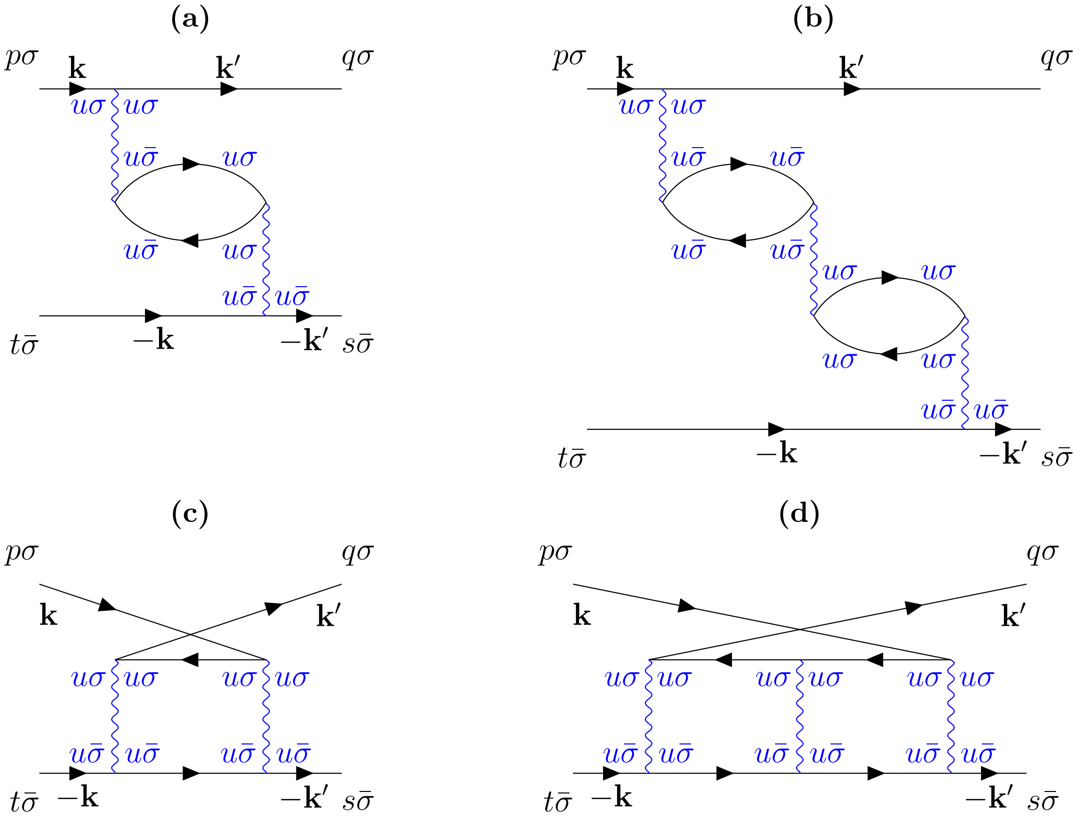

Figure 4.10: Feynman diagrams that contribute to the two-particle vertex. Diagrams (a) and (b) have bubble topology, while diagrams (c) and (d) have twisted ladder topology. Diagrams (a) and (c) are second order in the interaction vertices, while diagrams (b) and (d) are third order.

susceptibility to the external legs is described precisely by the interaction tensors U^c and U^s, we already know that further terms in the two-particle vertex must have the structure $U^c\chi^cU^c$ and $U^s\chi^sU^s$. The question is only what the correct prefactors to those terms are.

To find those prefactors, we concentrate on the Feynman diagrams with only intra-orbital Coulomb (U) interaction vertices. Since we have seen before that a generalization of the single-orbital case using the interaction tensors U^c and U^s is justified, we can obtain the formulas for the multi-orbital case in this way. We have also conducted extensive calculations for the Feynman diagrams contributing to the two-particle vertex in the multi-orbital case, taking into account second and third order diagrams in the interaction vertices. The derivations are by far too long to be shown here, but confirmed the validity of the derivation via the single-orbital case.

The interesting diagrams in the perturbation expansion of the two-particle vertex are of *bubble* and *twisted ladder* topology (see Fig. 4.10). In Fig. 4.10(a) we see that diagrams, which are even order in the interaction vertices, do not contribute to the two-particle vertex, since the internal susceptibility parts of the diagram include Green's functions, which mix spins. Such mixing of different spins is, however, forbidden by the kinetic Hamiltonian and, therefore, such even order diagrams evaluate to zero, in contrast to the odd order term shown in Fig. 4.10(b). The twisted ladder diagrams shown in Fig. 4.10(c) and (d) contribute in all orders.

Since the pairs of internal counterpropagating Green's functions can be written as susceptibilities, we can evaluate the contributions from the diagrams shown in Fig. 4.10. The factorial prefactor from the expansion order (see Eq. 4.116) is cancelled by the number of possible contractions that lead to a diagram with identical symmetry. Therefore, the diagram in Fig. 4.10(b) contributes $U^3\chi^2(\mathbf{k}-\mathbf{k}')$, while diagrams in Fig. 4.10(c) and (d) contribute $U^2\chi(\mathbf{k}+\mathbf{k}')$ and $U^3\chi^2(\mathbf{k}+\mathbf{k}')$ respectively. Finally, we can write down the contribution up to infinite order in the interaction vertices for the bubble and twisted ladder diagrams. Summing up all contributions from bubble type diagrams we get:

$$U^3\chi^2(\mathbf{k}-\mathbf{k}') + U^5\chi^4(\mathbf{k}-\mathbf{k}') + U^7\chi^6(\mathbf{k}-\mathbf{k}') + \dots \tag{4.124}$$

$$=U^3\chi^2(\mathbf{k}-\mathbf{k}')\left[1 + U^2\chi^2(\mathbf{k}-\mathbf{k}') + U^4\chi^4(\mathbf{k}-\mathbf{k}') + \dots\right] \tag{4.125}$$

$$=\frac{U^3\chi^2(\mathbf{k}-\mathbf{k}')}{1-U^2\chi^2(\mathbf{k}-\mathbf{k}')} \tag{4.126}$$

$$=\frac{U^2}{2}\left[\frac{\chi(\mathbf{k}-\mathbf{k}')}{1-U\chi(\mathbf{k}-\mathbf{k}')} - \frac{\chi(\mathbf{k}-\mathbf{k}')}{1+U\chi(\mathbf{k}-\mathbf{k}')}\right] \tag{4.127}$$

From the twisted ladder diagrams we get:

$$U^2\chi(\mathbf{k}+\mathbf{k}') + U^3\chi^2(\mathbf{k}+\mathbf{k}') + U^4\chi^3(\mathbf{k}+\mathbf{k}') + \dots \tag{4.128}$$

$$=U^2\chi(\mathbf{k}+\mathbf{k}')\left[1 + U\chi(\mathbf{k}+\mathbf{k}') + U^2\chi^2(\mathbf{k}+\mathbf{k}') + \dots\right] \tag{4.129}$$

$$=U^2\frac{\chi(\mathbf{k}+\mathbf{k}')}{1-U\chi(\mathbf{k}+\mathbf{k}')} \tag{4.130}$$

Noting that Eqs. 4.127 and 4.130 contain the charge and spin susceptibilities (see Eqs. 4.47 and 4.48) and including the first order contribution (see Eq. 4.123), we can write the two-particle vertex as

$$\begin{aligned}\Gamma^{pq}_{st}(\mathbf{k},\mathbf{k}') =&\frac{1}{2}\Big[\big(U^s\big)^{ab}_{st}\big(\chi^s\big)^{cd}_{ab}(\mathbf{k}-\mathbf{k}')\big(U^s\big)^{pq}_{cd} - \big(U^c\big)^{ab}_{st}\big(\chi^c\big)^{cd}_{ab}(\mathbf{k}-\mathbf{k}')\big(U^c\big)^{pq}_{cd}\Big] \\ &+ \big(U^s\big)^{ab}_{st}\big(\chi^s\big)^{cd}_{ab}(\mathbf{k}+\mathbf{k}')\big(U^s\big)^{pq}_{cd} + \frac{1}{2}\Big[\big(U^c\big)^{pq}_{st} + \big(U^s\big)^{pq}_{st}\Big].\end{aligned} \tag{4.131}$$

The charge and spin susceptibilities that are meant to be inserted here, are the random phase approximated ones (see Eqs. 4.114 and 4.115).

At the beginning of the chapter we stated that we want to investigate spin-singlet superconductivity. In this subsection we, however, assumed only a pairing between electrons with different spin, which does not yet make a singlet. Therefore, the singlet-symmetrization has to be applied explicitly to the two-particle vertex.

$$\big(\Gamma^s\big)^{pq}_{st}(\mathbf{k},\mathbf{k}') = \frac{1}{2}\Big[\Gamma^{pq}_{st}(\mathbf{k},\mathbf{k}') + \Gamma^{pq}_{st}(\mathbf{k},-\mathbf{k}')\Big] \tag{4.132}$$

After the singlet-symmetrization the result presented in Eq. 4.131 agrees with the literature result in Ref. [94].

$$\begin{aligned}\big(\Gamma^{s}\big)^{pq}_{st}(\mathbf{k},\mathbf{k}') =& \frac{3}{2}\big(U^{s}\big)^{ab}_{st}\big(\chi^{s}\big)^{cd}_{ab}(\mathbf{k}\pm\mathbf{k}')\big(U^{s}\big)^{pq}_{cd} - \frac{1}{2}\big(U^{c}\big)^{ab}_{st}\big(\chi^{c}\big)^{cd}_{ab}(\mathbf{k}\pm\mathbf{k}')\big(U^{c}\big)^{pq}_{cd} \\ &+ \frac{1}{2}\Big[\big(U^{c}\big)^{pq}_{st} + \big(U^{s}\big)^{pq}_{st}\Big]. \qquad (4.133)\end{aligned}$$

Note that we neglected the frequency dependence of the susceptibilities. In principle it can be re-introduced by treating all momenta as a combined momentum and Matsubara frequency variable $\mathbf{k} = (\mathbf{k}, i\nu_n)$.

4.2.8 Eigenvalue equation for the two-electron pairing vertex

The two-particle vertex Γ^{pq}_{st} contains information about electron-pairing mediated by the charge and spin fluctuation processes included in the RPA diagram expansion. Currently, this object is still written in orbital space. We, however, would like to know the symmetry of the superconducting pairing for electrons that live on the Fermi surface. The idea is now to set all frequencies to zero and transform the singlet-symmetrized two-particle vertex Γ^{pq}_{st} into band space. This is done by applying the matrix elements from the diagonalization of the kinetic Hamiltonian and summing out all orbital indices. Here, we make the approximation that the electrons in the pair have the same band index.

$$\Gamma_{mn}(\mathbf{k},\mathbf{k}') = \mathrm{Re}\Bigg[\sum_{\substack{pq\\st}} a^{p*}_{m}(\mathbf{k})a^{t*}_{m}(-\mathbf{k})\,\big(\Gamma^{s}\big)^{pq}_{st}(\mathbf{k},\mathbf{k}',\nu=0)\,a^{q}_{n}(\mathbf{k}')a^{s}_{n}(-\mathbf{k}')\Bigg] \qquad (4.134)$$

In this form, the two-particle vertex is accessible to calculations. We can discretize the Fermi surface and insert those discretized momenta for $\mathbf{k}$ and $\mathbf{k}'$. Furthermore, from Eq. 4.134 we see that the band index m is associated with momentum $\mathbf{k}$ and the band index n is associated with momentum $\mathbf{k}'$. Those combinations can be calculated easily from the kinetic Hamiltonian. Therefore, we can determine $\Gamma_{mn}(\mathbf{k},\mathbf{k}')$ for a set of discretized momenta and diagonalize this object in the combined indices $(m,\mathbf{k})$ and $(n,\mathbf{k}')$. The eigenfunctions we find this way are possible symmetries of the superconducting gap on the Fermi surface.

A restriction to the Fermi surface is plausible, since both momentum and energy have to be conserved in all diagrams we consider. If we restrict ourselves to the Fermi surface, only momentum conservation is in question and the weight of diagrams is controlled only by the momentum dependence of the charge and spin susceptibilities. If we had allowed Feynman diagrams with nonzero energy transfer, we would have introduced a lot of new diagrams out of which only few would have given a finite contribution, since momentum and energy conservation can only be fulfilled for few out of all diagrams. In fact, this approximation has been quantified in Ref. [96]. Note, however, that the two-particle pairing vertex might be peaked at finite frequency, if there are electronic bands that come close to, but do not cross the Fermi level. We will not apply our formalism to such cases.

The calculational procedure discussed previously can be put into equations by considering an eigenvalue problem for the two-particle vertex, in which the pairing amplitude λ and a dimensionless symmetry function $g(\mathbf{k})$ appear. Note that the momenta are not yet restricted to the Fermi surface.

$$\lambda g(\mathbf{k}_n) = -\sum_{\mathbf{k}_m} \Gamma(\mathbf{k}_m, \mathbf{k}_n) g(\mathbf{k}_m) \tag{4.135}$$

The negative sign appears, since we want the maximally attractive solution to have the largest positive eigenvalue. Now we explicitly restrict the energies to the Fermi surface.

$$\lambda g(\mathbf{k}_n)\delta(E_{\mathbf{k}_n} - E_F) = -\sum_{\mathbf{k}_m} \Gamma(\mathbf{k}_m, \mathbf{k}_n) g(\mathbf{k}_m)\delta(E_{\mathbf{k}_m} - E_F)\delta(E_{\mathbf{k}_n} - E_F) \tag{4.136}$$

We rewrite this expression by exploiting a property of the delta distribution and the definition of the so-called *Fermi velocity.*

$$\delta(E_{\mathbf{k}_n} - E_F) = \frac{\delta(\mathbf{k}_n - \mathbf{k}_F)}{|\nabla_{\mathbf{k}_n} E(\mathbf{k})|_{\mathbf{k}=\mathbf{k}_n}} = \frac{\delta(\mathbf{k}_n - \mathbf{k}_F)}{\hbar|\mathbf{v}(\mathbf{k}_n)|} \tag{4.137}$$

That means we can solve an effective eigenvalue equation, in which all momenta are restricted to the Fermi surface.

$$\lambda g(\mathbf{k}_n) = -\sum_{\mathbf{k}_m} \frac{\Gamma(\mathbf{k}_m, \mathbf{k}_n)}{\hbar|\mathbf{v}(\mathbf{k}_m)|} g(\mathbf{k}_m) \tag{4.138}$$

This equation allows us to extract a symmetry function, which characterizes the superconducting state in momentum space, and a dimensionless measure for the pairing strength. The strategy for an efficient numerical solution of the eigenvalue problem and all necessary preceding calculations are detailed in a separate section.

4.2.9 Diagrammatic structure of the two-particle vertex in the multi-orbital case

Based on the derivation of the two-particle vertex in the single-orbital case, one could assume that diagrams in the expansion for the multi-orbital case have only bubble and twisted ladder topology as shown in Fig. 4.10.

While the intra-orbital Coulomb interaction indeed only generates diagrams with those topologies, the multi-orbital case naturally comes with the possibility of having diagrams with mixed interaction vertices, which allow for new arrangements of the Green's function lines. In Fig. 4.11 we show a few examples of such diagrams, which are generated by the perturbation expansion for the two-particle vertex at second order in the interaction tensor and which involve the intra-orbital and inter-orbital Coulomb interactions. Note that the inter-orbital Coulomb interaction involves same spin, as well as different spin interactions (see Eq. 4.35).

The two internal Green's function lines in Fig. 4.11(a) and (b) can be written as an unperturbed susceptibility. Therefore, this type of vertex correction diagrams is naturally

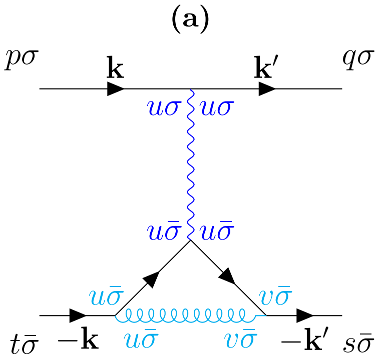
(a)
$p\sigma$
$\mathbf{k}$
$\mathbf{k}'$
$q\sigma$
$u\sigma$
$u\sigma$
$u\bar{\sigma}$
$u\bar{\sigma}$
$u\bar{\sigma}$
$v\bar{\sigma}$
$t\bar{\sigma}$
$-\mathbf{k}$
$u\bar{\sigma}$
$v\bar{\sigma}$
$-\mathbf{k}'$
$s\bar{\sigma}$

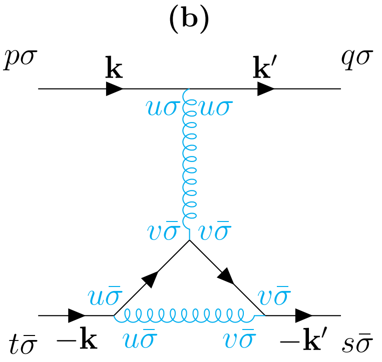
(b)
$p\sigma$
$\mathbf{k}$
$\mathbf{k}'$
$q\sigma$
$u\sigma$
$u\sigma$
$v\bar{\sigma}$
$v\bar{\sigma}$
$u\bar{\sigma}$
$v\bar{\sigma}$
$t\bar{\sigma}$
$-\mathbf{k}$
$u\bar{\sigma}$
$v\bar{\sigma}$
$-\mathbf{k}'$
$s\bar{\sigma}$

Figure 4.11: Feynman diagrams with vertex correction topology that contribute to the two-particle vertex $\Gamma^{bb}_{ab}(\mathbf{k},\mathbf{k}')$ at second order in the interaction vertices.

generated from the perturbation expansion of the two-particle pairing vertex. In particular we found that all mixed interaction diagrams generated by the multi-orbital tensor formulation of RPA (see Eq. 4.131) are physical in the sense that they could in principle also be generated from a perturbation expansion.

4.3 Numerical implementation

4.3.1 Prerequesites

Before we can turn to the implementation of the unperturbed susceptibility, we need an efficient code for solving the kinetic Hamiltonian in momentum space. For bandstructure calculations, a direct implementation of Eq. 2.73, which we reprint here for ease of reading, in terms of a momentum-dependent Hamiltonian matrix $H^W_{nm}(\mathbf{k})$ that uses the orbitals n and m as row and column indices is usually sufficient.

$$H^W_{nm}(\mathbf{k}) = \langle\tilde{\psi}_{n\mathbf{k}}|H|\tilde{\psi}_{m\mathbf{k}}\rangle = \sum_{\mathbf{R}} e^{i\mathbf{kR}} \underbrace{\langle n\mathbf{0}|H|m\mathbf{R}\rangle}_{=t^{nm}_{\mathbf{0R}}}$$

Since we, however, want to calculate susceptibilities, we will need to acccess the eigenenergies and matrix elements that connect orbital and band space possibly for on the order of 10^5 different momenta $\mathbf{k}$. Although the cost for building and diagonalizing the Hamiltonian once is negligible, the accumulated cost for all diagonalizations is not.

Unfortunately, the use of space group symmetries would significantly complicate the implementation. Therefore, we decided to use only the self-adjoint property of the Hamiltonian and restrict the calculation of the Hamiltonian matrix to the upper triangle. A numerical library that can handle such matrices and avoids overhead from unnecessary function calls is the free software library *Eigen*. It is implemented as a C++ template library and, therefore, it can be compiled directly into the programs that use it, possibly even employing function inlining. This strategy is particularly successful whenever the function call for the diagonalization is not negligible compared to the actual computation time needed for diagonalizing the Hamiltonian. Since we are dealing with matrices of size up to about 8 × 8 entries, this an important ingredient of our optimization strategy.

Furthermore, we implement the diagonalization routine for the Hamiltonian not as a standalone program, but as a class, in which all data structures are initialized once. For every individual diagonalization process we reuse these data structures. Furthermore, we store all hopping amplitudes t and all associated hopping vectors $\mathbf{R}$ along with the diagonalization routine to avoid reading those input parameters more than once. With these optimizations we found that the subroutines for solving the kinetic Hamiltonian are sufficiently fast.

4.3.2 Efficient calculation of the unperturbed susceptibility

Since we have previously defined a two-particle pairing vertex at zero frequency (see Eq. 4.134), we will concentrate here on calculating the unperturbed susceptibility at zero excitation frequency. When calculating at finite excitation frequency one has to decide either for a calculation on the imaginary-frequency axis, with bosonic Matsubara frequencies and a subsequent numerical continuation to the real-frequency axis, or a direct calculation on the real-frequency axis. In the former case the calculation on the naturally discretized Matsubara axis is rather simple, but the numerical continuation to the real-frequency axis is a major issue. A direct calculation on the artificially discretized real-frequency axis is usually computationally more demanding, since the sampling has to be done with a very fine grid. However, these are technical details that we mention only for completeness, but they are not important for the calculations we are about to perform.

For ease of reading we reprint Eq. 4.22 for the unperturbed susceptibility, which we evaluate at zero Matsubara frequency ($\nu_n = 0$).

$$\begin{aligned}\chi^{pq}_{st}(\mathbf{q}, i\nu_n) = -\sum_{\mathbf{k},l,m} & a^{p*}_l(\mathbf{k}) a^t_l(\mathbf{k}) a^{s*}_m(\mathbf{k}+\mathbf{q}) a^q_m(\mathbf{k}+\mathbf{q}) \\ & \times \frac{n_F(E_l(\mathbf{k})) - n_F(E_m(\mathbf{k}+\mathbf{q}))}{E_l(\mathbf{k}) - E_m(\mathbf{k}+\mathbf{q}) + i\nu_n}\end{aligned}$$

Before we discuss in detail the algorithm for calculating this object, we have to turn our attention to some problems of Eq. 4.22. Obviously, the difference of band energies in the denominator can become zero, which will lead to a divergence for $\nu_n = 0$. Often such problems are cured by adding a small imaginary part, as discussed, for example, in the context of Eq. 3.41. However, the susceptibility in total does not actually diverge, since the difference of Fermi functions in the enumerator also vanishes. In fact, we can evaluate the case $E_l \to E_m$ with l'Hospital's rule.

$$\lim_{E_l \to E_m} \frac{n_F(E_l(\mathbf{k})) - n_F(E_m(\mathbf{k}+\mathbf{q}))}{E_l(\mathbf{k}) - E_m(\mathbf{k}+\mathbf{q})} = -\beta \frac{e^{\beta E_m}}{(e^{\beta E_m}+1)^2} \tag{4.139}$$

In practive we apply this expression if the magnitude of the difference in energies becomes smaller than 0.1 μeV.

Furthermore, we have to deal with the fact that we neglected in the analytical derivation some diagrams that contribute only for $\mathbf{q} = 0$. Therefore, the zero momentum susceptibility calculated from Eq. 4.22 is wrong and shows a discontinuous jump when compared to values for nonzero momenta. Numerically this problem is easy to cure. When calculating the susceptibility at $\mathbf{q} = 0$ we simply insert the values for the susceptibility calculated for the momentum $\mathbf{q} = (10^{-13}, 10^{-13}, 10^{-13})$ measured in units of the reciprocal lattice vectors.

Now that we have discussed how to solve the numerical problems of the susceptibility formula, we can formulate the algorithm for carrying out the actual calculation. We first note that we are dealing with two distinct momentum variables: the momentum $\mathbf{k}$, which we sum over, and the momentum $\mathbf{q}$, for which we evaluate the susceptibility. The momentum variable $\mathbf{k}$ must sample the entire Brillouin zone, for example using a regular grid, while the momentum $\mathbf{q}$ could be restricted to a few values of interest, for example a high-symmetry path in the Brillouin zone. In the worst case it also samples the Brillouin zone. Therefore, the number of samples for $\mathbf{q}$ is equal or significantly smaller than the number of samples for $\mathbf{k}$.

For the calculation of the susceptibility this means we first calculate the energies and matrix elements for a momentum $\mathbf{k}$ and then calculate the contribution of the susceptibility for all momenta $\mathbf{q}$. In this way, we can save the matrix elements $a_l^{p*}(\mathbf{k})$ and $a_l^t(\mathbf{k})$ and the energy $E_l(\mathbf{k})$ during the entire program loop over $\mathbf{q}$. If we had reversed the order of momentum loops, we would have had to recalculate all matrix elements and all energies. Saving the matrix elements and energies for all $\mathbf{k}$ requires an unpractical amount of memory and the problematic number of Hamiltonian diagonalizations anyway comes from the terms with momentum $\mathbf{k}+\mathbf{q}$, because they result in $n_\mathbf{k} \cdot n_\mathbf{q}$ diagonalizations. One could in principle reduce this to on the order of $n_\mathbf{k}$ diagonalizations by folding all momenta $\mathbf{k}+\mathbf{q}$ back to the first Brillouin zone and reconstruct the energies and matrix elements from the saved data for momenta $\mathbf{k}$. This would, however, require an extremely high resolution in $\mathbf{k}$, since the matrix elements can vary quite rapidly.

An alternative approach is the introduction of improved techniques for carrying out the summation over $\mathbf{k}$ in order to reduce the necessary resolution in this variable. Tetrahedron integration methods have been discussed in the literature [104]. Such optimizations were, eventually, not necessary in our case. From Eq. 4.22 one can furthermore see that the unperturbed susceptibility obeys the symmetry $\chi_{st}^{pq}(\mathbf{q}) = \left(\chi_{qp}^{ts}(\mathbf{q})\right)^*$ at $\nu_n = 0$. Finally, we parallelize the susceptibility calculation over the momentum variable $\mathbf{q}$ using the free software *OpenMPI* framework.

4.3.3 Finding the Fermi surface

Since we build our algorithm on a Fermi surface approximation, we have to clarify how to represent the Fermi surface numerically. We choose to discretize it in terms of a finite set of points.

In two dimensions points on the Fermi surface can in principle be found easily by following the band energies on a grid and finding pairs of points between which the band energy changes sign. Between those two points the Fermi surface can be found by solving a linear interpolant for the momentum corresponding to zero energy. This prescription, however,

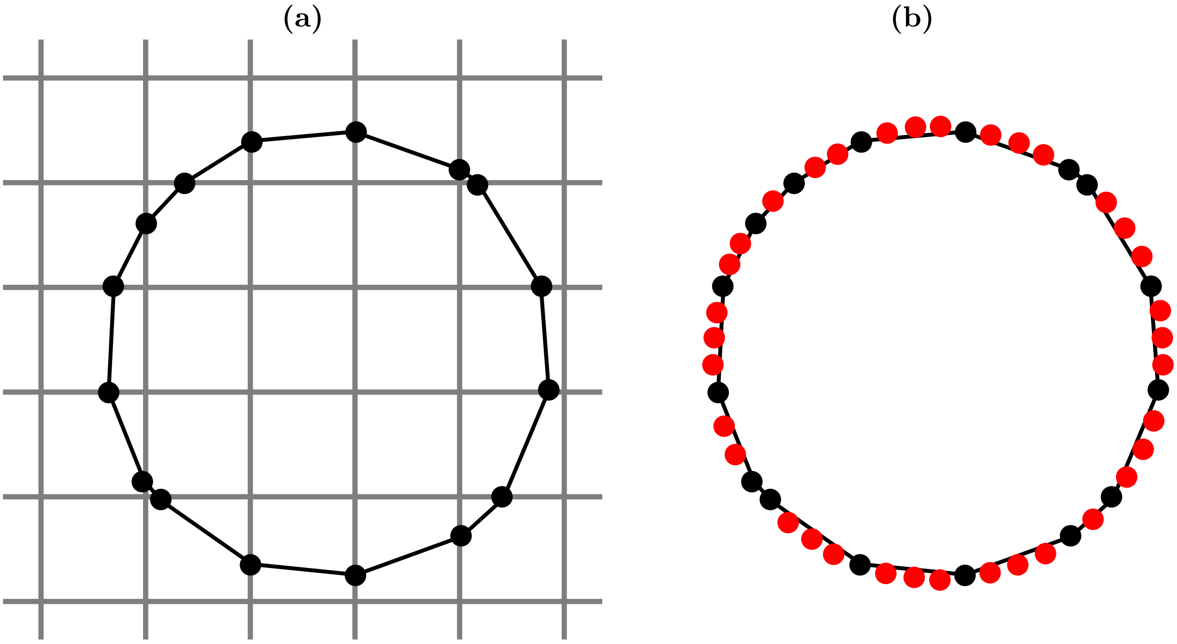

Figure 4.12: (a) The two-dimensional regular grid of band energies is shown in grey. The Fermi surface, represented by black dots, is found by linear interpolation. The segments are shown as black lines. (b) Further points, shown here in red, are inserted into the segments between the points found from interpolation on the grid. The positions of the inserted points are corrected via Newton-Raphson iteration, so that they do not necessarily lie on the black segments any more.

has a severe disadvantage. Namely, small parts of the Fermi surface will be represented by few points, whereas large parts will be represented by many. Although this imbalance seems natural at first glance, small parts of the Fermi surface can have a very large contribution to the two-particle pairing vertex, if their Fermi velocity becomes small (see Eq. 4.138). Therefore, we rather seek to converge all results with respect to the number of points on the discretized Fermi surface.

One way to increase the resolution of the discretization would of course be to simply increase the resolution of the regular grid on which we carry out the linear interpolation. This, however, leads to many unnecessary evaluations of the kinetic Hamiltonian. We rather fix the resolution of the regular grid, so that all parts of the Fermi surface are found, possibly with very low resolution. Then we use a contouring algorithm to build a set of two-point segments that characterize the Fermi surface. Compared to a collection of single points this has the advantage that we do not have to increase the overall grid resolution to find further points on the Fermi surface. Instead we can purposefully insert new points into each segment (see Fig. 4.12). These points will in general not lie exactly on the Fermi surface, but very close to it. Therefore, we correct the position of those points

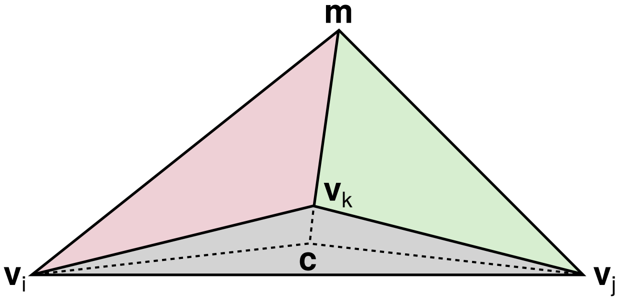

Figure 4.13: Triangle on the Fermi surface defined by the vertices $\mathbf{v}_i$, $\mathbf{v}_j$ and $\mathbf{v}_k$. The centroid is denoted as $\mathbf{c}$, while the fourth Fermi surface point $\mathbf{m}$ forms a pyramid with the three vertices. The grey base triangle is not used in the calculation of the two-particle pairing vertex.

using the iterative Newton-Raphson method.

$$x_{i+1} = x_i - \frac{f(x_i)}{f'(x_i)} \tag{4.140}$$

In fact, we employ this equation to solve the function $f = E(\mathbf{k}+\lambda\mathbf{k}_F)$ for the parameter λ, at which the energy vanishes ($E = 0$). The direction in which we correct the point position is given by the Fermi momentum $\mathbf{k}_F$, which is directly proportional to the Fermi velocity. Thus, we can iteratively refine the position of the inserted points until they lie on the Fermi surface within a small numerical threshold. Although using numerical derivatives in the Newton-Raphson method is usually disencouraged in the literature [105], it works very well here, leading to convergence within one to three iteration steps, because most inserted points are already very close to their exact counterparts.

For the three-dimensional case we use a representation of the Fermi surface in terms of triangles as implemented in the free software *GNU triangulated surface library.* In contrast to the two-dimensional case, we can not simply use the corners of the triangles to construct a point cloud on which we carry out all calculations, since the maximally achievable resolution at constant number of points is much lower in three dimensions compared to two. Therefore, we choose to represent every surface triangle, given by the library in terms of its vertices $\mathbf{v}_i$, $\mathbf{v}_j$ and $\mathbf{v}_k$, by its centroid $\mathbf{c}$.

$$\mathbf{c} = \frac{1}{3}\left(\mathbf{v}_i + \mathbf{v}_j + \mathbf{v}_k\right) \tag{4.141}$$

Since the centroid $\mathbf{c}$ does not lie exactly on the Fermi surface, we again use the Newton-Raphson method (Eq. 4.140) to construct an associated point $\mathbf{m}$ that does lie on the Fermi surface. The point m and the vertices $\mathbf{v}_i$, $\mathbf{v}_j$ and $\mathbf{v}_k$ form a pyramid (see Fig. 4.13). In the calculation of the two-particle vertex we let the point $\mathbf{m}$ represent the surface of that pyramid, excluding the base plane. We calculate this surface area from elementary geometry and let it enter Eq. 4.138 as an additional weighting factor. The Fermi velocity is calculated at the point $\mathbf{m}$.

4.3.4 Efficient calculation of the two-particle pairing vertex

Calculating the two-particle vertex following Eq. 4.133 we first need to construct the charge and spin susceptibilities at momentum $\mathbf{k}-\mathbf{k}'$, where $\mathbf{k}$ and $\mathbf{k}'$ lie on the Fermi surface. We have to evaluate the susceptibility for the momentum combinations $\mathbf{k}-\mathbf{k}'$ and $\mathbf{k}+\mathbf{k}'$, because of the singlet-symmetrization (see Eq. 4.132). If we have m points on the Fermi surface, this will result in $2m^2$ evaluations of the susceptibility. If we increase the resolution on the Fermi surface to about 1000 points, this would already require the calculation of susceptibility tensors for two million different momenta. Although we cannot get around evaluating the susceptibility for that many momentum combinations, we can greatly reduce the numerical effort by employing interpolation. If we sample the susceptibility on a regular grid of, for example, $25^3 \approx 1.6 \cdot 10^4$ points and construct the rest of the needed data from interpolation, the calculation can be carried out at much lower cost.

For the susceptibility interpolation works very well, since we have calculated it at finite temperature, which results in a smooth momentum dependence. We use simple *trilinear interpolation* for each element of the susceptibility tensor in orbital space. Our interpolation algorithm is based on the elemental volume of the regular grid around our point of interest.

$$\begin{aligned} f(x,y,z) =& f_{000}\,(1-x)(1-y)(1-z) + f_{100}\,x(1-y)(1-z) \\ &+ f_{010}\,(1-x)y(1-z) + f_{001}\,(1-x)(1-y)z \\ &+ f_{101}\,x(1-y)z + f_{011}\,(1-x)yz \\ &+ f_{110}\,xy(1-z) + f_{111}\,xyz \end{aligned} \tag{4.142}$$

The function values on the corners of the elemental volume are denoted by f_{ijk} with $i,j,k=\{0,1\}$. The scaled coordinates within that elemental volume are given by x,y,z, where f_{000} is equivalent to $x=y=z=0$.

Since the sampled susceptibility tensor can become so large that it does not fit into random access memory, we have to devise a system to save those samples to a hard disk. Once the data are saved, it becomes a problem to find the right elements in the sampled data. For this purpose we use a binary format, in which the data positions of all elements in the binary file can be calculated from the regular grid indices next to the momentum point of interest. A trivial plain text format would be far too slow, since we would have to search line by line through the entire file to locate the needed data. Alternatively, we also implemented loading the entire binary susceptibility file into random access memory, if its size does not exceed a certain threshold. This can result in a significant speedup for the interpolation process in the case of small susceptibility files.

A further advantage of interpolation is that we do not need to recalculate the unperturbed susceptibility if we change the number of points on the Fermi surface. Eventually, calculating the susceptibility only for a few momenta scattered in three-dimensional space would also make the data useless for plotting the susceptibility, for example in a certain momentum plane, whereas this is in fact very easy for the samples on a regular grid.

Since the two-particle vertex in orbital space is an extremely large object with four orbital and two momentum indices (see Eq. 4.133), we never save it explicitly, but directly calculate its contribution to the two-particle vertex in band space (see Eq. 4.134), which has only two band indices left, which are actually identical to its momentum indices. The Fermi velocity (see Eq. 4.137) can be calculated easily by replacing the derivative by a numerically evaluated finite difference. Furthermore, the calculation of the two-particle vertex can be trivially parallelized over one of the momentum indices, for example $\mathbf{k}$, using OpenMPI. In particular this parallelizes the numerically intense calculation of the charge and spin susceptibilities from the precalculated unperturbed susceptibilities. The eigenvalues and eigenvectors of the two-particle vertex according to Eq. 4.138 are finally obtained using the Eigen library. We do not use parallelization at this point, since efficient libraries for parallel linear algebra with dense matrices are not yet available.

The eigenvectors of the two-particle pairing vertex are the symmetry functions $g(\mathbf{k})$, which can be interpreted as the superconducting order parameter in momentum space. The eigenvalues are the pairing amplitudes λ. The symmetry function corresponding to the largest eigenvalue is predicted to be realized.

In the case of a three-dimensional pairing calculation, the symmetry function is given on a set of points scattered in three-dimensional space. For reconstructing the symmetry function on two-dimensional cuts without redoing any pairing calculations we use *radial basis function interpolation* from the free software library *ALGLIB*.

Chapter 5

Influence of molecular conformations on the electronic structure of kappa-type organic charge transfer salts

D. Guterding, R. Valentí, H. O. Jeschke,
Phys. Rev. B **92**, 081109(R) (2015).

Before we start to discuss superconductivity in organic charge transfer salts, we take a brief detour via the phenomenon of metastable molecular conformations in those materials. Since we are dealing with molecular crystals, it is natural to assume that not only intermolecular, but also intra-molecular degrees of freedom can be relavant for the physics of those materials.

In fact, it was realized in the very early days of organic superconductors that the superconducting transition temperature T_c of the first ambient pressure ET-based superconductor β-(ET)$_2$I$_3$ can be enhanced from 1.5 K to 8 K by application of shear and pressure. It was shown that degrees of freedom within the ET molecules, which are disordered at ambient pressure, become ordered by the application of pressure [106–112]. These degrees of freedom are the conformations of the terminal ethylene groups within the ET molecules, which can be aligned either parallel or canted, often also referred to as *eclipsed* or *staggered* (see Fig. 5.1).

The properties of κ-(ET)$_2X$ materials are very sensitive to disorder. Irradiation experiments have shown that lattice disorder lowers the T_c of κ-(ET)$_2$Cu(SCN)$_2$ [113] and causes electron localization in κ-(ET)$_2$Cu[N(CN)$_2$]Br [114]. It was also recognized that disorder is introduced into these materials by the metastability of eclipsed and staggered ethylene endgroups, which can display a glass-like freezing upon cooling [9, 48, 50, 115–117]. The energetically favorable configuration is not universal for different packing motifs and anions X.

Recently, it was shown that ethylene endgroup disorder can be used to reversibly tune κ-(ET)$_2$Cu[N(CN)$_2$]Br through a metal-to-insulator transition [46–48]. Since κ-(ET)$_2X$ are believed to have a common phase diagram, which is mainly controlled by the value of the on-site Coulomb repulsion U over the electronic bandwidth, it is natural to ask whether endgroup disorder could be related to at least one of the two. Nevertheless, changes in physical properties in the presence of ethylene endgroup disorder have so far been interpreted as a consequence of lattice disorder, with the exception of recent scanning tunneling spectroscopy experiments [49]. Surprisingly, the effect of different ethylene endgroup configurations on the electronic structure, and especially the electronic bandwidth, of κ-$(\mathrm{ET})_2X$ has only been investigated in a single material using the extended Hückel method [50], while calculations for ET molecules and dimers in vacuum are available [48, 51, 52].

In this chapter we examine the electronic structure of endgroup *ordered* crystals in both staggered and eclipsed conformation for various members of the κ-$(\mathrm{ET})_2\mathrm{X}$ family of materials using density functional theory calculations. For each material and conformation we construct a low-energy effective Hamiltonian via a Wannier downfolding scheme. We find that ethylene endgroup configurations of ET molecules influence the electronic bandwidth of the crystalline materials investigated here. We present a simplified interpretation of our results in terms of the anisotropic triangular lattice Hubbard model and connect our findings to recent experiments, especially emphasizing the possibility that changes in the electronic structure through ethylene endgroup disorder and strongly enhanced electron correlation are relevant for explaining the metal-to-insulator transition in addition to commonly considered lattice disorder. Our findings were written up in a publication [118], which this chapter is based on.

5.1 Methodology and calculation setup

The crystal structures of materials with ethylene endgroup disorder show great uncertainties regarding the positions of atoms within and next to the ethylene groups. The positions of hydrogen atoms can often not be inferred from X-ray diffraction experiments and positions given in the literature are often calculated with simple analytical approximations. Furthermore, we would also like to investigate materials for which the crystal structure of only one of the possible endgroup conformations has been reported in the literature.

We first take a look at κ''-$(\mathrm{ET})_2\mathrm{Cu}[\mathrm{N}(\mathrm{CN})_2]\mathrm{Cl}$, for which crystal structures in both endgroup conformations have been determined [119]. Important information is contained in the so-called *displacement ellipsoids* obtained from the X-ray diffraction experiment. These represent the amount of uncertainty regarding the measured positions of atoms within the crystal. In Fig. 5.1 we show the displacement ellipsoids within an ET molecule of κ''-$(\mathrm{ET})_2\mathrm{Cu}[\mathrm{N}(\mathrm{CN})_2]\mathrm{Cl}$ according to Ref. [119]. Ethylene endgroup disorder is included on the right end of the molecule in the form of fractionally occupied atomic positions. Furthermore, we see that the positions of the terminal carbon and the adjacent sulfur atoms are much more uncertain than those in the center of the molecule. Hydrogen positions have no experimental uncertainty, since they are calculated.

Based on this analysis and the previously mentioned requirements, we formulate a method to obtain comparable crystal structures for various materials in both endgroup conformations. Namely, we take experimental crystal structures and keep all atomic positions fixed except for those within the ethylene endgroups and the adjacent sulfur atoms. The endgroup and adjacent sulfur positions are optimized using the GPAW implementa-

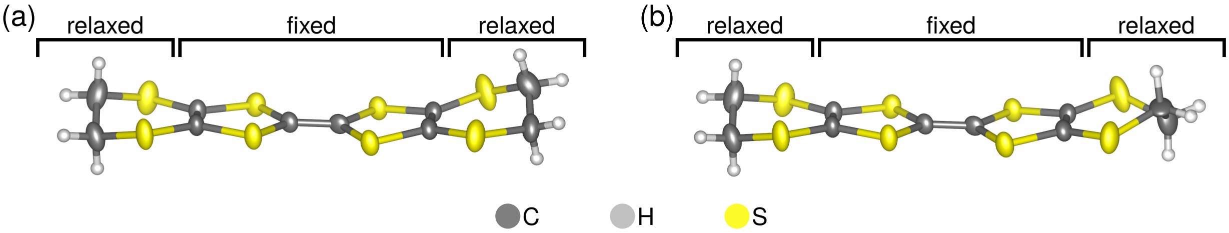

Figure 5.1: ET molecule with displacement ellipsoids from the experimental structure determination of κ''-(ET)$_2$Cu[N(CN)$_2$]Cl. The size of the ellipsoids scales with the amount of uncertainty regarding the respective atomic position. Ethylene endgroup disorder is included on the right end of the molecule. The eclipsed conformation is shown in (a), while (b) shows the staggered conformation. The bars above the molecule indicate which parts of the ET molecules are relaxed in our DFT calculations and which atomic positions remain at their experimental values.

tion [120] for the PAW formulation of density functional theory. Since we use the local L-BFGS algorithm to optimize the total energy, we can obtain relaxed crystal structures for both the ground state and the metastable endgroup conformations. In cases where one of the endgroup conformations is experimentally not available, we simply set up the endgroup atoms manually and relax them as for the experimental structures. The GPAW calculations were performed using $2 \times 2 \times 2$ k-point grids and GGA exchange-correlation functional [75]. The atomic positions were minimized until forces were below $10\,\mathrm{meV/Å}$, while the unit cell parameters were left unaltered.

We apply this recipe to the materials κ-(ET)$_2$Cu[N(CN)$_2$]I, κ''-(ET)$_2$Cu[N(CN)$_2$]Cl and κ-(ET)$_2$Cu$_2$(CN)$_3$ ($T = 200$ K), for which both endgroup conformations have been measured experimentally [115, 119, 121]. The crystal structure of κ-(ET)$_2$Cu[N(CN)$_2$]I has been measured both at $T = 127\,\mathrm{K}$ and $T = 295\,\mathrm{K}$. If not denoted otherwise, we use the low temperature structure. The room temperature structure serves as a consistency check. Furthermore, we apply it to the material of interest κ-(ET)$_2$Cu[N(CN)$_2$]Br, for which the crystal structure in one of the conformations is missing in the literature [115].

Subsequently, we performed DFT calculations within the FPLO method [76] to calculate the electronic bandstructure based on the optimized crystal structures. We used $6 \times 6 \times 6$ k-point grids and the GGA exchange-correlation functional [75]. From those DFT calculations we constructed low-energy models using projective molecular orbital Wannier functions as implemented in FPLO [122]. The states included into the Wannier Hamiltonian are the *highest occupied* (HOMO) and *lowest unoccupied molecular orbitals* (LUMO) of all (ET)$_2^+$ dimers within the crystal. The resulting Hamiltonian is 3/4-filled and consists of four bands corresponding to the four ET sites. We keep the largest four elements (t_1,t_2,t_3,t_4) of the kinetic Hamiltonian (see Fig. 5.2). The lattice sites are located at the center of the innermost C-C bond within each ET molecule.

The 3/4-filled model can be related to the anisotropic triangular lattice Hubbard model by projecting out only the LUMO states, which results in a 1/2-filled model with two bands.

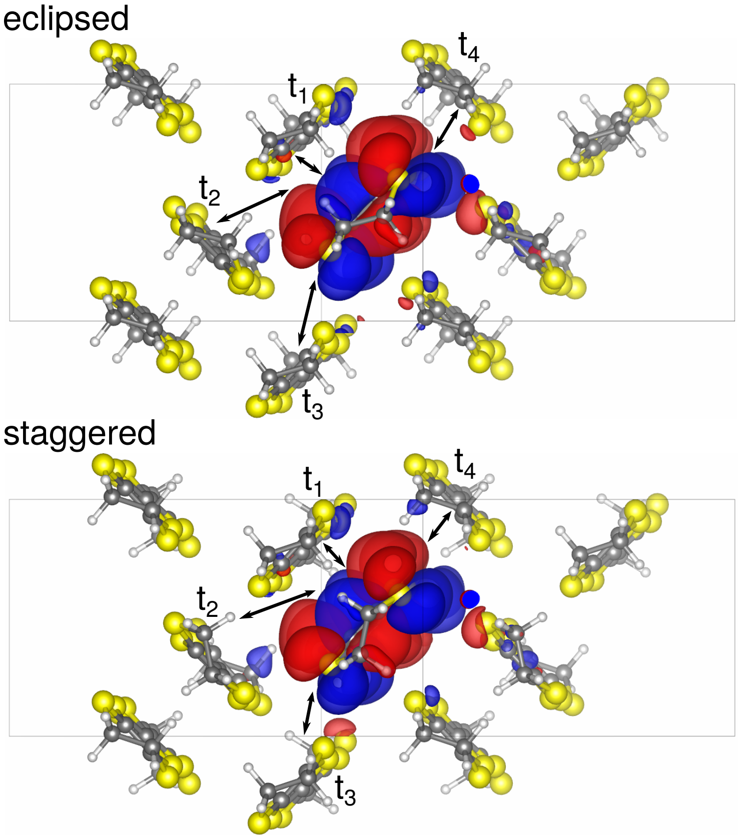

Figure 5.2: Molecular Wannier function of an ET molecule in staggered and eclipsed configuration for κ-(ET)$_2$Cu[N(CN)$_2$]Br. The arrows denote the directions of dominant hopping processes (t_1,t_2,t_3,t_4). Figure taken from Ref. [118].

On the level of the hopping parameters this can be done using geometric formulas [17].

$$t = (|t_2| + |t_4|)/2 \tag{5.1}$$

$$t' = |t_3|/2 \tag{5.2}$$

Even the intra-orbital Coulomb repulsion within the anisotropic triangular lattice model can be estimated as

$$U \approx 2|t_1|. \tag{5.3}$$

This method of obtaining a t, t' and U LUMO-only model (or so-called *dimer model*) has recently been criticized, because this estimate for U implies that the unscreened intermolecular Coulomb repulsion V_1 within an $(\mathrm{ET})_2^+$ dimer vanishes. In DFT parametrizations of this model, V_1 was, however, found to be non-negligible [51, 52, 123]. Furthermore, calculations in constrained random phase approximation have shown sizeable screening effects in the LUMO-only model not accounted for in the geometric formulas [124]. Nevertheless, dimer approximated Hamiltonians and subsequent many-body calculations show remarkable success in explaining most of the qualitative properties of ET based materials [25, 32]. Therefore, the approximate dimer model is sufficient for the case we investigate here.

material	low-energy conf.	ΔE in meV
κ-$(ET)_2Cu_2(CN)_3$	staggered	130
κ''-$(ET)_2Cu[N(CN)_2]Cl$	eclipsed	72
κ-$(ET)_2Cu[N(CN)_2]Br$	eclipsed	110
κ-$(ET)_2Cu[N(CN)_2]I$	staggered	38

Table 5.1: Lowest energy conformations of the ethylene endgroups determined from our DFT relaxed structures. The energy difference ΔE to the high energy conformation is calculated per ET molecule from the FPLO total energies. Table taken from Ref. [118].

5.2 Results and discussion

First, we investigate the energy difference between eclipsed and staggered states based on the FPLO total energies. The energy differences and ground state molecular conformations are given in Table 5.1. Values for the energy differences calculated with GPAW are in good agreement. The energy ordering of staggered and eclipsed configurations comes out correctly for all investigated materials with the exception of κ-$(ET)_2Cu[N(CN)_2]I$ at $T = 295K$, where the energy difference is the smallest and the distribution of endgroup configurations measured experimentally was found to be 51%:49% [115, 119, 121].

The value for ΔE we determined is the energy difference between the two local minima of the energy corresponding to staggered and eclipsed configurations, which is not to be confused with the activation energy. The latter denotes the height of the potential barrier between those minima, which can be significantly larger than ΔE [46, 116]. Instead, our DFT calculated values constitute a lower bound for the activation energy: κ-$(ET)_2Cu[N(CN)_2]I$ with the smallest energy difference is known to be completely endgroup disordered at room temperature [115] and κ''-$(ET)_2Cu[N(CN)_2]Cl$ contains about 20% disorder at room temperature [119], while in the other two materials the amount of endgroup disorder is in a range of few percent.

The electronic bandstructures obtained from the molecular Wannier function analysis of the DFT results are shown in Fig. 5.3 for both eclipsed and staggered ethylene endgroup configurations. In all bandstructures shown the difference between staggered and eclipsed configurations lies in the electronic bandwidth. Going from eclipsed to staggered, the overall bandwidth increases, while the width of the two bands closest to the Fermi level decreases.

We analyse these bandstructures using a minimal model [18] for a κ-packed layer of individual ET molecules (Fig. 5.2) using the four largest parameters (t_1,t_2,t_3,t_4), also commonly denoted as (b_1,p,b_2,q). These hopping parameters are given in Table 5.2. Parameters t_1 (b_1) and t_3 (b_2) decrease from staggered to eclipsed configurations, while t_4 (q) increases and t_2 (p) remains about constant.

These changes in hopping parameters can be rationalized based on the Wannier functions shown in Fig. 5.2. Although the molecular Wannier function hardly resides on the terminal ethylene groups, overlaps with neighboring ET molecules are influenced by the configuration of the endgroups through the direction of their bonds with the neighboring

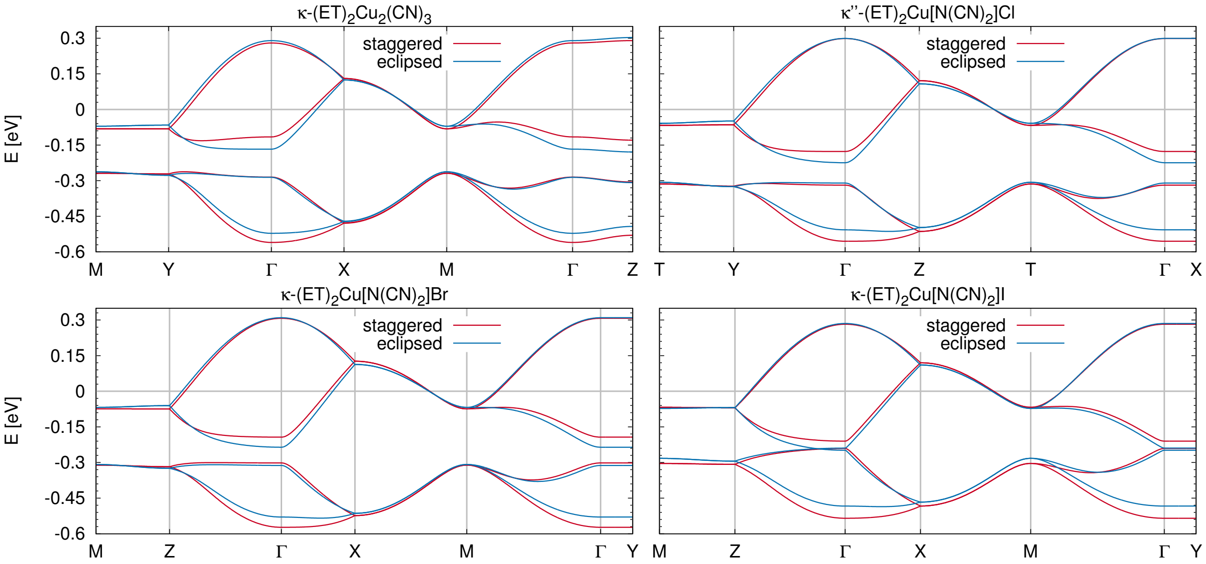

Figure 5.3: Electronic bandstructure of all investigated materials for staggered and eclipsed ethylene endgroup configurations. Staggered ethylene endgroups produce a larger overall bandwidth than eclipsed ones, but reduce the width of the two bands closest to the Fermi level. Figure taken from Ref. [118].

sulfur atoms.

Especially the hopping t_3 is strongly enhanced, because the tails of the Wannier function on the neighboring ET molecule are enlarged. The Wannier functions remain largely unaltered in the direction that corresponds to t_2. Therefore, this parameter largely remains constant. In the direction of t_4 the tail on the neighboring ET molecule is enhanced in the staggered configuration, but the Wannier function on the central molecule turns away from this tail because of the altered sulfur-ethylene bond direction. Consequently, t_4 is reduced. The relative changes in t_1 are rather small, which is consistent with our analysis of the Wannier functions.

Finally, we analyze the effective Hubbard model on the anisotropic triangular lattice (t,t',U) corresponding to each set of (t_1,t_2,t_3,t_4) to understand the metal-insulator transition in κ-(ET)$_2$Cu[N(CN)$_2$]Br. Fig. 5.4 shows the result of our dimer model estimates. The change from eclipsed to staggered ethylene group configuration universally increases both the frustration t'/t and the relative strength of the Coulomb repulsion U/t, i.e. U over the bandwidth.

Comparison of our findings with cellular dynamical mean-field theory [25] and exact diagonalization results for the anisotropic triangular lattice Hubbard model [32] explains why κ-(ET)$_2$Cu[N(CN)$_2$]Br can be tuned into a Mott insulating [46, 47] state by activating the energetically less favorable endgroup configuration: First, the material in its lowest energy configuration is already close to a Mott insulating phase. Second, the lowest energy configuration is the eclipsed one, so U/t can be strongly increased by activating the staggered configuration. Therefore, the system crosses the phase transition line and a Mott insulator is realized.

material				t_1	t_2	t_3	t_4	t'/t	U/t
κ-$(ET)_2Cu_2(CN)_3$	I	eclipsed		167	84.9	70.4	30.3	0.61	5.8
		staggered	x	176	78.0	81.4	18.7	0.84	7.3
κ''-$(ET)_2Cu[N(CN)_2]Cl$	M	eclipsed	x	174	97.3	50.5	35.9	0.38	5.2
		staggered		188	93.4	64.0	26.6	0.53	6.3
κ-$(ET)_2Cu[N(CN)_2]Br$	SC	eclipsed	x	178	99.0	59.5	35.8	0.44	5.3
		staggered		187	97.1	70.2	24.9	0.58	6.1
κ-$(ET)_2Cu[N(CN)_2]I$, 127 K	M	eclipsed		152	101	47.2	29.2	0.36	4.7
		staggered	x	170	99.0	52.4	18.9	0.44	5.8
κ-$(ET)_2Cu[N(CN)_2]I$, 295 K	M	eclipsed		153	92.0	49.9	31.5	0.40	4.9
		staggered		164	92.0	54.8	22.2	0.48	5.8

Table 5.2: Values of the molecule model parameters (t_1,t_2,t_3,t_4) in meV, also commonly denoted as (b_1,p,b_2,q). Dimer model parameters are given as ratios t'/t and U/t calculated from (t_1,t_2,t_3,t_4) using Eqs. 5.1, 5.2 and 5.3. The second column states the experimental ground state of the respective material (I=insulator, M=metal, SC=superconductor). The x in the fourth column marks the low energy configuration of the ethylene endgroups. Table taken from Ref. [118].

Note that the phase diagram of the anisotropic triangular lattice Hubbard model is not entirely settled and slightly different results have been obtained using other numerical methods [23, 31].

5.3 Summary and outlook

We demonstrated that DFT reliably reproduces the ground state ethylene endgroup configuration for various κ-phase materials. While previous discussion of endgroup conformations in the literature considered only lattice disorder a relevant issue, we have shown that the relative orientation of ethylene endgroups within ET molecules crucially influences the electronic bandwidth of κ-type organic charge transfer salts. Switching an ET molecule from eclipsed to staggered configuration decreases the electronic bandwidth and in turn enhances the relative strength of the Coulomb repulsion, bringing the material closer to a Mott insulating state.

Recent experiments, where κ-$(ET)_2Cu[N(CN)_2]Br$ was reversibly switched from a metallic to an insulating state by tuning the endgroup configurations, can be understood based on our picture. In κ-type materials that are not close to any phase transition, the effects of ethylene endgroup disorder may not manifest as dramatically as in κ-$(ET)_2Cu[N(CN)_2]Br$. Based on our estimates of model parameters, similar behavior may be encountered in κ''-$(ET)_2Cu[N(CN)_2]Cl$.

The effect of disorder was, however, neglected entirely in our study. Since we only investigated endgroup ordered crystals, the actual mechanism of the metal-to-insulator transition may also involve the disorder of hopping parameters and Coulomb repulsion. The length scale on which this disorder manifests is currently unknown. In particular, it

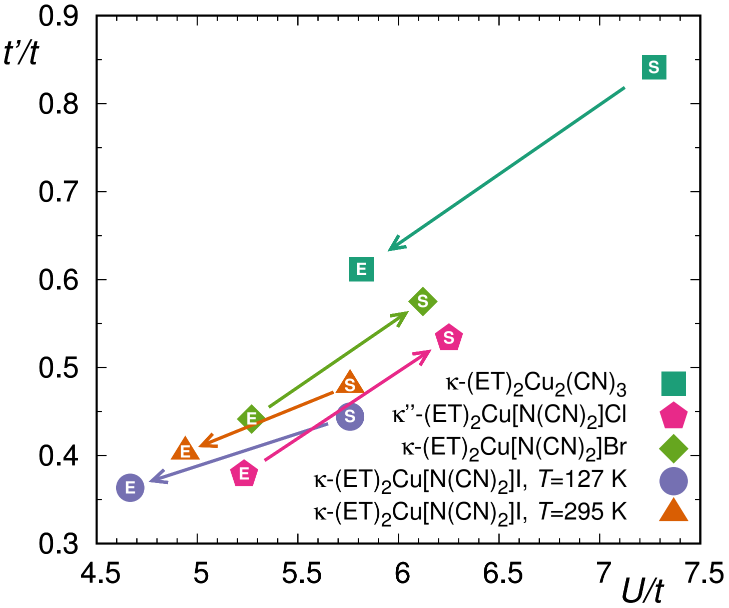

Figure 5.4: Parameter ratios t'/t and U/t in the effective dimer model. The direction of the arrows indicates the direction of change in the model parameters going from the low to the high energy configuration of the ethylene endgroups. Eclipsed (E) endgroup configurations are located on the left side (small U/t) of the plot, while staggered (S) endgroup configurations are located on the right side (large U/t). Figure taken from Ref. [118].

is an open question how, in the actual experiments, the few percent of ET molecules that are in the high-energy conformation corresponding to the Mott state can drive the entire sample insulating.

Chapter 6

Symmetry of the superconducting pairing in kappa-type organic charge transfer salts

D. Guterding, M. Altmeyer, H. O. Jeschke, R. Valentí,
Phys. Rev. B **94**, 024515 (2016).

D. Guterding, S. Diehl, M. Altmeyer, T. Methfessel,
U. Tutsch, H. Schubert, M. Lang, J. Müller, M. Huth,
H. O. Jeschke, R. Valentí, M. Jourdan, H.-J. Elmers,
Phys. Rev. Lett. **116**, 237001 (2016).

Even though the subject of superconductivity in kappa-type organic charge transfer salts is several decades old, no consensus regarding the nature of the superconducting state has been reached. As discussed in the introductory section, the variety of experiments performed on these materials, as well as the multitude of accompanying contradictory interpretations, is outstanding. Since this situation is in contrast to the unanimity of theorists regarding the symmetry of the superconducting state in anisotropic triangular lattice Hubbard model, which only explains a small fraction of experiments on superconductivity, a fresh theoretical approach is needed.

In particular, the dimer model on the anisotropic triangular lattice is only an approximation with *a priori* unclear range of applicability to the real lattice structure of κ-(ET)$_2X$ charge transfer salts. In a seminal paper [125] Kuroki *et al.* investigated the superconducting pairing taking into account the realistic lattice structure and in fact found a phase transition between $d_{x^2-y^2}$- and d_{xy}-symmetric states when lowering the degree of dimerization.

We build upon the idea by Kuroki *et al.* and derive a set of realistic molecule-based low-energy models for superconducting κ-(ET)$_2X$ materials from density functional theory calculations. After identifying the parameter region relevant for the real materials, we investigate the symmetry of the superconducting pairing in this model within a random phase approximation spin-fluctuation approach. Our results show that the position of many materials in the phase diagram is close to a phase-transition line between states with extended $s + d_{x^2-y^2}$ and d_{xy} pairing symmetry. Furthermore, we clarify that the customary dimer model not only fails in the limit of weak dimerization, but also when the in-plane anisotropy of hopping integrals becomes too large, which we find to be the case for all investigated materials. We simulate tunneling spectra in the superconducting state for selected cases and compare our findings to *scanning tunneling spectroscopy* (STS) experiments, which we analyze in great detail.

This chapter is based on two publications: the theoretical foundations are explained in Ref. [126], while the combined theoretical and experimental STS study is contained in Ref. [44].

6.1 Methods and models

6.1.1 Ab initio calculations and model Hamiltonian

We use density functional theory calculations within the FPLO method [76] to calculate the electronic bandstructure. For the exchange-correlation functional we employ the generalized gradient approximation [75]. All calculations are converged on $6 \times 6 \times 6$ k-point grids. We use crystal structures from Refs. [127–129]. In the case of Ref. [127], where crystal structures were measured for several temperatures, we use the data taken at 100 K.

In contrast to the customary dimer approximation, we model the κ-$(\mathrm{ET})_2^+$ layer taking into account each individual ET molecule as a lattice site (see Fig. 6.1). Tight-binding parameters are obtained from projective molecular orbital Wannier functions as implemented in FPLO [122]. Therefore, the number of bands in the tight-binding model is equal to the number of ET molecules in the crystallographic unit cell. With the molecular Wannier function method almost perfect representations of the DFT bandstructures can be obtained and ambiguities from fitting procedures are avoided. The latter is especially important for many-body calculations based on the obtained low-energy Hamiltonians.

In the following model investigation, we only keep the four largest in-plane hopping elements (t_1,t_2,t_3,t_4) between ET molecules [see Fig. 6.1(a)]. The resulting hopping structure is a generalization of the Shastry-Sutherland lattice [130], which is reached in the limit of $t_2 = t_4$ and $t_3 = 0$. In cases where the unit cell contains multiple κ-type layers, we discard all but one of the layers after the Wannierization procedure, because the interlayer coupling is negligible. In some of the investigated compounds, the crystal symmetry is lowered with respect to the high-symmetry orthorhombic space group *Pnma* of κ-$(\mathrm{ET})_2\mathrm{Cu}[\mathrm{N}(\mathrm{CN})_2]\mathrm{Br}$, which leads to a small additional splitting of the hoppings t_i into $\tilde{t}_i$ and $\tilde{t}'_i$. For simplicity, this particular anisotropy is discarded in our study by averaging the hopping integrals as $t_i = (\tilde{t}_i + \tilde{t}'_i)/2$. As a result, we obtain the kinetic part of a four-band Hamiltonian which is 3/4-filled and of the same form for all materials investigated.

Alternatively, because ET molecules in κ-type arrangement are quite strongly dimerized, it is popular to approximate the κ-$(\mathrm{ET})_2^+$ layer by dimers on an anisotropic triangular lattice, integrating out the intra-dimer degrees of freedom. The parameters of this dimer model can be calculated directly from the molecule model using geometric formulas [17],

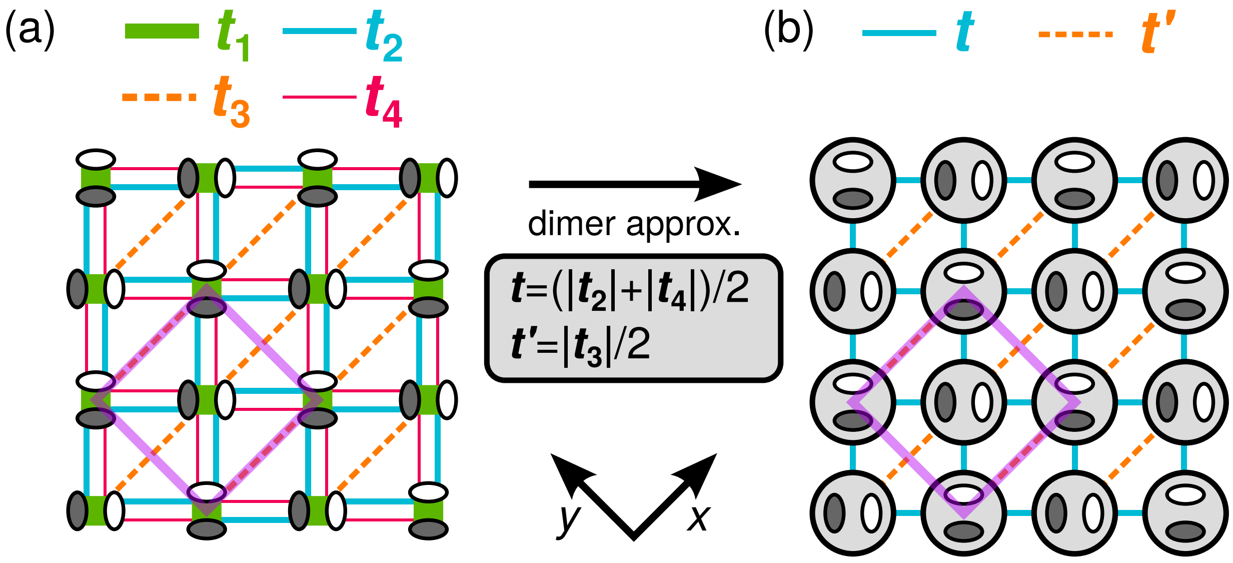

Figure 6.1: (a) Molecule model of the κ-(ET)$_2^+$ layer. Individual ET molecules are represented by white and dark grey ellipsoids. The four dominant hopping integrals are (t_1,t_2,t_3,t_4). Note the pronounced asymmetry in magnitude between t_2 and t_4, which is indicated here by different line thickness. (b) Dimer approximated κ-(ET)$_2^+$ layer. Two molecules are contracted into one dimer site indicated by a bold shaded circle. The intra-dimer hopping integral t_1 is integrated out, while t_2 and t_4 are averaged. Therefore, the dimer model is characterized by only two hopping parameters $\{t,t'\}=\{(|t_2|+|t_4|)/2,|t_3|/2\}$. In both subfigures the unit cell considered in our work is indicated by a bold magenta colored line. Figure taken from Ref. [126].

which we introduced in the previous chapter (see Eqs. 5.1 and 5.2).

$$\begin{aligned} t &= (|t_2| + |t_4|)/2 \\ t' &= |t_3|/2 \end{aligned}$$

By convention the dimer approximation uses the crystallographic unit cell containing two dimers [see Fig. 6.1(b)]. Therefore, the dimer-approximated Hamiltonian consists of two bands, which are half-filled. Note that based on the geometric formulas, any anisotropy between t_2 and t_4 of the molecule model is discarded when going from the molecule to the dimer model. With few exceptions [131], the dimer approximated model nevertheless reproduces well the low-energy part of the original bandstructure. It has recently been demonstrated that improved estimates for dimer model parameters can be obtained by a Wannier function calculation [121, 124, 132].

The two-band dimer model can be unfolded to a one-band model by transforming to a unit cell of half the size and rotated by 45 degrees. The so-obtained model is directly related to the square lattice Hubbard model, but with an additional coupling along one of the diagonals. Results obtained in the one-band model are, therefore, rotated by 45 degrees with respect to the physical Brillouin zone of organic charge transfer salts, so

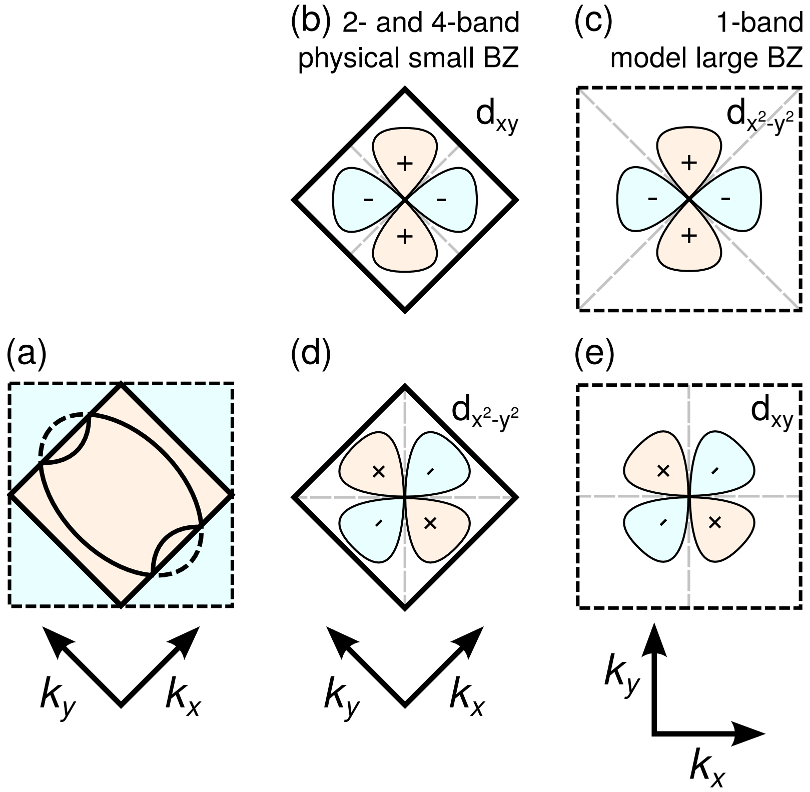
(b) 2- and 4-band physical small BZ
(c) 1-band model large BZ
dxy
dx²-y²
+
-
(a)
(d)
(e)
dx²-y²
dxy
×
ky
kx
ky
kx
ky
kx

Figure 6.2: (a) The inner bold lines show Brillouin zone and Fermi surface of a generic κ-(ET)$_2X$ material. The outer dashed lines show Brillouin zone and Fermi surface of the unfolded one-band dimer model. (b) d$_{xy}$ order parameter in the physical Brillouin zone. Nodes are located in the x- and y-directions. (c) d$_{x^2-y^2}$ order parameter in the unfolded Brillouin zone. Nodes are located along the Brillouin zone diagonals. The different designation is only due to a rotation of the coordinate axes by 45°. (d) d$_{x^2-y^2}$ order parameter in the physical Brillouin zone. (e) d$_{xy}$ order parameter in the unfolded Brillouin zone. Figure taken from Ref. [126].

that, e.g., different d-wave order parameters exchange their designation when going from one to the other Brillouin zone (see Fig. 6.2). Thus, the same physical order parameter which has d_{xy}-symmetry in the realistic four molecule/two dimer unit cell [Fig. 6.2(b)] has $d_{x^2-y^2}$-symmetry in the model one dimer/one band unit cell [Fig. 6.2(c)]. In our study, we always work in the physical unit cell containing two dimers [Fig. 6.2(b) and (d)]. We refer to the small backfolded part of the Fermi surface close to the Brillouin zone boundary as the *elliptic* part of the Fermi surface, while we call those sheets running almost parallel to the k_y-direction *quasi-1D*.

An overview of unit cell and hopping paths for molecule and dimer model is shown in Fig. 6.1. Now we list the kinetic part of the Hamiltonian for the dimer model in one- and two-band representation, and for the four-band molecule model. We denote the unit cell parameters in x- and y-direction as a and b respectively. The multi-band Hamiltonians are given as matrix elements $\langle i|H_{\mathrm{hop}}|j\rangle$, where states $|i\rangle$ denote the orbitals living on a dimer/molecule with site index i. Only unique matrix elements are listed. The rest of the elements are generated by using $\langle i|H_{\mathrm{hop}}|j\rangle = \langle j|H_{\mathrm{hop}}|i\rangle^*$. In all models there is only one orbital per lattice site. The single-band representation of the dimer model is given by:

$$H_{\mathrm{hop}}(\mathbf{k}) = 2t\left[\cos(k_x a) + \cos(k_y b)\right] + 2t'\left[\cos(k_x a)\cos(k_y b) - \sin(k_x a)\sin(k_y b)\right] \tag{6.1}$$

The two-band representation of the dimer model can be written as:

$$\langle 0|H_{\mathrm{hop}}|0\rangle = \langle 1|H_{\mathrm{hop}}|1\rangle = 2t'\cos(k_x a) \tag{6.2}$$

$$\langle 0|H_{\mathrm{hop}}|1\rangle = 2t\left(1 + e^{ik_x a} + e^{ik_y b} + e^{ik_x a}e^{ik_y b}\right) \tag{6.3}$$

The four-band molecule model is given by:

$$\langle 0|H_{\mathrm{hop}}|1\rangle = t_1 + t_3\, e^{ik_x a} \tag{6.4}$$

$$\langle 0|H_{\mathrm{hop}}|2\rangle = t_4\left(1 + e^{-ik_y b}\right) \tag{6.5}$$

$$\langle 0|H_{\mathrm{hop}}|3\rangle = t_2\left(1 + e^{-ik_x a}\right) \tag{6.6}$$

$$\langle 1|H_{\mathrm{hop}}|2\rangle = t_2\, e^{-ik_y b}\left(1 + e^{-ik_x a}\right) \tag{6.7}$$

$$\langle 1|H_{\mathrm{hop}}|3\rangle = t_4\, e^{-ik_x a}\left(1 + e^{-ik_y b}\right) \tag{6.8}$$

$$\langle 2|H_{\mathrm{hop}}|3\rangle = t_1 + t_3\, e^{-ik_x a} \tag{6.9}$$

To obtain the correct electron filling, one has to introduce a chemical potential μ, so that $H_0 = H_{\mathrm{hop}} - \mu \sum_{i\sigma} c^\dagger_{i\sigma} c_{i\sigma}$ is 1/2-filled for the dimer model in either representation and 3/4-filled for the molecule model.

6.1.2 RPA spin-fluctuation calculations

In κ-(ET)$_2X$ materials there is strong evidence for antiferromagnetic spin-fluctuations [133]. Therefore, we investigate the superconducting state of these materials based on the RPA spin-fluctuation approach in the singlet channel. Compared to the FLEX approximation used in Ref. [125], our RPA method uses only states at the Fermi level and neglects the electronic self-energy correction. While this approximation prevents us from making quantitative statements about the superconducting transition temperature T_c, it reduces significantly the numerical cost compared to FLEX, so that we can calculate the momentum structure of the superconducting order parameter for numerous input parameter sets and with high angular resolution. Competing magnetically ordered or paramagnetic Mott insulating states are not investigated in our study. Furthermore, we do not investigate possible time-reversal symmetry-breaking superconducting states or spin-triplet pairing.

The kinetic Hamiltonians discussed before (see Eqs. 6.1 to 6.9) are used in a multi-site single-orbital Hubbard model in analogy to Eq. 1.5.

$$\begin{aligned} H =& H_0 + H_{\mathrm{int}} \\ =& \sum_{ij\sigma} t_{ij}(c^\dagger_{i\sigma} c_{j\sigma} + h.c.) + \frac{U}{2}\sum_{i\sigma} n_{i\sigma} n_{i\bar{\sigma}} \end{aligned} \tag{6.10}$$

Here, σ represents the spin and $n_{i\sigma} = c^{\dagger}_{i\sigma} c_{i\sigma}$. The sum over i runs over all ET sites in the unit cell. The interaction strength U is treated as a parameter. Note that the Coulomb repulsion on a dimer and the Coulomb repulsion on a molecule are not identical. Especially the role of intermolecular Coulomb repulsion in κ-(ET)$_2X$ materials is currently unclear. The investigation of interaction terms beyond on-site repulsion is an important topic of future research.

The calculation of susceptibility and two-particle vertex follows the presentation in Chapter 4. However, since the interaction term defined in Eq. 6.10 is local and we have only one orbital per lattice site, we can restrict the calculation to the diagonal elements of the multi-orbital susceptibility tensor and use scalar equations for the RPA-enhanced susceptibilities.

$$\chi_L^{s,\mathrm{RPA}}(\mathbf{q}) = \frac{\chi_L^0(\mathbf{q})}{1 - U\chi_L^0(\mathbf{q})} \tag{6.11}$$

$$\chi_L^{c,\mathrm{RPA}}(\mathbf{q}) = \frac{\chi_L^0(\mathbf{q})}{1 + U\chi_L^0(\mathbf{q})} \tag{6.12}$$

Here, χ_L with $L = \{llll\}$ denotes the diagonal element of the susceptibility tensor associated with an ET site indexed by l. Note that this formulation allows us to treat multiple inequivalent ET sites in the unit cell, keeping the individual $\mathbf{q}$-dependence of their associated susceptibilities. Therefore, the symmetry of the susceptibility follows the symmetry of the ET layer in the crystallographic unit cell, which is important for checking the simplified four-parameter model against *ab initio* Hamiltonians, which can have monoclinic, as, e.g., in κ-(ET)$_2$Cu(NCS)$_2$, or even triclinic symmetry, as in κ-α_1'-(ET)$_2$Ag(CF$_3$)$_4$(TCE).

The total spin susceptibility is given by the sum over all site-resolved contributions.

$$\chi^s(\mathbf{q}) = \frac{1}{2}\sum_L \chi_L^{s,\mathrm{RPA}}(\mathbf{q}) \tag{6.13}$$

All other equations are used exactly as presented in Chapter 4. For the numerical calculations we evaluated the susceptibility $\chi^0(\mathbf{q})$ using 50×50 point grids for $\mathbf{q}$ and the integrated-out variable $\mathbf{k}$ (see Eq. 4.22). The inverse temperature in the susceptibility calculation is fixed to $\beta = 160/t_1$ for the molecule model and $\beta = 60/t$ for the dimer model. These values result in about the same effective temperature. For the models considered here about 250 points on the Fermi surface yield sufficient resolution. The intra-orbital Coulomb repulsion parameter U is chosen in all calculations so that the leading eigenvalue in the effective eigenvalue equation for the two-particle pairing vertex (Eq. 4.138) is $\lambda = 0.99 \pm 0.001$. For most combinations of input parameters this leads to a clear separation of the leading and the first subleading eigenvalue. The pairing symmetries corresponding to the leading and sub-leading eigenvalues do not change as a function of U.

6.1.3 Simulation of tunneling spectra in the superconducting state

The central quantity measured in scanning tunneling spectroscopy (STS) experiments on superconductors is the local density of states (DOS) in the superconducting phase. We start from the standard Bardeen-Cooper-Schrieffer (BCS) theory for isotropic s-wave superconductors. A simple approximate extension allows us to treat realistic Fermi surfaces and unconventional pairing symmetries derived from *ab initio* calculations combined with RPA spin-fluctuation theory as presented before. Coauthor Michaela Altmeyer contributed significantly to the development of the formalism presented in this subsection.

To derive an approximation for the DOS of a superconductor, we start with the Hamiltonian for Cooper pairs with vanishing total momentum [6].

$$H = \sum_{\mathbf{k},\sigma} \epsilon_{\mathbf{k}\sigma} c^\dagger_{\mathbf{k}\sigma} c_{\mathbf{k}\sigma} + \sum_{\mathbf{k},\mathbf{k}'} U(\mathbf{k},\mathbf{k}') c^\dagger_{\mathbf{k}\uparrow} c^\dagger_{-\mathbf{k}\downarrow} c_{-\mathbf{k}'\downarrow} c_{\mathbf{k}'\uparrow} \tag{6.14}$$

The interaction can be treated in mean field theory ($\delta(c^\dagger c^\dagger) = c^\dagger c^\dagger - \langle c^\dagger c^\dagger \rangle$), where terms quadratic in δ are neglected. The resulting Hamiltonian is diagonalized using the Bogoliubov-Valatin transformation, which introduces quasiparticle creation and annihilation operators $\gamma^\dagger_{\mathbf{k}\sigma}$ and $\gamma_{\mathbf{k}\sigma}$. The quasiparticle excitation energies are given as

$$E_{\mathbf{k}} = \sqrt{\epsilon^2_{\mathbf{k}} + |\Delta_{\mathbf{k}}|^2}, \tag{6.15}$$

where

$$\Delta_{\mathbf{k}} = \Delta(\mathbf{k}) = \sum_{\mathbf{k}'} U(\mathbf{k},\mathbf{k}') \langle c_{-\mathbf{k}'\downarrow} c_{\mathbf{k}'\uparrow} \rangle. \tag{6.16}$$

The BCS Hamiltonian can be rewritten in terms of the quasiparticle creation and annihilation operators.

$$H_{\mathrm{BCS}} = \sum_{\mathbf{k},\sigma} E_{\mathbf{k}} \gamma^\dagger_{\mathbf{k}\sigma} \gamma_{\mathbf{k}\sigma} + \sum_{\mathbf{k}} \epsilon_{\mathbf{k}} - \sum_{\mathbf{k},\mathbf{k}'} U(\mathbf{k},\mathbf{k}') \langle c^\dagger_{\mathbf{k}\uparrow} c^\dagger_{-\mathbf{k}\downarrow} \rangle \langle c_{-\mathbf{k}'\downarrow} c_{\mathbf{k}'\uparrow} \rangle \tag{6.17}$$

The excitation spectrum of the quasiparticles $E_{\mathbf{k}}$ is gapped and defined only for positive energies. The density of states of quasiparticles in an isotropic s-wave superconductor can be calculated from the normal state density of states $\rho(\epsilon)$ and the constant superconducting gap $\Delta_{\mathbf{k}} = \Delta$.

$$\rho_{\mathrm{qp}}(E) = \frac{1}{N} \sum_{\mathbf{k}} \delta(E - E_{\mathbf{k}}) \tag{6.18}$$

$$= \int d\epsilon\, \rho_0(\epsilon) \frac{\sqrt{\epsilon^2 + |\Delta|^2}}{\epsilon} \delta(\epsilon - \sqrt{E^2 - |\Delta|^2}) \tag{6.19}$$

$$= \begin{cases} \rho_0(\sqrt{E^2 - |\Delta|^2}) \frac{E}{\sqrt{E^2 - |\Delta|^2}} & E > |\Delta| \\ 0 & E < |\Delta| \end{cases} \tag{6.20}$$

The previous derivation assumed an isotropic gap and an energy dispersion of free electrons to identify the normal state DOS ρ_0. For realistic electronic structure and anisotropic gap Δ_k this factorization of contributions is not easily possible due to the non-trivial momentum dependence of both functions:

$$\rho_{\text{qp}}(E) = \int d\epsilon \frac{1}{N} \sum_{\mathbf{k}} \delta(\epsilon - \epsilon_{\mathbf{k}}) \delta(|E| - \sqrt{\epsilon^2 + |\Delta_{\mathbf{k}}|^2}) \tag{6.21}$$

$$\neq \int d\epsilon \, \rho_N(\epsilon) \, \delta(|E| - \sqrt{\epsilon^2 + |\Delta_{\mathbf{k}}|^2}) \tag{6.22}$$

However, in a widely used ansatz [134, 135] the electrons with effective mass m^* are considered to be free, i.e. the Fermi surface is approximated by a concentric circle, and the gap only depends on the angle θ.

$$\rho_{\text{qp}}(E) \approx \frac{1}{(2\pi)^2} m^* \text{Re} \int d\theta \frac{|E|}{\sqrt{E^2 - |\Delta(\theta)|^2}} \tag{6.23}$$

We introduce in this expression a finite quasiparticle lifetime [136] by adding an imaginary part Γ to the quasiparticle excitation energies. This allows us to carry out calculations with finite angular resolution and facilitates comparison to experiment. Furthermore, we improve upon the circular integration by replacing it with a summation over the discretized realistic Fermi surface and drop the irrelevant prefactors to obtain the final expression for the quasiparticle DOS in our study:

$$\rho_{\text{qp}}(E) \propto \sum_{\mathbf{k}} \text{Re} \frac{|E + i\Gamma|}{\sqrt{(E + i\Gamma)^2 - \Delta(\mathbf{k})^2}} \tag{6.24}$$

In this form, the connection to the *ab initio* and RPA spin-fluctuation calculations is easily obtained: the vectors $\mathbf{k}$ in Eq. 6.24 all lie on the Fermi surface determined from the *ab initio* derived tight-binding model and the gap $\Delta(\mathbf{k})$ on the Fermi surface can be substituted by the symmetry function $g_i(\mathbf{k})$ extracted from RPA (see Eq. 4.138). Note that the overall energy scale of the superconducting gap is not included in $g_i(\mathbf{k})$ because our formalism neglects the electronic self-energy and lacks a self-consistency condition.

We checked that our approximation agrees well with a direct calculation of the quasiparticle spectrum based on Eq. 6.17, which is numerically several orders of magnitude more costly. For this purpose we used one of our results for the gap-symmetry of κ-(ET)$_2$Cu[N(CN)$_2$]Br and calculated the quasiparticle DOS from Eq. 6.24 using a small broadening of $\Gamma = 0.07$ meV and the electron DOS from Eq. 6.17 employing a tetrahedron integration method [137] on a $4000 \times 4000 \times 2$ point grid for the momentum $\mathbf{k}$. In the latter case we inserted the microscopically calculated gap symmetry according to Eq. 6.16.

The comparison of results is shown in Fig. 6.3. Peak positions are identical. Only the background far away from the Fermi level is not well represented by the quasiparticle approximation. This, however, must be the case, since the quasiparticle formalism neglects the electronic bandstructure, which is fully taken into account in a calculation based directly on Eq. 6.17.

The quasiparticle DOS $\rho_{\text{qp}}(E)$ corresponds to the local density of states (LDOS) measured in STS experiments. In order to achieve a direct comparison to the experimental

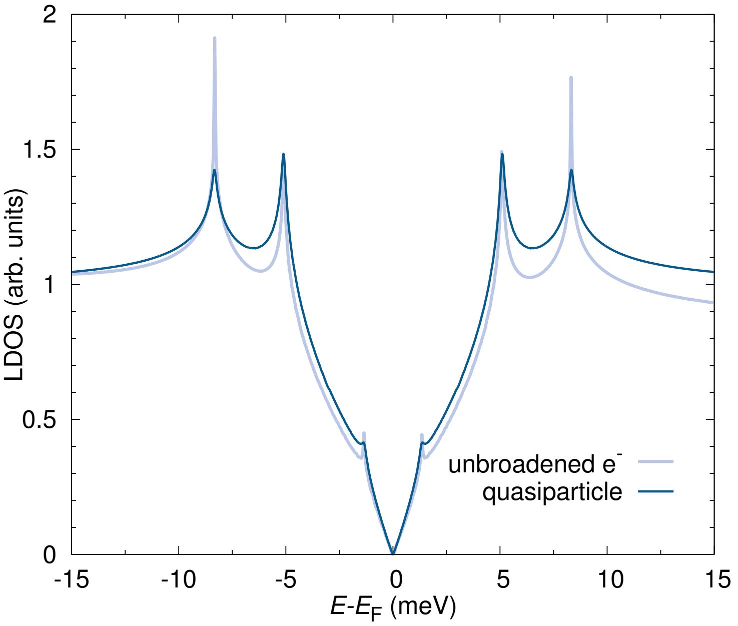

Figure 6.3: Comparison of unbroadened electron DOS and broadened ($\Gamma = 0.07$ meV) quasiparticle DOS for identical gap symmetry and magnitude.

results provided by the group of Hans-Joachim Elmers [44], we also have to take into account thermal broadening via the Fermi function and a scaling variable x that cancels the effect of parasitic conduction paths. Using the variable V for the bias voltage in the STS experiment, we have the following relation for the experimentally measured spectrum:

$$S(V) \propto \int_{-\infty}^{\infty} dE\ [\rho_{qp}(E)(1-x)+x]\,\frac{-df(E+eV)}{dV} \tag{6.25}$$

The experimental data also had to be corrected for effects such as electronic disorder [49, 118] via the density of states of the Anderson-Hubbard model [138]. Since the idea of how to apply the results for the Anderson-Hubbard model to our experimental situation were already developed by our experimental coauthors, we refer the reader to Ref. [49] and the supplemental information of Ref. [44] for further details.

6.2 Results and discussion

6.2.1 Ab initio calculations

Using DFT calculations and subsequent Wannier downfolding we determine the parameter sets (t_1,t_2,t_3,t_4) corresponding to superconducting κ-(ET)$_2X$ materials with anions $X \in \{$Ag(CF$_3$)$_4$(TCE), I$_3$, Ag(CN)$_2$·H$_2$O, Cu(NCS)$_2$, Cu[N(CN)$_2$](CN), Cu[N(CN)$_2$]Br$\}$, as well as polymorphs κ-α_1'-(ET)$_2$Ag(CF$_3$)$_4$(TCE) and κ-α_2'-(ET)$_2$Ag(CF$_3$)$_4$(TCE), that also contain charge-ordered insulating α'-type layers. The calculated parameters are listed

i	material	T_c in K	t_1	t_2	t_3	t_4	t_2/t_1	t_3/t_1	t_4/t_1	t_4/t_2
1	κ-$(\mathrm{ET})_2\mathrm{Ag}(\mathrm{CF}_3)_4(\mathrm{TCE})$	2.6	168	102	60.8	33.4	0.610	0.362	0.199	0.362
2	κ-$(\mathrm{ET})_2\mathrm{I}_3$	3.6	180	119	52.2	31.7	0.661	0.289	0.176	0.266
3	κ-$(\mathrm{ET})_2\mathrm{Ag}(\mathrm{CN})_2\cdot\mathrm{H}_2\mathrm{O}$	5.0	185	104	60.4	23.6	0.567	0.326	0.173	0.305
4	κ-α_1'-$(\mathrm{ET})_2\mathrm{Ag}(\mathrm{CF}_3)_4(\mathrm{TCE})$	9.5	166	97.6	65.8	35.3	0.588	0.396	0.213	0.362
5	κ-$(\mathrm{ET})_2\mathrm{Cu}(\mathrm{NCS})_2$	10.4	190	102	82.4	17.5	0.538	0.387	0.092	0.171
6	κ-α_2'-$(\mathrm{ET})_2\mathrm{Ag}(\mathrm{CF}_3)_4(\mathrm{TCE})$	11.1	165	98.4	66.7	36.3	0.596	0.404	0.220	0.369
7	κ-$(\mathrm{ET})_2\mathrm{Cu}[\mathrm{N}(\mathrm{CN})_2](\mathrm{CN})$	11.2	175	100	78.5	17.3	0.574	0.344	0.099	0.172
8	κ-$(\mathrm{ET})_2\mathrm{Cu}[\mathrm{N}(\mathrm{CN})_2]\mathrm{Br}$	11.6	177	95.6	60.0	36.2	0.541	0.339	0.205	0.379

Table 6.1: Values of the molecule model parameters (t_1,t_2,t_3,t_4), also commonly denoted as (b_1,p,b_2,q), for selected superconducting κ-$(\mathrm{ET})_2X$ materials. All values are given in meV. Hopping integrals for the $(\mathrm{ET})_2\mathrm{Ag}(\mathrm{CF}_3)_4(\mathrm{TCE})$ family are averages of the parameters given in Ref. [131], where we used the same method and settings to calculate the parameters as in the present study. Crystal structures for these materials were taken from Refs. [128, 129]. All other crystal structures are taken from Ref. [127]. The values for T_c are taken from Refs. [127, 139–141]. Table taken from Ref. [126].

in Table 6.1. In the case of $(\mathrm{ET})_2\mathrm{Ag}(\mathrm{CF}_3)_4(\mathrm{TCE})$ polymorphs (TCE abbreviates 1,1,2-trichloroethane) we rely on a previous *ab initio* calculation with identical setup [131]. The small asymmetry of hoppings due to the lowered symmetry in these materials is averaged out to obtain a four-parameter model. For the original models, see Ref. [131].

We observe that all materials fall into a narrow region of parameters: $t_1 \in [165,190]$ meV, $t_2 \in [95.6,119]$ meV, $t_3 \in [52.2,82.4]$ meV and $t_4 \in [17.3,36.3]$ meV. Normalizing t_2, t_3 and t_4 with respect to t_1, this means all materials lie in the range $t_2/t_1 \in [0.538,0.661]$, $t_3/t_1 \in [0.289,0.404]$ and $t_4/t_1 \in [0.099,0.220]$. Note the pronounced anisotropy between t_2 and t_4. These intervals of t_2/t_1, t_3/t_1 and t_4/t_1 obtained from the *ab initio* calculations determine the parameter ranges for our following model investigation.

We sorted the materials according to their superconducting transition temperature T_c, but we found no correlation of T_c with either t_1, t_2, t_3 or t_4. The ratios t_2/t_1, t_3/t_1 or t_4/t_1 are also not obviously connected to T_c.

6.2.2 Pairing symmetry in the dimer model

First, we apply the RPA spin-fluctuation formalism to the dimer model in the range $t'/t \in [0,1]$. We evaluate the superconducting order parameter in fine steps of t'/t and compare the leading eigenfunctions. In all cases we find that a d_{xy} state is the leading pairing symmetry.

Relating the dimer model back to the one-band model explained in the methods section, the d_{xy} state we find is identical to the $d_{x^2-y^2}$ state of the square lattice Hubbard model after unfolding the Brillouin zone (see Fig. 6.2). Typical superconducting κ-$(\mathrm{ET})_2X$ materials lie in the region $t'/t \lesssim 0.65$ [118, 124, 143], where a d_{xy}-solution is to be expected, as the dimer model is basically a square lattice of hoppings t, perturbed by the additional diagonal coupling t'. The diagonal coupling t' breaks the C_4-symmetry of the underlying square lattice and gives the Fermi surface its elliptic shape, but the dominant terms in the Hamiltonian remain square lattice-like. For a full account of possible pairing symmetries in the one-band Hubbard model on the square lattice, see Ref. [142].

An early theoretical study of the antiferromagnetic phase of κ-type materials concluded that the two molecules within a dimer carry the same spin and that the spins are flipped between neighboring dimers [18], giving rise to (π, π) magnetic order as in the parent compounds of high-temperature cuprate superconductors [7]. This result is consistent with our observation that a dimerized model gives a d_{xy} order parameter in the physical Brillouin zone, which becomes a $d_{x^2-y^2}$-symmetry in the unfolded zone of the one-band model (see Fig. 6.2), again emphasizing the deep connection between cuprates and quasi-two-dimensional organic superconductors.

We would also like to note that the authors of Ref. [43], referring to the physical Brillouin zone, invoked a d_{xy} superconducting symmetry close to insulating patches and a $d_{x^2-y^2}$ state in the bulk to explain the findings of their STS study on deuterated κ-(ET)$_2$Cu[N(CN)$_2$]Br. As the antiferromagnetic insulating state is dimerized (see Ref. [18]), the dimer approximation naturally applies and gives a d_{xy} order parameter in accordance with the experimental observation. What remains to be answered in an approach beyond the dimer model, as presented in the next sections, is why the superconducting order parameter of the bulk is $d_{x^2-y^2}$.

6.2.3 Pairing symmetry in the molecule model

The obvious step for going beyond the dimer model is to use the original crystal lattice, i.e. the molecule model explained before (see Fig. 6.1). In order to compare the results of the molecule model to those of the dimer model we do the following consideration: via the geometric formulas (Eqs. 5.1 and 5.2) the four-parameter molecule model is mapped onto a two-parameter dimer model. With this procedure we are left with two adjustable parameters in the molecule model whose variation discloses important features of the systems, not captured in the resulting dimer model which remains unchanged. These adjustable parameters are: the degree of dimerization $t_1/\max(t_2, t_3, t_4)$ and the in-plane anisotropy t_4/t_2.

The degree of dimerization obviously decides whether the dimer approximation applies to a material or not. Its influence on the superconducting pairing was quantified by Kuroki *et al.*, who found a transition to a $d_{x^2-y^2}$ state in the physical Brillouin zone at low dimerization (see Ref. [125]).

Less obvious is how this $d_{x^2-y^2}$ state emerges from the underlying hopping structure and how important the anisotropy between t_2 and t_4 is for the pairing state. To investigate these issues, we construct a series of molecule models with fixed value of $t_3/t_1 = 0.333$ and vary the ratio t_4/t_2 in the range [0,1] (for the values realized in real materials see Table 6.1). We fix the sum of t_2 and t_4 so that the molecule models correspond to the same dimer model $t_3/(t_2 + t_4) = t'/t = 0.6$. The maximum value of t_2 is, therefore, $t_2^{\max} = 0.556$ and its minumum value is $t_2^{\min} = 0.278$. As t_4 is increased, the in-plane anisotropy decreases and the dimerization defined as $t_1/\max(t_2, t_3, t_4)$ increases.

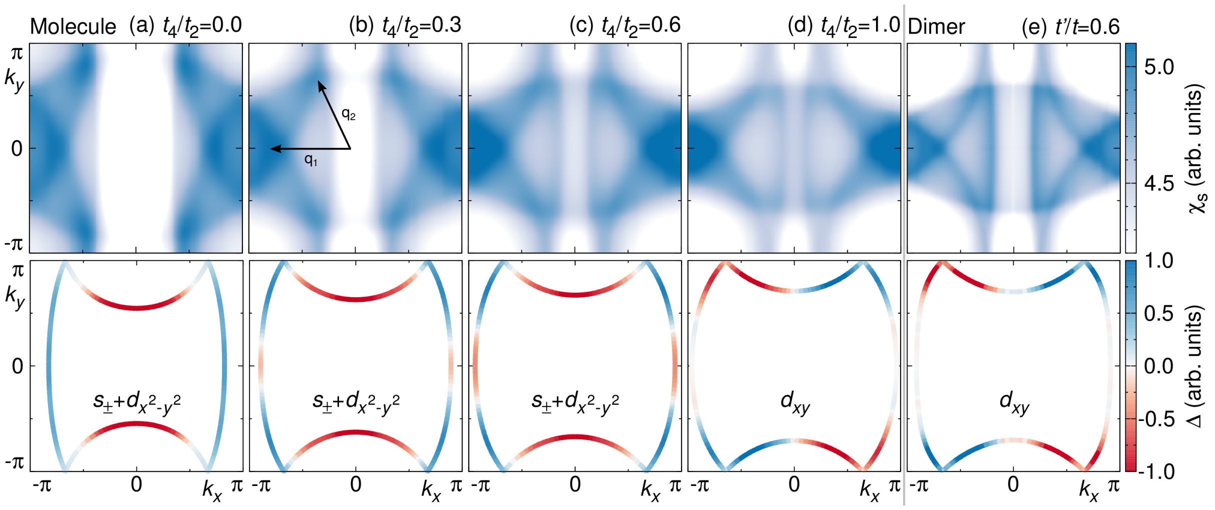

Figure 6.4: Comparison of molecule models (a)-(d) with different ratios of t_4/t_2, which all correspond to the same dimer model (e) with $t'/t = 0.6$. The top panel shows the spin susceptibilities, where arrows $\mathbf{q}_1$ and $\mathbf{q}_2$ indicate the main features, while the bottom panel shows the leading eigenfunction of the superconducting gap equation on the Fermi surface. In the molecule models $t_3/t_1 = 0.333$ is fixed, while the ratio of t_4/t_2 is varied under the condition $t_3/(t_2 + t_4) = t'/t = 0.6$. Figure taken from Ref. [126].

In Fig. 6.4 we show the spin susceptibilities and leading pairing symmetries in the molecule model as a function of t_4/t_2 compared to the associated dimer model. In the isotropic limit $t_4/t_2 = 1$ we find a d_{xy}-symmetric state, similar to the one found in the dimer model [compare Fig. 6.4(d) and Fig. 6.4(e)]. Upon lowering t_4/t_2 the maxima of the superconducting gap shift towards the position where the nodes in a d_{xy}-symmetric state are and additional nodes appear on the quasi-1D part of the Fermi surface close to $(\pm\pi, 0)$. As this shift is equivalent to a rotation by 45 degrees, the state with eight nodes can be expected to have a significant $d_{x^2-y^2}$ contribution. In the limit of $t_4 \ll t_2$ the additional set of nodes on the quasi-1D part of the Fermi surface vanishes [see Fig. 6.4(a)]. The remaining four nodes are situated close to the Brillouin zone boundary, where the smaller elliptic part of the Fermi surface is folded back. The details of the pairing symmetry are discussed further below. In what follows we investigate the origin of the gap maxima shifts.

As an example we show in Fig. 6.5 how extrema of the gap magnitude with opposite sign appear where parts of the Fermi surface can be connected by a wave-vector $\mathbf{q}$ that shows a peak in the spin susceptibility. Note that in Fig. 6.5 the Brillouin zone is shifted by a vector (π, π), because the relevant vectors $\mathbf{q}$ connect pieces of the Fermi surface across the boundaries of the Brillouin zone used in Fig. 6.4.

Now we come back to the discussion of the results presented in Fig. 6.4. At $t_4/t_2 = 0$ peaks appear at $\mathbf{q}_1 \approx (\pm 0.7\pi, 0)$ and $\mathbf{q}_2 \approx (\pm\pi/2, \pm\pi)$, the dominant contribution to the spin susceptibility being the peak at $\mathbf{q}_2$. As t_4/t_2 is increased, the position of $\mathbf{q}_1$ remains about the same, while $\mathbf{q}_2$ shifts towards $(\pm\pi/4, \pm\pi/2)$ and decreases in intensity.

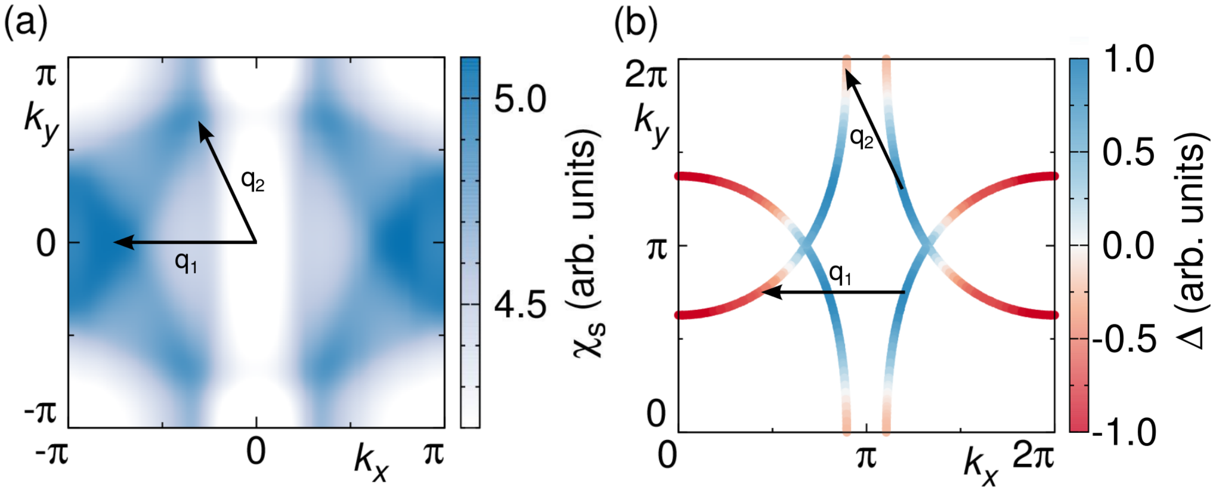

Figure 6.5: (a) Spin susceptibility of the molecule model at $t_2/t_1 = 0.417$, $t_3/t_1 = 0.333$ and $t_4/t_1 = 0.139$ with arrows $\mathbf{q}_1$ and $\mathbf{q}_2$ indicating the main features. The data shown are the same as in Fig. 6.4(b). (b) Superconducting gap function on the Fermi surface for the same parameter values as in (a). Vectors $\mathbf{q}_1$ and $\mathbf{q}_2$ are the same as in (a) and connect parts of the Fermi surface with different signs of the gap. Note that the plot range of the Brillouin zone is shifted by a vector (π, π) compared to Fig. 6.4. Figure taken from Ref. [126].

At $t_4/t_2 = 1$, the peak at $\mathbf{q}_1$ becomes the dominant contribution to the spin susceptibility. Since we do not work in the limit of infinite dimerization, even the case $t_4/t_2 = 1$ does not reproduce the dimer model spin susceptibility exactly. The similarities are, however, apparent.

These peak shifts in the spin susceptibility are reflected in the pairing symmetry: the gap maxima of different sign in the d_{xy}-symmetry are separated by a wave-vector $\mathbf{q}_1$, while $\mathbf{q}_2$ is responsible for the sign change between the upper and lower half of the elliptic Fermi surface. Furthermore, $\mathbf{q}_2$ enforces an enlarged nodal region close to $(\pm\pi, 0)$, since it would otherwise connect parts of the Fermi surface with the same sign of the gap. In the intermediate region of t_4/t_2, $\mathbf{q}_2$ connects the 1D parts of the Fermi surface, where it induces an additional set of nodes. The large gap on the elliptic part of the Fermi surface is connected to the 1D sheets by $\mathbf{q}_1$. The shift of the vertical lines in the susceptibility, which widen towards $k_x \approx \pm\pi/2$, merely reflect the changing shape of the Fermi surface. For $t_4 \ll t_2$ the additional set of nodes on the 1D sheets vanishes, because they are no longer connected by $\mathbf{q}_2$, which now points from 1D sheet to the elliptic parts just like q_1. This consideration shows that the pairing symmetry transition in the molecule model is driven by a peculiar competition between $\mathbf{q}_1$ and $\mathbf{q}_2$ nesting vectors.

Now we connect the structure of the susceptibility and the superconducting pairing to the underlying lattice model. The feature at $\mathbf{q}_1$ is obviously connected to the t_3 hopping parameter, since it is the only hopping exclusively in x-direction (see Fig. 6.6). All other t-parameters can only be responsible for a four-peak structure, as they occur pointing along

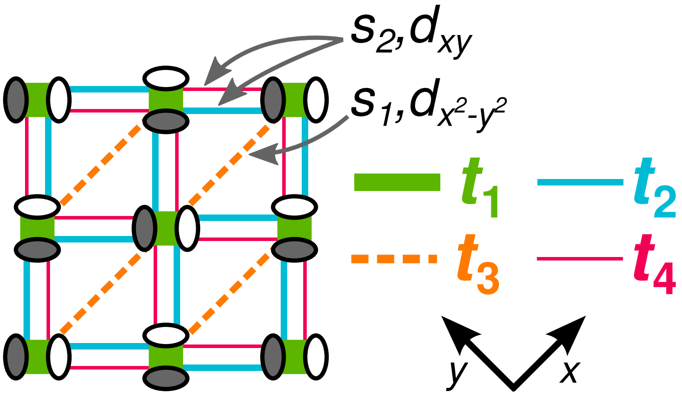

Figure 6.6: Hopping structure in the molecule model for the κ-(ET)$_2^+$ layer. The dark grey arrows indicate the connection between hopping parameters and the symmetry functions appearing in the solution of the superconducting gap equation. Figure taken from Ref. [126].

both diagonals of the physical unit cell. The influence of the competition between t_2, t_3 and t_4 on the feature at $\mathbf{q}_2$ is, however, hard to quantify directly. Therefore, we decompose the superconducting order parameter in terms of extended s- and d-wave basis functions f_i appropriate for a square lattice geometry. For each of the d-wave basis functions, we also take into account the associated extended s-wave function, because we expect that a significant extended s-wave component could mix with the d-wave states to accomodate the orthorhombicity of the model:

$$\begin{aligned} f_{s_1}(\mathbf{k}) &= \cos k_x + \cos k_y \\ f_{d_{x^2-y^2}}(\mathbf{k}) &= \cos k_x - \cos k_y \\ f_{s_2}(\mathbf{k}) &= \cos k_x \cdot \cos k_y \\ f_{d_{xy}}(\mathbf{k}) &= \sin k_x \cdot \sin k_y \end{aligned} \tag{6.26}$$

Rotated into the Brillouin zone of κ-type materials, gap functions $f_{d_{xy}}$ and f_{s_2} are to be expected from antiferromagnetic exchange along square-like bonds (t_2, t_4), while f_{s_1} and $f_{d_{x^2-y^2}}$ correspond to exchange paths along diagonal bonds (t_3), see Fig. 6.6.

Following an idea of coauthor Harald O. Jeschke, we fit the pairing symmetries calculated from RPA to a linear combination of the previously defined pairing symmetries and determine their relative contributions c_i.

$$\tilde{g}(\mathbf{k}) = c_{s_1} f_{s_1} + c_{d_{x^2-y^2}} f_{d_{x^2-y^2}} + c_{s_2} f_{s_2} + c_{d_{xy}} f_{d_{xy}} \tag{6.27}$$

For the d_{xy} state we find $c_{d_{xy}} = 1$ and all other contributions zero, i.e. except for the not well reproduced extended nodal region close to $(\pm\pi, 0)$ the dimer model and the molecule model at $t_4/t_2 \lesssim 1$ are dominated by the square-lattice physics of t or t_2, t_4 respectively. For the $d_{x^2-y^2}$-like solution at $t_4 \ll t_2$ we find negligible contributions from f_{s_1} and $f_{d_{xy}}$, dominant f_{s_2} and sub-dominant $f_{d_{x^2-y^2}}$. For increasing t_4/t_2 the ratio of coefficients $c_{d_{x^2-y^2}}/c_{s_2}$ decreases, i.e. the square-lattice physics becomes dominant when the asymmetry between

t_2 and t_4 is removed. Using the symmetry functions f_i, all details of the superconducting gap in the $d_{x^2-y^2}$-like state including the additional nodes can be reproduced by Eq. 6.27.

Our findings provide a clear picture of the pairing competition in the molecule model: in the realistic region of parameters, where the dimerization measured by $t_1/\max(t_2, t_3, t_4)$ and the anisotropy of t_2 and t_4 are finite, the competition of square-like (t_2, t_4) and diagonal (t_3) hopping realizes a unique linear combination of functions $f_{d_{x^2-y^2}}$ and f_{s_2} as the leading pairing symmetry. We refer to this linear combination as $s_\pm + d_{x^2-y^2}$, or extended $s + d_{x^2-y^2}$. The s-wave contribution is equivalent to the $s_\pm$ pairing state believed to be realized in iron-based superconductors (see e.g. Ref. [54]) and has been overlooked entirely in the literature on quasi-two-dimensional organic charge transfer salts. When the lattice becomes more square-like ($t_4 \lesssim t_2$), i.e. the molecule model approaches the dimer limit, the d_{xy}-symmetry known from the dimer model takes over. In other words, in the context of realistic modelling of κ-type materials, the d_{xy} symmetry found in the dimer model ($d_{x^2-y^2}$ in the unfolded one-band model) is mostly an artifact of the underlying approximation to the real lattice structure (Eqs. 5.1 and 5.2).

Finally, we checked our results obtained with the four parameter molecule model against the original hopping structure obtained from projective Wannier functions, which includes longer range processes. As expected, the differences induced by the distance cutoff and parameter averaging are negligible.

6.2.4 Pairing symmetry phase diagram of the molecule model

To complete our study of the pairing symmetry competition, we investigated the leading pairing symmetry of the molecule model as a function of t_2/t_1, t_3/t_1 and t_4/t_1 in the range of parameters realized in actual superconducting κ-type materials.

In Fig. 6.7 we show the obtained phase diagram, which consists of a d_{xy}-symmetric phase at low t_2/t_1 and t_3/t_1, while the rest of the phase diagram shows a $s_\pm + d_{x^2-y^2}$ state. The consecutively numbered symbols in Fig. 6.7 correspond to the position of real materials as listed in Table 6.1 within this phase diagram. As we scanned the phase diagram several times for different fixed t_4/t_1, materials were sorted into the cut with the closest value of t_4/t_1.

At low t_2/t_1 the phase boundary is almost horizontal, i.e. independent of the precise value of t_2/t_1. For larger values of t_2/t_1 the model becomes more asymmetric with respect to t_2 and t_4 and a smaller diagonal coupling t_3 is sufficient to drive the system into the $s_\pm + d_{x^2-y^2}$ state. The size of the d_{xy}-symmetric region is obviously determined by the value of t_4/t_1 as explained in the previous section.

In the numerical calculations we observed that the leading two pairing symmetries are almost degenerate in a broad parameter region. This is to be expected, because the $s_\pm + d_{x^2-y^2}$ state emerges precisely as a compromise between two different nesting vectors, of which one rather fits to a pure d_{xy}-symmetry. To clarify this degeneracy, we calculated the eigenvalues of the leading and sub-leading solutions of the gap equation at fixed t_2/t_1 and t_3/t_1 and varied t_4/t_2 in the range [0,1]. Fig. 6.8 shows the eigenvalues of both possible pairing states as a function of the in-plane anisotropy t_4/t_2. We observe a pronounced asymmetry: While the d_{xy} state is competitive even for low values of t_4/t_2, the $s_\pm + d_{x^2-y^2}$

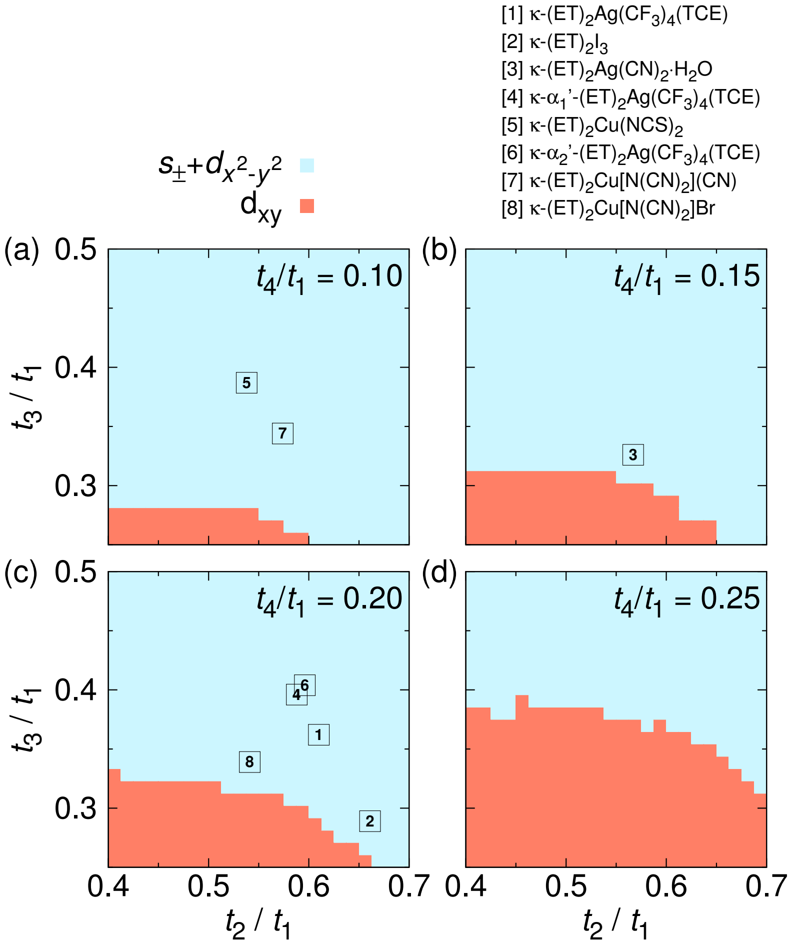

Figure 6.7: Superconducting phase diagram of the individual molecule model. Different symmetries of the superconducting order parameter are color coded. A d_{xy} symmetry of the pairing interaction is favored when the orthorhombicity of the system is small, i.e. when $t_4 \lesssim t_2$ and $t_3 \ll t_2$. In the rest of the phase diagram an extended $s + d_{x^2-y^2}$ symmetry prevails. The numbered symbols correspond to the location of real materials in the phase diagram, enumerated as in Table 6.1. Materials were sorted into the subplot to which their true value of t_4/t_1 is closest. Figure taken from Ref. [126].

state quickly becomes irrelevant when approaching the isotropic case ($t_4/t_2 = 1$).

Finally, based on our parameter estimates, all materials investigated lie in the $s_\pm + d_{x^2-y^2}$ region of the phase diagram. Materials particularly close to the phase transition line are κ-(ET)$_2$I$_3$, κ-(ET)$_2$Ag(CN)$_2$·H$_2$O and κ-(ET)$_2$Cu[N(CN)$_2$]Br. These can be expected to realize the $s_\pm + d_{x^2-y^2}$ order parameter with eight nodes.

When materials are close to the phase transition line, small changes of the hopping parameters might drive them into the d_{xy} state, which is always present as a sub-dominant pairing symmetry. For such local changes of parameters, for instance lattice defects [113, 114] or disorder of molecular conformations could be responsible. In Ref. [118] we have

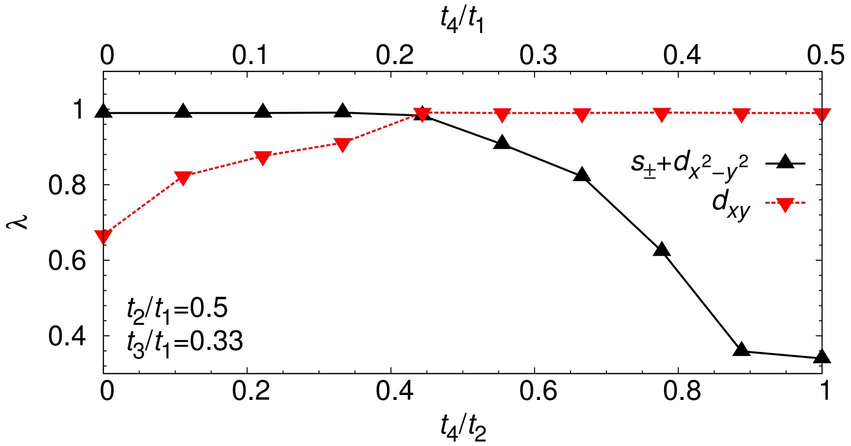

Figure 6.8: Eigenvalues of the gap equation for $s_\pm + d_{x^2-y^2}$ and d_{xy} pairing symmetries as a function of the in-plane anisotropy t_4/t_2. The isotropic case is realized for $t_4/t_2 = 1$. Only t_4 was varied. The other parameters were fixed to $t_2/t_1 = 0.5$ and $t_3/t_1 = 0.33$. Figure taken from Ref. [126].

shown that different conformations of ET molecules result in decidedly different ratios of t_4/t_2. The degree of conformational disorder can be controlled experimentally by adjusting the sample cooling rate [46, 48].

In Ref. [18] a square lattice-like antiferromagnetic order was found for the insulating state of κ-type materials. Therefore, we expect significant competition between antiferromagnetism and d_{xy}-symmetric superconductivity, while the $s + d_{x^2-y^2}$-symmetric state is realized farther away from the magnetically ordered insulating phase. Within this picture, recent results by Oka *et al.* [43], who interpreted their experiment in terms of patches with a d_{xy} order parameter and a $d_{x^2-y^2}$-symmetric bulk, can be qualitatively explained.

At this point we would like to emphasize that most experimental studies assume a four-node d-wave order parameter upon data analysis, which excludes from the start the detection of the $s_\pm$-component we found. In particular, the realization of the $s_\pm + d_{x^2-y^2}$ state with eight nodes which lie along the diagonals and close to the crystallographic axes, may explain the considerable disagreement in the experimental literature regarding the node positions.

6.2.5 Simulation of scanning tunneling spectroscopy

Most transport experiments on κ-(ET)$_2X$ materials have proven to be difficult to interpret and could not resolve the symmetry of the superconducting pairing so far. However, recent improvements in sample preparation for low-temperature scanning tunneling spectroscopy (STS) experiments have allowed for progress towards a resolution of the superconducting order parameter [43, 44, 49].

Therefore, in this section we simulate tunneling spectra in the superconducting state for molecule model parameters $t_2/t_1 = 0.4375$, $t_4/t_1 = 0.1$ and various values of t_3/t_1: a four-node $s_\pm + d_{x^2-y^2}$ state is obtained for $t_3/t_1 = 0.5$, an eight-node $s_\pm + d_{x^2-y^2}$ state for $t_3/t_1 =$

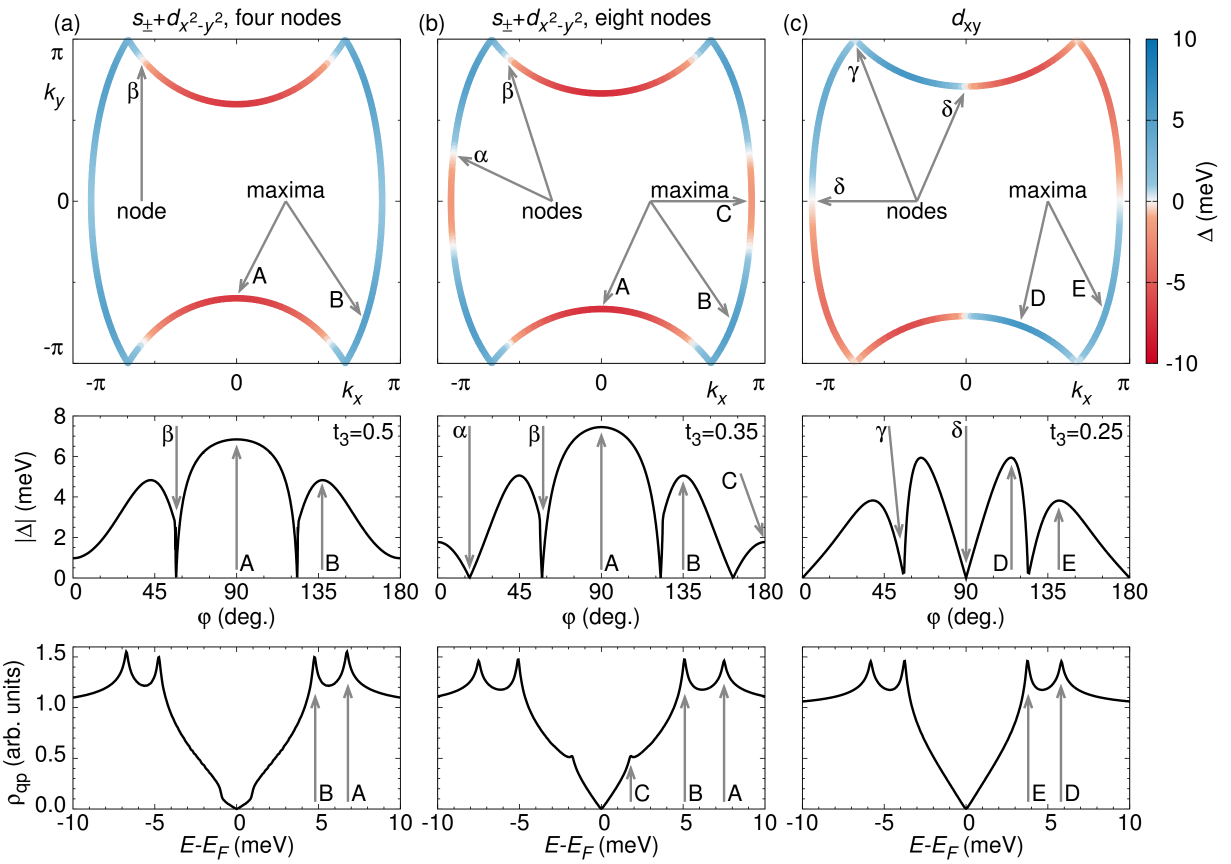

Figure 6.9: Gap function on the Fermi surface (top panel), magnitude of the gap function versus angle measured with respect to the k_x direction (mid panel) and simulated quasiparticle density of states in the superconducting state (bottom panel). In all cases we assumed an energy scale $\Delta_0 = 10$ meV. Only t_3/t_1 is varied. Other parameters are fixed to $t_2/t_1 = 0.4375$ and $t_4/t_2 = 0.1$. Maxima of the superconducting gap magnitude are labelled with capital letters. Nodes of the superconducting order parameter are labelled with greek letters. All nodes and maxima not labelled explicitly are symmetry equivalent to the labelled ones. Column (a) shows the case of $s_\pm + d_{x^2-y^2}$-symmetry with four nodes ($t_3/t_1 = 0.5$). Column (b) shows the results for $s_\pm + d_{x^2-y^2}$-symmetry with eight nodes ($t_3/t_1 = 0.3475$). Column (c) shows the d_{xy} case ($t_3/t_1 = 0.25$). Figure taken from Ref. [126].

0.3475 and d_{xy} for $t_3/t_1 = 0.25$. We employ the representation of the superconducting gap in terms of symmetry functions introduced in Eq. 6.27, which we multiply with a prefactor $\Delta_0 = 10$ meV to obtain a spectrum with reasonable energy scale. The gap on the Fermi surface is then given by $\Delta(\mathbf{k}) = \Delta_0\, \tilde{g}(\mathbf{k})$. We use this expression together with Eq. 6.24 to calculate the quasiparticle density of states ρ_{qp}, which corresponds to the local density of states (LDOS) observed in STS experiments. The finite quasiparticle lifetime is modelled by $\Gamma = 0.07$ meV. In the d_{xy} case we ignore the small anisotropy found in the RPA calculation.

In Fig. 6.9 we show (i) the obtained gap on the Fermi surface, (ii) the magnitude of the gap versus angle measured from the k_x-direction and (iii) the simulated tunneling spectrum for the three cases investigated.

The magnitude of the gap versus the angle is distributed anisotropically on the Fermi surface [Fig. 6.9(a-c) top panel]. Maxima of the gap magnitude are indicated by arrows labelled with capital letters, while nodes in the gap are indicated by arrows labelled with greek letters. The global maximum of the gap magnitude (labelled A or D) resides in all cases on the elliptic part of the Fermi surface, while the second largest maximum (labelled B or E) is located on the quasi-one-dimensional part. A third smallest maximum (labelled C) is possible on the quasi-1D sheet. In the d_{xy}-case the nodes labelled γ appear in addition to the expected set of nodes δ, because the Fermi surface touches the Brillouin zone boundary. The γ-nodes lead to the second maximum (labelled E) of the gap magnitude [Fig. 6.9(a-c) middle panel], but are otherwise irrelevant for the low-energy physics. Since the three possible gap structures share two maxima of slightly different size, the simulated quasiparticle DOS looks quite generic [Fig. 6.9(a-c) bottom panel]. A two-peak structure is observed far away from the Fermi level, which corresponds to the energy values of the two largest maxima in the gap magnitude.

Important differences are, however, revealed at low energies: the d_{xy} state is featurelessly V-shaped [Fig. 6.9(c) bottom panel], while the spectrum of the eight-node state has an additional peak close to 2 meV [Fig. 6.9(b) bottom panel], which is linked to the small gap (labelled C) on the quasi-1D sheet. This leads to an outer and an inner V-shape with different slopes. For the four-node $s_\pm + d_{x^2-y^2}$ state we observe a peculiar dip around 1 meV in the quasiparticle spectrum [Fig. 6.9(a) bottom panel]. This corresponds to the minimum value of the gap magnitude on the quasi-one-dimensional part of the Fermi surface. Inside of this dip a V-shaped region emerging from the β-nodes is again observed.

We emphasize that our predictions are to be taken as qualitative, not quantitative, regarding the overall energy scale and the relative gap sizes. The main features explained before are, however, robust. The detection of such low-energy structures is certainly not an easy task, but we believe it will be possible with state-of-the-art equipment and proper sample preparation.

In a first attempt to do this, the group of Hans-Joachim Elmers performed STS experiments on *in situ* cleaved single crystals of κ-(ET)$_2$Cu[N(CN)$_2$]Br, for which we predicted an $s_\pm + d_{x^2-y^2}$ mixed-symmetry order parameter with eight nodes. In fact they could resolve the signatures of three conductance peaks in the second derivative of the measured conductance [see Fig. 6.10(a)], which correspond to the three gap maxima we found for the eight node state [see Fig. 6.9(b)].

Using the decomposition of the microscopically calculated superconducting order parameter into symmetry functions (Eq. 6.26), we investigate whether quantitative agreement with the experimentally measured $S(V)$ can be reached by fine-tuning some parameters. In this process the symmetry of the superconducting state is kept fixed to the theoretical prediction (mixed extended $s + d_{x^2-y^2}$). We re-evaluate Eqs. 6.24 and 6.25 with parameter sets $\{\Delta_0, c_{s_1}, c_{d_1}, c_{s_2}, x, \Gamma\}$ until optimal agreement with the experimental spectra in the interval $[-12, +12]$ meV is reached. The corresponding calculated spectra are shown in

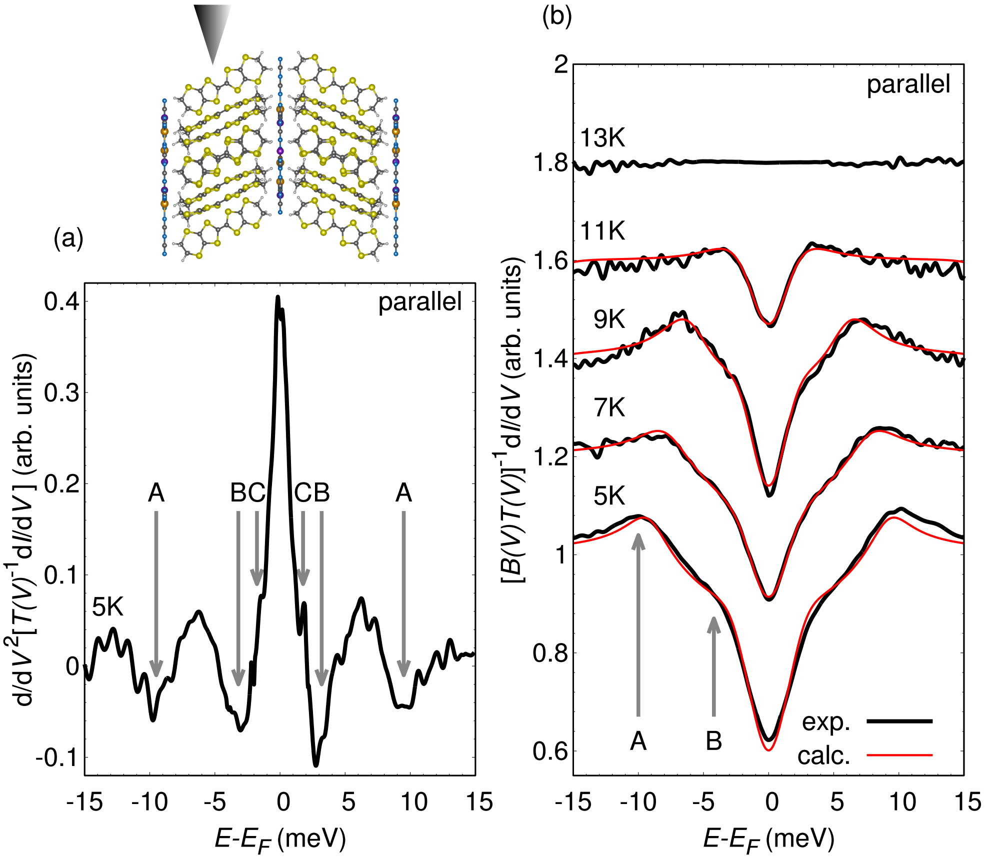

Figure 6.10: (a) Second derivative of the conductance spectrum $\mathrm{d}I/\mathrm{d}V/T(V)$ at $T = 5$ K. Arrows labeled by A, B and C indicate three pairs of minima which are symmetric to the origin, corresponding to the coherence peaks partially seen in (b). (b) Conductance spectra $S(V) = 1/[B(V)T(V)]\ dI/dV$ of the superconducting state as a function of $eV = E - E_F$ at different temperatures measured parallel to the layered crystal structure. The red lines show mappings of Eq. 6.25 to the measured data. Figure taken from Ref. [44].

Fig. 6.10(b) as solid red lines. The optimal parameter values listed in Table 6.2 are consistent throughout the investigated parameter range. Only the origin of the non-monotonous behavior of Γ is currently unclear. Therefore, the experimental results are fully consistent with the order parameter with eight nodes that we predicted.

6.3 Summary and outlook

In summary, we investigated the superconducting state of κ-(ET)$_2X$ charge transfer salts in an individual molecule model based on a combination of *ab initio* density functional theory and random phase approximation spin-fluctuation calculations. We obtained kinetic parameters of the molecule Hamiltonian for eight superconducting κ-type materials using projective Wannier functions. We found that the superconducting order parameter

T (K)	c_{s_1}	c_{d_1}	c_{s_2}	Δ_0 (meV)	Γ (meV)	x
5	-0.109	-0.276	-0.615	12.218	0.690	0.520
7	-0.128	-0.280	-0.592	10.638	0.641	0.603
9	-0.064	-0.317	-0.620	7.376	0.000	0.466
11	-0.158	-0.200	-0.642	2.984	0.035	0.188

Table 6.2: Values of the parameters in Eq. 6.25 obtained by mapping the calculated $S(V)$ to the experimental spectra. Table taken from Ref. [44].

in a realistic molecule model is different from the one in the usual dimer approximated Hamiltonian for all investigated materials. The superconducting phase diagram of the molecule description is dominated by an extended $s + d_{x^2-y^2}$-symmetry that emerges from the competition between square-like and diagonal hopping processes on the original κ-type lattice, while the physics of the dimer model is reproduced also for finite dimerization in the limit of isotropic parameters $t_4 \lesssim t_2$. The anisotropy of square-like hoppings t_2 and t_4 is, however, not negligible in real materials. For precisely this reason, the dimer approximation does not apply to superconducting κ-(ET)$_2X$ charge transfer salts. It overestimates the importance of square lattice physics through the averaging contained in the geometric formulas, which are exact only in the limit of infinite dimerization.

Furthermore, the $s_\pm + d_{x^2-y^2}$ state, which features nodes both along the crystallographic axes and the Brillouin zone diagonals, may explain the multitude of contradictory experimental results regarding the nodal positions. We also simulated tunneling spectroscopy experiments for all nodal configurations encountered in our phase diagram. The difference between those pairing states unfortunately manifests itself only at very low energies, making experimental detection difficult, but not impossible. Based on the *ab initio* calculated model parameters we found that the well-studied material κ-(ET)$_2$Cu[N(CN)$_2$]Br is situated near the phase transition line between $s_\pm + d_{x^2-y^2}$ and d_{xy} superconducting states, which supports the interpretation of recent scanning tunneling spectroscopy experiments.

A question unanswered by our study is why superconducting transition temperatures among quasi-two-dimensional charge transfer salts can differ by more than a factor of four. As there is no obvious connection between T_c and the parameters of the kinetic Hamiltonian, a method that can qualitatively reproduce the ordering of transition temperatures in real materials is required to elucidate this issue.

In conclusion, we believe that a significant part of the physics in quasi-two-dimensional charge transfer salts has unfortunately been overlooked so far, because theory has adhered to the dimer model for too long and too many experiments have been interpreted based on a dichotomy of d_{xy} and $d_{x^2-y^2}$ states, which is inappropriate for the orthorhombic lattice realized in κ-(ET)$_2X$ materials.

It is an interesting open question, whether the magnetic, insulating and possible quantum spin-liquid states known from the anisotropic triangular lattice are also present in the molecule model. The investigation of these phases is left for future studies.

Chapter 7

Importance of charge doping and interlayer distance in intercalated FeSe

D. Guterding, H. O. Jeschke, P. J. Hirschfeld, R. Valentí,
Phys. Rev. B **91**, 041112(R) (2015).

We now focus our attention on iron-based superconductors. After their discovery in 2008, transition temperatures were quickly improved to ∼ 56 K by chemical substitution [144]. Recently, the possible discovery of superconductivity with $T_c = 65$ K [145] and even $T_c \sim 100$ K [59] in single-layer FeSe films grown by molecular beam epitaxy on $SrTiO_3$ showed that temperatures close to and above the boiling point of liquid nitrogen (77 K) may be achievable. These results have initiated an intensive debate regarding the origin of the high superconducting temperatures and the role played by electron doping via substrate, dimensionality and lattice strain.

While bulk FeSe has a T_c of only 8-10 K, it has been known for some time that it can be substantially enhanced to 40 K or higher by alkaline intercalation [146]. Materials with a single alkaline A = K, Cs, Rb between FeSe layers of nominal form $A_xFe_{2-y}Se_2$ have been studied intensively, and display a wide variety of unusual behaviors relative to the iron pnictide superconducting materials [147]. These include likely phase separation into an insulating phase with block antiferromagnetism and ordered Fe vacancies, and a superconducting phase that is strongly alkaline deficient and whose Fermi surface, as measured by angle-resolved photoemission spectroscopy, apparently contains no hole-like Fermi surface pockets, in contrast to iron pnictides. Since the popular spin fluctuation scenario for $s_\pm$ pairing relies on near nesting of hole and electron pockets, it has been speculated that a different mechanism for pairing may be present in these materials, but even within the spin fluctuation approach, different gap symmetries including *d*-wave pairing have been proposed [99, 148–150]. The gap symmetry and structure is, therefore, still controversial [151, 152].

In addition to the unusual doping, speculation on the origin of the higher T_c has centered on the intriguing possibility that enhancing the FeSe layer spacing improves the two-dimensionality of the band structure and, hence, Fermi surface nesting [153, 154]. In an effort to investigate this latter effect, organic molecular complexes including alkaline atoms were recently intercalated between the FeSe layers [55, 153–159], yielding transition

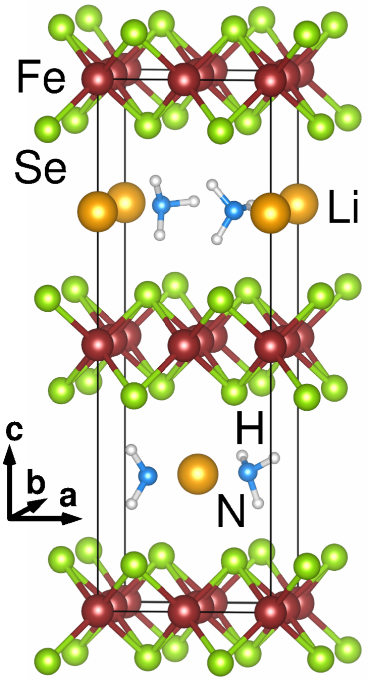

Figure 7.1: Idealized crystal structure of $Li_{0.5}(NH_3)Fe_2Se_2$. For a detailed discussion of experimental crystal structures see Refs. [55, 155]. Figure taken from Ref. [101].

temperatures of up to 46 K. The most intensively studied materials incorporate molecules including ammonia, for example $Li_{0.56}(NH_2)_{0.53}(NH_3)_{1.19}Fe_2Se_2$ with $T_c = 39$ K [155] and $Li_{0.6}(NH_2)_{0.2}(NH_3)_{0.8}Fe_2Se_2$ with $T_c = 44$ K [55]. The crystal structure of a stoichiometric version of these materials is shown in Fig. 7.1. Recently, Noji *et al.* [154] compared data on a wide variety of FeSe intercalates and noted a strong correlation of T_c with interlayer spacing, corresponding to a nearly linear increase between 5 to 9 Å, followed by a rough independence of spacing with further increase between 9 to 12 Å.

In this chapter we study the question of how exactly doping and interlayer distance influence T_c in molecular intercalates of FeSe, whether these effects are separable, and what gives rise to the apparent upper limit for T_c in this family of iron chalcogenides. Using a combination of DFT calculations for the electronic structure of several materials in this class together with model calculations of spin fluctuation pairing based on these band structures, we argue that strength and wave-vector of spin fluctuations in lithium/ammonia intercalated FeSe can be controlled by tuning the Li^+:NH_2^- ratio in the spacer layer. We show that the evolution of T_c with electron doping can be understood from the shape of the density of states close to the Fermi level. As long as hole pockets are present, we find that the superconducting pairing is of $s_\pm$ character and identify a subleading $d_{x^2-y^2}$ instability. We believe that our interpretation is valid in a broad class of related materials. Our findings have been published in Ref. [101], which this chapter is based on.

7.1 Methods and materials

We performed density functional theory calculations for $Li_{0.5}(NH_2)_y(NH_3)_zFe_2Se_2$ at various ratios of NH_2^- to NH_3 content, starting from the experimentally determined structures $Li_{0.56}(NH_2)_{0.53}(NH_3)_{1.19}$ [155] and $Li_{0.6}(NH_2)_{0.2}(NH_3)_{0.8}$ [55], which include fractionally occupied atomic sites for lithium, hydrogen and nitrogen. In order to accommodate the experimental stoichiometry we construct a $2 \times 1 \times 1$ (4 Fe) supercell for the former, and a $2 \times 2 \times 1$ (8 Fe) supercell for the latter compound. We replace all fractionally occupied nitrogen positions by fully occupied positions. Since hydrogen positions are not known precisely from experiment, we arrange the hydrogen atoms so that we obtain NH_3 groups with angles of about 108° as encountered in ammonia and further relax these positions within the local density approximation (LDA) [74] with the projector augmented wave (PAW) basis [77] as implemented in GPAW [120] until forces are below 2 meV/Å. In the $2 \times 1 \times 1$ supercell we place the lithium atom in one half of the unit cell and leave the lithium position in the other half unoccupied. In the $2 \times 2 \times 1$ supercell we arrange the lithium atoms in a checkerboard pattern of occupied and vacant sites (Fig. 7.1). We used $6 \times 6 \times 6$ k-point grids within the GPAW code and checked the remaining forces in the FPLO code with a $12 \times 12 \times 12$ k-point mesh. We found the atomic positions to be sufficiently converged.

Initially, we only consider charge neutral NH_3 ammonia groups in the spacer and no NH_2^- . In this way, we obtain idealized structures with formula units $Li_{0.5}(NH_3)Fe_2Se_2$ and $Li_{0.5}(NH_3)_2Fe_2Se_2$, where chalcogen height and unit cell parameters are chosen as in the experimental structures [55, 155]. Both structures belong to space group P1 because of NH_3 situated in the spacer layer. Note that by setting up both structures with neutral NH_3, we are able to disentangle possible effects of the structural differences from the effect of doping through the composition of the spacer layer.

The experimentally available samples [55, 155] contain both NH_3 and NH_2^-. The radical NH_2^- neutralizes the charge donated to the FeSe layer by Li^+ and reduces the doping level. In order to capture this compensation of charge in our simulations, we use the virtual crystal approximation (VCA) starting from supercells $Li_{0.5}(NH_3)Fe_2Se_2$ and $Li_{0.5}(NH_3)_2Fe_2Se_2$, which correspond to the maximally electron doped compounds. The VCA can be used to interpolate continuously between the properties of an atom with nuclear charge Z and its neighbors in the periodic table of elements with nuclear charges $Z-1$ or $Z+1$. In the study presented here, we fractionally replaced nitrogen ($Z = 7$) by carbon ($Z = 6$). Because of the different valence of nitrogen and carbon this procedure interpolates between charge neutral ammonia (NH_3) and a methyl radical (CH_3^-). Since ammonia (NH_3) and methane (CH_4) are structurally similar, VCA should provide a sufficient description of the spacer layer. The use of VCA has the advantage that doping is treated in a continuous and rather isotropic, but not rigid band fashion. We checked these calculations by removing hydrogen atoms explicitly instead of doing VCA and found the differences to be negligible.

The analysis of the band structure of these supercells is done within FPLO and we use LDA as exchange-correlation functional [74]. We then use projective Wannier functions as implemented in FPLO [122] to downfold the band structure. In our tight binding models, we keep the Fe $3d$ and Se $4p$ states. The energy window we used for the downfolding spans

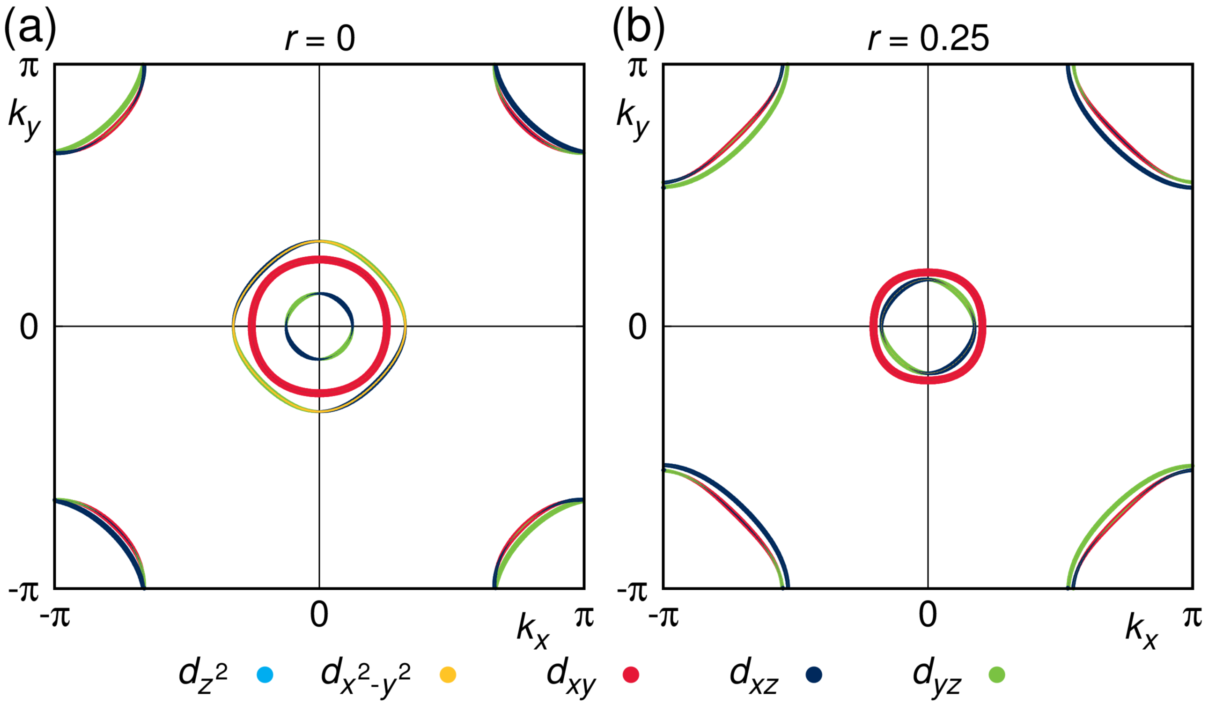

Figure 7.2: Fermi surface in the 16 band tight binding model for (a) $r = 0.0$ and (b) $r = 0.25$ in the 2-Fe Brillouin zone at $k_z = 0$. The colors indicate the weights of Fe 3d states. Figure taken from Ref. [101].

approximately the range from -6 eV to $+2$ eV. In order to obtain band structure and Fermi surface of the supercells in the conventional two iron unit cell, we use our recently developed technique [160] to translationally unfold the 32 and 64 band supercell models to a 16 band model of the 2 Fe equivalent Brillouin zone. For calculations of susceptibility and superconducting pairing, we use subsequent glide reflection unfolding [160] of the bands to obtain the 8 band model of the 1 Fe equivalent Brillouin zone.

The static susceptibility is calculated on a $30 \times 30 \times 10$ k-point mesh at an inverse temperature of $\beta = 40$ eV^{-1}. To explore how the superconducting state depends on interlayer spacing and doping, we use the three-dimensional version of our RPA implementation for the multi-orbital Hubbard model (Eq. 1.4). We keep the selenium states in the entire calculation, but consider interactions only between Fe 3d states. We assume spin rotation-invariant interaction parameters $U = 1.35$ eV, $V = U/2$ and $J = J' = U/4$. The effective interaction in the singlet pairing channel is constructed via the multi-orbital RPA procedure explained before. The effective eigenvalue equation is then solved using ~ 1000 points on the three-dimensional Fermi surface.

7.2 Results and discussion

First, we investigated the properties of the maximally electron doped compounds in our study, $Li_{0.5}(NH_3)Fe_2Se_2$ (ammonia poor) and $Li_{0.5}(NH_3)_2Fe_2Se_2$ (ammonia rich). Both

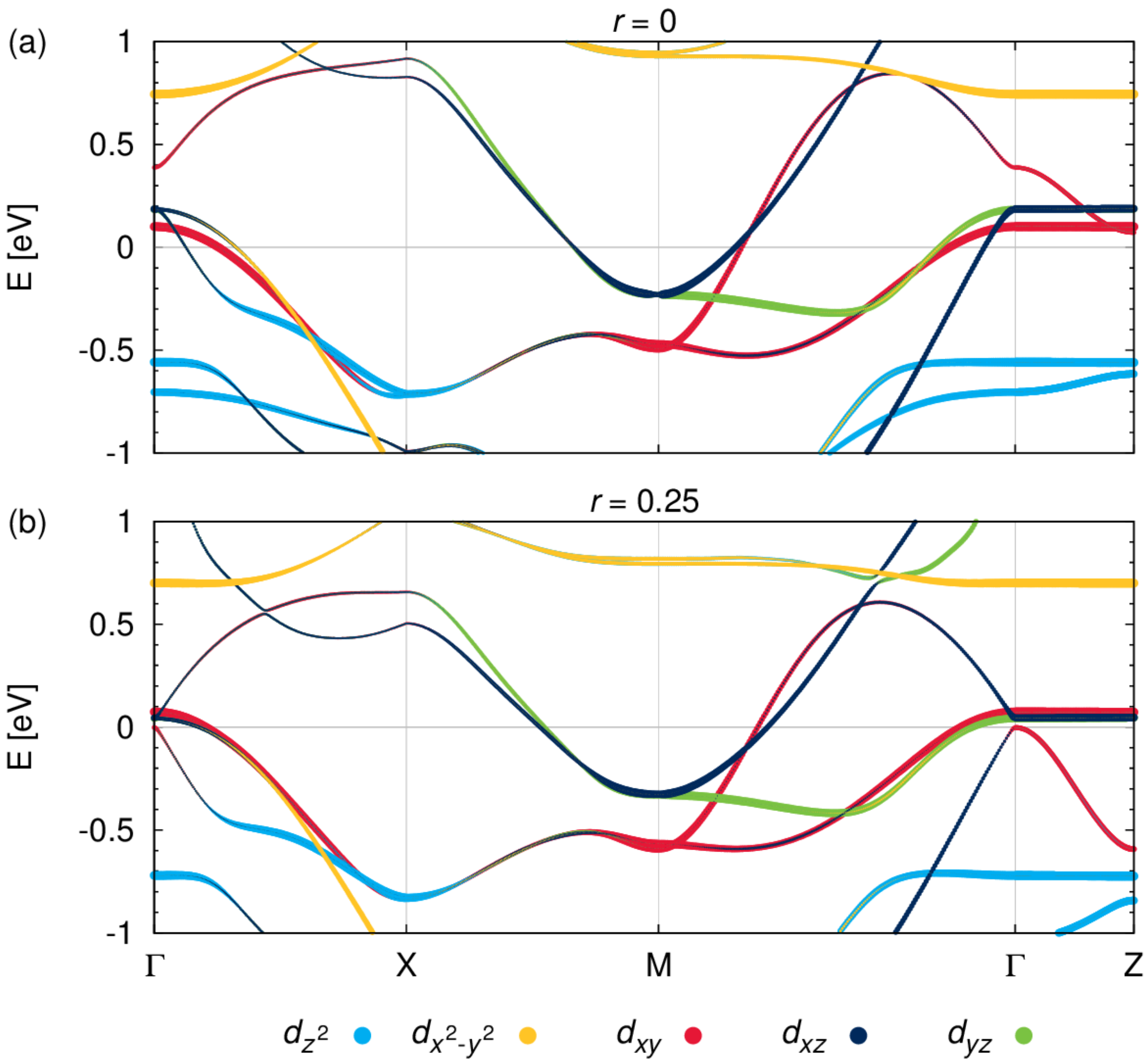

Figure 7.3: Band structure in the 16 band tight binding model for (a) $r = 0.0$ and (b) $r = 0.25$ in the 2-Fe Brillouin zone. The colors indicate the weights of Fe $3d$ states. Figure taken from the supplemental information of Ref. [101].

feature at the Fermi level two large electron pockets in the corners of the 2 Fe Brillouin zone and two small hole pockets around Γ. This confirms that the lithium atoms donate electrons to the FeSe layer. Both systems have the same electron doping, but different interlayer spacing. This is observed in the k_z-dispersion of the Fermi surface, where the smaller interlayer distance of the ammonia poor compound leads to a slightly increased corrugation of the cylinders.

In the experimentally realized compounds $Li_{0.56}(NH_2)_{0.53}(NH_3)_{1.19}$ and $Li_{0.6}(NH_2)_{0.2}(NH_3)_{0.8}$ the spacer layer nominally donates a charge of 0.015 and 0.2 electrons per iron atom respectively. These doping levels are lower than in our model materials $Li_{0.5}(NH_3)Fe_2Se_2$ and $Li_{0.5}(NH_3)_2Fe_2Se_2$. To investigate the doping dependence of the electronic

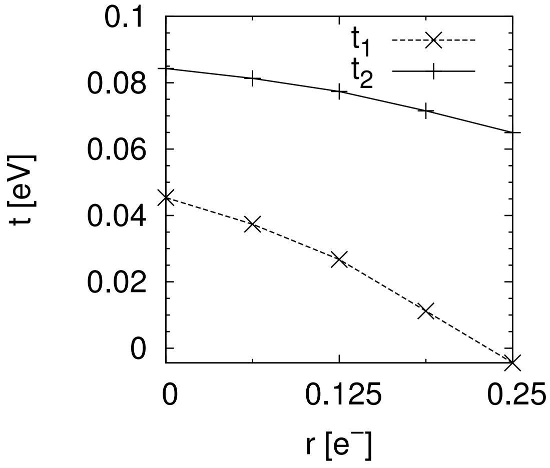

Figure 7.4: Nearest and next-nearest neighbor hopping (t_1 and t_2 respectively) in the Fe $3d_{xy}$ orbital within a five band iron only picture. Figure taken from the supplemental information of Ref. [101].

structure at a given interlayer spacing, we consider $\mathrm{Li_{0.5}(NH_3)Fe_2Se_2}$ and hole dope it by means of the virtual crystal approximation as explained above. To simplify the notation, we label compounds from now on not by their full chemical formula, but by an index $r = \{0.0, \dots, 0.25\}$, which refers to the chemical formula $\mathrm{Li_{0.5}(NH_2)_{0.5-2\mathit{r}}(NH_3)_{0.5+2\mathit{r}}Fe_2Se_2}$. $r = 0.25$ refers to the compound $\mathrm{Li_{0.5}(NH_3)Fe_2Se_2}$ with maximal electron doping, where lithium nominally transfers a quarter of an electron to each iron atom. Increasing the $\mathrm{NH_2^-}$ content immediately brings up a third hole pocket to the Fermi level, which is three-dimensional at intermediate doping and becomes two-dimensional once the charge introduced by lithium is fully compensated by $\mathrm{NH_2^-}$ groups. $r = 0$ denotes the compound where the charge introduced by lithium is nominally compensated by $\mathrm{NH_2^-}$ and no electrons are donated to the FeSe layer. The Fermi surfaces of the end members ($r = 0.0$ and $r = 0.25$) are shown in Fig. 7.2. The electronic band structure on a high-symmetry path is shown in Fig. 7.3.

To understand the effects of electron doping on a microscopic level, we constructed five band Fe-only models by downfolding also the Se $4p$ states using an energy window ranging from -3 eV to $+2$ eV. As shown in Fig. 7.4, the nearest neighbor hopping t_1 in the Fe $3d_{xy}$ orbital is affected much stronger by the electron doping than the next-nearest neighbor hopping t_2. Therefore, the hole pockets do not only shrink because the electron doping raises the Fermi level, but also because the nearest neighbor hopping in the Fe $3d_{xy}$ orbital decreases steeply as a function of electron doping

The band structure effects of changing individual hopping parameters have been worked out in great detail in Ref. [162]. In the materials investigated here, the change in t_1 serves to shift the hole bands down (see Fig. 7.3), which gives rise to an increased density of states at the Fermi level. In Fig. 7.5 we plot the orbital resolved density of states for the 8 band model at $r = 0.25$. The positive slope close to the Fermi level and the edge of the hole bands at $+0.1$ eV are clearly visible.

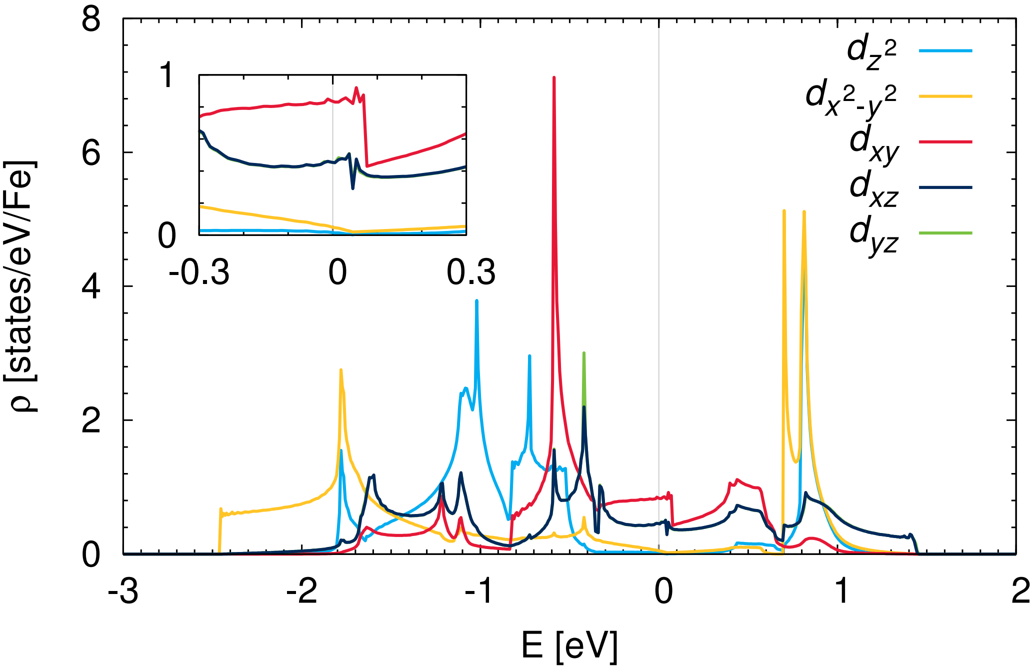

Figure 7.5: Orbital resolved Fe $3d$ density of states of the 8 band tight binding model for $r = 0.25$. Figure taken from the supplemental information of Ref. [101].

Next, we investigate the doping dependence of spin fluctuations. The non-interacting static susceptibility on the high-symmetry path calculated in the 1-Fe Brillouin zone for $r = 0.0$ and $r = 0.25$ is shown in Fig. 7.6. In the undoped compound ($r = 0.0$) the structure of the static susceptibility resembles strongly what is found for materials like LaFeAsO or $BaFe_2As_2$. The electron doping notably shifts the maximum from $X = (\pi, 0)$ towards $M = (\pi, \pi)$ and the former valley at M transforms into a peak. The absence of a $(\pi, 0)$ peak in electron doped compounds suggests why no orthorhombic phase or stripe-like magnetism have been found in FeSe intercalates so far [163].

The shifts of the dominant vectors of spin fluctuations can be understood from nesting properties and orbital character on the Fermi surface in the 1-Fe Brillouin zone. The undoped compound ($r = 0.0$) is dominated by $(\pi, 0)$ nesting of electron and hole pockets, whereas the electron doped compound ($r = 0.25$) (see Fig. 7.7) features scattering between electron and hole pockets with altered wave vector competing with scattering between electron pockets. The dominant contributions to the static susceptibility originate from the d_{xy} and $d_{xz/yz}$ orbitals.

Now we focus on the superconducting state. For all values of electron doping (structures $r = 0.0$ to $r = 0.25$) and interlayer spacing (structures $Li_{0.5}(NH_3)Fe_2Se_2$ and $Li_{0.5}(NH_3)_2$ Fe_2Se_2) considered we find the leading instability to be of nodeless $s_\pm$ character, while subleading solutions are of nodal $s_\pm$ and $d_{x^2-y^2}$ type (see Fig. 7.8 for structure $r = 0.25$). These are the leading states expected in the case of a nearly 2D system with both hole and electron pockets. Repulsive electron-hole $d_{xz/yz}$ and d_{xy} interactions favor nodeless $s_\pm$ pairing, while inter-electron pocket interactions, orbital weight variations around the Fermi

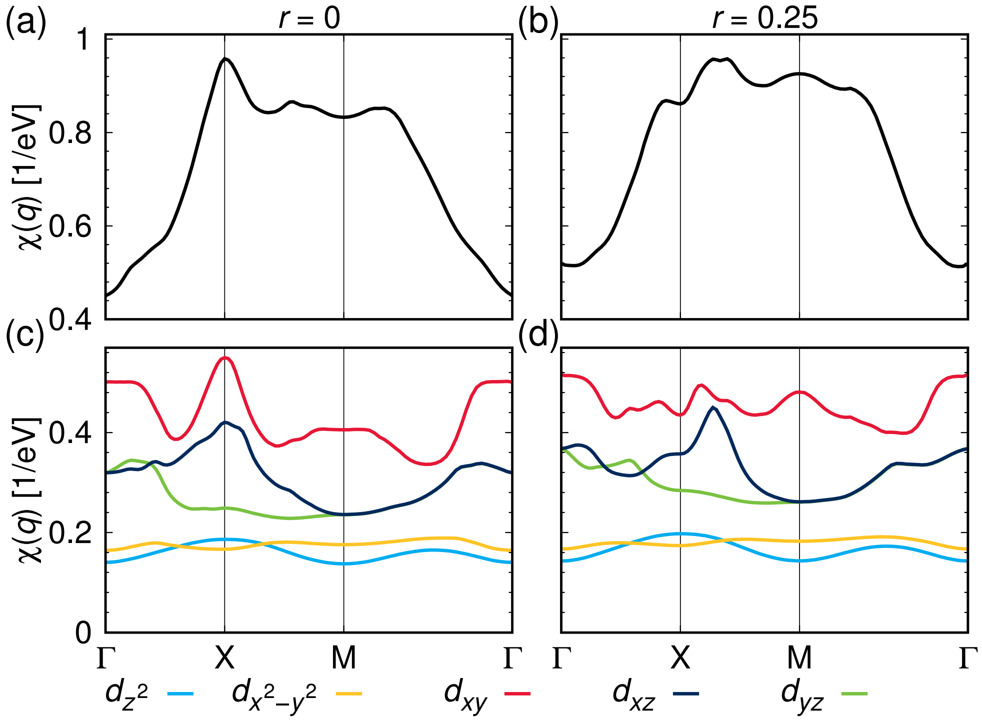

Figure 7.6: Summed static susceptibility (upper panel) and its diagonal components χ_{aa}^{aa} (lower panel) in the 8 band tight binding model for $r = 0.0$ (a,c) and $r = 0.25$ (b,d) in the 1-Fe Brillouin zone. The colors identify the Fe 3d states. Figure taken from Ref. [101].

surface, and intraband Coulomb interactions are known to frustrate the $s_\pm$ interaction and drive nodal behavior and eventually d-wave interactions when hole pockets disappear [150, 164].

We observe that the source of the moderate quantitative enhancement of T_c with electron doping lies in an increased density of states at the Fermi level. For both the d_{xy} and the $d_{xz/yz}$ orbitals the slope of density of states near the Fermi level is positive [Fig. 7.9 (b)] so that electron doping leads to an enhanced susceptibility and superconducting pairing strength as the doping approaches the edge of the hole bands, which appears as a sharp drop of the d_{xy} DOS (see Fig. 7.5). The small initial decrease of the pairing eigenvalue at low electron doping [Fig. 7.9 (a)] is a consequence of the degraded nesting.

Alternatively, when we keep the electron doping levels fixed to the same value and analyze only the interlayer spacing effect (structures $\mathrm{Li_{0.5}(NH_3)Fe_2Se_2}$ with $c = 8.1$ Å and $\mathrm{Li_{0.5}(NH_3)_2Fe_2Se_2}$ with $c = 10.3$ Å), we find that the Fermi surface turns completely two-dimensional for a c-axis length between 8.1 Å and 10.3 Å, where T_c saturates in experiment. Analyzing the susceptibility and superconducting pairing for both structures, we find no qualitative differences. Quantitatively, the perfectly two-dimensional Fermi surface of the ammonia rich compound leads to an increased susceptibility and larger pairing eigenvalue than in the ammonia poor compound. The increased pairing eigenvalue would correspond to an enhanced T_c.

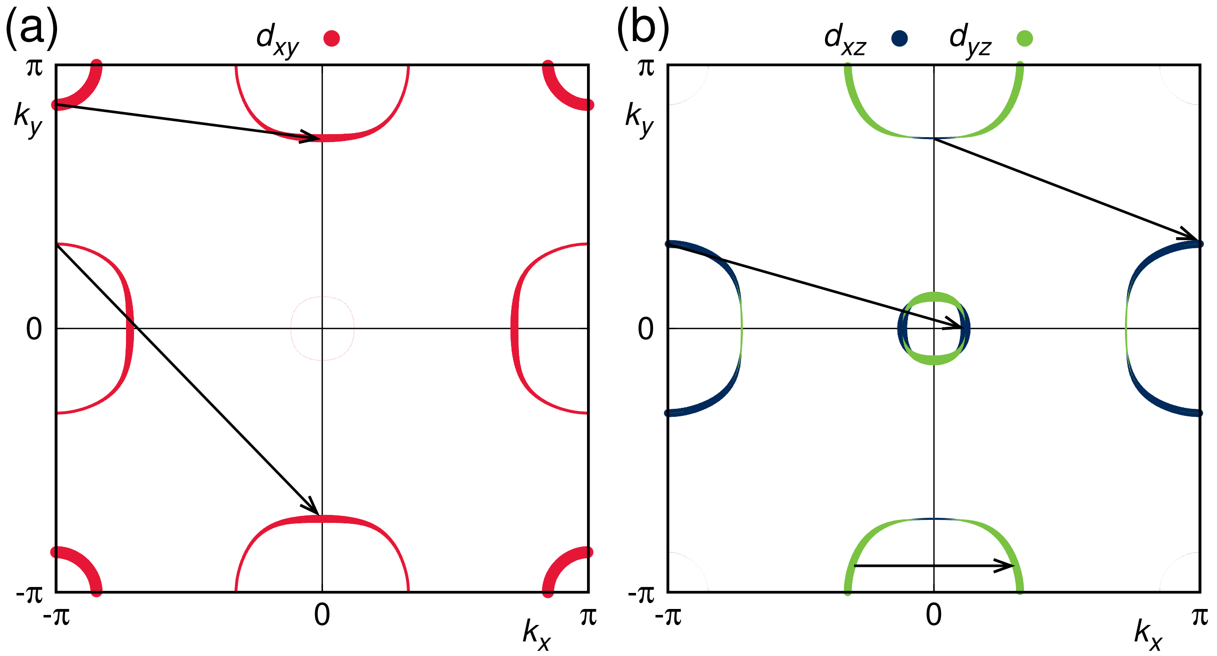

Figure 7.7: Fermi surface in the 8 band tight binding model for $r = 0.25$ in the 1-Fe Brillouin zone at $k_z = 0$. Shown are the orbital characters for (a) the d_{xy} and (b) the $d_{xz/yz}$ orbitals. The arrows represent dominant interaction vectors identified from peaks in the susceptibility. Figure taken from Ref. [101].

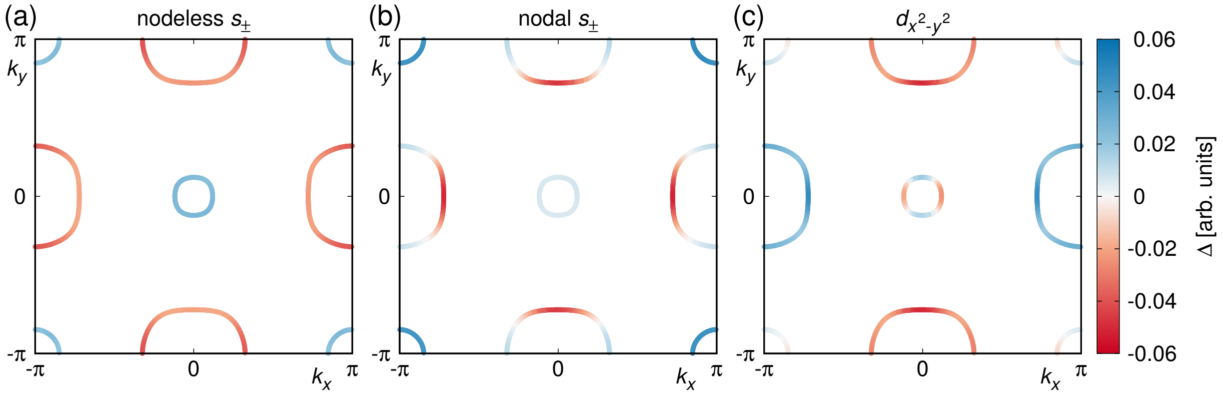

Figure 7.8: Solutions of the linearized gap equation on the Fermi surface within the 8 band tight binding model for $r = 0.25$ in the 1-Fe Brillouin zone at $k_z = 0$. The relevant instabilities are (a) nodeless $s_{\pm}$, (b) nodal $s_{\pm}$ and (c) $d_{x^2-y^2}$. We assume spin rotation-invariant interaction parameters $U = 1.35$ eV, $V = U/2$, $J = J' = U/4$. Figure taken from Ref. [101].

Our calculations show that both increasing electron doping and lattice spacing contribute to enhancing T_c. However, experimentally it is found that the ammonia poor compound (larger electron doping) with smaller c-axis shows a higher T_c ($\mathrm{Li}_{0.6}(\mathrm{NH}_2)_{0.2}(\mathrm{NH}_3)_{0.8}\mathrm{Fe}_2\mathrm{Se}_2$, $T_c = 44$ K) than the ammonia rich compound (smaller electron doping) with larger c-axis

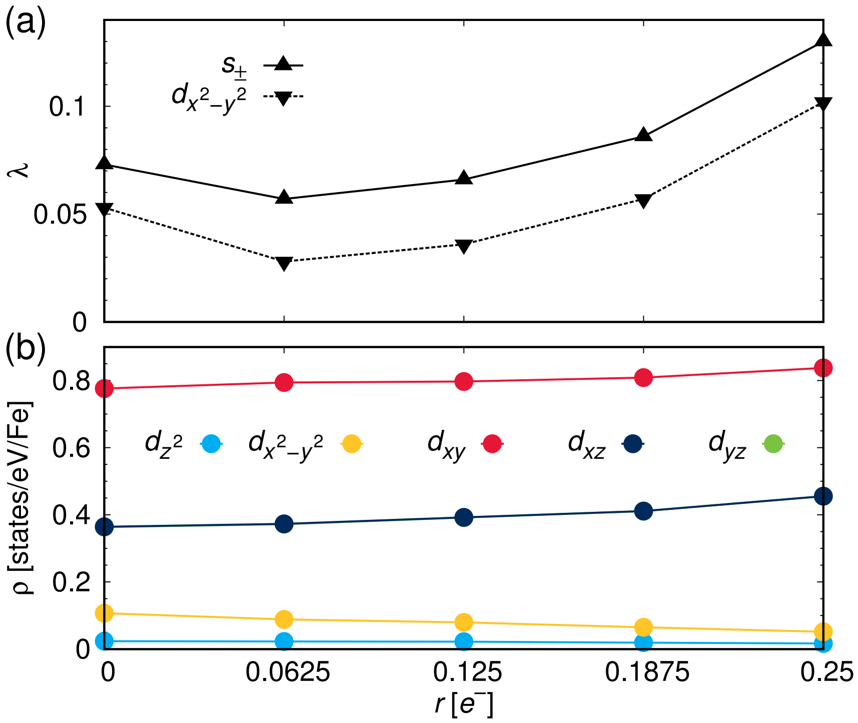

Figure 7.9: (a) Trend of the eigenvalues of $s_\pm$ and $d_{x^2-y^2}$ solutions and (b) orbital resolved Fe $3d$ density of states at the Fermi level with doping. Figure taken from Ref. [101].

($Li_{0.56}(NH_2)_{0.53}(NH_3)_{1.19}Fe_2Se_2$, $T_c = 39$ K). Therefore, the variations in lattice parameters observed experimentally cannot be the source of the enhancement of T_c. Within our picture, this leaves only the electron doping level as the controlling parameter. Hence, we conclude that T_c is mainly controlled by the electron doping level when the Fermi surface is mostly two-dimensional. Therefore, it is unlikely that T_c can be enhanced further by intercalation of larger molecules.

7.3 Summary

We investigated the $Li_x(NH_2)_y(NH_3)_zFe_2Se_2$ family of FeSe intercalates and found that the FeSe layer is moderately electron doped. The electron doping moves the Fermi level towards the edge of the hole-bands, which gives rise to increased superconducting transition temperatures due to an increase in the density of states at the Fermi level. We also showed that recently achieved interlayer distances in FeSe intercalates already produce a two-dimensional Fermi surface, which is optimal for T_c. Further experimental work should therefore concentrate on the charge doping through the spacer layer.

Chapter 8

Symmetry of the superconducting pairing in KFe_2As_2 under pressure

D. Guterding, S. Backes, H. O. Jeschke, R. Valentí,
Phys. Rev. B **91**, 140503(R) (2015).

After treating electron doped intercalates in the last chapter, we now focus our attention on extremely hole doped bulk materials. The family of AFe_2As_2 (A= Ba, Ca, Eu, K, Sr) superconductors, also called *122 materials*, has been intensively investigated in the past due to their richness in structural, magnetic and superconducting phases upon doping or application of pressure [57, 165–169]. One phase whose properties have been recently scrutinized at length is the collapsed tetragonal (CT) phase present in $BaFe_2As_2$, $CaFe_2As_2$, $EuFe_2As_2$, and $SrFe_2As_2$ under pressure and in $CaFe_2P_2$ [170–177]. The structural collapse of this phase has been shown to be assisted by the formation of As $4p_z$-As $4p_z$ bonds between adjacent Fe-As layers giving rise to a bonding-antibonding splitting of the As p_z bands [178]. It has been argued that this phase does not support superconductivity due to the absence of hole cylinders at the Brillouin zone center and the corresponding suppression of spin fluctuations [173, 179, 180]. However, recently Ying *et al.* [181] investigated the hole-doped end member of $Ba_{1-x}K_xFe_2As_2$, KFe_2As_2, under high pressure and observed a boost of the superconducting critical temperature T_c up to 12 K, precisely when the system undergoes a structural phase transition to a CT phase at a pressure pf $P_c \sim 15$ GPa. These authors attributed this behavior to possible correlation effects. Moreover, measurements of the Hall coefficient showed a change from positive to negative sign upon pressure, indicating that the effective nature of charge carriers changes from holes to electrons with increasing pressure. Similar experiments are also reported in Ref. [182].

KFe_2As_2 has a few distinct features: at ambient pressure, the system shows superconductivity at $T_c = 3.4$ K and follows a V-shaped pressure dependence of T_c for moderate pressures with a local minimum at a pressure of 1.55 GPa [183]. The origin of such behavior and the nature of the superconducting pairing symmetry are still under debate [150, 184–189]. However, it has been established by a few experimental and theoretical investigations based on angle-resolved photoemission spectroscopy, de Haas-van Alphen measurements, and density functional theory combined with dynamical mean field theory (DFT+DMFT) calculations that correlation effects crucially influence the behavior of this system at $P = 0$ GPa [161, 190–196]. Application of pressure should nevertheless reduce the relative importance of correlations with respect to the bandwidth increase. In fact, recent DFT+DMFT studies on $CaFe_2As_2$ in the high-pressure CT phase show that the topology of the Fermi surface is basically unaffected by correlations [197, 198]. One could argue though, that at ambient pressure $CaFe_2As_2$ is less correlated than KFe_2As_2 and, therefore, in KFe_2As_2 correlation effects may be still significant at finite pressure.

In order to resolve these questions, we performed density functional theory (DFT) and DFT+DMFT calculations for KFe_2As_2 in the CT phase. The DMFT part of the work was done by coauthor Steffen Backes. Our results show that the origin of superconductivity in the collapsed tetragonal phase in KFe_2As_2 lies in the qualitative changes in the electronic structure (Lifshitz transition) experienced under compression to a collapsed tetragonal phase and correlations play only a minor role. Whereas in the tetragonal phase at $P = 0$ GPa KFe_2As_2 features predominantly only hole pockets at the Brillouin zone center, at $P \sim$ 15 GPa in the CT phase significant electron pockets emerge at the Brillouin zone boundary, which together with the hole pockets at the Brillouin zone center favor a superconducting state with $s_\pm$ symmetry, as we show in our calculations of the superconducting gap function using the random phase approximation (RPA) spin fluctuation approach. Moreover, our results in the tetragonal phase of KFe_2As_2 at $P = 10$ GPa suggest a change of pairing symmetry from d_{xy} (tetragonal) to $s_\pm$ upon entering the collapsed phase (see Fig. 8.1). This scenario is distinct from the physics of the CT phase in $CaFe_2As_2$, where the hole pockets at the Brillouin zone center are absent. For comparison, we will present the susceptibility of collapsed tetragonal $CaFe_2As_2$, which is representative for the collapsed phase of AFe_2As_2 (A= Ba, Ca, Eu, Sr). Our findings also suggest an explanation for the change of sign in the Hall coefficient upon entering the CT phase in KFe_2As_2. This chapter is based on a publication [102], in which we summarized our results.

8.1 Methods

Density functional theory calculations were carried out using the FPLO code [76]. For the exchange-correlation functional we use the generalized gradient approximation (GGA) by Perdew, Burke, and Ernzerhof [75]. All calculations were converged on $20 \times 20 \times 20$ k-point grids.

The structural parameters for the CT phase of KFe_2As_2 were taken from Ref. [181]. We used the data points at $P \approx 21$ GPa, deep in the CT phase, where $a = 3.854$ Å and $c = 9.6$ Å. The fractional arsenic z-position ($z_{\mathrm{As}} = 0.36795$) was determined *ab-initio* via structural relaxation using the FPLO code. We also performed calculations for the crystal structure of Ref. [182], where a preliminary experimental value for the arsenic z-position was given. The electronic structure is very similar to the one reported here. For the CT phase of $CaFe_2As_2$ we used experimental lattice parameters from Ref. [199] ($T = 40$ K, $P \approx 21$ GPa) and determined the fractional arsenic z-position ($z_{\mathrm{As}} = 0.37045$) using FPLO. All Fe $3d$ orbitals are defined in a coordinate system rotated by 45° around the z-axis with respect to the conventional $I\,4/mmm$ unit cell.

Furthermore, we constructed 16-band tight-binding models from the DFT results using projective Wannier functions as implemented in FPLO [122]. We keep the Fe $3d$ and As $4p$ states, which correspond to an energy window from -7 eV to $+6$ eV. Subsequently,

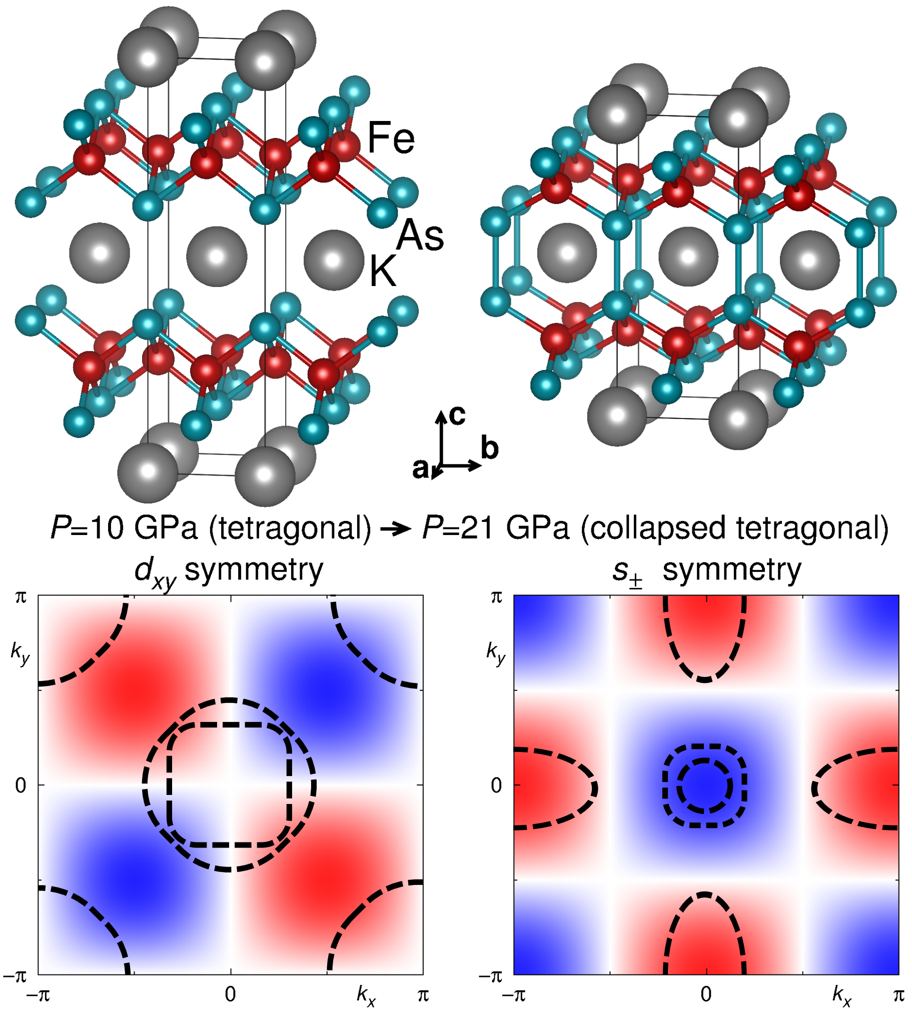

Figure 8.1: Crystal structure, schematic Fermi surface (dashed lines) and schematic superconducting gap function (background color) of KFe_2As_2 in the one-Fe Brillouin zone before and after the volume collapse. The Lifshitz transition associated with the formation of As $4p_z$-As $4p_z$ bonds in the CT phase changes the superconducting pairing symmetry from d_{xy} to $s_\pm$. Figure taken from Ref. [102].

we unfold the 16-band model using our recently developed glide reflection unfolding technique [160], which produces an effective eight-band model of the three-dimensional one-Fe Brillouin zone.

We analyze these eight-band models using the 3D version of our RPA implementation. The arsenic states are kept in the entire calculation, but the multi-orbital interactions are considered only between Fe $3d$ states. For calculating the susceptibility we used $30\times30\times10$ k-point grids and an inverse temperature of $\beta = 40$ eV^{-1}. The pairing interaction is constructed using about 800 points on the three-dimensional Fermi surface. The multi-orbital Hubbard model includes the on-site intra (inter) orbital Coulomb interaction U

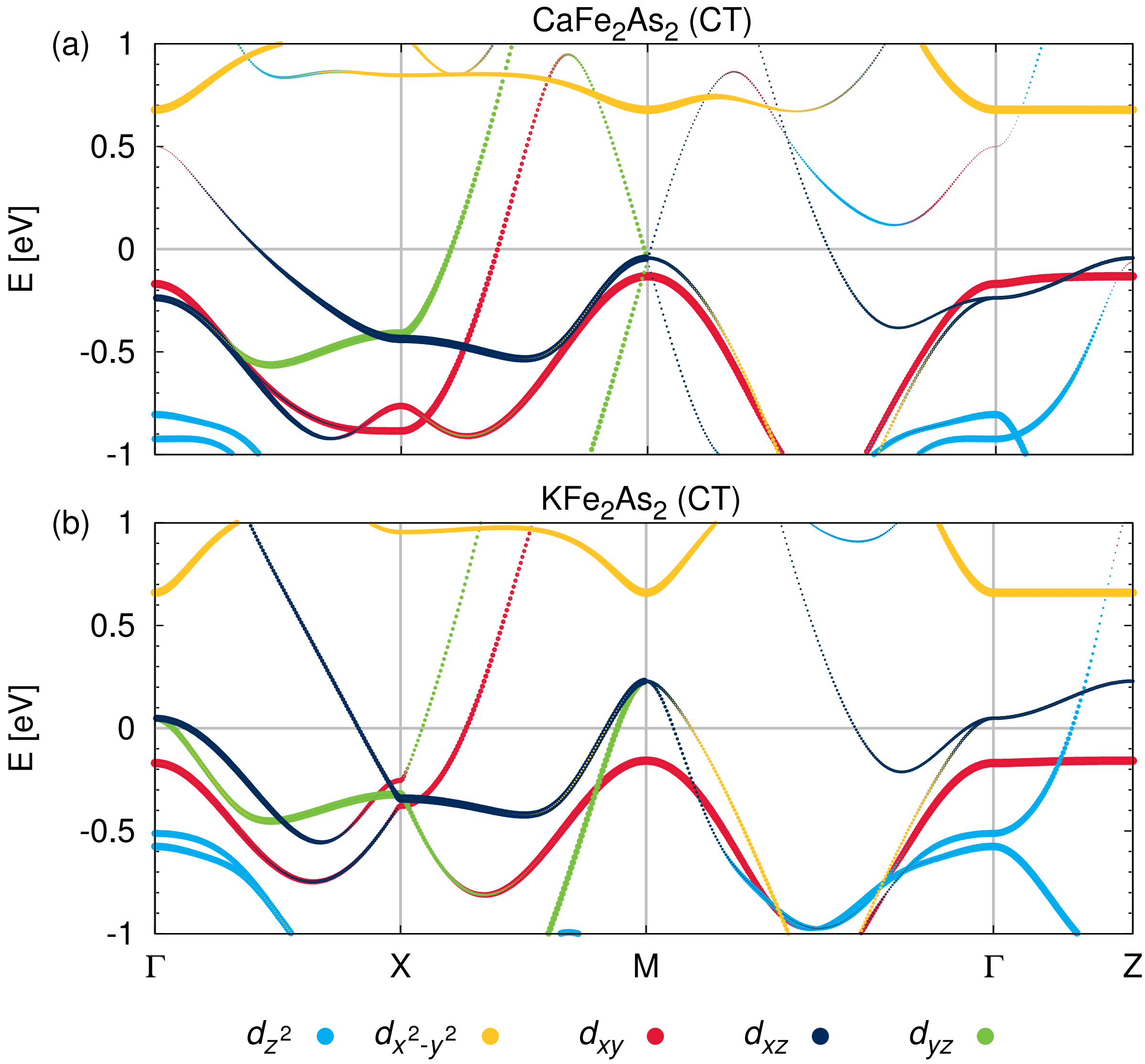

Figure 8.2: Electronic bandstructure of the collapsed tetragonal phase in (a) CaFe$_2$As$_2$ and (b) KFe$_2$As$_2$. The path is chosen in the one-Fe equivalent Brillouin zone. The colors indicate the weights of Fe 3d states. Figure taken from Ref. [102].

(V), the Hund's rule coupling J and the pair hopping energy J'. We assume spin rotation-invariant interaction parameters $U = 2.4$ eV, $V = U/2$, and $J = J' = U/4$. Because of the large bandwidth in the collapsed tetragonal phase, these comparatively large values are necessary to bring the system close to the RPA instability. Note however, that the symmetry of the superconducting gap in this system does not change, even if significantly reduced parameter values are considered.

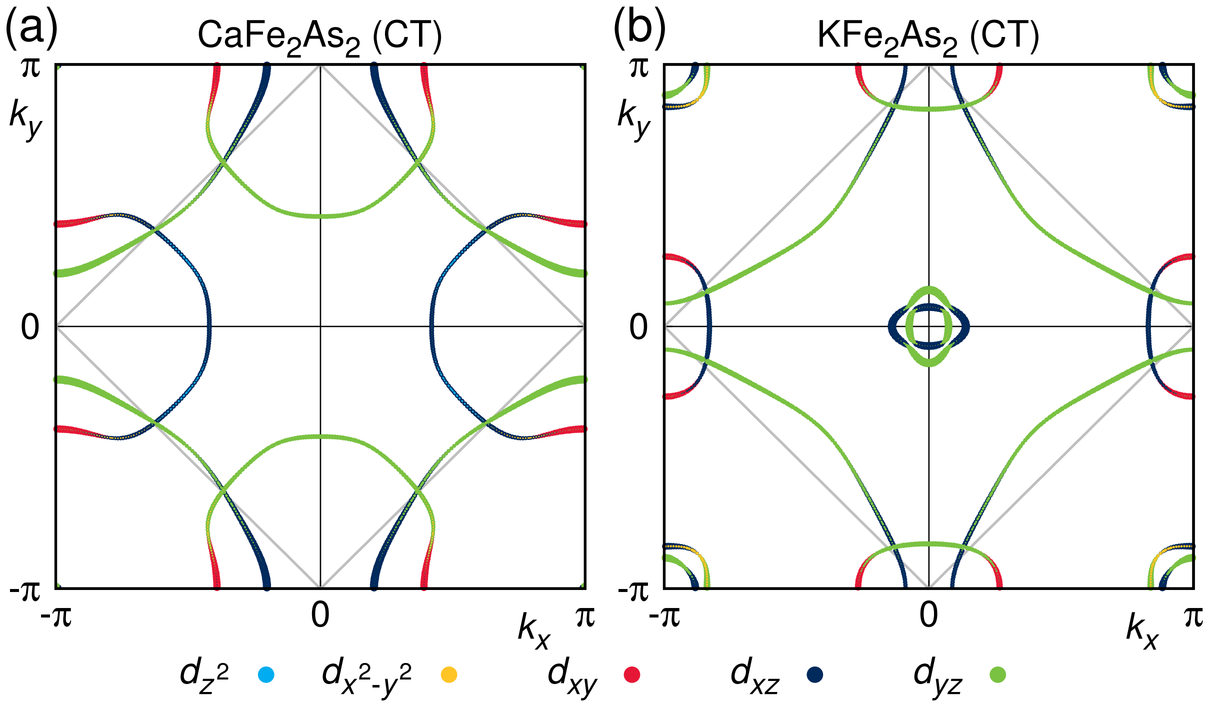

Figure 8.3: Fermi surface of the collapsed tetragonal phase in (a) $CaFe_2As_2$ and (b) KFe_2As_2 at $k_z = 0$. The full plot spans the one-Fe equivalent Brillouin zone, while the area enclosed by the grey lines is the two-Fe equivalent Brillouin zone. The colors indicate the weights of Fe $3d$ states. Figure taken from Ref. [102].

8.2 Results and discussion

The electronic bandstructure in the collapsed tetragonal phase of $CaFe_2As_2$ and KFe_2As_2 is shown in Fig. 8.2. These results already reveal a striking difference between the CT phases of $CaFe_2As_2$ and KFe_2As_2: while the former does not feature hole bands crossing the Fermi level at Γ and only one band crossing the Fermi level at M $(\pi, \pi, 0)$, the latter does feature hole-pockets at both Γ and M in the one-Fe equivalent Brillouin zone. The reason for this difference in electronic structure is that KFe_2As_2 is strongly hole-doped compared to $CaFe_2As_2$.

In Fig. 8.3 we show the Fermi surface in the one-Fe equivalent Brillouin zone at $k_z = 0$. In both cases, the Fermi surface is dominated by Fe $3d_{xz/yz}$ character. The hole cylinders in KFe_2As_2 span the entire k_z direction of the Brillouin zone, while only a small three-dimensional hole-pocket is present in $CaFe_2As_2$ (below the resolution of Fig. 8.3). For KFe_2As_2, the hole-pockets at M $(\pi, \pi, 0)$ and the electron pockets at X $(\pi, 0, 0)$ are clearly nested, while no nesting is observed for $CaFe_2As_2$. It is important to note here, that the folding vector in the 122 family of iron-based superconductors is (π, π, π), so that the hole-pockets at M $(\pi, \pi, 0)$ will be located at Z $(0, 0, \pi)$ after unfolding the bands to the effective one-Fe picture [160].

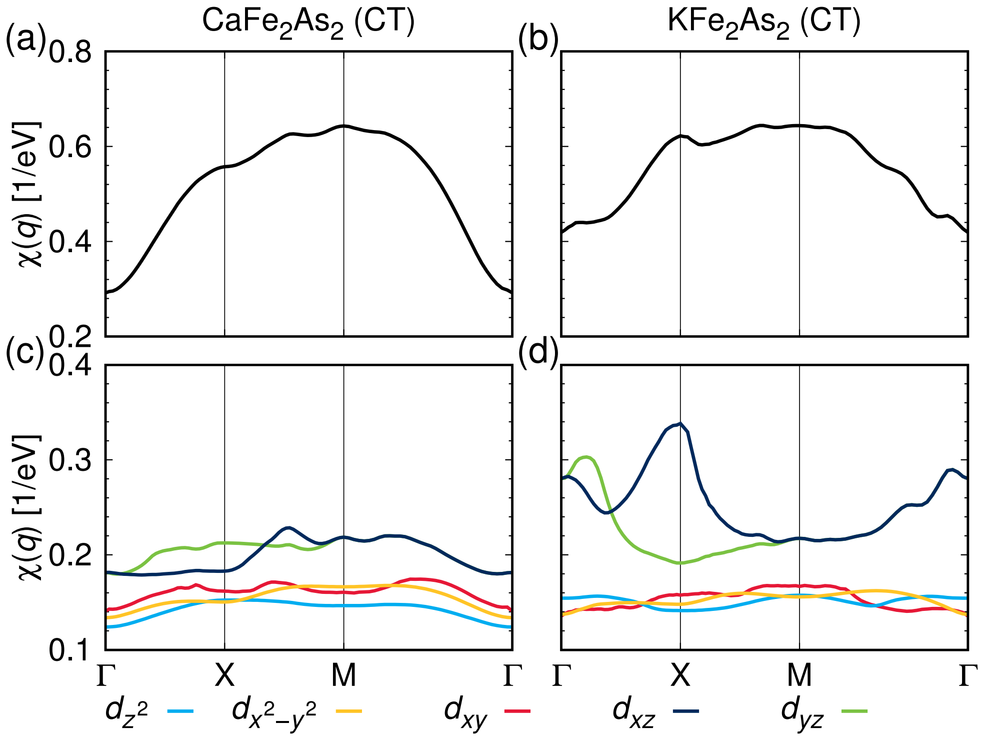

Figure 8.4: Summed static susceptibility (top) and its diagonal components χ_{aa}^{aa} (bottom) in the eight-band tight-binding model for [(a) and (c)] $CaFe_2As_2$ and [(b) and (d)] KFe_2As_2 in the one-Fe Brillouin zone. The colors identify the Fe $3d$ states. Figure taken from Ref. [102].

After qualitatively identifying the difference between the CT phases of $CaFe_2As_2$ and KFe_2As_2, we calculate the non-interacting static susceptibility to verify that the better nesting of KFe_2As_2 generates stronger spin fluctuations. At first glance, the observable static susceptibility displayed in Fig. 8.4 is comparable for $CaFe_2As_2$ and KFe_2As_2. A key difference is however revealed upon investigation of the largest elements, i.e. the diagonal entries χ_{aa}^{aa}. These show that in $CaFe_2As_2$ the susceptibility has broad plateaus, while in KFe_2As_2 the susceptibility has a strong peak at X $(\pi, 0, 0)$ in the one-Fe Brillouin zone, which corresponds to the usual $s_\pm$ pairing scenario that relies on electron-hole nesting. In $CaFe_2As_2$ the pairing interaction is highly frustrated, because there is no clear peak in favor of one pairing channel.

We have also performed spin-polarized calculations for KFe_2As_2 at $P \approx 21$ GPa in order to confirm the antiferromagnetic instability we find in the linear response calculations. Out of ferromagnetic, Néel and stripe antiferromagnetic order only the stripe antiferromagnet is stable with small moments of $0.07\mu_B$ on Fe, in agreement with our calculations for the susceptibility.

The leading superconducting gap function of KFe_2As_2 in the CT phase is shown in Fig. 8.5. As expected from our susceptibility calculations, the pairing symmetry is s-wave with a sign-change between electron and hole-pockets. While the superconducting gap is

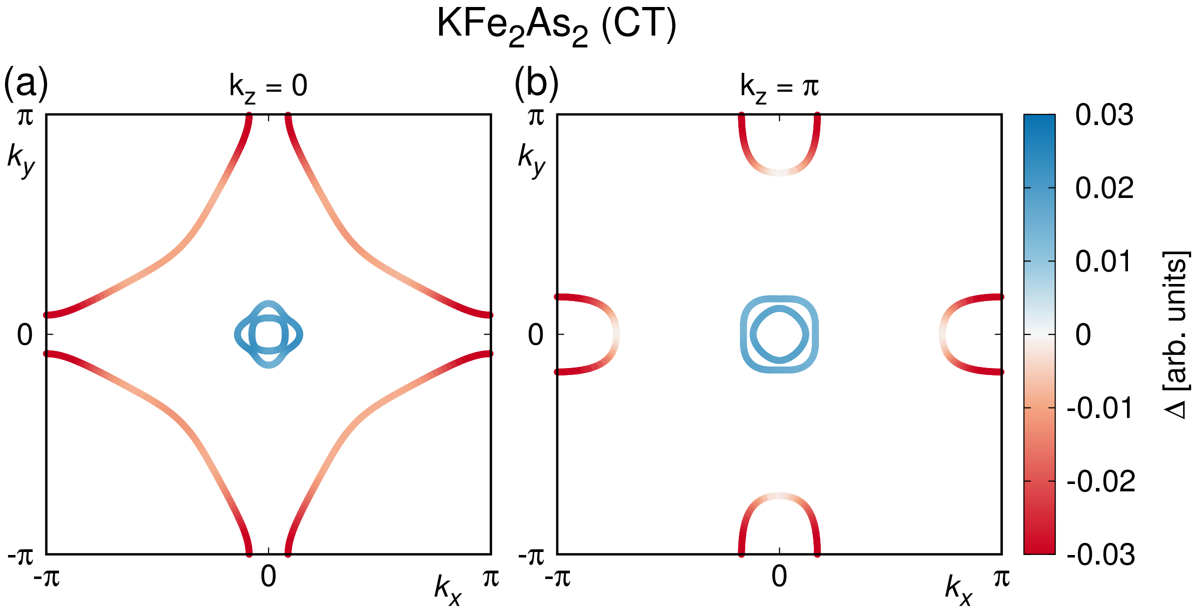

Figure 8.5: Leading superconducting gap function ($s_\pm$) of the eight-band model in the one-Fe Brillouin zone of KFe$_2$As$_2$ in the CT phase at (a) $k_z = 0$ and (b) $k_z = \pi$. Figure taken from Ref. [102].

nodeless in the $k_z = 0$ plane, the $k_z = \pi$ plane does show nodes where the orbital character changes from Fe $3d_{xz/yz}$ to Fe $3d_{xy}$. Note that this $k_z = \pi$ structure of the superconducting gap is exactly the same as in the well studied LaFeAsO compound [96], which shows that the CT phase of KFe$_2$As$_2$ closely resembles usual iron-based superconductors, although it is much more three-dimensional than, e.g., in LaFeAsO.

We have also calculated the superconducting gap function for KFe$_2$As$_2$ at $P = 10$ GPa in the tetragonal phase and find d_{xy} as the leading pairing symmetry [102]. The dominant $d_{x^2-y^2}$-solution obtained in model calculations based on rigid band shifts [150, 185] is also present in our calculation, but as a sub-leading solution. Our results strongly suggest that the Lifshitz transition, which occurs upon entering the collapsed tetragonal phase, changes the symmetry of the superconducting gap function from d-wave (tetragonal) to s-wave (CT) (see Fig. 8.1). The possible simultaneous change of pairing symmetry, density of states and T_c potentially opens up different routes to understanding their quantitative connection.

In order to estimate the strength of local electronic correlations in collapsed tetragonal KFe$_2$As$_2$, we performed fully charge self-consistent DFT+DMFT calculations. We found that the strength of local electronic correlations in the CT phases of KFe$_2$As$_2$ and CaFe$_2$As$_2$ [49, 197] are comparable. As in CaFe$_2$As$_2$, the effects of local electronic correlations on the Fermi surface are negligible. The higher T_c of the collapsed phase in absence of strong correlations raises the question how important strong correlations are in general for iron-based superconductivity. This issue demands further investigation.

Finally, the change of dominant charge carriers from hole-like to electron-like states measured in the Hall-coefficient under pressure [181] is naturally explained from our calculated Fermi surfaces. While KFe_2As_2 is known to show only hole-pockets at zero pressure, the CT phase features also large electron pockets. On a small fraction of these electron pockets, the dominating orbital character is Fe $3d_{xy}$ (Fig. 8.3). It was shown in Ref. [200] that quasiparticle lifetimes on the Fermi surface can be very anisotropic and long-lived states are favored where marginal orbital characters appear. As Fe $3d_{xy}$ character is only present on the electron pockets, these states contribute significantly to transport and are responsible for the negative sign of the Hall coefficient.

8.3 Summary

We have shown that the electronic structure of the collapsed tetragonal phase of KFe_2As_2 qualitatively differs from that of other known collapsed materials. Upon entering the CT phase, the Fermi surface of KFe_2As_2 undergoes a Lifshitz transition with electron pockets appearing at the Brillouin zone boundary, which are nested with the hole pockets at the Brillouin zone center. Thus, the spin fluctuations in collapsed tetragonal KFe_2As_2 resemble those of other iron-based superconductors in non-collapsed phases and the superconducting gap function assumes the well-known $s_\pm$ symmetry. This is in contrast to other known materials in the CT phase, like $CaFe_2As_2$, where hole pockets at the Brillouin zone center are absent and no superconductivity is favored. Based on our LDA+DMFT calculations, the CT phase of KFe_2As_2 is significantly less correlated than the tetragonal phase, and mass enhancements are comparable to the CT phase of $CaFe_2As_2$. Finally, we suggest that the change of dominant charge carriers from hole-like to electron-like can be explained from anisotropic quasiparticle lifetimes.

Chapter 9

Non-trivial role of interlayer cations in iron-based superconductors

D. Guterding, H. O. Jeschke, I. I. Mazin,
J. K. Glasbrenner, E. Bascones, R. Valentí,
arXiv:1610.08626.

After the initial discovery of high-temperature superconductivity in doped LaFeAsO [53], a large variety of other iron pnictide and chalcogenide have been shown to be superconductors [54], with some reports of the transition temperature T_c as high as 100 K [59]. On the other hand, isoelectronic and isostructural iron germanides are either non-superconducting [60–63] or possibly superconduct at very low temperatures [64, 65]. The currently most intensively debated material is YFe_2Ge_2, for which superconductivity below 2 K has been reported [65]. Its electronic structure is very similar to that of $CaFe_2As_2$ in the collapsed tetragonal phase, but with significant hole-doping [65, 201, 202]. This led to speculation [65] about a connection between superconductivity in YFe_2Ge_2 and the collapsed phase of the extreme hole-doped pnictide, KFe_2As_2 [102, 181, 182]. Furthermore, Wang *et al.* [203] recently found YFe_2Ge_2 to be close to a magnetic instability and X-ray absorption and photoemission experiments show evidence for strong spin fluctuations [204] and moderate correlation effects [205] in this material.

It is generally agreed that magnetism plays an important role in superconductivity of Fe-based superconductors (FeBS) [54, 206–212]. It is, therefore, natural to ask whether the magnetic tendencies in iron germanides are fundamentally different from those in iron pnictides and chalcogenides and why that is the case. In a first attempt to understand the lack of superconductivity in Fe germanides, a few authors investigated the electronic properties of the isoelectronic and isostructural materials MgFeGe and LiFeAs [213–215]. The former is a paramagnetic metal, while the latter is a superconductor. An important conclusion was that the dominant magnetic exchange interactions in MgFeGe are ferromagnetic, while those in LiFeAs are antiferromagnetic. The microscopic origin of this different behavior was, however, not further explored.

In this chapter we show that (i) ferromagnetism is a general trait in iron germanides, which is detrimental for superconductivity, and that (ii) the ferromagnetic itendencies arise from the interaction of the cation spacer with the FeGe layer. In fact, the hole-doping or collapse of the c-axis in YFe_2Ge_2 are not essential for this behavior, but the key is in substitution of As by Ge and the corresponding substitution of monovalent or

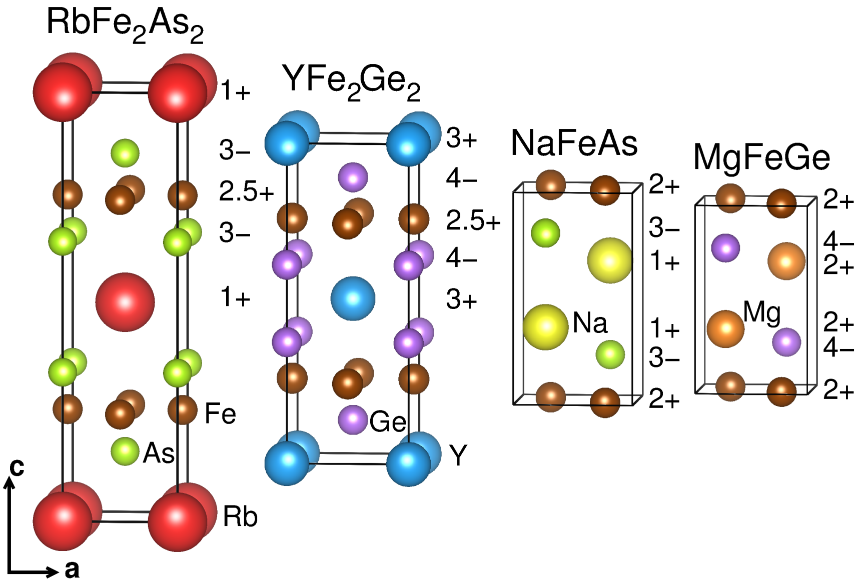

Figure 9.1: Crystal structures of $RbFe_2As_2$, YFe_2Ge_2, NaFeAs and MgFeGe. The unit cells and interatomic distances are true to scale. The numbers next to the unit cells indicate the nominal valence of atoms at the same vertical positions. Figure taken from Ref. [219].

divalent spacers by divalent or trivalent cations, respectively. This modifies the electronic bandstructure in a wide range of energies at and away from the Fermi level and creates ferromagnetic tendencies, which suppress superconductivity. Hence, one can go from As to Se/Te, *i.e.*, right in the periodic table, and find further FeBS, but not to the left towards Ge. In agreement with recent NMR measurements [216], our study highlights the role of ferromagnetic fluctuations in determining the value of T_c in FeBS.

Our analysis shows that conventional low-energy models of FeBS, which only incorporate the d and p states of Fe with the nearest cations, are not sufficient to explain key features of FeBS. Although these models usually reproduce the Fermi surface very well, they do not reflect the physical instabilities of the actual materials, because they neglect the interaction with the spacer between the FeX (X=As, Se, Ge,...) layers. Although bulk FeSe does not contain spacer layers, our arguments might be relevant for intercalates [55, 101], alkali-dosed thick-films [218] and monolayered FeSe on $SrTiO_3$ [59]. This chapter is based on Ref. [219], in which our findings are published.

9.1 Methods and materials

We compare isoelectronic iron arsenides and iron germanides from (i) the so-called hole-doped *122-family* where iron is in a nominal oxidation $Fe^{2.5+}$ with $d^{5.5}$ occupation [161, 196, 220] and (ii) the so-called *111-family* with Fe^{2+} in a d^6 configuration [161, 221, 222]. The crystal structures of $RbFe_2As_2$, YFe_2Ge_2, NaFeAs and MgFeGe are shown in Fig. 9.1, where we also indicate the nominal valences of the atoms in each compound. Lattice constants and internal positions were taken from experiment [63, 223–225].

The most obvious structural difference between iron arsenides and iron germanides is a shrinking of the c-axis (Fig. 9.1). From NaFeAs to MgFeGe it is not as pronounced as from $RbFe_2As_2$ to YFe_2Ge_2, where Ge p_z-p_z bonds may form (in MgFeGe direct Ge-Ge bonding is not possible). Although these materials are isoelectronic, the germanides have a stronger charge transfer between the FeX (X= As, Ge) and the spacer layers.

The isoelectronic substitution of As by Ge, Rb by Y, and Na by Mg was simulated within the virtual crystal approximation (VCA). To disentangle effects originating from direct atomic substitution from effects coming from small changes of bond-distances and -angles in real materials, we performed all calculations for the *122-family* with the structural parameters of YFe_2Ge_2 [223] and those for the *111-family* with the structural parameters of MgFeGe [63].

We calculate the magnetic exchange interactions based on a $2 \times 2 \times 1$ supercell containing eight Fe atoms. This leads to 17 inequivalent magnetic configurations for the *122-compounds* and 13 inequivalent configurations for the *111-compounds.* We used 8^3 k-point grids for converging these magnetic calculations. The Heisenberg exchange couplings were extracted by mapping DFT total energies of all inequivalent magnetic configurations to a classical Heisenberg model for each composition. These calculations were performed by coauthor Harald O. Jeschke.

We also analyze the density of states by using the extended Stoner model [226, 227], which is a simple tool for understanding the origin of itinerant ferromagnetism. Within the extended Stoner theory the total magnetization energy can be written as

$$E(m) = \frac{1}{2}\int_0^m \frac{m'dm'}{\bar{N}(m')} - \frac{Im^2}{4}, \tag{9.1}$$

where m is the magnetzation and $\bar{N}(m)$ is the paramagnetic density of states averaged between the Fermi levels of the spin-up and the spin-down channels. In the limit of $m \to 0$ the effective Stoner DOS is simply the total DOS at the Fermi level. For all other moments m the effective Stoner DOS is the average total DOS within an increasingly large energy window around the Fermi energy. The density of states is evaluated within the rigid-band approximation starting from the paramagnetic state. The first term is the one-electron energy, because the change in energy for a single electron upon generating a moment m is half the energy difference $\Delta(m)$ between the Fermi levels of the spin-up and spin-down channels. Using $\Delta(m)\bar{N}(m) = m$ we get

$$\frac{dE}{dm} = \frac{\Delta(m)}{2} = \frac{m}{2\bar{N}(m)}. \tag{9.2}$$

Integrating this expression one obtains the first term in Eq. 9.1. The second term is the so-called Stoner parameter, which parametrizes the ferromagnetic exchange-interactions between electrons in an averaged form.

Now we derive the conditions under which the paramagnetic state is unstable towards ferromagnetism. We start by finding the extrema in the energy for Eq. 9.1. These are given by

$$0 \overset{!}{=} \frac{dE}{dm} = \bar{N}(m)^{-1} - I. \tag{9.3}$$

Next we find the condition under which this extremum is a minimum in the magnetization energy. It is given by

$$0 \overset{!}{<} \frac{d^2E}{dm^2} = \frac{1}{2\bar{N}(m)} - m\frac{d\bar{N}(m)/dm}{2\bar{N}(m)^2} - \frac{I}{2} = -m\frac{d\bar{N}(m)/dm}{2\bar{N}(m)^2}, \tag{9.4}$$

where we used $I = \bar{N}(m)^{-1}$. Since all moments m and effective densities of states are positive, the resulting condition is

$$0 > d\bar{N}(m)/dm. \tag{9.5}$$

Combining Eqs. 9.3 and 9.5 we find that the paramagnetic state is unstable towards ferromagnetism if the conditions $1/I = \bar{N}(m)$ and $0 > d\bar{N}(m)/dm$ are fullfilled at some m, where $\bar{N}(m)$ is the paramagnetic density of states averaged over an energy window that contains a sufficient number of states to realize an Fe moment m, and I is the Stoner parameter.

The Stoner parameter I can be obtained from fixed-moment spin-polarized DFT calculations by inserting the DFT energies for $E(m)$ into Eq. 9.1, using the paramagnetic DFT density of states to calculate $\bar{N}(m)$ and performing a numerical optimization to obtain the value of I on the parabolic term in Eq. 9.1. The effective Stoner parameter I was calculated from a fit to DFT total energies of ferromagnetic configurations with a moment of up to 3 μ_B per iron site. All calculations for the Stoner analysis were converged using 20^3 k-point grids.

9.2 Results and discussion

We first calculated the DFT energies of various spin configurations. By means of the VCA we interpolated between $RbFe_2As_2$ and YFe_2Ge_2 [via $SrFe_2(As_{0.5}Ge_{0.5})_2$] and between NaFeAs and MgFeGe. Using a two-dimensional Heisenberg model to parametrize the DFT energies we observe that the nearest-neighbor exchange coupling J_1 universally changes from antiferromagnetic to ferromagnetic when going continuously from As to Ge without changing the electron count, while all other exchange couplings are almost unaffected (Fig. 9.2). Only in the *111-family* the next-nearest-neighbor exchange J_2 is also reduced, but it does not change sign. At the germanide end-point the ferromagnetic J_1 becomes the dominant exchange interaction.

Remarkably, we also obtained a large ferromagnetic J_1 for NaFeAs after we expanded the structure used for Fig. 9.2 by 10% along the c-axis but kept all distances within the FeAs layer unchanged by the expansion. These results indicate that NaFeAs can also be turned ferromagnetic by separating the FeAs layers and by shifting Na further away from the layers.

From this analysis we conclude that previous suggestions [203] that iron germanides and iron pnictides show similar magnetic behavior don't hold. While both families have a

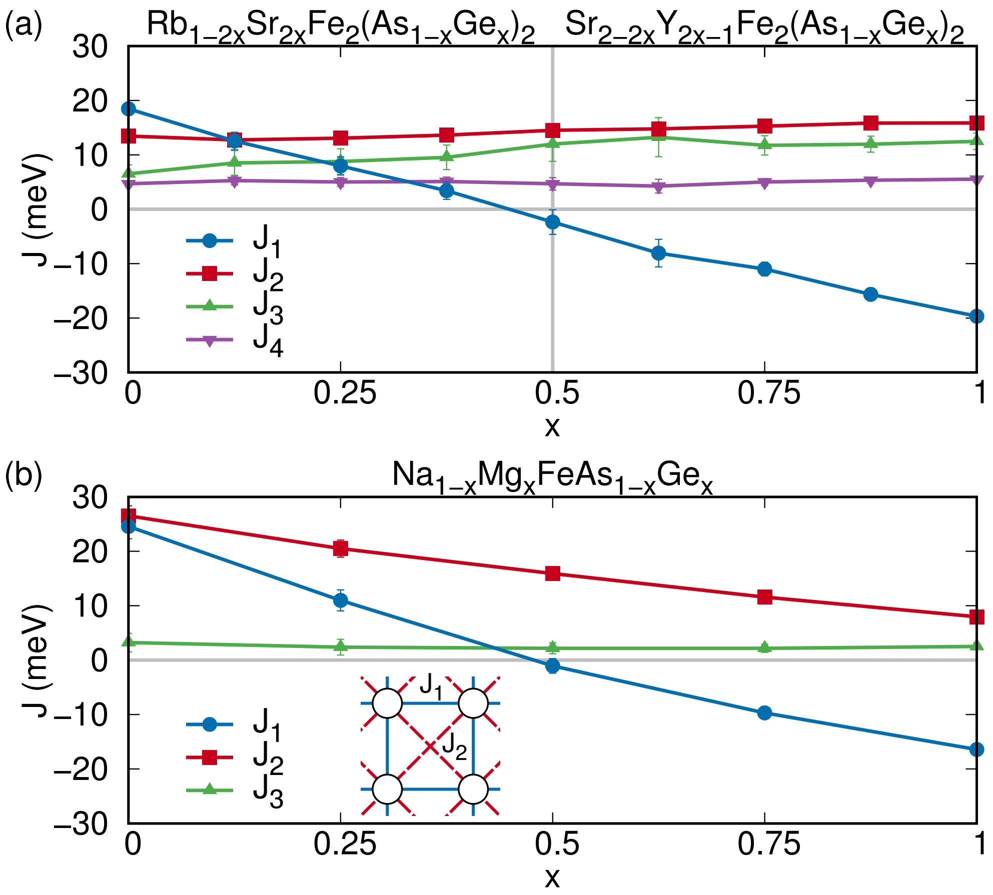

Figure 9.2: Calculated Heisenberg exchange parameters for (a) the VCA interpolation between $RbFe_2As_2$ and YFe_2Ge_2 [via $SrFe_2(As_{0.5}Ge_{0.5})_2$] and (b) the VCA interpolation between NaFeAs and MgFeGe. Lines are guides to the eye. The error bars represent the statistical errors of the fit. The inset of (b) shows the structure of the two-dimensional Heisenberg model we use to fit the DFT energies. J_1 is the nearest-neighbor coupling in the square lattice of Fe atoms, while J_2 is the next-nearest neighbor coupling. J_3 and J_4 are longer-range exchange couplings. Positive values of J correspond to antiferromagnetic exchange. Note that all calculations were performed in the crystal structures of YFe_2Ge_2 and MgFeGe respectively. Figure taken from Ref. [219].

stripe antiferromagnetic ground state, the nature of excitations is entirely different. This is reflected in the presence of a nearest neighbor ferromagnetic exchange J_1 in iron germanides and antiferromagnetic J_1 in the iron pnictides albeit the very similar crystal structure and electronic structure at the Fermi level. In particular, the results on the expanded NaFeAs suggest that the origin of this different behavior lies dominantly on the relative distance of the spacer to the FeX plane.

A further distinctive feature of the germanides is that the magnetism of Fe in YFe_2Ge_2 appears to be rather peculiar. There is a low- and a high-moment solution for Fe, the former more stabilized for shorter Fe-Ge bond length (in pnictides, either a high-spin

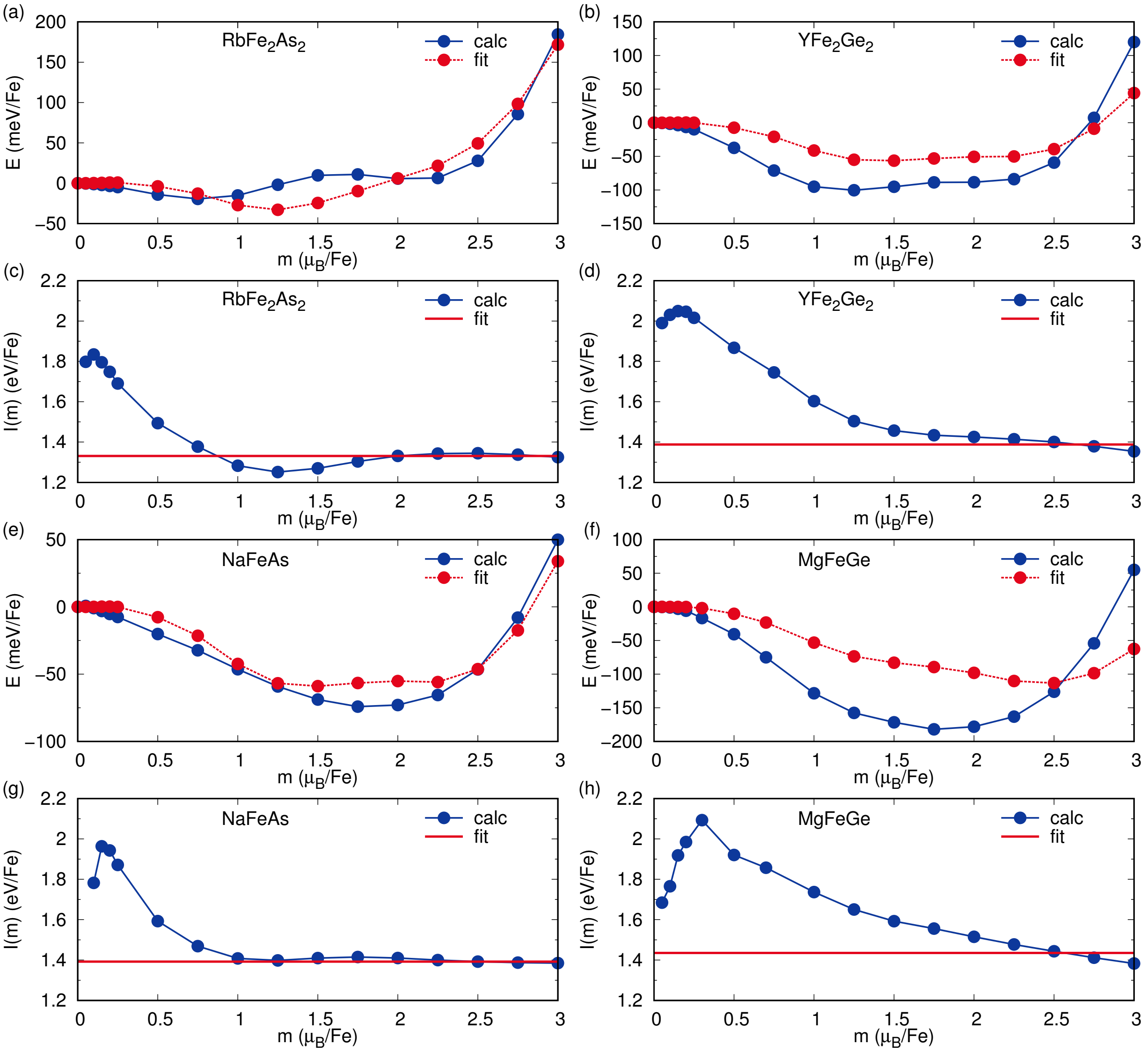

Figure 9.3: (a),(b),(e),(f) Fit of Eq. 9.1 to the fixed-moment energies calculated from DFT. (c),(d),(g),(h) Same data as in (a),(b),(e),(f) after subtracting the one-electron energies (first term in Eq. 9.1) and dividing by $-m^2/4$. Figure taken from Ref. [219].

solution is realized, or magnetism collapses completely).

To understand in a simple framework the origin of the magnetic behavior presented before we investigate the effective density of states $\bar{N}$ as a function of the magnetic moment m within the extended Stoner model. We first calculated the Stoner parameter for each material. The results are shown in Fig. 9.3. The values for the Stoner parameters are 1.331 eV ($RbFe_2As_2$ in YFe_2Ge_2 structure), 1.388 eV (YFe_2Ge_2), 1.392 eV (NaFeAs in MgFeGe structure) and 1.435 (MgFeGe). Note that the fit is good in the high moment region. The deviation for low moments probably originates from an admixture of non-Fe

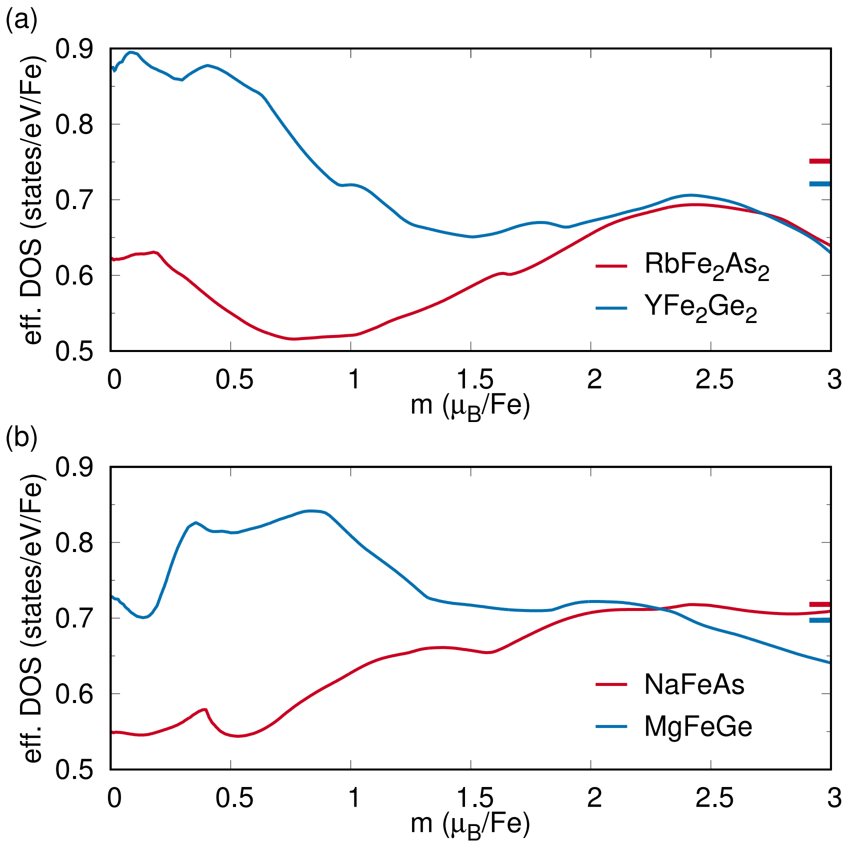

Figure 9.4: Effective density of states in the extended Stoner model as a function of magnetic moment for (a) $RbFe_2As_2$ and YFe_2Ge_2 and (b) NaFeAs and MgFeGe. The colored bars on the right y-axis indicate the calculated inverse Stoner parameters $1/I$ for the respective case. All calculations were performed in the crystal structures of YFe_2Ge_2 and MgFeGe respectively. Figure taken from Ref. [219].

states, which increases the effective Stoner parameter. This would also explain why the fit is generally worse for germanide compounds, where also a significant amount of interlayer cation states is at the Fermi level. Since we use extended Stoner theory only as a qualitative tool, these discrepancies are of minor importance.

Upon analyzing the various materials we observe that (i) iron germanides have in general a higher DOS at the Fermi level and (ii) a significant number of states is shifted from higher energies towards the Fermi level, as compared to pnictides. This is signalled by the strong increase of the effective DOS at low moments (see Fig. 9.4 where results for YFe_2Ge_2 versus $RbFe_2As_2$ and MgFeGe versus NaFeAs are shown). Interestingly, the changes in the high-moment region ($m \sim 2.4\ \mu_B$) are marginal, while they are considerable in the low-moment region ($m < 1.0\ \mu_B$). Furthermore, we find that the Stoner parameter I is almost independent of the material and that $1/I$ lies between 0.7 eV^{-1} and 0.75 eV^{-1}. Therefore, by looking for crossings of $\bar{N}(m)$ with $1/I$ in Fig. 9.4, we establish that the

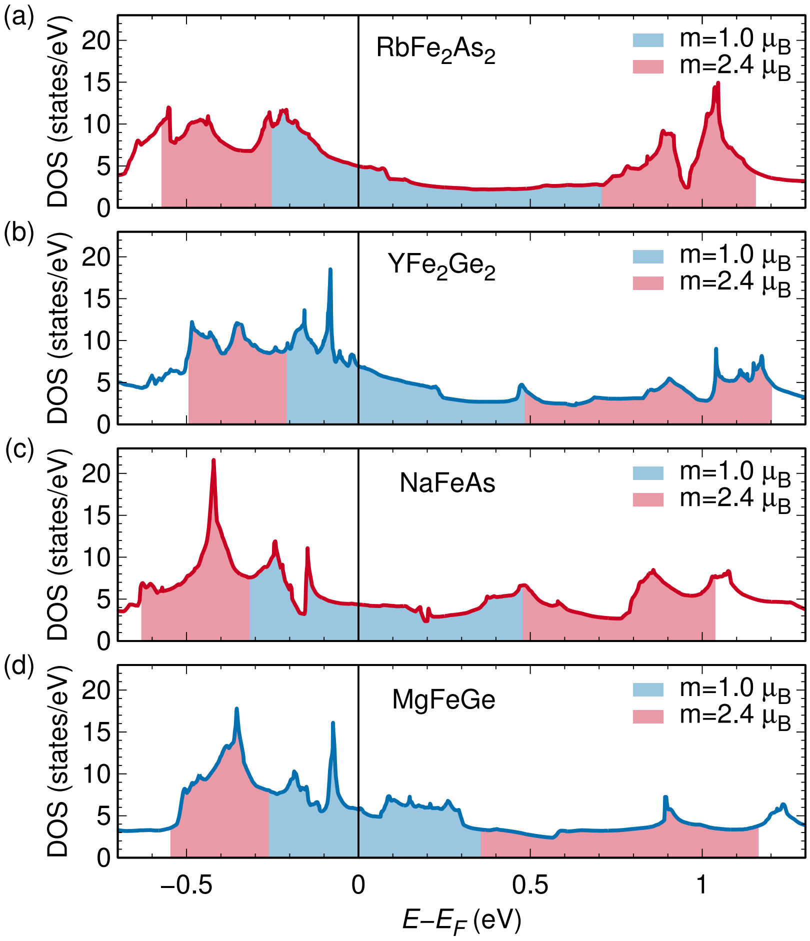

Figure 9.5: Total density of states calculated from DFT for (a) $RbFe_2As_2$, (b) YFe_2Fe_2, (c) NaFeAs and (d) MgFeGe. The shaded areas below the curves correspond to the energy range needed to realize a moment of $1.0\,\mu_B$ or $2.4\,\mu_B$ per iron within the extended Stoner model. All calculations were performed in the crystal structures of YFe_2Ge_2 and MgFeGe respectively. Figure taken from Ref. [219].

extended Stoner criterion for ferromagnetism is fulfilled in iron germanides, but not in pnictides. Moreover, the metastability of different magnetic moments in YFe_2Ge_2 [203] is also evident from this analysis, since the effective DOS almost fulfills the extended Stoner criterion also for large moments of about 2.5 μ_B.

Fig. 9.5 shows the total calculated DOS for $RbFe_2As_2$ vs. YFe_2Ge_2, and NaFeAs vs. MgFeGe, where we colored the energy regions corresponding to magnetic moments of $m = 1.0\ \mu_B$ (blue) and $m = 2.4\ \mu_B$ (red) in the extended Stoner model. The energy range corresponding to $m = 1.0\ \mu_B$ is compressed when going from arsenides to germanides, while the energy range corresponding to $m = 2.4\ \mu_B$ even increases marginally in germanides. As the density of states in the window shown is dominated by Fe states, this implies that the bandwidth of some of the Fe states must be selectively reduced in iron germanides,

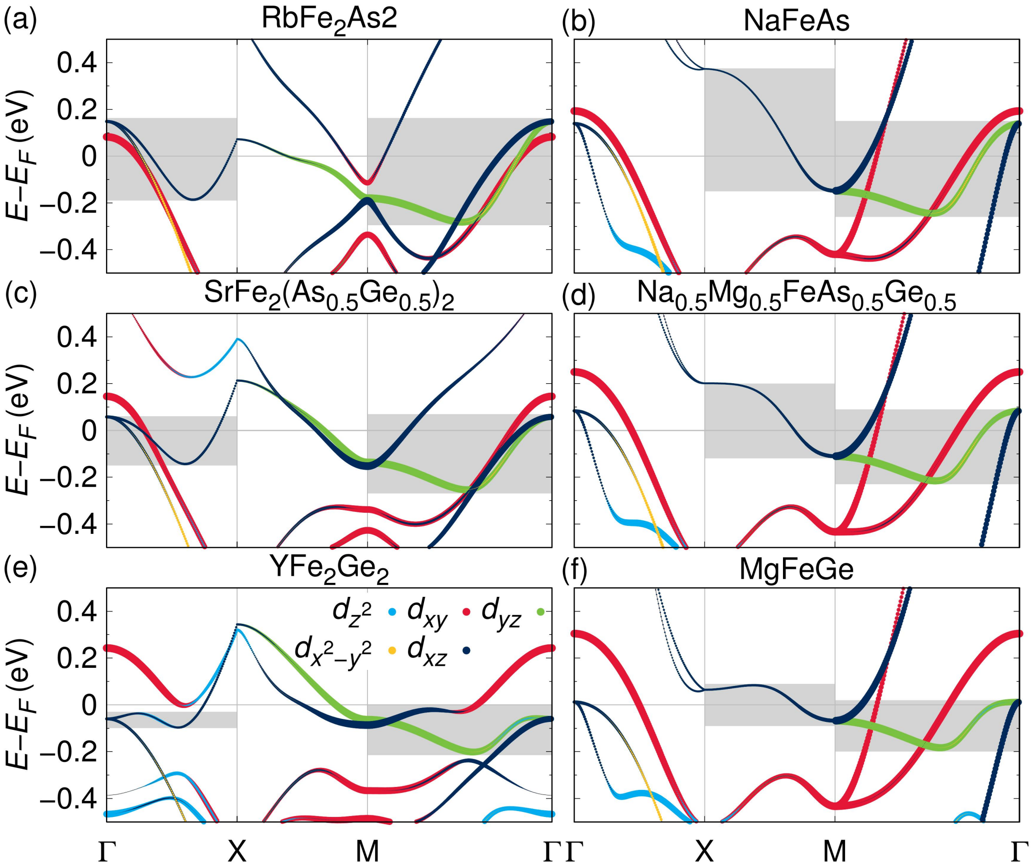

Figure 9.6: Electronic bandstructure for (a) $RbFe_2As_2$, (b) NaFeAs, (c) $SrFe_2(As_{0.5}Ge_{0.5})_2$, (d) $Na_{0.5}Mg_{0.5}FeAs_{0.5}Ge_{0.5}$, (e) YFe_2Ge_2 and (f) MgFeGe. The weights of Fe $3d$ orbitals are indicated by the colors. The areas shaded in light grey highlight regions in which bands become more flat when going from the arsenide to the corresponding germanide compound via VCA. All calculations were performed in the crystal structures of YFe_2Ge_2 and MgFeGe respectively.

while the overall bandwidth is about constant.

The electronic bands in the relevant energy range are shown in Fig. 9.6. The energy and momentum regions in which the bands become flat when going from the arsenide to the corresponding germanid compound via VCA are shaded in light grey. The analysis shows that in this energy window mostly Fe $3d_{xz/yz}$ states are affected by the substitution of elements.

9.3 Summary and outlook

We have established in this work that iron germanides have a general tendency towards ferromagnetism which proves detrimental for superconductivity, even though the Fermi surface is very similar to that of isoelectronic pnictides. Most importantly, this tendency can be traced down to the flattening of some bands near the Fermi level and a modified electronic bandstructure in a wide range of energies at and away from the Fermi level. Neither the collapse of the c-axis, nor the hole-doping of the *122* germanides are essential for the emergence of ferromagnetism. However, the character and position of the intercalating species, normally considered irrelevant and not included in any theory or model, plays a decisive role.

Our findings have important implications for iron-based superconductivity in general: (i) The Fermi surface geometry and topology is an important, but not the only condition for emerging superconductivity. The character of spin fluctuations, even on the level of the simple ferromagnetic-antiferromagnetic dichotomy, may be qualitatively different in seemingly similar materials. (ii) A quantitative theory of T_c in iron-based superconductors must include the interaction between all constituents of the unit cell, including, in some cases, the so-called *space-fillers.* (iii) While FeGe layers *per se* are not necessarily ferromagnetic, the fact that they have to be spaced with different elements (*e.g.,* Mg vs. Na, or Y vs. Sr) drives them ferromagnetic. (iv) In a more general way, it does matter what we place next to or on top of an Fe-ligand layer. This observation may be directly related to an apparent role that interfacial effects play in high-T_c Fe chalcogenides, such as FeSe monolayers deposited on specially prepared surfaces or $K_xFe_{2-y}Se_2$ filaments embedded in the magnetic $K_2Fe_4Se_5$ phase.

The microscopic explanation for the differences between iron pnictides and isoelectronic germanides is an important subject of further study and will likely elucidate further the conditions for superconductivity in iron-based materials.

Chapter 10

Summary and Outlook

In this work we developed a scheme for investigating the symmetry of the superconducting state in quasi-two-dimensional organic charge transfer salts and iron-based materials using a combination of *ab initio* density functional theory calculations and diagrammatic many-body theory in the form of the random phase approximation. After a general introduction in chapter 1, we explained the fundamentals of density functional theory and low-energy model construction in chapter 2. In chapter 3 we presented the formalism of Green's functions, its representation in terms of Feynman diagrams and its application to the many-body problem. The diagrammatic approach to the problem of the order parameter of superconductivity mediated by spin fluctuations is developed in chapter 4. We put particular emphasis on the approximations needed for the formalism to be practical and its efficient numerical implementation.

Based on density functional theory, in chapter 5 we uncovered the importance of molecular conformations for the electronic structure of kappa-type organics, contributing an important ingredient to the explanation of the experimentally observed cooling-rate dependent metal-to-insulator transition. In the same class of materials we revealed in chapter 6, using a combination of density functional theory and random phase approximation, a phase transition between two superconducting states with different symmetry of the order parameter, potentially resolving a two-decades-long controversy among experimentalists.

Our fresh theoretical approach based on the molecular lattice also raises questions regarding the nature of magnetically ordered insulating and possible quantum spin-liquid states that have been observed in kappa-type materials. These, however, will likely not be answered using our RPA approach. Suitable techniques could be, for example, exact diagonalization, the density matrix embedding technique [228] or cluster dynamical mean-field theory [229], since these methods are not based on an analytic expansion including only diagrams of certain topology. Furthermore, the role of inter-molecular Coulomb repulsion, which we neglected in our studies, should be clarified in future work.

In the field of iron-based superconductors we could resolve material-specific questions regarding intercalates of iron selenide (see chapter 7) and the high-pressure superconducting phase of KFe_2As_2 (see chapter 8). We showed that the superconducting transition temperature in intercalated iron selenide is controlled by the dimensionality of the material, intimately connected to the distance between FeSe layers, and the electron doping level. Our prediction that T_c is maximized in the two-dimensional limit and for large electron doping has meanwhile been confirmed by several experimental works [230–233].

For KFe_2As_2 we showed that its electronic structure after the pressure-induced structural collapse shares some features with undoped pnictides in a non-collapsed phase, thereby explaining the unexpected appearance of superconductivity in a collapsed phase of iron pnictides.

Furthermore, we believe that our work on iron germanides in chapter 9 will stimulate the field to explore new ways of microscopic modelling, since it challenges all assumptions that low-energy models of iron-based superconductors depend on. An important topic of future research is to find the microscopic origin of the ferromagnetic tendencies that we uncovered and the minimal model of iron-based materials that contains them.

The application of RPA to the problems and materials discussed in this thesis would not have been possible without extensive development work. We created a tight-binding code that can treat multi-site and multi-orbital models in a unified framework and implemented an interface to density functional theory for supplying the kinetic part of the underlying Hubbard model with virtually unlimited complexity. We structured the equations for the RPA approach to superconductivity in a away that allows for massive parallelization of the necessary calculations. Building upon these developments we created an advanced implementation of the RPA method, which can easily treat models with eight orbitals, such as the up to now rarely investigated *dp*-model of iron-based superconductors adopted in this work, and is fast enough to solve thousands of model Hamiltonians in the four orbital case, as demonstrated in the context of organic charge transfer salts.

Bibliography

[1] H. Kamerlingh Onnes, *Further experiments with liquid helium. C. On the change of electric resistance of pure metals at very low temperatures etc. IV. The resistance of pure mercury at helium temperatures*, Proc. K. Ned. Akad. Wet. **13**, 1274 (1911).

[2] J. E. Hirsch, M. B. Maple, and F. Marsiglio, *Superconducting materials classes: Introduction and overview*, Physica C **514**, 8 (2015).

[3] J. G. Bednorz and K. A. Müller, *Possible high T_c superconductivity in the Ba-La-Cu-O system*, Z. Physik B - Condensed Matter **64**, 189 (1986).

[4] M. K. Wu, J. R. Ashburn, C. J. Torng, P. H. Hor, R. L. Meng, L. Gao, Z. J. Huang, Y. Q. Wang, and C. W. Chu, *Superconductivity at 93 K in a new mixed-phase Y-Ba-Cu-O compound system at ambient pressure*, Phys. Rev. Lett. **58**, 908 (1987).

[5] A. P. Drozdov, M. I. Eremets, I. A. Troyan, V. Ksenofontov, and S. I. Shylin, *Conventional superconductivity at 203 kelvin at high pressures in the sulfur hydride system*, Nature **525**, 73 (2015).

[6] J. Bardeen, L. N. Cooper, and J. R. Schrieffer, *Theory of Superconductivity*, Phys. Rev. **108**, 1175 (1957).

[7] D. J. Scalapino, *A common thread: The pairing interaction for unconventional superconductors*, Rev. Mod. Phys. **84**, 1383 (2012).

[8] C. C. Tsuei and J. R. Kirtley, *Pairing symmetry in cuprate superconductors*, Rev. Mod. Phys. **72**, 969 (2000).

[9] N. Toyota, M. Lang, and J. Müller, *Low-Dimensional Molecular Metals*, Springer-Verlag, Berlin, Heidelberg, 2007, ISBN 978-3-540-49576-5.

[10] J. Müller, *Fluctuation Spectroscopy: A New Approach for Studying Low-Dimensional Molecular Metals*, ChemPhysChem **12**, 1222 (2011).

[11] B. J. Powell, R. H. McKenzie, *Strong electronic correlations in superconducting organic charge transfer salts*, J. Phys.: Condens. Matter **18**, R827 (2006).

[12] H. Elsinger, J. Wosnitza, S. Wanka, J. Hagel, D. Schweitzer, and W. Strunz, *κ-(BEDT-TTF)$_2$Cu[N(CN)$_2$]Br: A Fully Gapped Strong-Coupling Superconductor*, Phys. Rev. Lett. **84**, 6098 (2000).

[13] Y. Shimizu, K. Miyagawa, K. Kanoda, M. Maesato, and G. Saito, *Spin Liquid State in an Organic Mott Insulator with a Triangular Lattice*, Phys. Rev. Lett. **91**, 107001 (2003).

[14] Y. Kurosaki, Y. Shimizu, K. Miyagawa, K. Kanoda, and G. Saito, *Mott Transition from a Spin Liquid to a Fermi Liquid in the Spin-Frustrated Organic Conductor* κ*-(ET)*$_2$*Cu*$_2$*(CN)*$_3$, Phys. Rev. Lett. **95**, 177001 (2005).

[15] F. Kagawa, K. Miyagawa, and K. Kanoda, *Unconventional critical behaviour in a quasi-two-dimensional organic conductor*, Nature (London) **436**, 534 (2005).

[16] R. H. McKenzie, *Similarities Between Organic and Cuprate Superconductors*, Science **278**, 820 (1997).

[17] M. Tamura, H. Tajima, K. Yakushi, H. Kuroda, A. Kobayashi, R. Kato, and H. Kobayashi, *Reflectance Spectra of* κ*-(BEDT-TTF)*$_2$$I_3$*: Electronic Structure of Dimeric BEDT-TTF Salts*, J. Phys. Soc. Jpn. **60**, 3861 (1991).

[18] H. Kino and H. Fukuyama, *Phase Diagram of Two-Dimensional Organic Conductors: (BEDT-TTF)*$_2$$X$, J. Phys. Soc. Jpn. **65**, 2158 (1996).

[19] J. Schmalian, *Pairing due to Spin Fluctuations in Layered Organic Superconductors*, Phys. Rev. Lett. **81**, 4232 (1998).

[20] H. Kino and H. Kontani, *Phase Diagram of Superconductivity on the Anisotropic Triangular Lattice Hubbard Model: An Effective Model of* κ*-(BEDT-TTF) Salts*, J. Phys. Soc. Jpn. **67**, 3691 (1998).

[21] H. Kondo and T. Moriya, *Spin Fluctuation-Induced Superconductivity in Organic Compounds*, J. Phys. Soc. Jpn. **67**, 3695 (1998).

[22] A. Benali, *Layered organic conductors* κ*-(BEDT-TTF)*$_2$$X$*: magnetic and superconducting properties*, Synthetic Metals **175**, 120 (2013).

[23] H. Morita, S. Watanabe, and M. Imada, *Nomagnetic Insulating States near the Mott Transitions on Lattices with Geometrical Frustration and Implications for* κ*-(ET)*$_2$*Cu*$_2$*(CN)*$_3$, J. Phys. Soc. Jpn. **71**, 2109 (2002).

[24] O. Parcollet, G. Biroli, and G. Kotliar, *Cluster Dynamical Mean Field Analysis of the Mott Transition*, Phys. Rev. Lett. **92**, 226402 (2004).

[25] B. Kyung and A.-M. S. Tremblay, *Mott Transition, Antiferromagnetism, and d-Wave Superconductivity in Two-Dimensional Organic Conductors*, Phys. Rev. Lett. **97**, 046402 (2006).

[26] C.-D. Hébert, P. Sémon, and A.-M. S. Tremblay, *Superconducting dome in doped quasi-two-dimensional organic Mott insulators: A paradigm for strongly correlated superconductivity*, Phys. Rev. B **92**, 195112 (2015).

[27] J. Liu, J. Schmalian, and N. Trivedi, *Pairing and Superconductivity Driven by Strong Quasiparticle Renormalization in Two-Dimensional Organic Charge Transfer Salts*, Phys. Rev. Lett. **94**, 127003 (2005).

[28] T. Watanabe, H. Yokoyama, Y. Tanaka, and J. Inoue, *Superconductivity and a Mott Transition in a Hubbard Model on an Anisotropic Triangular Lattice*, J. Phys. Soc. Jpn. **75**, 074707 (2006).

[29] L. F. Tocchio, H. Feldner, F. Becca, R. Valentí, and C. Gros, *Spin-liquid versus spiral-order phases in the anisotropic triangular lattice*, Phys. Rev. B **87**, 035143 (2013).

[30] L. F. Tocchio, C. Gros, R. Valentí, and F. Becca, *One-dimensional spin liquid, collinear, and spiral phases from uncoupled chains to the triangular lattice*, Phys. Rev. B **89**, 235107 (2014).

[31] T. Koretsune, Y. Motome, and A. Furusaki, *Exact Diagonalization Study of Mott Transition in the Hubbard Model on an Anisotropic Triangular Lattice*, J. Phys. Soc. Jpn. **76**, 074719 (2007).

[32] R. T. Clay, H. Li, and S. Mazumdar, *Absence of Superconductivity in the Half-Filled Band Hubbard Model on the Anisotropic Triangular Lattice*, Phys. Rev. Lett. **101**, 166403 (2008).

[33] J. Müller, M. Lang, R. Helfrich, R. Steglich, and T. Sasaki, *High-resolution ac-calorimetry studies of the quasi-two-dimensional organic superconductor* κ-*(BEDT-TTF)*$_2$*Cu(NCS)*$_2$, Phys. Rev. B **65**, 140509(R) (2002).

[34] J. Wosnitza, S. Wanka, J. Hagel, M. Reibelt, D. Schweitzer, and J. A. Schlueter, *Thermodynamic properties of quasi-two-dimensional organic superconductors*, Synth. Met. **133**, 201 (2003).

[35] O. J. Taylor, A. Carrington, and J. A. Schlueter, *Specific-Heat Measurements of the Gap Structure of the Organic Superconductors* κ-*(ET)*$_2$*Cu[N(CN)*$_2$*]Br and* κ-*(ET)*$_2$*Cu(NCS)*$_2$, Phys. Rev. Lett. **99**, 057001 (2007).

[36] O. J. Taylor, A. Carrington, and J. A. Schlueter, *Superconductor-insulator phase separation induced by rapid cooling of* κ-*(ET)*$_2$*Cu[N(CN)*$_2$*]Br*, Phys. Rev. B **77**, 060503(R) (2008).

[37] L. Malone, O. J. Taylor, J. A. Schlueter, and A. Carrington, *Location of gap nodes in the organic superconductors* κ-*(ET)*$_2$*Cu(NCS)*$_2$ *and* κ-*(ET)*$_2$*Cu[N(CN)*$_2$*]Br determined by magnetocalorimetry*, Phys. Rev. B **82**, 014522 (2010).

[38] S. Milbradt, A. A. Bardin, C. J. S. Truncik, W. A. Huttema, A. C. Jacko, P. L. Burn, S. C. Lo, B. J. Powell, and D. M. Broun, *In-plane superfluid density and microwave conductivity of the organic superconductor* κ-*(ET)*$_2$*Cu[N(CN)*$_2$*]Br: Evidence for d-wave pairing and resilient quasiparticles*, Phys. Rev. B **88**, 064501 (2013).

[39] K. Izawa, H. Yamaguchi, T. Sasaki, and Y. Matsuda, *Superconducting Gap Structure of κ-(BEDT-TTF)$_2$Cu(NCS)$_2$ Probed by Thermal Conductivity Tensor*, Phys. Rev. Lett. **88**, 027002 (2001).

[40] J. M. Schrama, E. Rzepniewski, R. S. Edwards, J. Singleton, A. Ardavan, M. Kurmoo, and P. Day, *Millimeter-Wave Magneto-optical Determination of the Anisotropy of the Superconducting Order Parameter in the Molecular Superconductor κ-(BEDT-TTF)$_2$Cu(NCS)$_2$*, Phys. Rev. Lett. **83**, 3041 (1999).

[41] T. Arai, K. Ichimura, K. Nomura, S. Takasaki, J. Yamada, S. Nakatsuji, and H. Anzai, *Tunneling spectroscopy on the organic superconductor κ-(BEDT-TTF)$_2$Cu(NCS)$_2$ using STM*, Phys. Rev. B **63**, 104518 (2001).

[42] K. Ichimura, M. Takami, and K. Nomura, *Direct Observation of d-Wave Superconducting Gap in κ-(ET)$_2$Cu[N(CN)$_2$]Br with Scanning Tunneling Microscopy*, J. Phys. Soc. Jpn. **77**, 114707 (2008).

[43] Y. Oka, H. Nobukane, N. Matsunaga, K. Nomura, K. Katono, K. Ichimura, and A. Kawamoto, *Tunneling Spectroscopy in Organic Superconductor κ-(BEDT-TTF-d[3,3])$_2$Cu[N(CN)$_2$]Br*, J. Phys. Soc. Jpn. **84**, 064713 (2015).

[44] D. Guterding, S. Diehl, M. Altmeyer, T. Methfessel, U. Tutsch, H. Schubert, M. Lang, J. Müller, M. Huth, H. O. Jeschke, R. Valentí, M. Jourdan, and H.-J. Elmers, *Evidence for eight node mixed-symmetry superconductivity in a correlated organic metal*, Phys. Rev. Lett. **116**, 237001 (2016).

[45] M. Dion, D. Fournier, M. Poirier, K. D. Truong, and A.-M. S. Tremblay, *Mixed pairing symmetry in κ-(BEDT-TTF)$_2$X organic superconductors from ultrasonic velocity measurements*, Phys. Rev. B **80**, 220511(R) (2009).

[46] B. Hartmann, J. Müller, and T. Sasaki, *Mott metal-insulator transition induced by utilizing a glasslike structural ordering in low-dimensional molecular conductors*, Phys. Rev. B **90**, 195150 (2014).

[47] B. Hartmann, D. Zielke, J. Polzin, T. Sasaki, and J. Müller, *Critical Slowing Down of the Charge Carrier Dynamics at the Mott Metal-Insulator Transition*, Phys. Rev. Lett. **114**, 216403 (2015).

[48] J. Müller, B. Hartmann, R. Rommel, J. Brandenburg, S. M. Winter, and J. A. Schlueter, *Origin of the glass-like dynamics in molecular metals κ-(BEDT-TTF)$_2$X: implications from fluctuation spectroscopy and ab-initio calculations*, New J. Phys. **17**, 083057 (2015).

[49] S. Diehl, T. Methfessel, U. Tutsch, J. Müller, M. Lang, M. Huth, M. Jourdan, and H.-J. Elmers, *Disorder-induced gap in the normal density of states of the organic superconductor κ-(BEDT-TTF)$_2$Cu[N(CN)$_2$]Br*, J. Phys.: Condens. Matter **27**, 265601 (2015).

[50] M. Watanabe, *Low temperature structures and insulating phases in quasi two-dimensional charge transfer salts at 3/4 filling*, Ph.D. Thesis (in Japanese), Graduate School of Natural Science and Technology, Okayama University, Japan (1999).

[51] E. Scriven and B. J. Powell, *Toward parametrization of the Hubbard model for salts of bis(ethylenedithio)tetrathiafulvalene: A density functional study of isolated molecules*, J. Chem. Phys. **130**, 104508 (2009).

[52] E. Scriven and B. J. Powell, *Effective Coulomb interactions within BEDT-TTF dimers*, Phys. Rev. B **80**, 205107 (2009).

[53] Y. Kamihara, T. Watanabe, M. Hirano, and H. Hosono, *Iron-Based Layered Superconductor* $La[O_{1-x}F_x]FeAs$ *(x = 0.05-0.12) with* $T_c = 26$ *K*, J. Am. Chem. Soc. **130**, 3296 (2008).

[54] H. Hosono and K. Kuroki, *Iron-based superconductors: Current status of materials and pairing mechanism*, Physica C **514**, 399 (2015).

[55] M. Burrard-Lucas, D. G. Free, S. J. Sedlmaier, J. D. Wright, S. J. Cassidy, Y. Hara, A. J. Corkett, T. Lancaster, P. J. Baker, S. J. Blundell, and S. J. Clarke, *Enhancement of the superconducting transition temperature of FeSe by intercalation of a molecular spacer layer*, Nat. Mater. **12**, 15 (2013).

[56] J.-Ph. Reid, A. Juneau-Fecteau, R. T. Gordon, S. René de Cotret, N. Doiron-Leyraud, X. G. Luo, *et al.*, *From d-wave to s-wave pairing in the iron-pnictide superconductor* $(Ba,K)Fe_2As_2$, Supercond. Sci. Technol. **25**, 084013 (2012).

[57] E. Gati, S. Köhler, D. Guterding, B. Wolf, S. Knöner, S. Ran, S. L. Bud'ko, P. C. Canfield, and M. Lang, *Hydrostatic-pressure tuning of magnetic, nonmagnetic, and superconducting states in annealed* $Ca(Fe_{1-x}Co_x)_2As_2$, Phys. Rev. B **86**, 220511(R) (2012).

[58] S. Iimura, S. Matsuishi, H. Sato, T. Hanna, Y. Muraba, S. W. Kim, J. E. Kim, M. Takata, and H. Hosono, *Two-dome structure in electron-doped iron arsenide superconductors*, Nat. Commun. **3**, 943 (2012).

[59] J.-F. Ge, Z.-L. Liu, C. Liu, C.-L. Gao, D. Qian, Q.-K. Xue, Y. Liu, and J.-F. Jia, *Superconductivity above 100 K in single-layer FeSe films on doped* $SrTiO_3$, Nat. Mater. **11**, 285 (2015).

[60] M. A. Avila, S. L. Bud'ko, and P. C. Canfield, *Anisotropic magnetization, specific heat and resistivity of* RFe_2Ge_2 *single crystals*, J. Magn. Magn. Mater. **270**, 51 (2004).

[61] S. Ran, S. L. Bud'ko, and P. C. Canfield, *Effects of substitution on low-temperature physical properties of* $LuFe_2Ge_2$, Philos. Mag. **91**, 4388 (2011).

[62] H. Kim, S. Ran, E. D. Mun, H. Hodovanets, M. A. Tanatar, R. Prozorov, S. L. Bud'ko, and P. C. Canfield, *Crystal growth and annealing study of fragile, non-bulk superconductivity in* YFe_2Ge_2, Philos. Mag. **95**, 804 (2015).

[63] X. Liu, S. Matsuishi, S. Fujitsu, and H. Hosono, *MgFeGe is an isoelectronic and isostructural analog of the superconductor LiFeAs*, Phys. Rev. B **85**, 104403 (2012).

[64] Y. Zou, Z. Feng, P. W. Logg, J. Chen, G. Lampronti, and F. M. Grosche, *Fermi liquid breakdown and evidence for superconductivity in* YFe_2Ge_2, Phys. Status Solidi RRL **8**, 928 (2014).

[65] J. Chen, K. Semeniuk, Z. Feng, P. Reiss, P. Brown, Y. Zou, P. W. Logg, G. I. Lampronti, and F. M. Grosche, *Unconventional Superconductivity in the Layered Iron Germanide* YFe_2Ge_2, Phys. Rev. Lett. **116**, 127001 (2016).

[66] Y. Qi and C. Xu, *Global phase diagram for magnetism and lattice distortion of iron-pnictide materials*, Phys. Rev. B **80**, 094402 (2009).

[67] R. M. Fernandes, A. V. Chubukov, J. Knolle, I. Eremin, and J. Schmalian, *Preemptive nematic order, pseudogap, and orbital order in the iron pnictides*, Phys. Rev. B **85**, 024534 (2012).

[68] R. M. Fernandes, A. V. Chubukov, and J. Schmalian, *What drives nematic order in iron-based superconductors?*, Nat. Phys. **10**, 97 (2014).

[69] R. M. Martin, *Electronic Structure: Basic Theory and Practical Methods*, Cambridge University Press, New York, 2004, ISBN 978-0-521-78285-2.

[70] G. Czycholl, *Theoretische Festkörperphysik*, Springer-Verlag, Berlin, Heidelberg, 2008 (third edition), ISBN 978-3-540-74789-5.

[71] P. Hohenberg and W. Kohn, *Inhomogeneous Electron Gas*, Phys. Rev. **136**, B864 (1964).

[72] W. Kohn and L. J. Sham, *Self-Consistent Equations Including Exchange and Correlation Effects*, Phys. Rev. **140**, A1133 (1965).

[73] D. M. Ceperley and B. J. Alder, *Ground State of the Electron Gas by a Stochastic Method*, Phys. Rev. Lett. **45**, 566 (1980).

[74] J. P. Perdew and Y. Wang, *Accurate and simple analytic representation of the electron-gas correlation energy*, Phys. Rev. B **45**, 13244 (1992).

[75] J. P. Perdew, K. Burke, and M. Ernzerhof, *Generalized Gradient Approximation Made Simple*, Phys. Rev. Lett. **77**, 3865 (1996).

[76] K. Koepernik and H. Eschrig, *Full-potential nonorthogonal local-orbital minimum-basis band-structure scheme*, Phys. Rev. B **59**, 1743 (1999).

[77] P. E. Blöchl, *Projector augmented-wave method*, Phys. Rev. B **50**, 17953 (1994).

[78] R. P. Hosteny, T. H. Dunning Jr., R. R. Gilman, A. Pipano, and I. Shavitt, *Ab-initio study of the π-electron states of trans-butadiene*, J. Chem. Phys. **62**, 4764 (1975).

[79] C. Rostgaard, *The Projector Augmented-wave Method*, arXiv:0910.1921 (unpublished).

[80] R. P. Feynman, *Forces in Molecules*, Phys. Rev. **56**, 340 (1939).

[81] D. C. Liu and J. Nocedal, *On the Limited Memory Method for Large Scale Optimization*, Mathematical Programming B **45**, 503 (1989).

[82] N. Marzari, A. A. Mostofi, J. R. Yates, I. Souza, and D. Vanderbilt, *Maximally localized Wannier functions: Theory and applications*, Rev. Mod. Phys. **84**, 1419 (2012).

[83] G. D. Mahan, *Many-Particle Physics*, Kluwer Academic/Plenum Publishers, New York, 2010 (third edition), ISBN 978-0-306-46338-5.

[84] M. Gell-Mann and F. Low, *Bound States in Quantum Field Theory*, Phys. Rev. **84**, 350 (1951).

[85] G. C. Wick, *The Evaluation of the Collision Matrix*, Phys. Rev. **80**, 268 (1950).

[86] A. A. Abrikosov, L. P. Gorkov, and I. E. Dzyaloshinski, *Methods of Quantum Field Theory in Statistical Physics*, Dover Publications Inc., New York, 1976, ISBN 978-0-486-63228-5.

[87] R. P. Feynman, *Space-Time Approach to Quantum Electrodynamics*, Phys. Rev. **76**, 769 (1949).

[88] D. Bohm and D. Pines, *A Collective Description of Electron Interactions. I. Magnetic Interactions*, Phys. Rev. **82**, 625 (1951).

[89] D. Pines and D. Bohm, *A Collective Description of Electron Interactions: II. Collective vs Individual Particle Aspects of the Interactions*, Phys. Rev. **85**, 338 (1952).

[90] D. Bohm and D. Pines, *A Collective Description of Electron Interactions: III. Coulomb Interactions in a Degenerate Electron Gas*, Phys. Rev. **92**, 609 (1953).

[91] M. Gell-Mann and K. A. Brueckner, *Correlation Energy of an Electron Gas at High Density*, Phys. Rev. **106**, 364 (1957).

[92] D. J. Scalapino, E. Loh, and J. E. Hirsch, *d-wave pairing near a spin-density-wave instability*, Phys. Rev. B **34**, 8190(R) (1986).

[93] N. E. Bickers and D. J. Scalapino, *Conserving approximations for strongly fluctuating electron systems. I. Formalism and calculational approach*, Ann. Phys. **193**, 206 (1989).

[94] T. Takimoto, T. Hotta, and K. Ueda, *Strong-coupling theory of superconductivity in a degenerate Hubbard model*, Phys. Rev. B **69**, 104504 (2004).

[95] K. Kuroki, H. Usui, S. Onari, R. Arita, and H. Aoki, *Pnictogen height as a possible switch between high-T_c nodeless and low-T_c nodal pairings in the iron-based superconductors*, Phys. Rev. B **79**, 224511 (2009).

[96] S. Graser, T. A. Maier, P. J. Hirschfeld, and D. J. Scalapino, *Near-degeneracy of several pairing channels in multiorbital models for the Fe pnictides*, New J. Phys. **11**, 025016 (2009).

[97] A. F. Kemper, T. A. Maier, S. Graser, H.-P. Cheng, P. J. Hirschfeld, and D. J. Scalapino, *Sensitivity of the superconducting state and magnetic susceptibility to key aspects of electronic structure in ferropnictides*, New J. Phys. **12**, 073030 (2010).

[98] Y. Wang, A. Kreisel, V. B. Zabolotnyy, S. V. Borisenko, B. Büchner, T. A. Maier, P. J. Hirschfeld, and D. J. Scalapino, *Superconducting gap in LiFeAs from three-dimensional spin-fluctuation pairing calculations*, Phys. Rev. B **88**, 174516 (2013).

[99] A. Kreisel, Y. Wang, T. A. Maier, P. J. Hirschfeld, and D. J. Scalapino, *Spin-fluctuations and superconductivity in $K_xFe_{2-y}Se_2$*, Phys. Rev. B **88**, 094522 (2013).

[100] K. Suzuki, H. Usui, S, Iimura, Y. Sato, S. Matsuishi, H. Hosono, and K. Kuroki, *Model of the Electronic Structure of Electron-Doped Iron-Based Superconductors: Evidence for Enhanced Spin Fluctuations by Diagonal Electron Hopping*, Phys. Rev. Lett. **113**, 027002 (2014).

[101] D. Guterding, H. O. Jeschke, P. J. Hirschfeld, and R. Valentí, *Unified picture of the doping dependence of superconducting transition temperatures in alkali metal/ammonia intercalated FeSe*, Phys. Rev. B **91**, 041112(R) (2015).

[102] D. Guterding, S. Backes, H. O. Jeschke, and R. Valentí, *Origin of the superconducting state in the collapsed tetragonal phase of KFe_2As_2*, Phys. Rev. B **91**, 140503(R) (2015).

[103] H. Arai, H. Usui, K. Suzuki, Y. Fuseya, and K. Kuroki, *Theoretical study of correlation between spin fluctuations and T_c in isovalent-doped 1111 iron-based superconductors*, Phys. Rev. B **91**, 134511 (2015).

[104] Ch. Heil, H. Sormann, L. Boeri, M. Aichhorn, and W. von der Linden, *Accurate bare susceptibilities from full-potential ab initio calculations*, Phys. Rev. B **90**, 115143 (2014).

[105] W. H. Press, S. A. Teukolsky, W. T. Vetterling, and B. P. Flannery, *Numerical Recipes: The Art of Scientific Computing*, Cambridge University Press, New York, 2007 (third edition), ISBN 978-0-521-88068-8.

[106] P. W. C. Leung, T. J. Emge, M. A. Beno, H. H. Wang, and J. M. Williams, *Novel Structural Modulation in the First Ambient-Pressure Sulfur-Based Organic Superconductor (BEDT-TTF)$_2$I$_3$*, J. Am. Chem. Soc. **106**, 7644 (1984).

[107] P. W. Leung, T. J. Emge, M. A. Beno, H. H. Wang, J. M. Williams, V. Petricek, and P. Coppens, *Novel Structural Modulation in the Ambient-Pressure Sulfur-Based Organic Superconductor β-(BEDT-TTF)$_2$I$_3$: Origin and Effects on Its Electrical Conductivity*, J. Am. Chem. Soc. **107**, 6184 (1985).

[108] A. J. Schultz, H. H. Wang, and J. M. Williams, *Effect of Structural Disorder on Organic Superconductors: A Neutron Diffraction Study of "High-T_c" β^*-(BEDT-TTF)$_2$I$_3$ at* 4.5 K *and* 1.5 kbar, J. Am. Chem. Soc. **108**, 7853 (1986).

[109] A. J. Schultz, M. A. Beno, H. H. Wang, and J. M. Williams, *Neutron-diffraction evidence for ordering in the high-T_c phase of β-di[bis(ethylenedithio)tetrathiafulvalene]triiodide [β^*-(ET)$_2$I$_3$]*, Phys. Rev. B **33**, 7823 (1986).

[110] J. E. Schirber, L. J. Azevedo, J. F. Kwak, E. L. Venturini, P. C. W. Leung, M. A. Beno, H. H. Wang, and J. M. Williams, *Shear-induced superconductivity in β-di[-Bis(ethylene- dithio)tetrathiafulvalene]triiodide [β-(BEDT-TTF)$_2$I$_3$]*, Phys. Rev. B **33**, 1987 (1986).

[111] V. N. Tauklin, E. E. Kostyuchenko, Yu. V. Sushko, I. F. Shchegolev, and E. B. Yagubskii, *Effect of pressure on the superconductivity of β-(BEDT-TTF)$_2$I$_3$*, Pis'ma Zh. Eksp. Theor. Fiz. **41**, 68 (1984) [JETP Lett. **41**, 81 (1985)].

[112] K. Murata, M. Tokumoto, H. Anzai, H. Bando, G. Saito, K. Kajimura, and T. Ishiguro, *Superconductivity with the Onset at* 8 K *in the Organic Conductor β-(BEDT-TTF)$_2$I$_3$ under Pressure*, J. Phys. Soc. Jpn. **54**, 1236 (1985).

[113] J. G. Analytis, A. Ardavan, S. J. Blundell, R. L. Owen, E. F. Garman, C. Jeynes, and B. J. Powell, *Effect of Irradiation-Induced Disorder on the Conductivity and Critical Temperature of the Organic Superconductor κ-(BEDT-TTF)$_2$Cu(SCN)$_2$*, Phys. Rev. Lett. **96**, 177002 (2006).

[114] K. Sano, T. Sasaki, N. Yoneyama, and N. Kobayashi, *Electron Localization near the Mott transition in the Organic Superconductor κ-(BEDT-TTF)$_2$Cu[N(CN)$_2$]Br*, Phys. Rev. Lett. **104**, 217003 (2010).

[115] U. Geiser, A. J. Schultz, H. W. Wang, D. M. Watkins, D. L. Stupka, J. M. Williams, J. E. Schirber, D. L. Overmeyer, D. Jung, J. J. Novoa, and M.-H. Whangbo, *Strain index, lattice softness and superconductivity of organic donor-molecule salts, Crystal and electronic structures of three isostructural salts κ-(BEDT-TTF)$_2$Cu[N(CN)$_2$]X (X = Cl, Br, I)*, Physica C **174**, 475 (1990).

[116] J. Müller, M. Lang, F. Steglich, J. A. Schlueter, A. M. Kini, and T. Sasaki, *Evidence for structural and electronic instabilities at intermediate temperatures in κ-(BEDT-TTF)$_2$X for X=Cu[N(CN)$_2$]Cl, Cu[N(CN)$_2$]Br and Cu(NCS)$_2$: Implications for the phase diagram of these quasi-two-dimensional organic superconductors*, Phys. Rev. B **65**, 144521 (2002).

[117] A. Aburto and E. Orgaz, *Ab initio electronic structure of the eclipsed and staggered conformations of the κ-(BEDT-TTF)$_2$Cu[N(CN)$_2$]Br organic superconductor*, Phys. Rev. B **78**, 113104 (2008).

[118] D. Guterding, R. Valentí, and H. O. Jeschke, *Influence of molecular conformations on the electronic structure of organic charge transfer salts*, Phys. Rev. B **92**, 081109(R) (2015).

[119] N. D. Kushch, A. V. Kazakova, L. I. Buravov, A. N. Chekhlov, A. D. Dubrovskii, E. B. Yagubskii, and E. Canadell, *The first polymorph, κ''-(ET)$_2$Cu[N(CN)$_2$]Cl, in the family of κ-(ET)$_2$Cu[N(CN)$_2$]X (X = Cl, Br, I) radical cation salts*, Journal of Solid State Chemistry **182**, 617 (2009).

[120] J. Enkovaara, C. Rostgaard, J. J. Mortensen *et al.*, *Electronic structure calculations with GPAW: a real-space implementation of the projector augmented-wave method*, J. Phys.: Condens. Matter **22**, 253202 (2010).

[121] H. O. Jeschke, M. de Souza, R. Valentí, R. S. Manna, M. Lang, and J. A. Schlueter, *Temperature dependence of structural and electronic properties of the spin-liquid candidate κ-(BEDT-TTF)$_2$Cu$_2$(CN)$_3$*, Phys. Rev. B **85**, 035125 (2012).

[122] H. Eschrig and K. Koepernik, *Tight-binding models for the iron-based superconductors*, Phys. Rev. B **80**, 104503 (2009).

[123] Y. Imamura, S. Ten-no, K. Yonemitsu, and Y. Tanimura, *Structures and electronic phases of the bis(ethylenedithio)tetrathiafulvalene (BEDT-TTF) clusters and κ-(BEDT-TTF) salts: A theoretical study based on ab initio molecular orbital methods*, J. Chem. Phys. **111**, 5986 (1999).

[124] K. Nakamura, Y. Yoshimoto, T. Kosugi, R. Arita, and M. Imada, *Ab initio Derivation of Low-Energy Model for κ-ET Type Organic Conductors*, J. Phys. Soc. Jpn. **78**, 083710 (2009).

[125] K. Kuroki, T. Kimura, R. Arita, Y. Tanaka, and Y. Matsuda, *$d_{x^2-y^2}$- versus d_{xy}-like pairings in organic superconductors κ-(BEDT-TTF)$_2$X*, Phys. Rev. B **65**, 100516(R) (2002).

[126] D. Guterding, M. Altmeyer, H. O. Jeschke, and R. Valentí, *Near-degeneracy of extended s+$d_{x^2-y^2}$ and d_{xy} order parameters in quasi-two-dimensional organic superconductors*, Phys. Rev. B **94**, 024515 (2016).

[127] T. Hiramatsu, Y. Yoshida, G. Saito, A. Otsuka, H. Yamochi, M. Maesato, Y. Shimizu, H. Ito, and H. Kishida, *Quantum spin liquid: design of a quantum spin liquid next to a superconducting state based on a dimer-type ET Mott insulator*, J. Mater. Chem. C **3**, 1378 (2015).

[128] J. A. Schlueter, L. Wiehl, H. Park, M. de Souza, M. Lang, H.-J. Koo, and M.-H. Whangbo, *Enhanced Critical Temperature in a Dual-Layered Molecular Superconductor*, J. Am. Chem. Soc. **132**, 16308 (2010).

[129] T. Kawamoto, T. Mori, A. Nakao, Y. Murakami, and J. A. Schlueter, *T_c of 11 K Identified for the Third Polymorph of the (BEDT-TTF)$_2$Ag(CF$_3$)$_4$(TCE) Organic Superconductor*, J. Phys. Soc. Jpn. **81**, 023705 (2012).

[130] B. S. Shastry and B. Sutherland, *Exact Ground State of A Quantum Mechanical Antiferromagnet*, Physica B **108**, 1069 (1981).

[131] M. Altmeyer, R. Valentí, and H. O. Jeschke, *Role of layer packing for the electronic properties of the organic superconductor (BEDT-TTF)$_2$Ag(CF$_3$)$_4$(TCE)*, Phys. Rev. B **91**, 245137 (2015).

[132] T. Koretsune and C. Hotta, *Evaluating model parameters of the κ- and β'-type Mott insulating organic solids*, Phys. Rev. B **89**, 045102 (2014).

[133] E. Yusuf, B. J. Powell, and R. H. McKenzie, *Antiferromagnetic spin fluctuations in the metallic phase of quasi-two-dimensional organic superconductors*, Phys. Rev. B **75**, 214515 (2007).

[134] Y. Tanaka and S. Kashiwaya, *Theory of Tunneling Spectroscopy of d-Wave superconductors*, Phys. Rev. Lett. **74**, 3451 (1995).

[135] Y. Hasegawa, *Density of States and NMR Relaxation Rate in Anisotropic Superconductivity with Intersecting Line Nodes*, J. Phys. Soc. Jpn. **65**, 3131 (1996).

[136] R. C. Dynes, V. Narayanamurti, and J. P. Garno, *Direct Measurement of Quasiparticle-Lifetime Broadening in a Strong-Coupled Superconductor*, Phys. Rev. Lett. **41**, 1509 (1978).

[137] P. E. Blöchl, O. Jepsen, and O. K. Andersen, *Improved tetrahedron method for Brillouin-zone integrations*, Phys. Rev. B **49**, 16223 (1994).

[138] H. Shinaoka and M. Imada, *Single-Particle Excitations under Coexisting Electron Correlation and Disorder: A Numerical Study of the Anderson-Hubbard Model*, J. Phys. Soc. Jpn. **78**, 094708 (2009).

[139] R. Kato, H. Kobayashi, A. Kobayashi, S. Moriyama, Y. Nishio, K. Kajita, and W. Sasaki, *A New Ambient-pressure Superconductor, κ-(BEDT-TTF)$_2$I$_3$*, Chem. Lett. **16**, 507 (1987).

[140] H. Mori, I. Hirabayashi, S. Tanaka, T. Mori, and H. Inokuchi, *A New Ambient-pressure Superconductor, κ-(BEDT-TTF)$_2$Ag(CN)$_2$H$_2$O (T_c = 5.0 K)*, Solid State Commun. **76**, 35 (1990).

[141] A. M. Kini, U. Geiser, H. H. Wang, K. D. Carlson, J. M. Williams, W. K. Kwok, K. G. Vandervoort, J. E. Thompson, D. L. Stupka, D. Jung, and M.-H. Whangbo, *A new ambient-pressure organic superconductor, κ-(ET)$_2$Cu[N(CN)$_2$]Br, with the highest transition temperature yet observed (inductive onset T_c = 11.6 K, resistive onset = 12.5 K)*, Inorg. Chem. **29**, 2555 (1990).

[142] A. T. Rømer, A. Kreisel, I. Eremin, M. A. Malakhov, T. A. Maier, P. J. Hirschfeld, and B. M. Andersen, *Pairing symmetry of the one-band Hubbard model in the paramagnetic weak-coupling limit: A numerical RPA study*, Phys. Rev. B **92**, 104505 (2015).

[143] H. C. Kandpal, I. Opahle. Y.-Z. Zhang, H. O. Jeschke, and R. Valentí, *Revision of Model Parameters for κ-Type Charge Transfer Salts: An Ab Initio Study*, Phys. Rev. Lett. **103**, 067004 (2009).

[144] G. Wu, Y. L. Xie, H. Chen, M. Zhong, R. H. Liu, B. C. Shi, Q. J. Li, X. F. Wang, T. Wu, Y. J. Yan, J. J. Ying, and X. H. Chen, *Superconductivity at 56 K in samarium-doped SrFeAsF*, J. Phys.: Condens. Matter **21**, 142203 (2009).

[145] S. Tan, Y. Zhang, M. Xia, Z. Ye, F. Chen, X. Xie, R. Peng, D. Xu, Q. Fan, H. Xu, J. Jiang, T. Zhang, X. Lai, T. Xiang, J. Hu, B. Xie, and D. Feng, *Interface-induced superconductivity and strain-dependent spin density waves in FeSe/SrTiO$_3$ thin films*, Nat. Mater. **12**, 634 (2013).

[146] J. Guo, S. Jin, G. Wang, S. Wang, K. Zhu, T. Zhou, M. He, and X. Chen, *Superconductivity in the iron selenide $K_xFe_2Se_2$ ($0 \leq x \leq 1.0$)*, Phys. Rev. B **82**, 180520 (2010).

[147] E. Dagotto, *Colloquium: The unexpected properties of alkali metal iron selenide superconductors*, Rev. Mod. Phys. **85**, 849 (2013).

[148] F. Wang, F. Yang, M. Gao, Z.-Y. Lu, T. Xiang, and D.-H. Lee, *The electron pairing of $K_xFe_{2-y}Se_2$*, Europhys. Lett. **93**, 57003 (2011).

[149] T. A. Maier, S. Graser, P. J. Hirschfeld, and D. J. Scalapino, *d-wave pairing from spin fluctuations in the $K_xFe_{2-y}Se_2$ superconductors*, Phys. Rev. B **83**, 100515 (2011).

[150] S. Maiti, M. M. Korshunov, T. A. Maier, P. J. Hirschfeld, and A. V. Chubukov, *Evolution of the Superconducting State of Fe-Based Compounds with Doping*, Phys. Rev. Lett. **107**, 147002 (2011).

[151] M. Xu, Q. Q. Ge, R. Peng, Z. R. Ye, J. Jiang, F. Chen, X. P. Shen, B. P. Xie, Y. Zhang, A. F. Wang, X. F. Wang, X. H. Chen, and D. L. Feng, *Evidence for an s-wave superconducting gap in $K_xFe_{2-y}Se_2$ from angle-resolved photoemission*, Phys. Rev. B **85**, 220504 (2012).

[152] I. I. Mazin, *Symmetry analysis of possible superconducting states in $K_xFe_ySe_2$ superconductors*, Phys. Rev. B **84**, 024529 (2011).

[153] E.-W. Scheidt, V. R. Hathwar, D. Schmitz, A. Dunbar, W. Scherer, F. Mayr, V. Tsurkan, J. Deisenhofer, and A. Loidl, *Superconductivity at $T_c = 44$ K in $Li_xFe_2Se_2(NH_3)_y$* Eur. Phys. J. B **85**, 279 (2012).

[154] T. Noji, T. Hatakeda, S. Hosono, T. Kawamata, M. Kato, and Y. Koike, *Synthesis and post-annealing effects of alkaline-metal-ethylenediamine-intercalated superconductors $A_x(C_2H_8N_2)_yFe_{2-z}Se_2$ (A = Li, Na) with $T_c = 45$ K*, Physica C **504**, 8 (2014).

[155] S. J. Sedlmaier, S. J. Cassidy, R. G. Morris, M. Drakopoulos, C. Reinhard, S. J. Moorhouse, D. O'Hare, P. Manuel, D. Khalyavin, and S. J. Clarke, *Ammonia-Rich High-Temperature Superconducting Intercalates of Iron Selenide Revealed through Time-Resolved in Situ X-ray and Neutron Diffraction*, J. Am. Chem. Soc. **136**, 630 (2014).

[156] H. Sun, D. N. Woodruff, S. J. Cassidy, G. M. Allcroft, S. J. Sedlmaier, A. L. Thompson, P. A. Bingham, S. D. Forder, S. Cartenet, N. Mary, S. Ramos, F. R. Foronda, B. J. Williams, X. Li, S. J. Blundell, and S. J. Clarke, *Soft Chemical Control of Superconductivity in Lithium Iron Selenide Hydroxides $Li_{1-x}Fe_x(OH)Fe_{1-y}Se$*, Inorg. Chem. **54**, 1958 (2015).

[157] T. P. Ying, X. L. Chen, G. Wang, S. F. Jin, T. T. Zhou, X. F. Lai, H. Zhang, and W. Y. Wang, *Observation of superconductivity at $30 \sim 46$ K in $A_xFe_2Se_2$ (A = Li, Na, Ba, Sr, Ca, Yb, and Eu)*, Sci. Rep. **2**, 426 (2012).

[158] A. Krzton-Maziopa, E. V. Pomjakushina, V. Yu. Pomjakushin, F. von Rohr, A. Schilling, and K. Conder, *Synthesis of a new alkali metal-organic solvent intercalated iron selenide superconductor with $T_c \approx 45$ K*, J. Phys.: Condens. Matter **24**, 382202 (2012).

[159] J. Guo, H. Lei, F. Hayashi, and H. Hosono, *Superconductivity and phase instability of NH_3-free Na-intercalated $FeSe_{1-z}S_z$*, Nat. Commun. **5**, 4756 (2014).

[160] M. Tomić, H. O. Jeschke, and R. Valentí, *Unfolding of electronic structure through induced representations of space groups: Application to Fe-based superconductors*, Phys. Rev. B **90**, 195121 (2014).

[161] Z. P. Yin, K. Haule, and G. Kotliar, *Kinetic frustration and the nature of the magnetic and paramagnetic states in iron pnictides and iron chalcogenides*, Nat. Mater. **10**, 932 (2011).

[162] O. K. Andersen and L. Boeri, *On the multi-orbital band structure and itinerant magnetism of iron-based superconductors*, Ann. Phys. (Berlin) **523**, 8 (2011).

[163] A. E. Taylor, S. J. Sedlmaier, S. J. Cassidy, E. A. Goremychkin, R. A. Ewings, T. G. Perring, S. J. Clarke, and A. T. Boothroyd, *Spin fluctuations away from $(\pi, 0)$ in*

the superconducting phase of molecular-intercalated FeSe, Phys. Rev. B **87**, 220508 (2013).

[164] T. A. Maier, S. Graser, D. J. Scalapino, and P. J. Hirschfeld, *Origin of gap anisotropy in spin fluctuation models of the iron pnictides*, Phys. Rev. B **79**, 224510 (2009).

[165] M. Rotter, M. Tegel, and D. Johrendt, *Superconductivity at 38 K in the Iron Arsenide* $(Ba_{1-x}K_x)Fe_2As_2$, Phys. Rev. Lett. **101**, 107006 (2008).

[166] S. A. J. Kimber, A. Kreyssig, Y. Z. Zhang, H. O. Jeschke, R. Valentí, F. Yokaichiya, E. Colombier, J. Yan, T. C. Hansen, T. Chatterji, R. J. McQueeney, P. C. Canfield, A. I. Goldman, and D. N. Argyriou, *Similarities between structural distortions under pressure and chemical doping in superconducting* $BaFe_2As_2$, Nat. Mater. **8**, 471 (2009).

[167] J. Paglione and R. L. Greene, *High-temperature superconductivity in iron-based materials*, Nat. Phys. **6**, 645 (2010).

[168] S. Lee, J. Jiang, Y. Zhang, C.W. Bark, J. D.Weiss, C. Tarantini, C. T. Nelson, H.W. Jang, C. M. Folkman, S. H. Baek, A. Polyanskii, D. Abraimov, A. Yamamoto, J.W. Park, X. Q. Pan, E. E. Hellstrom, D. C. Larbalestier, and C. B. Eom, *Template engineering of Co-doped* $BaFe_2As_2$ *single-crystal thin films*, Nat. Mater. **9**, 397 (2010).

[169] A. Leithe-Jasper, W. Schnelle, C. Geibel, and H. Rosner, *Superconducting State in* $SrFe_{2-x}Co_xAs_2$ *by Internal Doping of the Iron Arsenide Layers*, Phys. Rev. Lett. **101**, 207004 (2008).

[170] W. Uhoya, A. Stemshorn, G. Tsoi, Y. K. Vohra, A. S. Sefat, B. C. Sales, K. M. Hope, and S. T. Weir, *Collapsed tetragonal phase and superconductivity of* $BaFe_2As_2$ *under high pressure*, Phys. Rev. B **82**, 144118 (2010).

[171] N. Ni, S. Nandi, A. Kreyssig, A. I. Goldman, E. D. Mun, S. L. Bud'ko, and P. C. Canfield, *First-order structural phase transition in* $CaFe_2As_2$, Phys. Rev. B **78**, 014523 (2008).

[172] Y.-Z. Zhang, H. C. Kandpal, I. Opahle, H. O. Jeschke, and R. Valentí, *Microscopic origin of pressure-induced phase transitions in the iron pnictide superconductors* AFe_2As_2*: An ab initio molecular dynamics study*, Phys. Rev. B **80**, 094530 (2009).

[173] R. S. Dhaka, R. Jiang, S. Ran, S. L. Bud'ko, P. C. Canfield, B. N. Harmon, A. Kaminski, M. Tomic, R. Valentí, and Y. Lee *Dramatic changes in the electronic structure upon transition to the collapsed tetragonal phase in* $CaFe_2As_2$ Phys. Rev. B **89**, 020511(R) (2014).

[174] D. Kasinathan, M. Schmitt, K. Koepernik, A. Ormeci, K. Meier, U. Schwarz, M. Hanfland, C. Geibel, Y. Grin, A. Leithe-Jasper, and H. Rosner, *Symmetry-preserving lattice collapse in tetragonal* $SrFe_{2-x}Ru_xAs_2$ *(x=0,0.2): A combined experimental and theoretical study*, Phys. Rev. B **84**, 054509 (2011).

[175] W. Uhoya, G. Tsoi, Y. K. Vohra, M. A. McGuire, A. S. Sefat, B. C. Sales, D. Mandrus, and S. T Weir, *Anomalous compressibility effects and superconductivity of* $EuFe_2As_2$ *under high pressures*, J. Phys.: Condens. Matter **22**, 292202 (2010).

[176] A. I. Coldea, C. M. J. Andrew, J. G. Analytis, R. D. McDonald, A. F. Bangura, J.-H. Chu, I. R. Fisher, and A. Carrington, *Topological Change of the Fermi Surface in Ternary Iron Pnictides with Reduced c/a Ratio: A de Haas-van Alphen Study of* $CaFe_2P_2$, Phys. Rev. Lett. **103**, 026404 (2009).

[177] N. Colonna, G. Profeta, A. Continenza, and S. Massidda, *Structural and magnetic properties of* $CaFe_2As_2$ *and* $BaFe_2As_2$ *from first-principles density functional theory*, Phys. Rev. B **83**, 094529 (2011).

[178] T. Yildirim, *Strong Coupling of the Fe-Spin State and the As-As Hybridization in Iron-Pnictide Superconductors from First-Principle Calculations*, Phys. Rev. Lett. **102**, 037003 (2009).

[179] D. K. Pratt, Y. Zhao, S. A. J. Kimber, A. Hiess, D. N. Argyriou, C. Broholm, A. Kreyssig, S. Nandi, S. L. Bud'ko, N. Ni, P. C. Canfield, R. J. McQueeney, and A. I. Goldman, *Suppression of antiferromagnetic spin fluctuations in the collapsed phase of* $CaFe_2As_2$, Phys. Rev. B **79**, 060510(R) (2009).

[180] J. H. Soh, G. S. Tucker, D. K. Pratt, D. L. Abernathy, M. B. Stone, S. Ran, S. L. Bud'ko, P. C. Canfield, A. Kreyssig, R. J. McQueeney, and A. I. Goldman, *Inelastic Neutron Scattering Study of a Nonmagnetic Collapsed Tetragonal Phase in Nonsuperconducting* $CaFe_2As_2$*: Evidence of the Impact of Spin Fluctuations on Superconductivity in the Iron-Arsenide Compounds*, Phys. Rev. Lett. **111**, 227002 (2013).

[181] J.-J. Ying, L.-Y. Tang, V. V. Struzhkin, H.-K. Mao, A. G. Gavriulik, A.-F. Wang, X.-H. Chen, and X.-J. Chen, *Tripling the critical temperature of* KFe_2As_2 *by carrier switch*, arXiv:1501.00330 (unpublished).

[182] Y. Nakajima, R. Wang, T. Metz, X. Wang, L. Wang, H. Cynn, S. T. Weir, J. R. Jeffries, and J. Paglione, *High-temperature superconductivity stabilized by electron-hole interband coupling in collapsed tetragonal phase of* KFe_2As_2 *under high pressure*, Phys. Rev. B **91**, 060508(R) (2015).

[183] F. F. Tafti, A. Juneau-Fecteau, M-È. Delage, S. René de Cotret, J-Ph. Reid, A. F. Wang , X-G. Luo, X. H. Chen, N. Doiron-Leyraud, and L. Taillefer, *Sudden reversal in the pressure dependence of* T_c *in the iron-based superconductor* KFe_2As_2, Nat. Phys. **9**, 349 (2013).

[184] K. Okazaki, Y. Ota, Y. Kotani, W. Malaeb, Y. Ishida, T. Shimojima, T. Kiss, S. Watanabe, C-T. Chen, K. Kihou, C-H. Lee, A. Iyo, H. Eisaki, T. Saito, H. Fukazawa, Y. Kohori, K. Hashimoto, T. Shibauchi, Y. Matsuda, H. Ikeda, H. Miyahara, R. Arita, A. Chainani, and S. Shin, *Octet-Line Node Structure of Superconducting Order Parameter in* KFe_2As_2, Science **337**, 1314 (2012).

[185] R. Thomale, Ch. Platt, W. Hanke, J. Hu, and B. A. Bernevig, *Exotic d-Wave Superconducting State of Strongly Hole-Doped* $K_xBa_{1-x}Fe_2As_2$, Phys. Rev. Lett. **107**, 117001 (2011).

[186] J-Ph. Reid, M. A. Tanatar, A. Juneau-Fecteau, R. T. Gordon, S. René de Cotret, N. Doiron-Leyraud, T. Saito, H. Fukazawa, Y. Kohori, K. Kihou, C-H. Lee, A. Iyo, H. Eisaki, R. Prozorov, and L. Taillefer, *Universal Heat Conduction in the Iron Arsenide Superconductor* KFe_2As_2*: Evidence of a d-Wave State*, Phys. Rev. Lett. **109**, 087001 (2012).

[187] K. Suzuki, H. Usui, and K. Kuroki, *Spin fluctuations and unconventional pairing in* KFe_2As_2, Phys. Rev. B **84**, 144514 (2011).

[188] F. F. Tafti, J. P. Clancy, M. Lapointe-Major, C. Collignon, S. Faucher, J. A. Sears, A. Juneau-Fecteau, N. Doiron-Leyraud, A. F. Wang, X.-G. Luo, X. H. Chen, S. Desgreniers, Y-J. Kim, and L. Taillefer, *Sudden reversal in the pressure dependence of* T_c *in the iron-based superconductor* $CsFe_2As_2$*: A possible link between inelastic scattering and pairing symmetry*, Phys. Rev. B **89**, 134502 (2014).

[189] F. F. Tafti, A. Ouellet, A. Juneau-Fecteau, S. Faucher, M. Lapointe-Major, N. Doiron-Leyraud, A. F. Wang, X. G. Luo, X. H. Chen, and L. Taillefer, *Universal V-shaped temperature-pressure phase diagram in the iron-based superconductors* KFe_2As_2*,* $RbFe_2As_2$*, and* $CsFe_2As_2$, Phys. Rev. B **91**, 054511 (2015).

[190] T. Terashima, M. Kimata, N. Kurita, H. Satsukawa, A. Harada, K. Hazama, M. Imai, A. Sato, K. Kihou, C-H. Lee, H. Kito, H. Eisaki, A. Iyo, T. Saito, H. Fukazawa, Y. Kohori, H. Harima, and S. Uji, *Fermi Surface and Mass Enhancements in* KFe_2As_2 *from de Haas-van Alphen Effect Measurements*, J. Phys. Soc. Jpn. **79**, 053702 (2010).

[191] T. Yoshida, I. Nishi, A. Fujimori, M. Yi, R. G. Moore, D-H. Lu, Z-X. Shen, K. Kihou, P. M. Shirage, H. Kito, C-H. Lee, A. Iyo, H. Eisaki, and H. Harima, *Fermi surfaces and quasi-particle band dispersions of the iron pnictide superconductor* KFe_2As_2 *observed by angle-resolved photoemission spectroscopy*, J. Phys. Chem. Solids **72**, 465 (2011).

[192] M. Kimata, T. Terashima, N. Kurita, H. Satsukawa, A. Harada, K. Kodama, K. Takehana, Y. Imanaka, T. Takamasu, K. Kihou, C-H. Lee, H. Kito, H. Eisaki, A. Iyo, H. Fukazawa, Y. Kohori, H. Harima, and S. Uji, *Cyclotron Resonance and Mass Enhancement by Electron Correlation in* KFe_2As_2, Phys. Rev. Lett. **107**, 166402 (2011).

[193] T. Sato, N. Nakayama, Y. Sekiba, P. Richard, Y-M. Xu, S. Souma, T. Takahashi, G. F. Chen, J. L. Luo, N. L. Wang, and H. Ding, *Band Structure and Fermi Surface of an Extremely Overdoped Iron-Based Superconductor* KFe_2As_2, Phys. Rev. Lett. **103**, 047002 (2009).

[194] T. Yoshida, S. Ideta, I. Nishi, A. Fujimori, M. Yi, R. G. Moore, S. K. Mo, D-H. Lu, Z-X. Shen, Z. Hussain, K. Kihou, P. M. Shirage, H. Kito, C-H. Lee, A. Iyo, H. Eisaki, and H. Harima, *Orbital character and electron correlation effects on two- and*

three-dimensional Fermi surfaces in KFe$_2$As$_2$ revealed by angle-resolved photoemission spectroscopy, Front. Physics **2**, 17 (2014).

[195] T. Terashima, N. Kurita, M. Kimata, M. Tomita, S. Tsuchiya, M. Imai, A. Sato, K. Kihou, C-H. Lee, H. Kito, H. Eisaki, A. Iyo, T. Saito, H. Fukazawa, Y. Kohori, H. Harima, and S. Uji, *Fermi surface in KFe$_2$As$_2$ determined via de Haas-van Alphen oscillation measurements*, Phys. Rev. B **87**, 224512 (2013).

[196] S. Backes, D. Guterding, H. O. Jeschke, and R. Valentí, *Electronic structure and de Haas-van Alphen frequencies in KFe$_2$As$_2$ within LDA+DMFT*, New J. Phys. **16**, 085025 (2014).

[197] S. Mandal, R. E. Cohen, and K. Haule, *Pressure suppression of electron correlation in the collapsed tetragonal phase of CaFe$_2$As$_2$: A DFT-DMFT investigation*, Phys. Rev. B **90**, 060501(R) (2014).

[198] J. Diehl, S. Backes, D. Guterding, H. O. Jeschke, and R. Valentí, *Correlation effects in the tetragonal and collapsed tetragonal phase of CaFe$_2$As$_2$*, Phys. Rev. B **90**, 085110 (2014).

[199] R. Mittal, S. K. Mishra, S. L. Chaplot, S. V. Ovsyannikov, E. Greenberg, D. M. Trots, L. Dubrovinsky, Y. Su, Th. Bruckel, S. Matsuishi, H. Hosono, and G. Garbarino, *Ambient- and low-temperature synchrotron x-ray diffraction study of BaFe$_2$As$_2$ and CaFe$_2$As$_2$ at high pressures up to 56 GPa*, Phys. Rev. B **83**, 054503 (2011).

[200] A. F. Kemper, M. M. Korshunov, T. P. Devereaux, J. N. Fry, H-P. Cheng, and P. J. Hirschfeld, *Anisotropic quasiparticle lifetimes in Fe-based superconductors*, Phys. Rev. B **83**, 184516 (2011).

[201] A. Subedi, *Unconventional sign-changing superconductivity near quantum criticality in YFe$_2$Ge$_2$*, Phys. Rev. B **89**, 024504 (2014).

[202] D. J. Singh, *Superconductivity and magnetism in YFe$_2$Ge$_2$*, Phys. Rev. B **89**, 024505 (2014).

[203] G. Wang and X. Shi, *Electronic strctures and magnetism of YM$_2$Ge$_2$ (M = Mn-Cu): Ge-height dependent magnetic ordering in YFe$_2$Ge$_2$*, Comput. Mater. Sci. **121**, 48 (2016).

[204] N. Sirica, F. Bondino, S. Nappini, I. Píš, L. Poudel, A. D. Christianson, D. Mandrus, D. J. Singh, and N. Mannella, *Spectroscopic evidence for strong quantum spin fluctuations with itinerant character in YFe$_2$Ge$_2$*, Phys. Rev. B **91**, 121102(R) (2015).

[205] D. F. Xu, D. W. Shen, D. Zhu, J. Jiang, B. P. Xie, Q. S. Wang, B. Y. Pan, P. Dudin, T. K. Kim, M. Hoesch, J. Zhao, X. G. Wan, and D. L. Feng, *Electronic structure of YFe$_2$Ge$_2$ studied by angle-resolved photoemission spectroscopy*, Phys. Rev. B **93**, 024506 (2016).

[206] P. J. Hirschfeld, M. M. Korshunov, and I. I. Mazin, *Gap symmetry and structure of Fe-based superconductors*, Rep. Prog. Phys. **74**, 124508 (2011).

[207] A. Chubukov, *Pairing Mechanism in Fe-Based Superconductors*, Annu. Rev. Condens. Matter Phys. **3**, 57 (2012).

[208] J. C. S. Davis and D.-H. Lee, *Concepts relating magnetic interactions, intertwined electronic orders, and strongly correlated superconductivity*, Proc. Natl. Acad. Sci. USA **110**, 17623 (2013).

[209] J. K. Glasbrenner, I. I. Mazin, H. O. Jeschke, P. J. Hirschfeld, R. M. Fernandes, and R. Valentí, *Effect of magnetic frustration on nematicity and superconductivity in Fe chalcogenides*, Nat. Phys. **11**, 953 (2015).

[210] Q. Si, R. Yu, and E. Abrahams, *High-temperature superconductivity in iron pnictides and chalcogenides*, Nature Reviews Materials **1**, 16017 (2016).

[211] J. Hu, *Identifying the genes of unconventional high temperature superconductors*, Sci. Bull. **61**, 561 (2016).

[212] D. Guterding, S. Backes, M. Tomić, H. O. Jeschke, and R. Valentí, *Ab-initio perspective on structural and electronic properties of iron-based superconductors*, Phys. Status Solidi B (in press), arXiv:1606.04411.

[213] H. O. Jeschke, I. I. Mazin, and R. Valentí, *Why MgFeGe is not a superconductor*, Phys. Rev. B **87**, 241105(R) (2013).

[214] Z. P. Yin, K. Haule, and G. Kotliar, *Spin dynamics and orbital-antiphase pairing symmetry in iron-based superconductors*, Nat. Phys. **10**, 845 (2014).

[215] M.-C. Ding and Y.-Z. Zhang, *Possible way to turn MgFeGe into an iron-based superconductor*, Phys. Rev. B **89**, 085120 (2014).

[216] P. Wiecki, B. Roy, D. C. Johnston, S. L. Bud'ko, P.C. Canfield, and Y. Furukawa, *Competing Magnetic Fluctuations in Iron Pnictide Superconductors: Role of Ferromagnetic Spin Correlations Revealed by NMR*, Phys. Rev. Lett. **115**, 137001 (2015).

[217] W. Li, H. Ding, Z. Li, P. Deng, K. Chang, K. He *et al.*, *KFe_2Se_2 is the Parent Compound of K-Doped Iron Selenide Superconductors*, Phys. Rev. Lett. **109**, 057003 (2012).

[218] C. H. P. Wen, H. C. Xu, C. Chen, Z. C. Huang, X. Lou, Y. K. Pu *et al.*, *Anomalous correlation effects and unique phase diagram of electron-doped FeSe revealed by photoemission spectroscopy*, Nat. Commun. **7**, 10840 (2016).

[219] D. Guterding, H. O. Jeschke, I. I. Mazin, J. K. Glasbrenner, E. Bascones, and R. Valentí, *Non-trivial role of interlayer cation states in iron-based superconductors*, arXiv:1610.08626 (unpublished).

[220] S. Backes, H. O. Jeschke, and R. Valentí, *Microscopic nature of correlations in multi-orbital AFe_2As_2 (A = K, Rb, Cs): Hund's coupling versus Coulomb repulsion*, Phys. Rev. B **92**, 195128 (2015).

[221] J. Ferber, K. Foyevtsova, R. Valentí, and H. O. Jeschke, *LDA+DMFT study of the effects of correlation in LiFeAs*, Phys. Rev. B **85**, 094505 (2012).

[222] G. Lee, H. S. Ji, Y. Kim, C. Kim, K. Haule, G. Kotliar, B. Lee, S. Khim, K. H. Kim, K. S. Kim, K.-S. Kim, and J. H. Shim, *Orbital Selective Fermi Surface Shifts and Mechanism of High Tc Superconductivity in Correlated AFeAs (A=Li, Na)*, Phys. Rev. Lett. **109**, 177001 (2012).

[223] G. Venturini and B. Malaman, *X-ray single crystal refinements on some RT_2Ge_2 compounds (R = Ca, Y,La,Nd, U; T = Mn-Cu,Ru-Pd): evolution of the chemical bonds*, J. Alloys Compd. **235**, 201 (1996).

[224] D. R. Parker, M. J. Pitcher, P. J. Baker, I. Franke, T. Lancaster, S. J. Blundell, and S. J. Clarke, *Structure, antiferromagnetism and superconductivity of the layered iron arsenide NaFeAs*, Chem. Commun. **16**, 2189 (2009).

[225] F. Eilers, K. Grube, D. A. Zocco, T. Wolf, M. Merz, P. Schweiss, R. Heid, R. Eder, R. Yu, J.-X. Zhu, Q. Si, T. Shibauchi, and H. v. Löhneysen, *Strain-Driven Approach to Quantum Criticality in AFe_2As_2 with A = K, Rb, and Cs*, Phys. Rev. Lett. **116**, 237003 (2016).

[226] O. K. Andersen, J. Madsen, U. K. Poulsen, O. Jepsen, and J. Kollár, *Magnetic ground state properties of transition metals*, Physica B+C **86-88**, 249 (1977).

[227] I. I. Mazin and D. J. Singh, *Electronic structure and magnetism in Ru-based perovskites*, Phys. Rev. B **56**, 2556 (1997).

[228] G. Knizia and G. K.-L. Chan, *Density Matrix Embedding: A Simple Alternative to Dynamical Mean-Field Theory*, Phys. Rev. Lett. **109**, 186404 (2012).

[229] T. Maier, M. Jarrell, T. Pruschke, and M. H. Hettler, *Quantum cluster theories*, Rev. Mod. Phys. **77**, 1027 (2005).

[230] F. Hayashi, H. Lei, J. Guo, and H. Hosono, *Modulation Effect of Interlayer Spacing on the Superconductivity of Electron-Doped FeSe-Based Intercalates*, Inorg. Chem. **54**, 3346 (2015).

[231] K. V. Yusenko, J. Sottmann, H. Emerich, W. A. Crichton, L. Malavasi, and S. Margadonna, *Hyper-expanded interlayer separations in superconducting barium intercalates of FeSe*, Chem. Commun. **51**, 7112 (2015).

[232] S. Hosono, T. Noji, T. Hatakeda, T. Kawamata, M. Kato, and Y. Koike, *Superconductivity and Intercalation State in the Lithium-Hexamethylenediamine-Intercalated Superconductor $Li_x(C_6H_{16}N_2)_yFe_{2-z}Se_2$: Dependence on the Intercalation Temperature and Lithium Content*, J. Phys. Soc. Jpn. **85**, 104701 (2016).

[233] T. Hatakeda, T. Noji, K. Sato, T. Kawamata, M. Kato, and Y. Koike, *New Alkali-Metal- and 2-Phenethylamine-Intercalated Superconductors* $A_x(C_8H_{11}N)_yFe_{1-z}Se$ *(A = Li, Na) with the Largest Interlayer Spacings and* $T_c \sim 40$ K, J. Phys. Soc. Jpn. **85**, 103702 (2016).

Acknowledgments

First and foremost, I would like to thank Prof. Roser Valentí for accepting me as a PhD student in her group. As her student I particularly enjoyed the multitude and diversity of projects I was assigned. I greatly appreciate the four years of support I have received from her.

Likewise, I thank Harald O. Jeschke for the excellent collaboration across a great variety of projects and his constant support in improving the presentation of our scientific results.

I would like to thank Peter J. Hirschfeld, Andreas Kreisel, Yan Wang, Thomas A. Maier, and Douglas J. Scalapino for numerous valuable discussions about superconductivity mediated by spin fluctuations.

Furthermore, I thank Igor I. Mazin, Matthew D. Watson, and Amalia I. Coldea for many insightful discussions about the physics of iron-based superconductors and the good cooperation across various projects.

I thank Stephen J. Blundell and Simon J. Clarke for making me aware of open questions in the field of intercalated iron selenide.

Moreover, I thank Benedikt Hartmann and Jens Müller for introducing me to the problem of ethylene endgroup conformations in organic charge transfer salts.

I thank my fellow students and researchers Steffen Backes, Michaela Altmeyer, Ryui Kaneko, Kira Riedl, Ying Li, Stephen M. Winter, Aaram J. Kim, Vladislav S. Borisov, Francesc Salvat-Pujol, and Milan Tomić for valuable discussions and the good collaboration.

Finally, I thank the German Academic Scholarship Foundation, as well as my family, for supporting my academic education. My doctoral research was supported by the German Research Foundation through grants SPP 1458 and SFB/TR 49.

Daniel Guterding

Curriculum Vitae

Education

09/13–11/16 **PhD studies in Physics**,
Goethe-Universität Frankfurt am Main, Germany,
Supervisor: Prof. Roser Valentí.

03/13–08/13 **Master of Science (MSc) in Physics**,
Goethe-Universität Frankfurt am Main, Germany,
Thesis title: Density functional study of the de Haas-van Alphen effect and magnetic anisotropy in iron pnictides,
Supervisor: Prof. Roser Valentí.

10/09–02/13 **Bachelor of Science (BSc) in Physics**,
Goethe-Universität Frankfurt am Main, Germany,
Thesis title: Molekulardynamiksimulationen für das Lennard-Jones-Potential,
Supervisor: Prof. Roser Valentí.

08/00–06/09 **High School**, *Butzbach, Germany*.

Scholarships

08/12–08/13 **Danaher Corporation**.

02/10–08/13 **German Academic Scholarship Foundation**.

Publications

16. **D. Guterding**, S. Backes, M. Tomić, H. O. Jeschke, and R. Valentí, *Ab-initio perspective on structural and electronic properties of iron-based superconductors*, Phys. Status Solidi B **254**, 1600164 (2017).
15. **D. Guterding**, H. O. Jeschke, I. I. Mazin, J. K. Glasbrenner, E. Bascones, and R. Valentí, *Non-trivial role of interlayer cation states in iron-based superconductors*, Phys. Rev. Lett. **118**, 017204 (2017).
14. M. Altmeyer, **D. Guterding**, P. J. Hirschfeld, T. A. Maier, R. Valentí, and D. J. Scalapino, *Role of vertex corrections in the matrix formulation of the random phase approximation for the multi-orbital Hubbard model*, Phys. Rev. B **94**, 214515 (2016).
13. J. L. Lado, **D. Guterding**, P. Barone, R. Valentí, and V. Pardo, *Quantum spin Hall effect in weak topological rutile-based oxide multilayers*, Phys. Rev. B **94**, 235111 (2016).
12. **D. Guterding**, R. Valentí, and H. O. Jeschke, *Reduction of magnetic interlayer coupling in barlowite through isoelectronic substitution*, Phys. Rev. B **94**, 125136 (2016).
11. **D. Guterding**, M. Altmeyer, H. O. Jeschke, and R. Valentí, *Near-degeneracy of extended* $s+d_{x^2-y^2}$ *and* d_{xy} *order parameters in quasi-two-dimensional organic superconductors*, Phys. Rev. B **94**, 024515 (2016).
10. K. Riedl, **D. Guterding**, H. O. Jeschke, M. J. P. Gingras, and R. Valentí, *Ab initio determination of spin Hamiltonians with anisotropic exchange interactions: the case of the pyrochlore ferromagnet* $Lu_2V_2O_7$, Phys. Rev. B **94**, 014410 (2016).
9. **D. Guterding**, S. Diehl, M. Altmeyer, T. Methfessel, U. Tutsch, H. Schubert, M. Lang, J. Müller, M. Huth, H. O. Jeschke, R. Valentí, M. Jourdan, and H.-J. Elmers, *Evidence for eight node mixed-symmetry superconductivity in a correlated organic metal*, Phys. Rev. Lett. **116**, 237001 (2016).
8. **D. Guterding**, H. O. Jeschke, and R. Valentí, *Prospect of quantum anomalous Hall and quantum spin Hall effect in doped kagome lattice Mott insulators*, Sci. Rep. **6**, 25988 (2016).

7. **D. Guterding**, R. Valentí, and H. O. Jeschke, *Influence of molecular conformations on the electronic structure of organic charge transfer salts*, Phys. Rev. B **92**, 081109(R) (2015).
6. **D. Guterding**, S. Backes, H. O. Jeschke, and R. Valentí, *Origin of the superconducting state in the collapsed tetragonal phase of* KFe_2As_2, Phys. Rev. B **91**, 140503(R) (2015).
5. **D. Guterding**, H. O. Jeschke, P. J. Hirschfeld, and R. Valentí, *Unified picture of the doping dependence of superconducting transition temperatures in alkali metal/ammonia intercalated FeSe*, Phys. Rev. B **91**, 041112(R) (2015).
4. J. Diehl, S. Backes, **D. Guterding**, H. O. Jeschke, and R. Valentí, *Correlation effects in the tetragonal and collapsed tetragonal phase of* $CaFe_2As_2$, Phys. Rev. B **90**, 085110 (2014).
3. S. Backes, **D. Guterding**, H. O. Jeschke, and R. Valentí, *Electronic structure and de Haas-van Alphen frequencies in* KFe_2As_2 *within LDA+DMFT*, New J. Phys. **16**, 085025 (2014).
2. M. D. Watson, A. McCollam, S. F. Blake, D. Vignolles, L. Drigo, I. I. Mazin, **D. Guterding**, H. O. Jeschke, R. Valentí, N. Ni, R. Cava, and A. I. Coldea, *Field-induced magnetic transitions in* $Ca_{10}(Pt_3As_8)((Fe_{1\text{-}x}Pt_x)_2As_2)_5$ *compounds*, Phys. Rev. B **89**, 205136 (2014).
1. E. Gati, S. Köhler, **D. Guterding**, B. Wolf, S. Knöner, S. Ran, S. L. Bud'ko, P. C. Canfield, and M. Lang, *Hydrostatic-pressure tuning of magnetic, nonmagnetic, and superconducting states in annealed* $Ca(Fe_{1\text{-}x}Co_x)_2As_2$, Phys. Rev. B **86**, 220511(R) (2012).